Journal of Multifunctional Composites

journal homepage: http://jmc.destechpub.com

Mechanical and Thermal Properties of Jute Fibre Reinforced Composites

MOHAMMAD MAZEDUL KABIR, MD MAINUL ISLAM* and HAO WANG

Centre of Excellence in Engineered Fibre Composites (CEEFC), Faculty of Engineering and Surveying, University of Southern Queensland, Toowoomba, Queensland 4350, Australia

KEYWORDS

Natural fibre
Jute
Alkali treatment
Mechanical
Thermal properties

ABSTRACT

Composite materials based on natural fibres, especially jute, have the potential to be used in engineering load bearing applications. Inherent flaws within natural fibres in terms of the presence of hydrophilic hydroxyl groups in their structure absorb atmospheric moisture which reduces the compatibility of these fibres with polymer matrices. Fibre surface modifications using chemical treatments have the potential to improve fibre-matrix compatibility. In this study, jute fibres were treated with different concentration of alkali (NaOH) solutions. The changes in fibre structure after treatment were investigated by Differential Scanning Calorimetry (DSC) and Thermogravimetric Analysis (TGA). Treated fibres were reinforced in polyester matrix to prepare composites by using hand lay-up method. The compatibility between fibre and matrix were analysed through mechanical property testing of the composites. Mechanical properties such as flexural and compressive strength, modulus and strain at break of composites were studied and compared. Best results were observed on compressive and flexural properties respectively for 5% and 7% NaOH treated samples. Thermal stability was also enhanced for the treated fibres. In general, thermal and mechanical properties of the treated fibres and their composites were superior to the untreated fibres.

1. INTRODUCTION

Natural fibres have recently attracted the attention to be used as reinforcement in plastics. The attractive features of these fibres are in the ecological advantages, commercially available and higher specific mechanical properties. These fibres are environmentally friendly, biodegradable, renewable and provides the facility to be used as a green sources of reinforcing materials. Low density, high specific strength and modulus properties of these fibres have the potential to be used in engineering fibre composites for load bearing application with partial replacement of synthetic fibres [1].

Natural fibres such as jute, flax, coir, sisal etc are widely being used as reinforcing fibres in thermoset and thermoplastic matrix. Among these fibres, jute (*Corchorus capsularis*) is commercially available and inexpensive source of lignocellulosic fibre. The approximate chemical composition of this fibre is cellulose (51–84%), hemicellulose (12–20%), lignin (5–13%), pectin (0.2%) and wax (0.5%) [2]. Cellulose is considered as the major framework component of the fibre structure. It provides strength, stiffness and structural stability of the fibre. The cellulose structure of the fibres is distinguished through crystalline and amorphous regions, whereas hemicellulose and lignin are completely amorphous. In cellulose crystalline region, large numbers of strongly linked hydroxyl groups are present. These hydroxyl groups are inaccessible and so other chemicals have difficulty penetrating the crystalline region. However, in the amorphous region, the hydroxyl groups are loosely linked with the fibre structure and are relatively free to react with other chemicals [3]. Due to this freedom, hydroxyl groups present in the amorphous region can easily combine with water molecules from the atmosphere. The hydroxyl groups present in the amorphous hemicellulose and lignin initially give the access of water molecules to penetrate the fibre surface. Wa-

*Corresponding author. tel. +61 7 4631 1338; fax. +61 7 4631 2110
Email: Mainul.Islam@usq.edu.au

doi:10.12783/issn.2168-4286/1.1/Islam

ter molecules then combine with the hydroxyl groups that are present in cellulose (in the amorphous region) and stay in the fibre structure. This makes the fibre hydrophilic and polar in character. Figure 1 shows the schematic structure and the orientation of fibre constituents that absorb moisture. Hydrophilic fibres worsen the ability to develop adhesive characteristics with most hydrophobic binder materials during composite processing. As a result strong bonding between fibre and the binder materials are compromised which reduced the composites mechanical properties. This problem can be addressed by treating these fibres with suitable chemicals. Treatments can decrease the amorphous hydroxyl groups, remove the lignin and hemicellulose coverings from the fibre surface and expose the cellulose structure to react with binder materials. Different types of fibre surface treatments were used by several researchers by using diverse type of chemicals and methods. Among which alkali treatment is economically viable and more effective fibre surface treatment to improve composite properties. Cellulose, hemicellulose and lignin constituents of fibre are sensitive to the action of NaOH [4]. Treatment reduces hydroxyl groups that present in the amorphous region of fibre (Fibre-OH + NaOH $\rightarrow$ Fibre-ONa + H_2O). Due to this hydrophilic nature of the fibre reduced. Alkali treatment also takes out a certain portion of hemicellulose and lignin covering materials. As a result, larger number of possible reaction sites of cellulose is available for matrix (binder) adhesion [5–6].

Yan *et al.* [7] and Dipa & Sarkar [8] reported that alkali treatment breaking down the fibre bundle by removing hemicellulose, lignin and waxy substances from the cellulose surface. This increases effective surface area of fibre and facilitate the cellulose hydroxyl groups to react with binder materials. Prasad *et al.* [9] used 5% NaOH for 76 hours and showed 40% higher flexural strength properties of treated coir-polyester composite compared to the untreated sample. Leonard *et al.* [10] used 0.16% NaOH treatment on hemp fibre for 48 hours and found treated fibre composites had 30% and 50% higher tensile and shear properties. Dipa *et al.* [11] used 5% NaOH treatment on jute fibres for 2 to 8 hours and showed 35% and 20% improved flexural strength and modulus respectively for the treatment of 4 hours. Viviana *et al.* [12] reported hemicellulose and lignin constituents were sensitive to higher temperature and removal of these constituents increased 4% higher thermal stability of hemp fibre after 8% NaOH treatment.

These studies have been focused on the different concen-

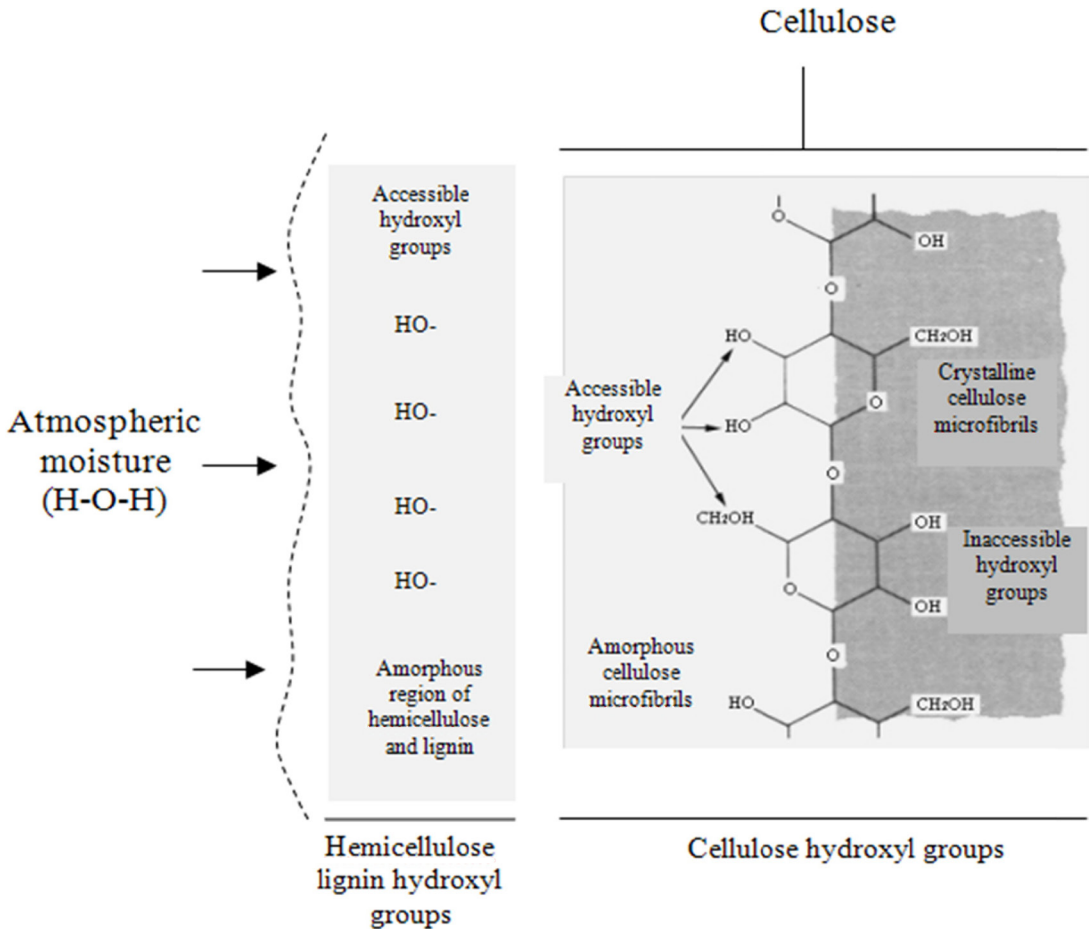

Figure 1. *Schematic presentation of the orientation of fibre constituents that absorb moisture.*

tration of alkali treatment on jute fibres. The treatment effect changes the content of cellulose, hemicellulose and lignin constituents of the fibre. Theses constituent changes can be detected by thermal (TGA and DSC) analysis. TGA aids in demonstrating the reaction mechanisms of fibres which occur at the molecular level of the fibre constituents as a function of progressive temperature. Fibre constituents degrades at different temperatures and results in weight loss. DSC allows a measurement of the chemical changes among the fibre constituents when subjected to heat. Untreated and treated jute fabric was reinforced in polyester matrix to prepare composites. The treatment effects on fibre-matrix interface bonding were investigated through mechanical property analysis. Experimental three point bending and compression tests were carried out in order to compare the stiffness and load-carrying capacity of these composites containing untreated and treated fibres.

2. EXPERIMENTAL

2.1. Constituent Materials

The woven jute fabric (jute gunny bag) was collected from the local market in Australia. T102 regular (paraffin) wax was used as a mold releasing agent. General purpose unsaturated polyester resin was used as matrix and methyl ethyl keton peroxide was utilised as a curing catalyst.

2.2. Fibre Surface Treatment

The alkali treatments used different concentrations of NaOH solution. The solution was prepared by adding 4%, 5%, and 7% NaOH (by weight) in a water ethanol mixture (water: ethanol = 80 : 20). It was then stirred at room temperature for an hour. Jute fabrics were soaked with different concentrations of NaOH solutions for 3 hours at room temperature. The fibres were then washed several times with distilled water to allow absorbed alkali to leach from the fibre. The washed fibres were dried at room temperature for 8 hours, and then oven dried at 100°C for another 6 hours. The dried fibres were stored in a sealed plastic bag to avoid atmospheric moisture contamination prior to thermal analysis and composite processing.

2.3. Composite Processing

Jute fabric reinforced polyester composite was prepared by hand lay-up process. In this process, the fibre-matrix mixing occurred in an open mould (a flat carbon steel sheet was used as a mould). The mould was waxed several times with a mould releasing agent. The first layer of jute fabric was laid over the mould and the polyester matrix (with 1.5% MEKP) was spread over the fibre carefully to ensure maximum fibre matrix wetting. A roller brush was used in the fibre-matrix mixing process. Extreme care was taken to achieve a uniform matrix distribution throughout the fibre cross-sections in the sample and removed any possible entrapped air in the matrix. Then the second layer of jute fabric was placed on the top of the first layer and above process was repeated. Afterwards, a waxed flat glass plate was placed on the top of the mat with a weight to ensure smother surface of the fabricated composites. The fibre content was 25% of the weight of the produced samples. The samples were kept at room temperature overnight then post cured at 80°C for 4 hours. The sample was released from the mould and kept in an oven at 80°C for 4 hours to post-cure. The cured panel (400 × 400 mm^2) was trimmed and sectioned for mechanical testing.

3. TEST METHODS

3.1. Differential Scanning Calorimetry (DSC)

DSC analysis on treated fibres was performed by using a thermal analyser (DSC Instrument, Model No. Q100). Fibre samples (between 6 to 10mg) were heated between the temperature ranges of 10°C to 450°C at a rate of 10°C/min. The experiment was conducted in a nitrogen environment purged at 20 ml/min. Nitrogen was used for efficient heat transfer and removal of volatiles from the sample. Each fibre sample was analysed separately and overlapped for comparison.

3.2. Thermogravimetric Analysis (TGA)

TGA analysis on treated fibres was carried out by a thermal gravimetric analyser (TGA-Model No. Q500). Between 6 mg to 10 mg of fibres was taken for analysis. Fibre samples were heated between the temperature range of 25°C to 500°C at a rate of 10°C/min. Experiments were carried out in a helium medium (60 ml/min) and the weight was recorded as a function of increasing temperature. The heating conditions were constant for all treated fibre samples.

3.3. Flexural Test

Flexural testing of the composites was conducted following ISO 14125 (1998) by using a 10 kN MTS testing machine at a loading rate of 2 mm/min. The specimens were simply supported and tested under 3-point loading with the span set at approximately 16 times the thickness of the specimen. Six specimens were tested for each sample. The test setup and instrumentation are presented in Figure 2. The load was applied at mid-span of the specimens, perpendicular to the fibre direction. Before each test, the loading pin was set to almost touch at the top surface of the specimen. To determine the strength and elastic properties in bending the load and mid-span deflection were recorded up to the specimen failure.

Figure 2. *Flexural test setup of composite specimen.*

3.4. Compression Test

Compression testing was carried out on the composites following ISO 14126 (1999) by using a 100 kN MTS machine with a loading rate of 1 mm/min. Six specimens were tested for each sample. The specimens were cut in to the dimension of $L \times W = 140$ mm $\times$ 12 mm and were clamped in a Wyoming Modified Celanese Compression test fixture. The load was applied in parallel to the fibre direction and the resulting deformation was recorded until failure.

4. RESULTS AND DISCUSSION

The thermal and mechanical properties of treated fibre and their composites were compared with the untreated samples.

4.1. DSC Analysis of Fibres

DSC analysis is used to determine the thermal energy released or absorbed via chemical reactions of the fibre constituents during heating. A series of exothermic and endothermic reactions take place during sample decomposition at different temperatures [13]. The magnitude and location of the exothermic and endothermic peaks indicate the thermal phase transformation of the fibre. In the case of an endothermic event, heat is absorbed by the sample, whereas heat is released in an exothermic event. Endothermic reactions provide information on sample melting, phase transitions, evaporation, dehydration and pyrolysis. Exothermic reactions provide information on crystallisation, oxidation, combustion, decomposition and chemical reactions [14].

From Figure 3 it can be observed that both untreated and treated fibres shows one broad endothermic peak between the temperatures of 10–150°C. This peak was corresponded to the evaporation of moisture absorbed by the fibre. From Table 1 it can be observed that, for untreated fibre moisture evaporation temperature (which was 77.07°C) was higher than that for the alkali treated fibres (79.18–85°C). This is might be the case of treated fibres has less moisture content compared to the untreated fibres [15].

The region between 150–250°C shows no exothermic or endothermic changes which reflects fibres are thermally stable between these temperatures. It was reported that, lignin starts degrading at a temperature around 200°C. Therefore, hemicellulose and cellulose degrades at higher temperatures [16]. Hence the exothermic peak higher than 200°C is associated with the thermal degradation of lignin, hemicellulose and cellulose constituents. The first exothermic peak in Figure 3 for untreated fibre was observed at a temperature around 300°C, which was associated to the degradation of hemicellulose. For treated fibres, the heat required to generate these peaks were higher than the untreated sample indicated treatment removed hemicellulose from the fibre. Afterwards, there was a very strong endothermic peak for untreated fibre at about 368°C, however, treated fibres showed exothermic peak at this region (340–400°C). This indicated the degradation of lignin and cellulosic matters form the treated fibres. From Table 1 it can be observed that less temperature (350–360°C) were required for the treated fibres exothermic peak compared to the untreated fibre (368°C). This was due to the removal of lignin and cellulosic matters from the treated fibre with the effect of alkali treat-

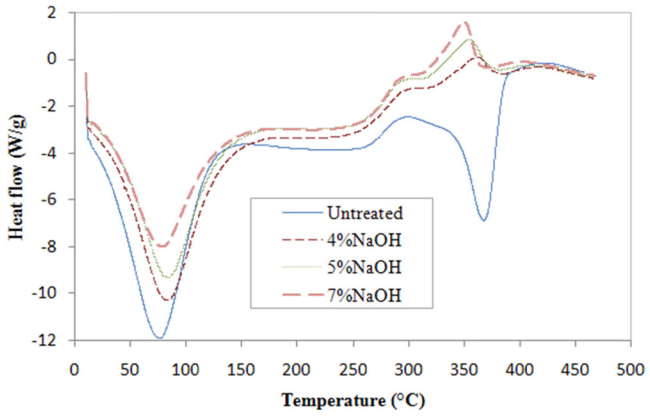

Figure 3. *DSC analysis of the fibres.*

Table 1. Thermal Analysis of Jute Fibre.

		DSC Analysis (Thermal Degradation)			TGA Analysis (Thermal Degradation)		
		1st Stage (Moisture Evaporation)	2nd Stage (Hemicelluloses and Lignin)	3rd Stage (Cellulosic Components)	1st Stage (Moisture Evaporation)	2nd Stage (Hemicelluloses and Lignin)	3rd Stage (Cellulosic Components)
Fibre Treatment		Tempt Range 10–150°C	Tempt Range 280–320°C	Tempt Range 340–400°C	Weight (%)	Weight (%)	Weight (%)
Untreated		77.07	299.26	368.44	8.88	26.10	80.41
NaOH treated	4%	84.07	307.99	361.04	5.55	18.32	75.59
	5%	84.90	312.21	354.95	7.98	21.07	63.40
	7%	79.17	290.80	350.40	6.75	28.91	61.02

ment. For untreated fibres these constituents were present and absorbed higher temperature to degrade. From this analysis it can be stated that, alkali treatment removed hemicellulose, lignin and cellulosic matters from the fibre surface. As a result fibres become more thermally stable, improved hydrophobic nature and facilitate better adhesion possibilities with the matrix.

4.2. TGA Analysis of Fibres

Thermo gravimetric analysis (TGA) was used to measure the weight loss of fibres as a function of rising temperature. The weight loss in fibres occurs due to the decomposition of cellulose, hemicellulose and lignin constituents during heating. Higher decomposition temperatures give greater thermal stability [17].

From Figure 4 it can be observed that, there are three stages of weight loss occurred as temperature increased. The first stage of weight loss was observed between 25–150°C, which was correspondence to the release of moisture content by the fibre. The second stage of weight loss occurred within the temperature between 200–380°C, which was related to the degradation of lignin and hemicellulose. The last stage of weight loss occurred between the temperature of 310–380°C, indicated the degradation of cellulose and other cellulosic matters from the fibre [15].

From Figure 4 it can be observed that, untreated fibre degraded faster than the treated fibres in the second stage of fibre degradation process. From this result, it can be stated that hemicellulose and lignin constituents were partially removed from the treated fibres which enhanced thermal stability of fibre. This was evidenced by the degradation rate of the treated fibre with higher temperature and by lowering the weight loss compared to the untreated fibre. From Table 1 it can be observed that in every stages of weight loss (%) for treated fibre was less than the untreated fibre. These results also indicated that treatment reduced the moisture and constituent (hemicellulose and lignin) contents of fibre and exhibited greater thermal properties.

4.3. Flexural Properties of the Composites

Flexural properties of untreated and treated fibre composites are shown in Figure 5 and Table 2. During testing various load distribution mechanisms, such as tension, compression and shear between fibre and matrix were taken place simultaneously [18]. As a result, different failure modes were observed such as bending, shear and matrix cracking on the tested samples. From Table 2 it is observed that treated fibre composites has higher flexural strength properties compared to the untreated fibre composites. The flexural strength of the untreated fibre composites was 39.63 MPa, whereas for 4%, 5% and 7% NaOH treated fibre composites showed 18%, 32% and 31% higher strength properties respectively. Figure 5 presents stress-strain behaviour of the untreated and treated samples. Treated samples exhibited higher failure strain (2.66–3.81%) properties compared to the untreated samples (2.52%). The difference in flexural properties of

Table 2. Mechanical Properties of the Composites.

		Flexural Properties			Compressive Properties		
Type of Reinforcing Fibre		Flexural Strength (MPa)	Flexural Modulus (GPa)	Strain at Break (%)	Compressive Strength (MPa)	Compressive Modulus (GPa)	Strain at Break (%)
Untreated		39.63	1.56	2.52	56.09	0.75	7.42
NaOH treated	%	47.91	1.77	2.70	57.42	0.44	12.97
	%	57.16	1.49	3.81	69.01	0.88	7.77
	%	56.75	2.13	2.66	55.63	0.65	8.59

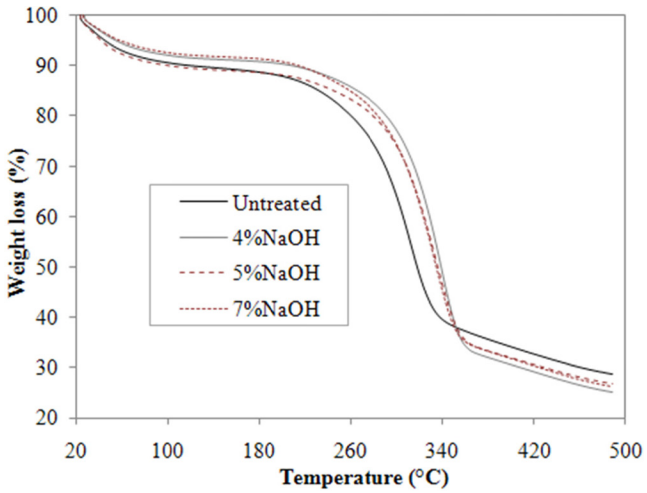

Figure 4. *TGA analysis of the fibres.*

the composites supported well as the untreated fibre holds moisture due to the presence of hemicellulose, lignin and cellulosic matters in its structure. As a result, ineffective interfacial bonding between the fibre and matrix occurred and showed poor mechanical properties. On the other hand, due to the partial removal of hemicellulose, lignin and cellulosic matters from the fibre by the action of alkali treatment better bonding with the matrix achieved and showed improved mechanical properties. Several authors reported similar observations on improved flexural properties after alkali treatment of reinforcing fibres [19].

4.4. Compressive Properties of the Composites

Compressive properties of untreated and treated fibre composites are presented in Figure 6 and Table 2. From Table 2 it is observed that, 5% treated sample showed 19% and 15% higher compressive strength and modulus than the untreated samples. The stress-strain behavior in Figure 6 also exhibited higher failure strain properties for the treated composites compared to the untreated samples. 4%, 5% and 7% treated fibre composites showed 48%, 45% and 22%

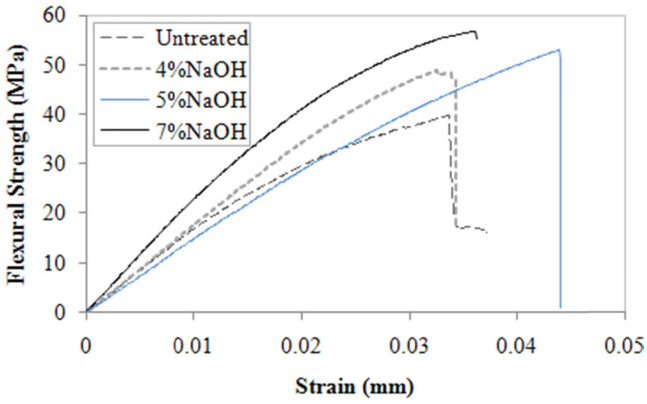

Figure 5. *Flexural properties of the composites.*

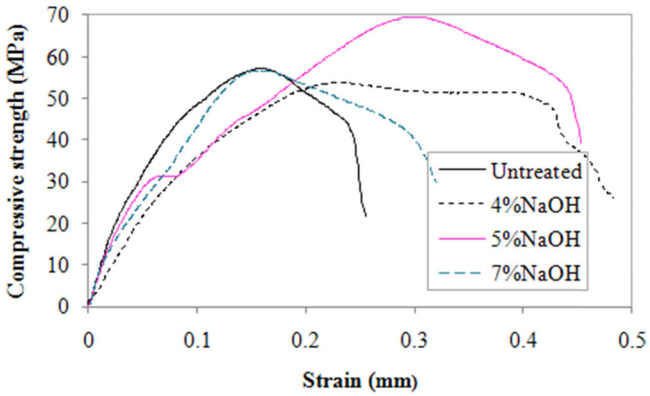

Figure 6. *Compressive properties of the composites.*

higher strain compared to the untreated samples. These results indicate that better fibre matrix interface bonding was achieved in case of treated fibre composites. This was due to the removal of fibre surface coverings (hemicellulose and lignin) by NaOH treatments. The removal of the fibre surface coverings facilitated strong interfacial bonding with matrix materials. Strong interfaces prevented fibre buckling into the matrix, which ultimately delayed the formation of matrix cracks. Greater stress transfer from matrix to fibres took place and thus composite exhibited higher compression properties.

5. CONCLUSIONS

Following conclusions can be drawn from the above results and discussion:

1. Jute fibre surface was modified by the different concentration of alkali treatment. This treatment removed hemicellulose, lignin and cellulosic constituents from the fibre. As a result, hydrophilic tendency of fibres were reduced and also exhibited higher thermal stability. This provides better interfacial adhesion between the fibre and matrix.
2. Alkali treated fibre composites had higher flexural properties compared to the untreated samples and the properties became greater at higher treatment concentrations (5-7%NaOH). These results indicate treatment reduced moisture from the fibre by removing hemicellulose, lignin and cellulosic constituents and thus improved compatibility with the matrix which resulted superior mechanical properties.
3. Compressive properties of treated composite samples showed higher failure strain properties. The higher properties indicate greater adhesion between the treated fibre and matrix were achieved which allowed the sample to take larger deflection before failure.

From the above discussion, it can be stated that alkali treatment on jute fibres achieved some degree of success in

improving thermal and mechanical properties of the fibre and composites. This method of fibre modification will help to develop natural fibre composites with better performance under load bearing conditions.

ACKNOWLEDGEMENT

The authors gratefully acknowledge assistance from Mr. Wayne Crowell in mechanical testing and providing helpful suggestions regarding this study.

REFERENCES

[1] D. Ray, B.K. Sarkar, A.K. Rana, N.R. Bose, Effect of alkali treated jute fibres on composite properties, *Bulletin of Materials Science,* Vol. 24, pp. 129–135 (2001). http://dx.doi.org/10.1007/BF02710089.

[2] A.K. Mohanty, M. Misra, G. Hinrichsen, Biofibres, biodegradable polymers and biocomposites: An overview, *Macromolecular Materials and Engineering,* Vol. 276-277, pp. 1–24 (2000). http://dx.doi.org/10.1002/(SICI)1439-2054(20000301)276:1<1::AID-MAME1>3.0.CO;2-W.

[3] J.C.F. Walker, Primary wood processing: principles and practice, 2nd edition, 2006, Springer Verlag, Netherlands. http://dx.doi.org/10.1007/s12034-009-0010-3.

[4] E. Sinha, S.K. Rout, Influence of fibre surface treatment on structural, thermal and mechanical properties of jute fibre and its composite, *Bulletin of Materials Science,* Vol. 32, pp. 65–76 (2009).

[5] Y.M. Leonard, M.P. Ansell, The effect of chemical treatment on the properties of hemp, sisal, jute and kapok fibres for composite reinforcement, *Angewandte Macromolecular Chemistry*, pp. 109–110 (1999).

[6] S.K. Acharya, P. Mishra, S. C. Mishra, Effect of environment on the mechanical properties of fly ash-jute-polymer composite, *Indian Journal of Engineering & materials Sciences,* Vol. 15, pp. 483–488 (2008).

[7] L. Yan, M. Yiu-wing, Y. Lin, Sisal fibre and its composites: a review of recent developments, *Composites Science and Technology,* Vol. 60, pp. 2037–2055 (2000). http://dx.doi.org/10.1016/S0266-3538(00)00101-9.

[8] R. Dipa, B.K. Sarkar, Characterization of alkali treated jute fibres for physical and mechanical properties, *Journal of Applied Polymer Science,* Vol. 80, pp. 1013–1020 (2001). http://dx.doi.org/10.1002/app.1184.

[9] S.V. Prasad, C. Pavithran, P.K. Rohatgi, Alkali treatment of coir fibres for coir-polyester composites, *Journal of Materials Science,* Vol. 18, pp. 1443–1454 (1983). http://dx.doi.org/10.1007/BF01111964.

[10] Y.M. Leonard, T. Nick, J.C. Andrew, Mechanical properties of hemp fibre reinforced euphorbia composites, *Macromolecular Materials and Engineering,* Vol. 292, pp. 993–1000 (2007). http://dx.doi.org/10.1002/mame.200700092.

[11] R. Dipa, B.K. Sarkar, A.K. Rana, N.R. Bose, Effect of alkali treated jute fibres on composite properties, *Bulletin of Materials Science,* Vol. 24, pp. 129–135 (2001). http://dx.doi.org/10.1007/BF02710089.

[12] P.C. Viviana, V. Claudia, M.K. Jose, V. Analia, Effect of chemical treatment on the mechanical properties of starch-based blends reinforced with sisal fibre, *Journal of Composite Materials,* Vol. 38(16), pp. 1387–1399 (2004). http://dx.doi.org/10.1177/0021998304042738.

[13] J.D. Menczel, L. Judovits, R.B. Prime, H.E. Bair, M. Reading, S. Swier, Differential scanning calorimetry (DSC), *Thermal Analysis of Polymers,* pp. 7–239 (2009).

[14] R. Ball, A. McIntosh, J. Brindley, Feedback processes in cellulose thermal decomposition: implications for fire-retarding strategies and treatments, *Combustion Theory and Modelling,* vol. 8 (2), pp. 281–91 (2004). http://dx.doi.org/10.1088/1364-7830/8/2/005.

[15] M. Pracella, D. Chionna, I. Anguillesi, Z. Kulinski, E. Piorkowska, Functionalization, compatibiliza-tion and properties of polypropylene composites with hemp fibres, *Composite Science and Technology,* Vol. 66, pp. 2218–2230 (2006). http://dx.doi.org/10.1016/j.compscitech.2005.12.006.

[16] E. Sinha, S.K. Rout, Influence of fibre surface treatment on structural, thermal and mechanical properties of jute fibre and its composite, *Bulletin of Materials Science,* Vol. 32, pp. 65–76 (2009). http://dx.doi.org/10.1007/s12034-009-0010-3.

[17] H.J. Kim, Y.G. Eom, Thermogravimetric analysis of rice husk flour for a new raw material of lignocellulosic fiber thermoplastic polymer composites, *Journal of the Korean Wood Science and Technology,* vol. 20 (3), pp. 59–67 (2001).

[18] G. Venkata Reddy, T. Shobha Rani, K. Chowdoji Rao, S. Venkata Naidu, Flexural, compressive and interlaminar shear strength properties of kapok/glass composites, *Journal of Reinforced Plastics and Composites,* Vol. 28, pp. 1665–1677 (2009). http://dx.doi.org/10.1177/0731684408090362.

[19] L. Mwaikambo, M. Ansell, Chemical modification of hemp, sisal, jute, and kapok fibers by alkalization, *Applied Polymer Science,* Vol. 84, pp. 2222–2234 (2002). http://dx.doi.org/10.1002/app.10460.

Journal of Multifunctional Composites

journal homepage: http://jmc.destechpub.com

Novel Approach for Optimisation of Fibre Bragg Grating Sensor Network for Efficient Damage Detection in Composite Structures

GAYAN C. KAHANDAWA[1,*], JAYANTH A. EPAARACHCHI[1], JOHN CANNING[2] and K.T. LAU[3]

[1]*Faculty of Engineering and Surveying, Centre of Excellence in Engineered Fibre Composites, University of Southern Queensland, Australia*
[2]*Interdisciplinary Photonic Laboratories, School of Chemistry, University of Sydney, Sydney, Australia*
[3]*The Hong Kong Polytechnic University, Hong Kong, China*

KEYWORDS

FBG Sensors
Composite structures
Structural Health Monitoring

ABSTRACT

With the increased use of fibre reinforced composites in load bearing structures especially in the aerospace industry, it is crucial to have *in-situ* structural health monitoring systems to ensure safe operation of the structure. When it comes to using fibre Bragg grating sensors for the task, it is not possible to monitor the structure using a single sensor. Consequently, many FBG sensors are needed for monitoring the integrity of a complex composite structure. Randomly placed or uniform sensor networks prevent the optimisation of sensor layout required for efficient detection of damage. In addition, provision for error or insensitivity must be avoided in the process of structural health monitoring.

This paper details research work conducted to develop a procedure for optimising an FBG sensor network. Furthermore, procedures for the immediate rehabilitation of FBG sensor networks due to obsolete/broken sensors, has also been investigated. In this study, an artificial neural network (ANN) was developed and successfully deployed to virtually simulate the broken/obsolete sensors in a FBG sensor network. The prediction of the ANN network was found to be within 0.1% error levels.

INTRODUCTION

The increased use of FRP composites for load bearing structures has alerted related industries to the urgent need for structural health monitoring (SHM) systems that ensure the safe operation of the critical composite structure. A major reason for this need is the unresolved problems associated with the failure modes and mechanisms of FRP composites. Damage detection in FRP structures using embedded FBG sensors, has been an emerging research topic for threedecades [1–6]. FBG based SHM systems are using multiple numbers of FBG sensors for competent and robust operation [5]. However, the addition of FBG sensors to a network simultaneously increases the complexity, installation problems and cost of implementation. A logical solution to these problems is the use of an optimized number of FBG sensor in a network. However, there is no engineering solution to replace a lost or obsolete FBG sensor in an optimized network attached to a composite component. This leaves a huge void in the process of developing FBG based SHM systems for composite structures.

Several researchers have used ANN based systems for SHM in different stages [7–9]. The excellent predictive ability of the ANN makes it ideal for the prediction of parameters correlated to multiple parameters. In circumstances where the correlation is complex and difficult to identify as a function, the learning process in an ANN provides the ability to work even without a function and provides promising results when fed inputs not encountered during the training process [10–12]. One of the commonly used neural network architectures for function approximation is the Multi-Layer Perceptron (MLP). Back-Propagation (BP) algorithms are used in a wide range of applications to design MLPs suc-

*Corresponding author. Email: gayan@usq.edu.au

doi:10.12783/issn.2168-4286/1.1/Kahandawa

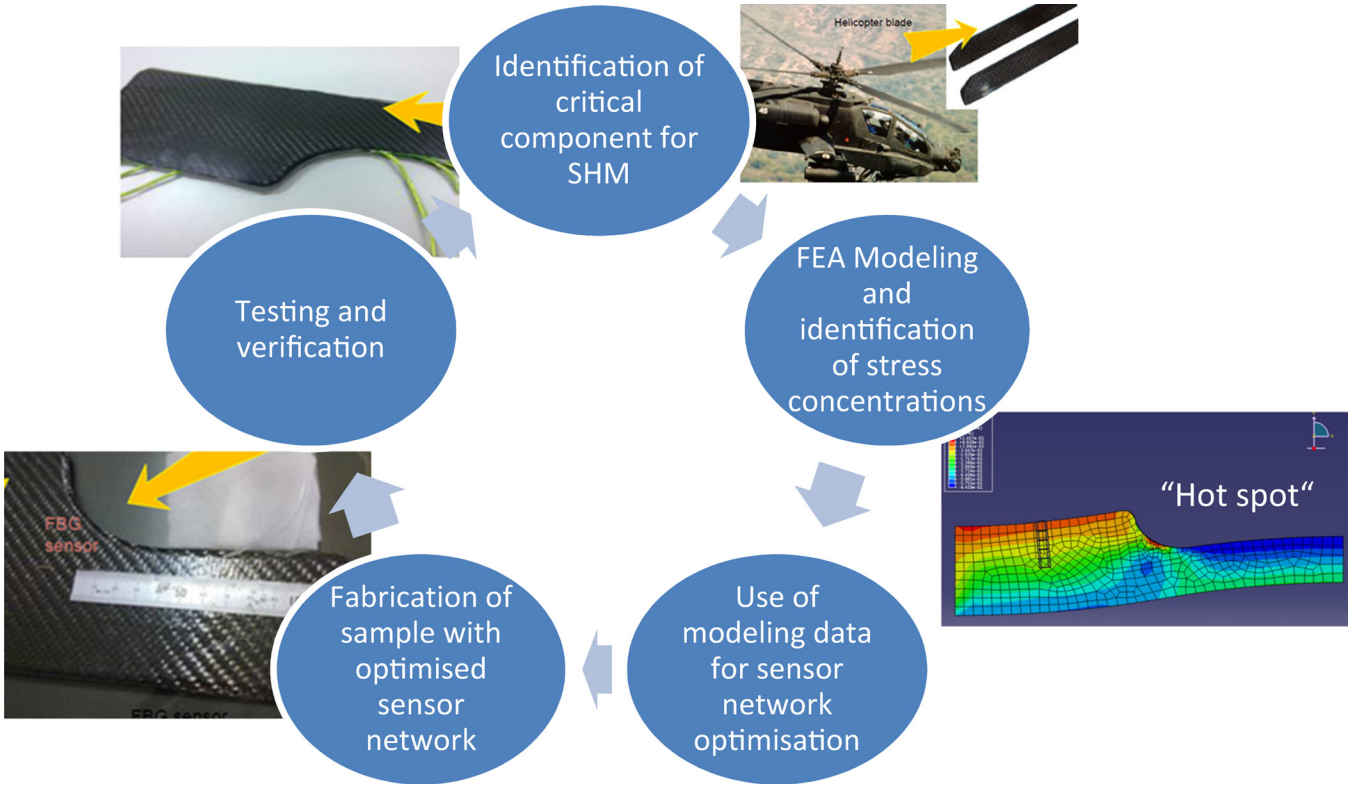

Figure 1. *Process of locating FBG sensors.*

cessfully [8].The ANN is famous for the classification of spectral data.

Zhang *et al.*, used an ANN to improve the FBG signal detection system [13]. They used an ANN to eliminate errors in the conversion of optical signal to electrical signal. Veiga *et al.* used an ANN to improve the reliability of the FBG signal under power variations of a light source [14]. Gayan *et al.* have shown a novel method to decode FBG spectrum and convert a wave length domain signal into a time domain signal which can easily be fed into any decision making system such as ANN [15]. As such the versatility ofan ANN for the processing of non-linear parameters is proven by internationally conducted research in a variety of fields. In this case of strain prediction using a highly complex strain field, the use of an ANN is highly advantageous. This paper details a study that was carried out for the optimization of a sensor network to monitor a complex strain field of a critical location of a helicopter blade using a developed ANN and a finite element simulation.

THE PROCESS OF OPTIMISATION OF A FBG SENSOR NETWORK

The process of optimisation of the FBG sensor network is graphically illustrated in Figure 1. Initially, the critical load bearing structural component needs to be identified. To identify the critical structural component, actual operating loading and/or the design loading can be used. To identify stress concentration as a whole and the stress variations in each layer, the component must be modelled in the FEA environment using all, or critical, load cases. The strain values around the stress concentration have been used as strain readings of simulated FBG sensors in those particular locations. The FEA

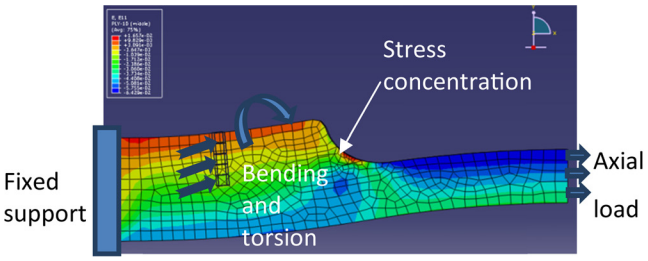

Figure 2. *Strain variation in helicopter blade base combined loading.*

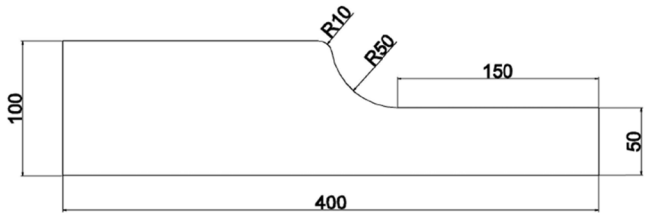

Figure 3. *Specimen configuration (all dimensions are in millimeters).*

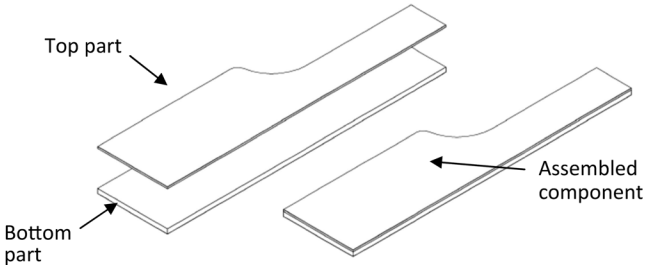

Figure 4. *Two parts of the model.*

generated strain values (simulated FBG readings) have been used with an ANN to identify damage and/or damage initiation in the pre-identified stress concentration.

To decide on the number of sensor locations, the learning rate (epoch) of ANN was used as the measure. The optimum number of FBG sensors was identified at the lowest epoch, which is obtained when the ANN is operating with its highest learning rate. The learning rate is a measure which gives the correlations in between ANN inputs. If the ANN inputs have strong correlation, learning of the ANN is efficient and the learning rate higher. Consequently, the epoch reduces. If the correlation in between ANN inputs is weak, the learning process is difficult and learning rate lower, and as a result, the epoch will be higher.

In this case study, the ANN inputs are the strain reading from FBG sensors (or simulated), and hence the learning rate or the epoch of ANN can be used as a measure of the correlation between each sensor in the sensor network. As a result, it is possible to identify the sensor network which gives the lowest epoch, indicating the identified sensor network where the sensors have a strong correlation to each other. Subsequently to find the optimized number of sensors for the network, the amount of sensors used in the network was reduced one by one and the ANN was trained for each case until lowest epoch remaining unchanged by a significant amount.

With the optimised number of FBG sensors and their corresponding locations, a specimen was fabricated for verification of the performance of the network. Using the same load cases used in the FEA modelling environment, the specimen was tested. The experimental data was used with the ANN and the result obtained was used to verify the optimised FBG network.

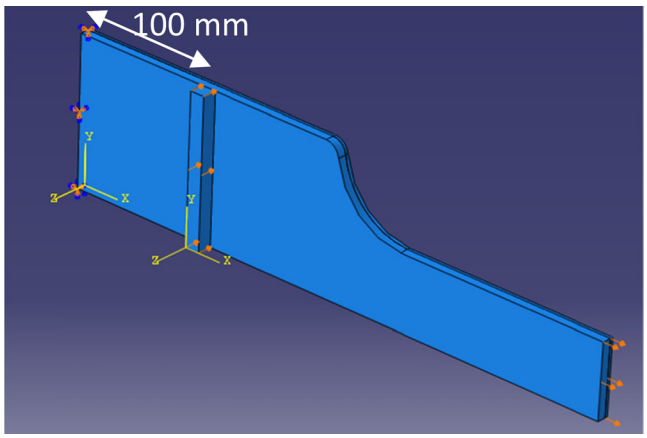

Figure 5. *Applied load on the component.*

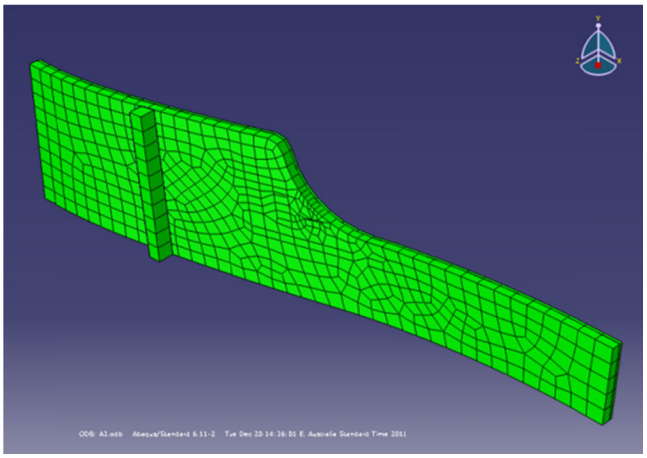

Figure 6. *Deformed shape of the component.*

The main advantage of this optimisation process is the possibility of deciding the number the locations of FBG sensors in the modelling environment. The following study details the use of the proposed process to optimise the FBG sensor network in a helicopter blade base structure.

IDENTIFICATION OF THE LOCATIONS OF FBG SENSORS IN A COMPOSITE STRUCTURE TO DETECT DAMAGE USING FEA SIMULATION

As a case study, a helicopter blade base structure has been investigated. A complete Finite Element Analysis (FEA) together with an experimental verification was used for the investigation. Thehelicopter blade base structures underwent complex loading conditions in the forms of axial, bending and torsion during the operation, [16,17] and combined loading was simulated in FEA.Initially, acritical section of the component wasidentified using FEA simulation. The strain values at particular locations in the structure (the simulated FBG sensors) were entered into an ANN (ANN1) and the ANN was trained for various combinations of strain values occurring under many different combined loading applications.This procedure was repeated until the ANN's prediction of strain at any location under any combined loading application within 0.1% accuracy.

Next,a delamination was introduced in the FEA mesh and the ANN was fed the strain values at the same locations. At this stage ANN output is decision on Yes/No for "extra-ordinary strain field change".

The procedure was repeated with varying numbers of FBG sensors until the prediction of the algorithm was reached within a 0.1% error level. The optimal number of FBGs was taken at 0.1% error level.

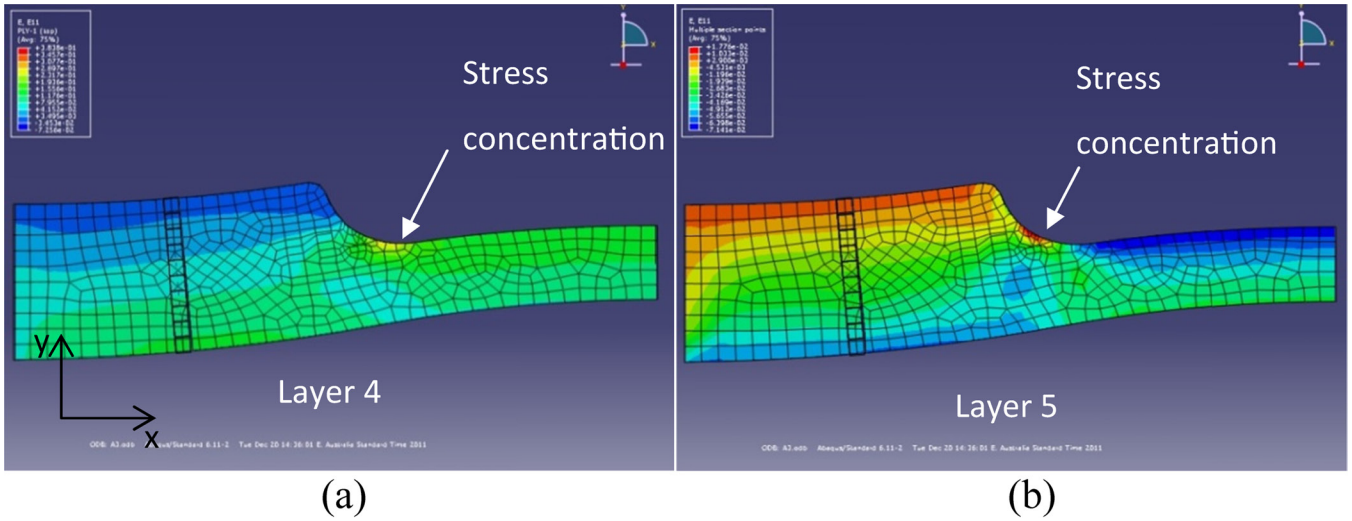

Figure 7. *Strain variation in x direction (E11) (a) layer 4 (b) layer 5.*

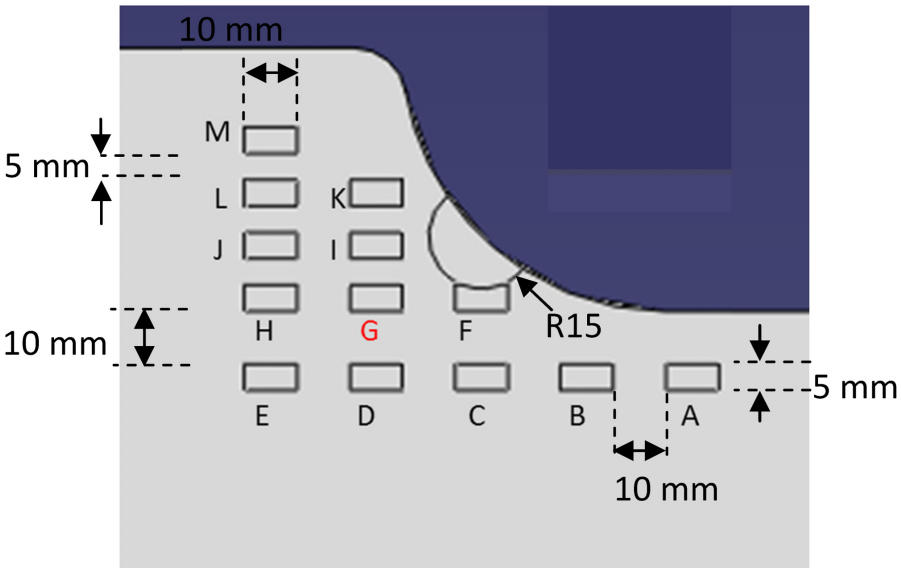

Figure 8. *Locations of the FBG sensors.*

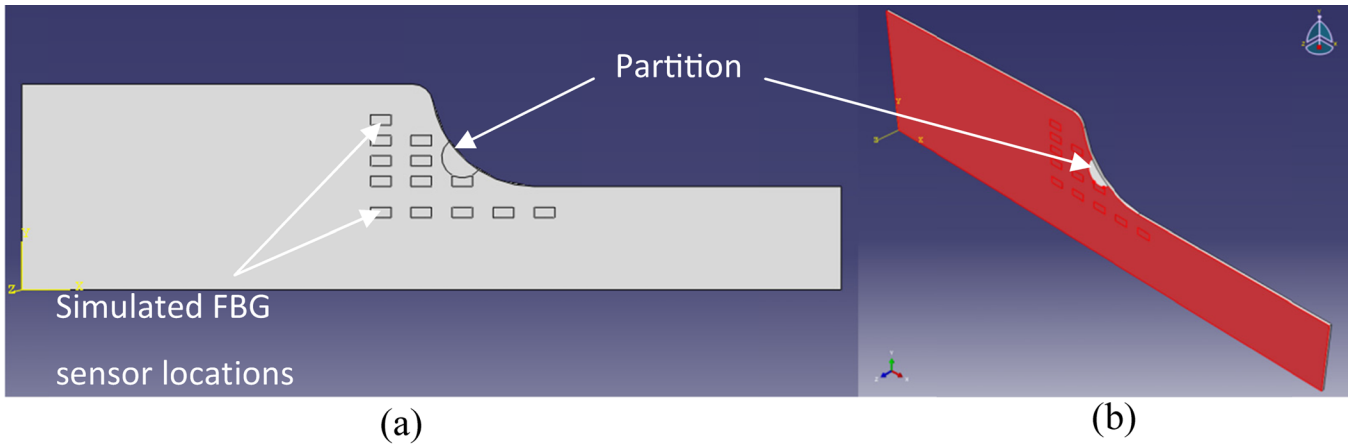

Figure 9. *Delamination in the component.*

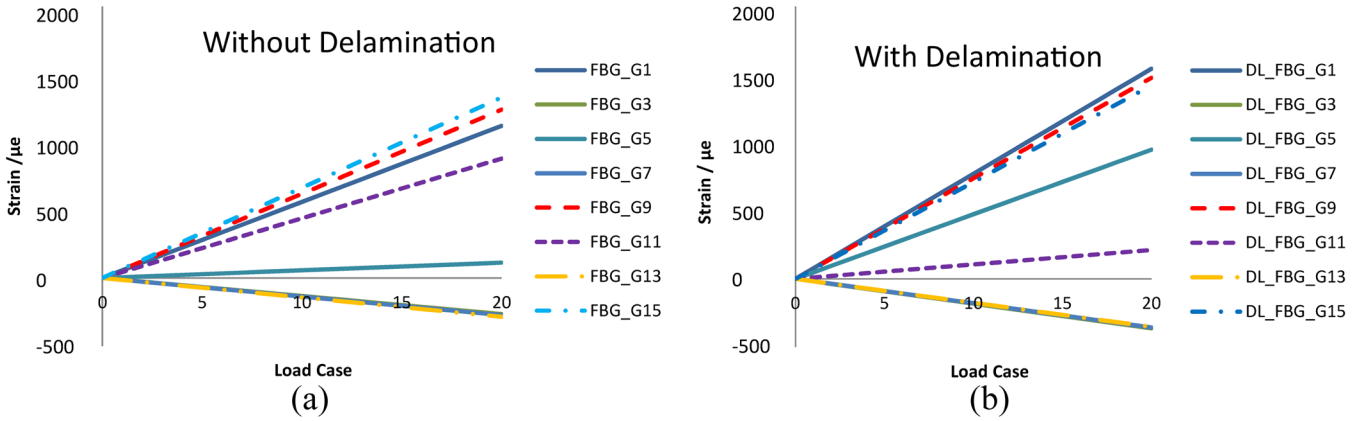

Figure 10. *Variation of strain in location G under combined loading.*

APPLICATION OF OPTIMISATION TECHNIQUES TO A FBG SENSOR NETWORK IN A HELICOPTER BLADE BASE STRUCTURE

A critical portion of a selected helicopter blade base structure was modelled with the commercial FEA software ABAQUS. The load cases were selected using the operation loads which a helicopter blade base would experience while in operation. Figure 2 shows the strain variation observed from simulation of a helicopter blade base under axial tension and torsion loading.

In the real testing environment, due to the limitations of the test equipment, it is difficult to load the specimen in axial, bending and torsion at the same time. Because of these limitations in the test rig, only axial and bending loading was used for the experiment. However, for the process of identifying stress concentrations in the modelling environment, axial, bending and torsional loading were used (as shown in the Figure 2).

The laminated structure with 16 layers with layup $[0°/0°/90°/90°/–45°/+45°/90°/0°/]_s$, was modelled and the geometry of component is given in Figure 3. To accommodate the modelling of delamination, the structure was modelled in two parts as shown in Figure 4. The top part of the specimen consisted of 4 layers with lay-up [0°/0°/90°/90°]of the total thickness 2 mm. The bottom part consisted of 12 layers with lay-up [–45°/+45°/90°/0°/0°/90°/+45°/–45°/90°/90°/0°/0°] of the total thickness 6 mm. Part 1 and Part 2 were initially rigidly connected to each other to make one component using surface constrains available in ABAQUS.

The bulk material properties were adopted as follows: E1 = 34.412 GPa, E2 = 6.531 GPa, E3 = 6.531 GPa, ν12 = 0.217, ν13 = 0.217, ν23 = 0.336, G12 = 2.433 GPa, G13 = 2.433 GPa, and G23 = 1.698 GPa in the direction of angle 0° (x axis). The model consisted of a mesh with 737 elements and 1674 nodes using SC8R elements which were 8-node quadrilateral in-plane general-purpose continuum shell elements. Use of SC8R elements reduces integration with hourglass control and finite membrane strains with the composite option for the cross-section description.The component was rigidly supported on one side as shown in Figure 5, and axial load of 10kN and bending load of 500N was applied in 20 steps. Table 1 shows the loading in each load case. The strain distribution of the component was ob-

Table 1. Load Cases Used in the FEA Loading.

Load Case	Axial Load (N)	Bending Load (N)
1	500	25
3	1500	75
5	2500	125
8	4000	200
10	5000	250
12	6000	300
15	7500	375
17	8500	425
20	10000	500

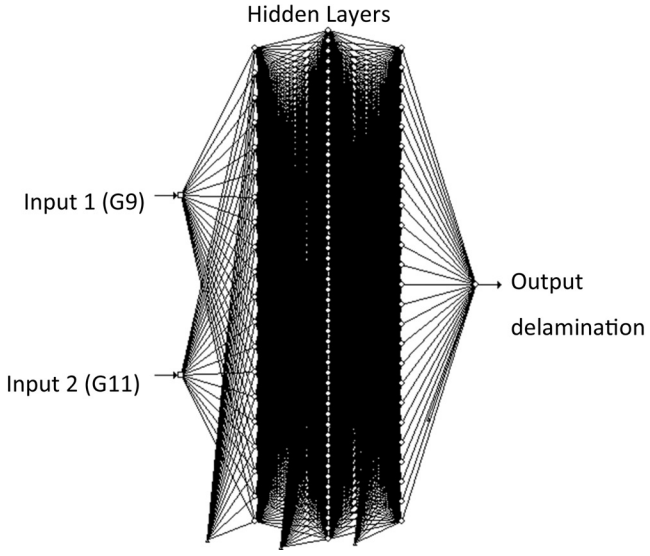

Figure 11. *ANN used to identify delamination (ANN1).*

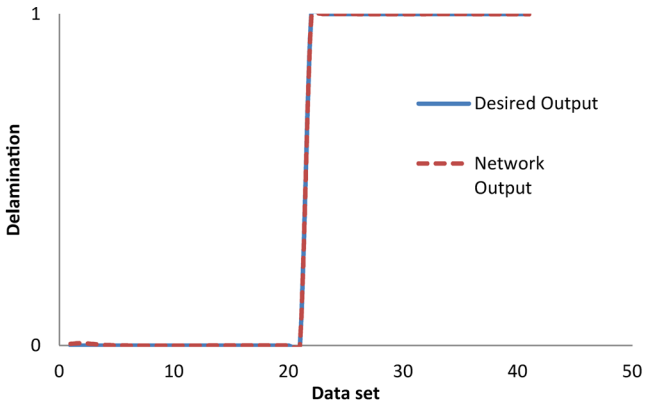

Figure 12. *Identification of delamination using ANN1.*

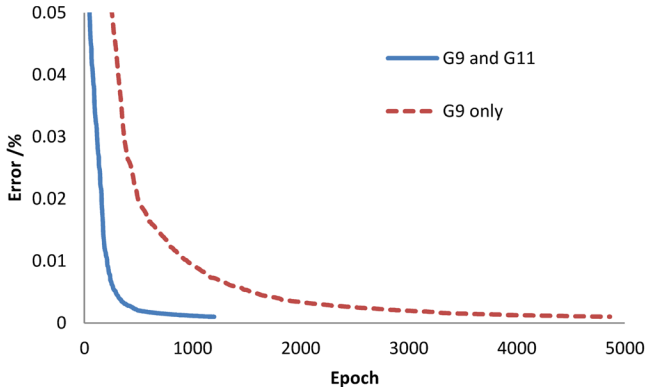

Figure 13. *Learning rate of the ANN with two sensor data (G9 and G11) and single sensor data (G9).*

served for each layer of the laminate. As the experimental test rig limited the loading in torsion, only axial and bending loading was used for the comparison with the experimental results.

Figure 6 shows the deformed shape of the 3D model at the end of the analyses (loading step 20, Table 1).The strain distribution of the component was observed for each layer of the laminate.

Figure 7 shows the stress concentrations in x direction (E11) in the adjacent layers, layers 4 and 5. The concentration point has shifted slightly from layer 4 to layer 5 as shown in theFigure 7(a) and Figure8(b). Considering the mismatch in strain distribution, the stress concentration was identified as a potential point for damage initiation.

Initially 13 locations (A to M) were selected as locations for FBG sensors, as shown in Figure 8. Reference source not found.8. Initial placement was arbitrary and strain readings from the top surface of each layer (1 to 16) were extracted. The total number of locations for FBG sensors was 208 (13 × 16) in the beginning of the study. For an example, the notation "A1" provides the sensor in location "A", layer 1. For the 20 loading steps, the strain reading in E11 direction were recorded.

In the FEA model, rectangular elements, 10mm long and 5 mm wide, were used as FBG sensors. Average top surface strain in X direction (E11) is used as a representation of strain calculated using the FBG sensors. Those simulated FBG readings were used to train the ANN.

After identifying the hot spot, in the next FEA model semicircular delamination was simulated in the "hot spot".

MODELLING DELAMINATION IN THE HELICOPTER BLADE BASE STRUCTURE

For modelling purposes, the delamination used in this study was considered as "ideal delamination" with no friction between separated surfaces. In the simulation of delamination, the contact surface of the top part was partitioned as shown in Figure 9(a). Only the partitioned semicircular section (Figure 9(b)) was not connected to the bottom part, and the surface interaction was set to "friction less".

Sensor G9 (which is the sensor in the location G and placed on top of layer 9) was used as the deteriorating sensor (obsolete sensor).

ANALYSIS OF FEA DATA WITH AN ANN

Extracted FEA data for E11 for all sensor locations for both models, first without delamination, and second with delamination, were used as representations of FBG readings in each load case. Strain readings in the location G for with-

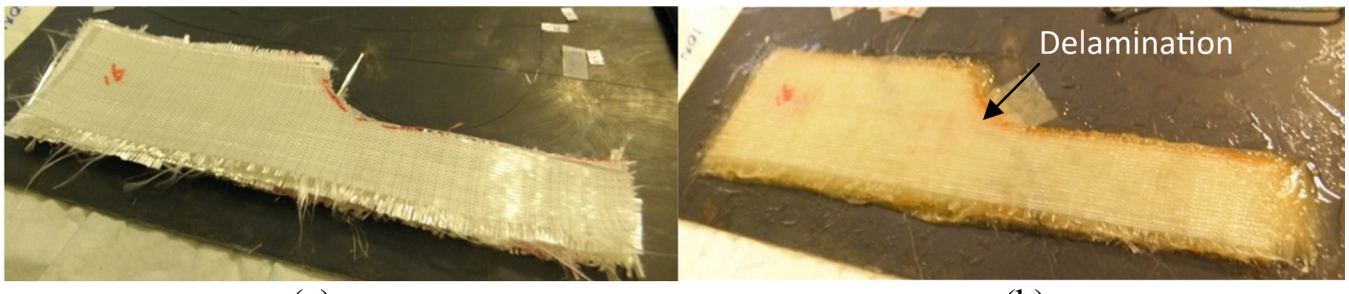

Figure 14. *The fabrication of the specimen with embedded FBG sensors.*

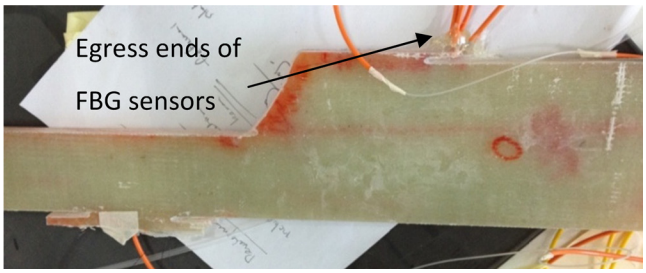

Figure 15. *Specimen with FBG sensors.*

out delamination and with delamination models are given in Figure 10(a) and Figure 10(b) respectively.

As illustrated in Figure 10, there was a clear effect on the strain reading at location G resulting from delamination. Sensor G9 is selected as the sensor for identification of delamination in the model. The delamination is located in between layers 4 and 5. Sensor G9 was placed in layer 9, and hence,was reasonably located to sense the strain variation due to the damage. Strain needs to be transferred through layers 6, 7 and 8 to layer 9. As illustrated in Figure 10, the strain level increased in layer 9, and in layer 11 the same strain levels decreased from the model with and without delamination.

IDENTIFICATION OF DELAMINATION USING FBG DATA GENERATED BY FEA

Generated FBG readings were used to identify the existence of delamination using an ANN1. In both the models, with delamination and without delamination, the data was extracted for each location (A to M) and each layer (1 to 16). But for the identification of delamination it was found that, even with a single sensor, the ANN could identify the delamination accurately. For the identification of the delamination in this study, an ANNwith three hidden layers has been used. Hidden layers 1, 2 and 3 contain 20, 50 and 25 neurons, as shown in Figure 11 (ANN1).

Figure 12 gives the ANN output and the actual existence of delamination. With sensor readings G9 and G11, the ANN predicted the existence of delamination in 1201 epoch.With sensor G9 only, it took 4878 epoch to identify delamination with 0.1% error. Figure 13 shows the learning rate of the ANN with two sensors and single sensor.

From the study, it was shown that the identification of delamination is possible with even a single sensor in the modelling environment. It is also important to investigate the effect of losing an embedded sensor to the efficient functionality of the damage detection mechanism.

EXPERIMENTAL VALIDATION OF THE OPTIMISED SYSTEM

Using the FEA analysed data and the ANN, the optimum number of sensors has been determined, as have the optimal sensor locations. With the results from the aforementioned study, an FRP specimen was fabricated with embedded FBG

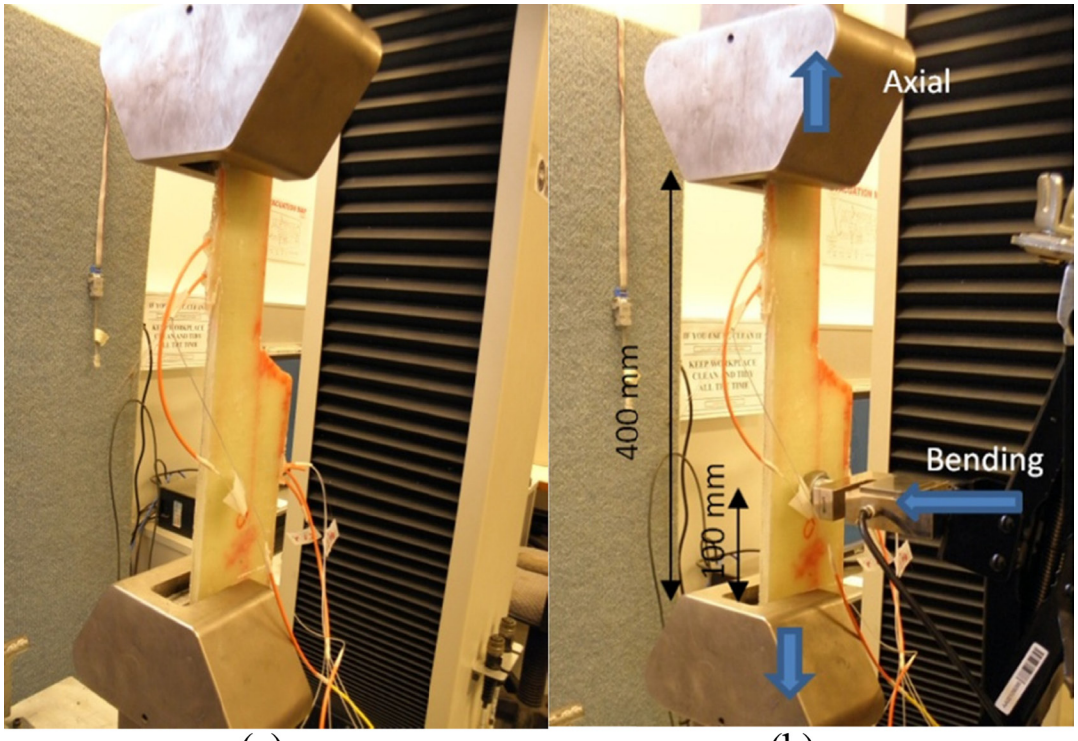

Figure 16. *Experimental setup.*

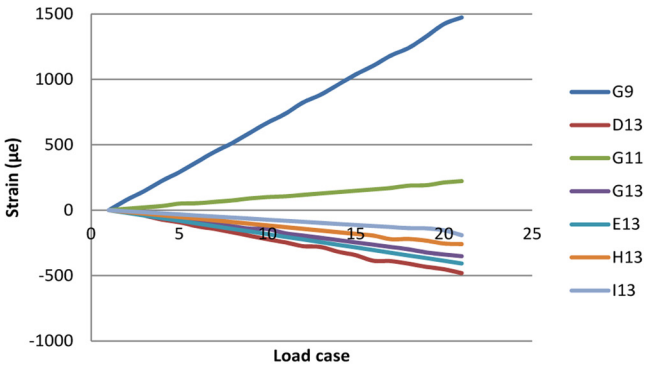

Figure 17. *Strain readings for 20 loading steps.*

sensors in identified locations (G9, D13, E13, G13, H13, G11 and I13).

Fabrication of the Specimen

The structural component was fabricated with E glass fibre mats using epoxy resin. The laminate was fabricated with fibre orientation $[0/0/90/90/–45/45/90/0]_s$, similar to the FEA model. The geometry of the specimen is illustrated in Figure 3. The woven fabric fibre layup is shown in the Figure 14(a). The locations of the FBG sensors were decided using the FEA analysis with the use of ANN1. The sensor G9 was used as the sensor to identify the delamination. During the fabrication of the sample, seven FBG sensors, in locations G9, D13, E13, G13, H13, G11 and I13, were embedded.

Furthermore, simulated delamination was created in the specimen as shown in the Figure 14(b). The completed specimen is shown in the Figure 15.

EXPERIMENTATION

The component was rigidly supported on one side as shown in Figure 16(a), and an axial load of 10kN and bending load of 500N were applied in 20 steps. The loading arrangement is shown in the Figure 16(b).

The FBG reading in each load case was decoded. The load cases are given in the Table 2.

Table 2. Load Cases for the Loading of the Component.

Load Case	Axial Load	Bending Load
1	500N	25N
5	2500N	125N
10	5000N	250N
15	7500N	375N
20	10000N	500N

RESULTS AND DISCUSSION

The strain reading at each load case was recorded, and is shown in Figure 17.

Figure 18 shows the comparison of FEA generated strain and recorded strain for sensor G9. The predictions for the other sensors showed similar accuracy.

Subsequently, the sensor G9 was disconnected and the other sensor readings were used to predict the G9 reading. Similarly, as in the case previously discussed, the FBG readings for sensors D13, E13, G13, H13, G11 and I13, were used with an ANN to predict the sensor G9 as shown in the

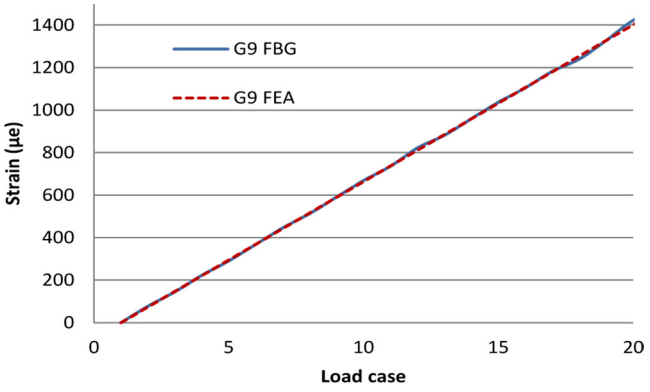

Figure 18. *Comparison of FEA results with FBG readings for sensor G9.*

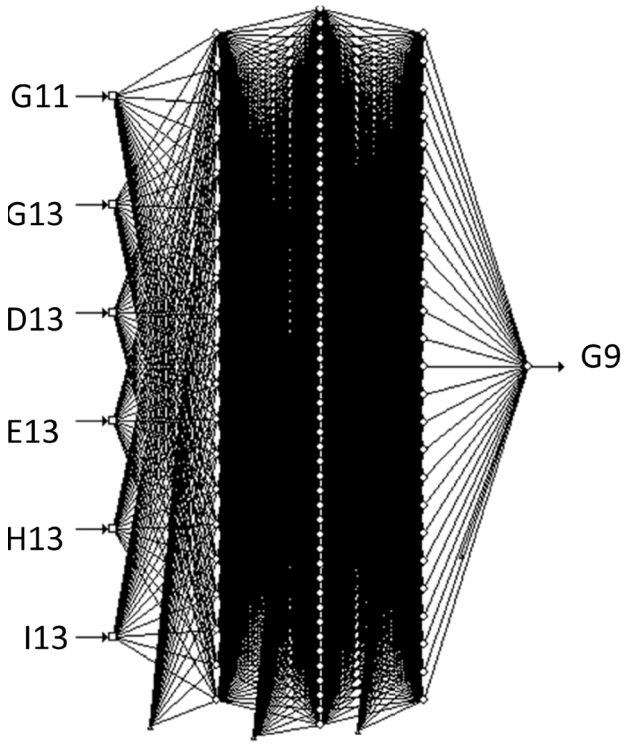

Figure 19. *ANN used to predict sensor G9 (ANN2).*

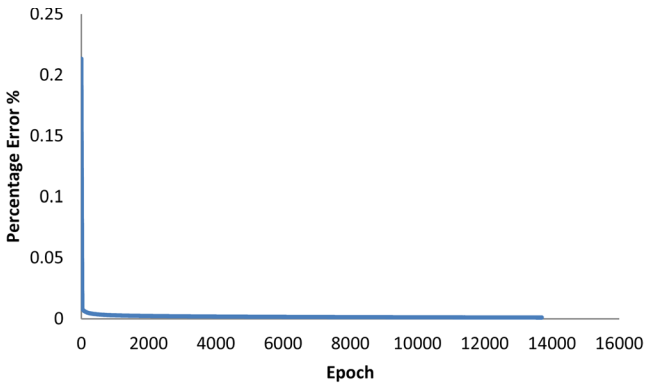

Figure 20. *Training rate of the ANN.*

Figure 19. The ANN (ANN2) used six input neurons and one output neuron. Three hidden layers, 1, 2, and 3, were used with 20, 50 and 25 neurons respectively.

The ANN predicted the sensor G9 with 0.1% accuracy after 13719 epoch as shown in the Figure 20.

The optimum number of sensors required to identify potential damage in a composite structure was considered. A complete FEA model was used to identify the sensor locations, to efficiently detect a defect. With the results, number and locations of the FBG sensors obtained from the modelling environment, an FRP sample was fabricated with embedded FBG sensors. The FRP sample was loaded and the FBG results were used with the ANN for prediction of obsolete sensor.

Compared to the training epoch 9236 obtained from the FEA data, the experimental data took 13719 epoch to predict the obsolete sensor with 0.1% accuracy.

CONCLUSIONS

A process for setting up an optimized FBG sensor network in a FRP structure was proposed using FEA modelling and ANNs. As a case study, the FBG sensor network in the root of a helicopter blade was investigated. The optimised FBG sensor network was fabricated into a FRP composite helicopter blade structure. The performance of the FBG network was found to be excellent.

Furthermore, the case of a lost critical FBG sensor from an optimised network while in operation was investigated. It was found that the operational data acquired from the FBG network while the obsolete sensor was in operation, can be used with an ANN to estimate the obsolete sensor. Hence, it was found that the use of an ANN for managing FBG sensor networks and post-processing FBG sensor network data, increases the efficiency and robustness of the SHM system.

REFERENCES

[1] Y. Okabe, T. Mizutani, S. Yashiro, N. Takeda, *Application of small-diameter FBG sensors for detection of damages in composites,* SPIE, Newport Beach, CA, United states, 2001, pp. 295–305.

[2] S. Takeda, Y. Okabe, N. Takeda, *Detection of delamination in composite laminates using small-diameter FBG sensors,* SPIE, San Diego, CA, United states, 2002, pp. 138–48.

[3] G. Kahandawa, J. Epaarachchi, H. Wang, K. Lau. Use of FBG sensors for SHM in aerospace structures. *Photonic Sensors. 2* (2012) 203–14. http://dx.doi.org/10.1007/s13320-012-0065-4.

[4] Y. Okabe, T. Mizutani, S. Yashiro, N. Takeda. Detection of microscopic damages in composite laminates. *Composites Science and Technology.* 62 (2002) 951–8. http://dx.doi.org/10.1016/S0266-3538(02)00009-X.

[5] G.C. Kahandawa, J.A. Epaarachchi, H. Wang, K.T. Lau, *Use of network of FBG sensors for efficient detection of delamination in FRP structures,* ACCM8, KualaLumpur, Malaysia, 2012.

[6] G.C. Kahandawa, Z.M. Hafizi, J.A. Epaarachchi, K.T. Lau, *Detecting delamination in a composite structure using an Embedded FBG—AE hybrid System,* ACAM 7, Adilade, Australia, 2012.

[7] A. Hosni Elhewy, E. Mesbahi, Y. Pu. Reliability analysis of structures using neural network method. *Probabilistic Engineering Mechanics.* 21 (2006) 44–53. http://dx.doi.org/10.1016/j.probengmech.2005.07.002.

[8] P.A.M. Lopes, H.M. Gomes, A.M. Awruch. Reliability analysis of laminated composite structures using finite elements and neural networks. *Composite Structures.* 92 (2010) 1603–13. http://dx.doi.org/10.1016/j.compstruct.2009.11.023.

[9] A.S. Paterno, J.C.C. Silva, M.S. Milczewski, L.V.R. Arruda, H.J. Kalinowski. Radial-basis function network for the approximation of FBG sensor spectra with distorted peaks. *Measurement Science and Technology.* 17 (2006) 1039. http://dx.doi.org/10.1088/0957-0233/17/5/S17.

[10] E. Lewis, C. Sheridan, M. O'Farrell, D. King, C. Flanagan, W.B. Lyons, et al. Principal component analysis and artificial neural network based approach to analysing optical fibre sensors signals. *Sensors and Actuators A: Physical.* 136 (2007) 28–38. http://dx.doi.org/10.1016/j.sna.2007.02.012.

[11] N. Lopes, B. Ribeiro, Hybrid learning in a multi-neural network architecture, Neural Networks, 2001. *Proceedings. IJCNN '01. International Joint Conference* on, 2001, pp. 2788–93 vol.4.

[12] S.V. Kartalopoulos. *Undertanding Neural Networks and Fuzzy Logic: Basic Concepts and Applications* IEEE Press, 1995.

[13] J. Zhang, H. Zhao, X.-w. Rong, *Application of BP neural network in FBG sensing system performance improvement, Electronic Packaging Technology & High Density Packaging,* 2008. ICEPT-HDP 2008. International Conference on, 2008, pp. 1–4.

[14] C.L.N. Veiga, L.S. Encinas, A.C. Zimmermann, Neural networks improving robustness on fiber Bragg gratings interrogation systems under optical power variations, in: D.S. David (Ed.), *SPIE,* 2008, p. 700462.

[15] G.C. Kahandawa, J.A. Epaarachchi, H. Wang, K.T. Lau, *Prediction of obsolete FBG sensor using ANN for efficient and robust operation of SHM systems,* APWSHM 2012, Melboune, Australia, 2012.

[16] P.M. Pawar, R. Ganguli. On the effect of progressive damage on composite helicopter rotor system behavior. *Composite Structures.* 78 (2007) 410–23. http://dx.doi.org/10.1016/j.compstruct.2005.11.043.

[17] R. Ganguli, I. Chopra, D.J. Haas. Helicopter rotor system fault detection using physics based model and neural networks. *AIAA J.* 36 (1998) 1078–86. http://dx.doi.org/10.2514/2.483.

Journal of Multifunctional Composites

journal homepage: http://jmc.destechpub.com

Hybrid Thin Film Lithium Ion-Graphite Composite Battery Laminates: An Experimental Quasi-static Characterization

FEDERICO GASCO* and PAOLO FERABOLI

Department of Aeronautics & Astronautics, University of Washington, Box 352400, Seattle, WA, 98195-2400, USA

KEYWORDS

Multifunctional structures
Energy harvesting
Energy storage
Smart structures

ABSTRACT

The concept of a multifunctional laminated composite airframe material for load bearing and electrical energy storage is proposed. The laminated structure is comprised of integrated solid state thin film lithium-ion batteries and carbon fiber/epoxy laminae. Mechanical and electromechanical tests were conducted in order to characterize the stress-strain field and determine the operational envelope of the hybrid laminate featuring the current thin film battery technology. The limits of applicability of classical analysis methods in mechanics of composite materials were assessed and several critical failure modes were determined to support the design of the next generation of airborne structural thin film batteries.

1. INTRODUCTION

The consolidation of batteries and airframe into a multifunctional structure can theoretically reduce the aircraft weight by exploiting the battery components as load bearing elements, by eliminating batteries supports and by enabling distributed power supply and storage, potentially reducing the amount of wiring. Currently sought-after for unmanned aerial vehicles (UAV), this design solution could lead to a significant improvement of the flight endurance of electrical propeller-driven aircraft [1,2]. To realize this vision, new constituents and a novel design of the composite material system have to be developed to enable simultaneous electrical energy storage and mechanical load bearing capabilities.

Research on lithium-polymer (Li-Po) batteries showed that elastic moduli and strengths of mechanically reinforced batteries as high as 1.02 GPa and 3.9 MPa respectively can be achieved, retaining a specific electrical energy of 160 Wh/kg [3,4]. These pioneering works proved the capability of the multifunctional airframe concept for a micro-UAV. However the lack of stiffness of the battery packaging [4], as well as the plasticized state of the relatively thick organic polymer electrolyte [5], compromises the mechanical properties of the current Li-Po technology. Furthermore today's available electrode materials, consisting of lithium intercalation compounds, are such that high specific energy and specific power, as well as good mechanical properties cannot be achieved [3,4,6,7]. In [6] a battery with an equivalent Young's modulus of 3.1 GPa was developed, whereas the specific energy dropped to 35 Wh/kg. The causes of the low electrochemical performance were the insufficient electrical capacity of the carbon nano-fiber reinforced lithium transition metal oxide cathode and the low ionic conductivity of the solid state polymer electrolyte. These multifunctional composites can lead to a system improvement for applications with either low mechanical or electrical demands. However, mechanical and electrical performances have to be simultaneously increased in order to fulfill the high specific modulus and strength, as well as the high specific electrical energy and power, required by a lightweight airborne application. The literature review gives evidence that improvements are needed not only in the multifunctional performance of the electrolyte and the electrodes, but also in the mechanical design of the composite structure.

Organic polymer electrolytes with engineered mechanical

*Corresponding author. Ph.: +1-206-979-6440. Fax: +1-206-543-0217;
Email: gasco@uw.edu

doi:10.12783/issn.2168-4286/1.1/Gasco

properties have been studied for three decades as solid state electrolytes [5]. Their ionic conductivity is still inadequate to deliver the power density required by most conventional applications, explaining why they are exclusively employed in a gel state obtained by plasticizing them with the addition of liquid electrolytes, as confirmed by the most recent studies, like [8]. Notably in [9–11] the effects of constituents concentration and glass transition temperature, polymers chemistry and architecture on the electrolyte multifunctional properties were thoroughly investigated by synthesizing and analyzing a large variety of vinyl ester-based solid electrolytes and epoxy-based gel electrolytes. The study demonstrated and characterized the inverse correlation between ionic conductivity and elastic modulus, but it also showed a promising trend of increased multifunctional performance, with conductivities approaching the values required for thin film batteries.

Cathode materials are the limiting factor in today's battery systems in terms of specific capacity and specific power, due to their low rate of ionic diffusion and electronic conductivity. For this reason they typically have to be mixed with electrically conductive diluents [12,13]. Adding a large quantity of structural binder to the mixture, as needed to accomplish the load bearing function, causes the specific and volumetric electrochemical performances to drop even more. This is particularly undesirable for aeronautical applications.

The development of a structural anode seems to be a relatively easier task because available anode bulk materials have an intrinsically higher specific capacity than cathode materials. Above all are silicon and graphite, the latter being not only an intercalation material for lithium ions, but also an electrically conductive and structural material [7].

In order to meet the requirements for the next generation of airborne load bearing batteries, solid state thin film Li-ion batteries (TFB) with nanostructured electrodes were recently proposed [8,14–25], Figure 1. The thin film structure maximizes the specific contact surface between electrodes and electrolyte, thereby increasing the stored energy and power per unit mass by increasing the fraction of reactants and the rate of the electrochemical reaction respectively. In fact, downsizing the electrodes and electrolyte to a thin film dramatically reduces the path length for ionic and electronic transport, allowing to achieve the desired conductivity without utilizing diluents or micro-porous compounds [5,14].

Scalable manufacturing processes for nanostructured materials, such as electrospinning, chemical vapor deposition (CVD), atomic layer deposition (ALD) and others are suitable for TFB manufacturing. The future application of nano-scale technology to the electrode materials can potentially lead to several advantages. First, it enables further increase of TFB specific energy and power by decreasing the path length of Li-ion and electronic transportation, allowing full exploitation of the theoretical electrical capacity of the materials [14–18]. It can also implement energy storage and load bearing multifunctionality more efficiently than bulk materials, through engineered nanocomposites comprised of electrochemically active nanostructures bound by an electrically conductive reinforced composite. Lastly, nanostructured materials allow better accommodation of the cycling strain induced by the mechanical boundary conditions and by Li-ion insertion and removal. The latter is a known cause for low durability and capacity fading of electrode materials, in particular for silicon, which provides the highest capacity among the known anode materials [15,19–21]. However, nanostructured electrodes are not technology ready. Although several of such cathode materials were synthesized from lithium transition metal oxides, vanadium or manganese oxides and transition metal phosphates [14,17,18], as well as anode materials from silicon and graphite [8,15,16], none of them are commercially available. The reason is the complex synthesis, the low packing of particles and the occurrence of undesirable reactions with the electrolyte that undermines durability.

Finally, all the battery materials have to be solid state

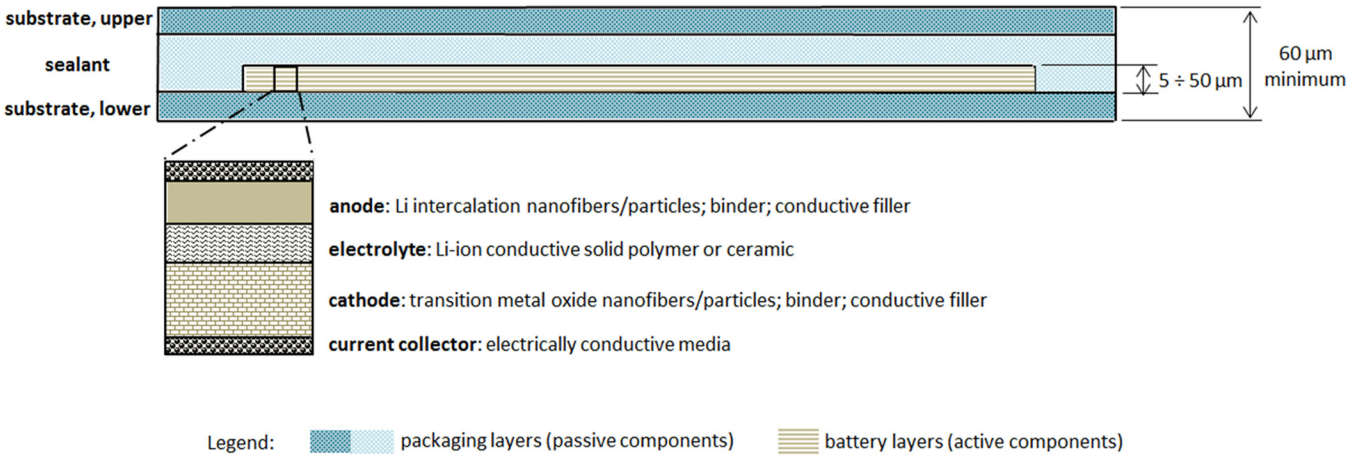

Figure 1. *Cross-sectional schematic of a next generation all-solid state thin film Li-ion battery (TFB). Typical thicknesses are indicated. Envisioned design is based on current research status on nanostructured electrode materials.*

to ensure three-dimensional continuity of the load path at any point within the structure, as the presence of discontinuities, such as porosity, voids or delaminations, is a major threat for the mechanical integrity of a composite laminate. Solid state batteries also ensure higher safety since they do not leak hazardous chemicals if a mechanical failure of the packaging occurs. In addition, the solid state electrolyte is also not combustible and does not suffer from thermal runaway, which can cause explosion of conventional lithium-ion prismatic batteries. Besides, a liquid electrolyte would not allow the manufacturing of a thin film cell because of its liquid surface tension and because of the need of a porous separator between the electrodes to avoid electrical shorting.

The low TFB thickness, typically less than 300 μm, facilitates the integration within thin sections and laminated composite structures, but it also implies that a significant weight fraction of the battery is constituted by the packaging layers. The simplest configuration of the battery packaging is comprised of three layers, Figure 1: a lower substrate provides mechanical support for the in-situ deposition process of the electrochemical cell components; a sealant layer ensures that the highly reactive and hygroscopic cell materials are sealed; an upper substrate provides an almost symmetric stacking sequence. Such a casing allows safe processing and lasting operation of the TFB outside of the deposition chamber, while providing in-plane strength and stiffness to the battery lamina.

The integration of TFBs and structural composite laminae, such as carbon fiber/epoxy (CFRP) plies, into a hybrid thin film lithium ion-graphite composite battery (TFB-CFRP) laminate poses manufacturing and design challenges. The compatibility of the commercial state-of-the-art TFB cell to the epoxy based composite curing pressures and temperatures was previously assessed by the authors. This electrochemical cell was comprised of a nanocrystalline lithium cobalt oxide ($LiCoO_2$) cathode, a ceramic LiPON ($Li_{2.9}PO_{3.3}N_{0.46}$) electrolyte and a metallic lithium (Li) anode, Figure 2 and Figure 3. The study, which is published separately, successfully determined the cure cycle and the TFB charge level that prevented the physiochemical degradation of the electrochemically active materials due to the high temperature exposure and preserved the full electrical functionality.

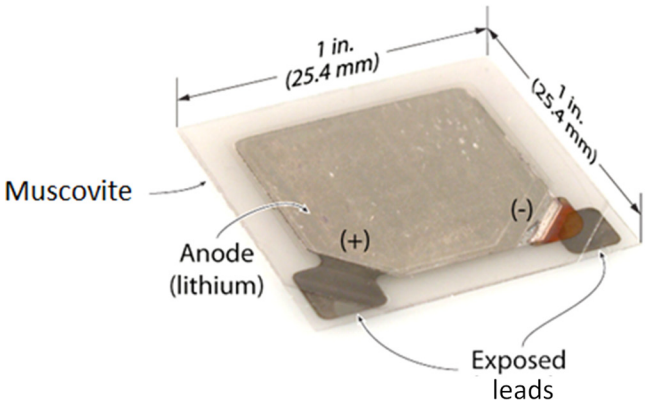

Figure 2. *Perspective photo of all-solid state thin film Li-ion battery with dimensions. Manufactured by FrontEdge Technology Inc.*

The multifunctioinal design of the battery packaging to achieve integrity of the electrochemical cell as well as efficient structural capability has never been investigated. Such a design is an enabling technology for the structural battery concept. The preliminary step is to characterize the stress-strain field and the electromechanical failure modes of the TFB-CFRP laminate under loading. Whether the TFB is embedded within the CFRP sub-laminate, Figure 4(a), or externally bonded onto its surface, Figure 4(b), a three-dimensional stress-strain field has to be considered because of the lay-up transition at the battery ends, as well as of the highly inhomogeneous mechanical properties of the material layers involved. Applicable failure modes include ply failure, disbonding, mixed-mode delamination at multiple bi-material interfaces and delamination buckling. Any of these mechani-

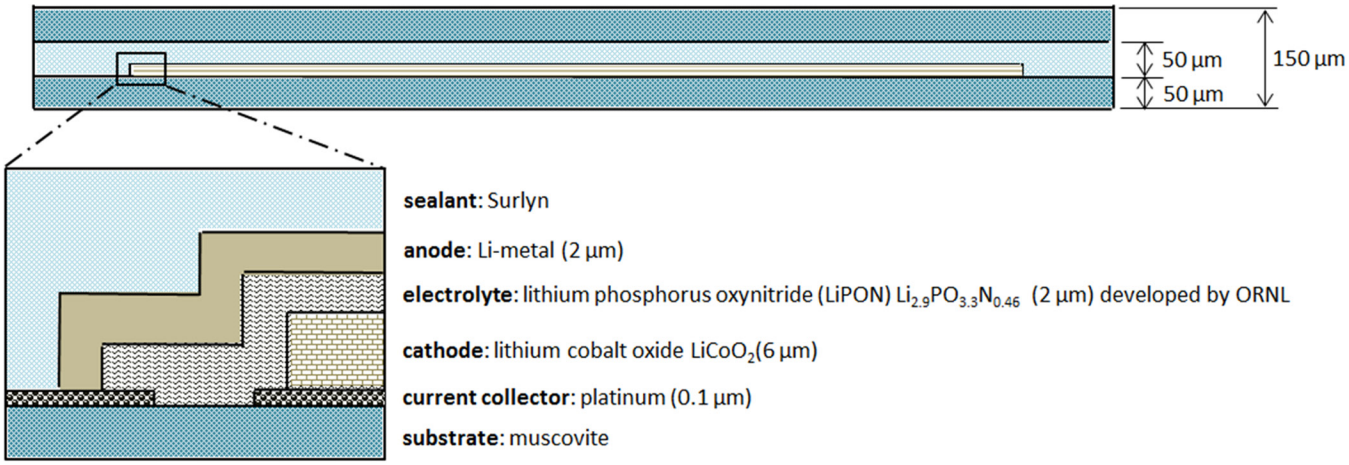

Figure 3. *Cross-sectional schematic of the commercially available TFB showed in Figure 2.*

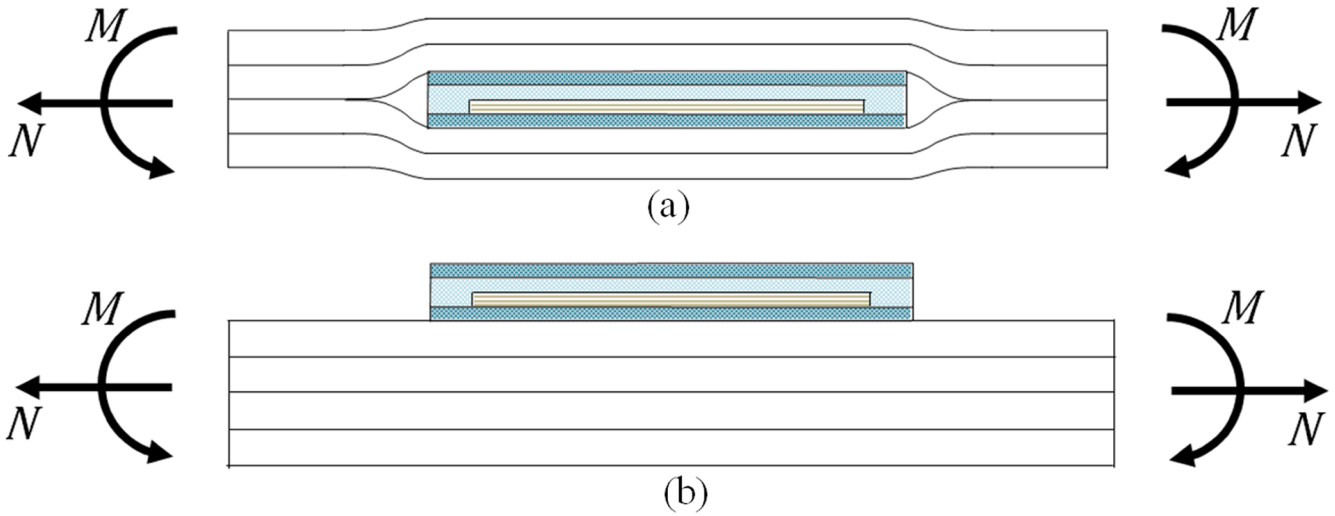

Figure 4. *Hybrid thin film lithium ion-graphite composite battery (TFB-CFRP) laminate configurations: thin film battery (a) embedded within the carbon fiber /epoxy laminate, or (b) bonded onto the laminate surface.*

cal failures can lead to the electrical failure by introducing an electrical discontinuity, an electrical short or a path for air and moisture through the battery packaging, leading to contamination of the electrochemically active materials.

Research conducted in [22,23] showed that the aforementioned commercial TFB was capable to operate up to a radius of curvature of 181 mm [22] and under out-of-plane pressures as high as 830 kPa [23] without any detrimental effects on the electrochemical performance. The same TFB type was successfully embedded in a CFRP laminate and electrochemically characterized under uniaxial mechanical tension. The study focused on the laminate residual mechanical strength and stiffness, which was not penalized by the presence of the TFB embedded at the laminate mid-plane. On the other hand the TFB electrical failure, which consisted of an irreversible and complete loss of capacity, occurred prematurely at about 50% of the laminate mechanical failure strain [24,25]. These electromechanical tests proved that the mechanical boundary conditions have no effect on the electrochemical performance up to a sudden electrical failure. This was confirmed by the multi-physics finite element analysis developed by [21]. The finding implies that the sudden electrical failure is caused by a mechanical failure, such as the failure of the packaging layers, with subsequent cell contamination or tearing, or by cracking of the electrodes or the electrolyte.

To date, neither the stress-strain field nor the mechanical failure modes have been characterized for basic loading conditions. This fundamental knowledge is required in order to prove the functionality and assess the benefits of an optimized TFB-CFRP system, which includes a battery packaging specifically designed for this multifunctional application. Unlike standard flexible electronics, the packaging has to be physically and chemically compatible with the TFB deposition and annealing process, as well as highly performing in terms of specific modulus and specific strength, and capable of ensuring sealing integrity when subjected to severe stress.

Taking advantage of the highest specific energy on the market, currently available TFBs used as structural elements could theoretically reduce the weight of certain aircraft types even without relying on load bearing electrodes, provided that the packaging possesses mechanical properties comparable to airframe structural materials. Hence the structural efficiency of substrate and sealant becomes a determining factor of success.

In order to clarify the concept we analyzed the weight reduction obtained by replacing the energy storage system of a propeller aircraft with a structural TFB system. The weight of the original propulsion system, based on an electric engine or an internal combustion engine, is assumed to be the same as an equivalent electric propulsion system. It is important to note that this assumption is applicable to reciprocating and small turbine engines, but it is not valid for turbofan cores, which have a higher energy density than any currently available electric motor [26]. The new aircraft weight W^* is given by

$$W^* = W - W_{F/B} + W_{TFB} \tag{1}$$

where W is the original gross weight at takeoff, $W_{F/B}$ is the weight of the fuel W_F or of the original batteries W_B and W_{TFB} is the weight of the TFB active components required to power the aircraft. For preliminary calculation purposes, it is assumed that the packaging has the same specific strength and specific modulus as the airframe materials being replaced. This permits omitting its weight from the above equation.

The new battery weight W_{TFB} is equal to the total propulsion energy required for the new aircraft configuration to complete a mission, E_S^*, divided by the product of the TFB energy density, e, and the efficiency of the new electric mo-

tor, η_M. The new mission energy, E_S^* is therefore defined as the energy delivered by the engine and is equivalent to the total drag of the new configuration multiplied by the flight range and divided by the propeller efficiency. For an electric aircraft, E_S^* is related to the total mission energy of the original configuration E_S as follows

$$E_S^* = E_S \frac{W^*}{W} \tag{2}$$

The above equation can be derived by assuming that the mission is comprised of a steady level flight only, and that cruise speed, aerodynamic efficiency and propeller efficiency of the new configuration are equal to the original configuration. Through algebraic substitution we obtain

$$\frac{W^*}{W} = \frac{1-\frac{W_B}{W}}{1-\frac{E_S}{e\eta_M}} \tag{3}$$

For an aircraft equipped with an internal combustion engine a similar equation can be derived with the additional assumptions that the rate of fuel consumption and the aerodynamic efficiency remain constant throughout the flight

$$\frac{W^*}{W} = \frac{1-\frac{W_B}{W}}{1-\frac{E_S}{e\eta_M}\frac{W}{W-W_F/2}} \tag{4}$$

Empirical data from different aircraft categories were averaged in order to calculate the nondimensional groups of aircraft weights in Equations (3) and (4). The data are summarized in Table 1. The electric motor efficiency, η_M, was assumed equal to 0.95. To calculate the mission energy, E_S, the original flat rated engine power was multiplied by the maximum range and divided by the cruise speed, thereby neglecting takeoff and landing. The resulting semi-empirical curves for the weight change ratio are plotted in Figure 5 at increasing TFB energy densities, starting from the today's available energy density of 353 Wh/kg. The white plot area identifies the aircraft configurations that benefit from weight saving. The grey plot area indicates weight increase. The model shows that weight saving could be currently achieved for electric aircraft such as High Altitude Long Endurance (HALE), mini-UAV and motor gliders. For aircraft characterized by higher mission energy per unit mass, such as UAVs with internal combustion engines and general aviation, further improvement in specific energy is required. However, a battery packaging with the assumed structural efficiency is not technology ready and its mechanical performance requirements have to be assessed.

Table 1. Aircraft Weight and Power Plant Energy Characteristics Utilized to Feed the Semi-empirical Weight Prediction Model Shown in Figure 5.

Aircraft	E_S [kWh]	W [kg]	$W_{F/B}$ [kg]	E_S/W [kWh/kg]
Pipistrel Taurus Electro G2[1]	7.17	472.50	101.00	0.015
NASA Helios[2,3]	21.00	929.00	148.75	0.023
AeroVironment RQ-11 Raven[4]	0.11	1.90	0.46	0.056
Solar Impulse[5]	120.00	2000.00	450.00	0.060
AAI RQ-7A Shadow[4]	34.25	154.00	23.10	0.222
AAI Shadow 400[4]	73.47	201.00	68.40	0.366
Cessna 172R[5]	565.51	1111.00	144.00	0.509
General Atomics RQ-1 Predator[4]	7680.4	1020.00	295.00	0.753
Pilatus PC-12[5]	4187.09	4740.00	1226.00	0.883
Piaggio P-180[5]	5291.84	5488.00	1271.00	0.964

[1]http://www.pipistrel.si/plane/taurus-electro/technical-data.
[2]http://www.nasa.gov/centers/dryden/news/FactSheets/FS-068-DFRC.html.
[3]Saft LO 26 SHX battery data sheet.
[4]Jane's Unmanned Aerial Vehicles and Targets, Issue thirty, May 2008.
[5]Jane's All the World's Aircraft 2010–2011.

The objective of this paper is to introduce the concept of hybrid TFB-CFRP laminate and to experimentally characterize the stress-strain field and failure mechanism of the multifunctional laminate subjected to uniaxial strain, single curvature and a combination of the two. This work is intended to support the future development of damage initiation and propagation analyses finalized to the optimization of the TFB packaging design. In this perspective, experimental data was required for determining the critical failure modes to be considered and for validating such analysis methods. The research also aims at providing a performance envelope for the current TFB technology that could be used as a baseline for the next generation of airborne thin film structural batteries.

2. METHODOLOGY

A commercially available TFB was utilized to manufacture TFB-CFRP laminates. The chemistry of the selected battery, as well as its manufacturing process, is representative of the commercial state-of-the-art that is currently adopted by all the manufacturers of solid state thin film lithium-ion batteries. The TFB selected for this study, Figure 2, was deemed the most suitable for this application because of the simplicity of the three-layer design and high stiffness of the packaging. Two laminate configurations were considered. The first was comprised of a TFB embedded at the laminate mid-plane and co-bonded within the CFRP sub-laminate, Figure 4(a). The second was the secondary bonding of the TFB onto the surface of a pre-cured CFRP sub-laminate, Figure 4(b).

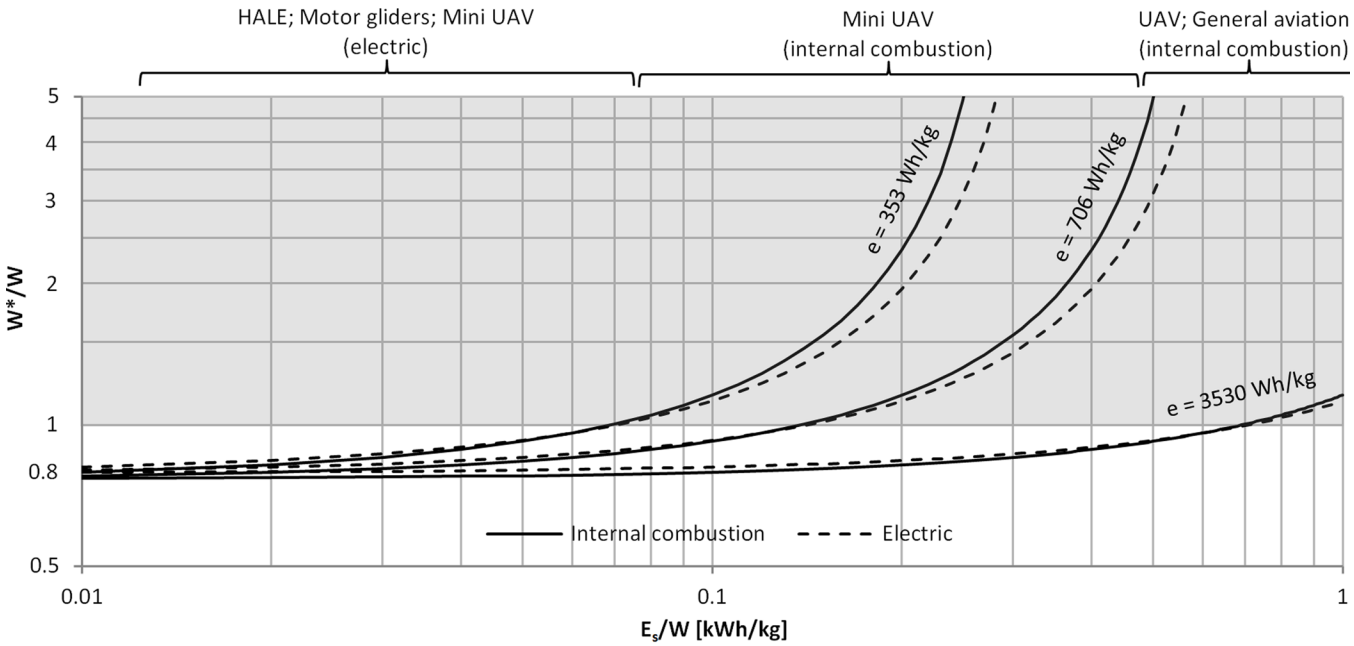

Figure 5. *Predicted gross weight of aircraft equipped with TFB energy storage system (W*) normalized by the original gross weight at takeoff (W), plotted as a function of the original specific mission energy. Semi-empirical curves [as per Equations (3) and (4) and averaged data from Table 1] plotted at increasing TFB specific energies (e).*

Mechanical tests were conducted in order to measure the stress-strain field under uniaxial loading and assess the applicability of classical analysis methods in mechanics of composite materials. Disbonding, delamination characteristics and laminate mechanical failure modes were also assessed in order determine the weakest link and critical properties that lead to mechanical failure. The cyclic TFB thickness variation due to the migration of the lithium ions during battery charge and discharge, which could generate interlaminar normal stress in the laminate, was also experimentally measured. Finally, an electrochemical characterization under mechanical loading was performed in order to determine the strain and curvature at electrical failure.

2.1. Materials

The TFBs utilized in this research are manufactured by FrontEdge Technology under license from the Oak Ridge National Laboratory (ORNL), Figure 2. Chemistry and thicknesses of the cell components are summarized in Figure 3. The active components are encased by two 50 μm thick muscovite substrates bound by a thermoplastic layer of Surlyn sealant, leading to a total thickness of 150 μm. The battery is a 25.4 mm square with a nominal voltage of 4.2V, and a nominal capacity of 1 mAh. The energy density measured by the authors with respect to the mass of active components is 353 Wh/kg, which drops to 22 Wh/kg with packaging weight included. Experimental characterizations of the same battery under mechanical loading were performed by [22–25].

The electrochemically active components of the battery are grown by a sequence of different physical vapor deposition (PVD) processes performed in-situ on the substrate. The need of annealing the cathode at temperatures of 300°C or higher to increase the ionic conductivity requires dimensional stability of the substrate material at those temperatures in order to avoid cracking, disbonding or undesired crystalline orientation of the cathode due to thermal stresses. Chemical stability is also important in order to avoid releasing contaminants in the controlled atmosphere of the deposition chamber. All these requirements have to be considered for the selection of a substrate material. The manufacturing process was discussed in detail in [27–31].

The active components are highly reactive with N_2 [27], O_2 [28] and H_2O [32], therefore the TFB has to be hermetically sealed. A failure of the sealant or substrate during manufacturing or operation of the TFB-CFRP leads to the failure of the battery by compromising its ability to store energy. The electrical capacity loss can be almost instantaneous or can fade progressively, depending on the flow rate of contaminants entering the battery. Since the CFRP material is hygroscopic, this failure mode applies to the embedded TFB configuration as well.

Mechanical properties of muscovite and Surlyn are listed in Table 2. The first is a crystalline mineral whose crystallographic structure is comprised of 1 nm thick layers separated by perfect basal cleavages. This characteristic determines low fracture toughness against cracks that are planar with the battery. On the other hand it can be considered quasi-isotropic in the battery plane [33] with an elastic modulus

Table 2. Relevant Mechanical Properties of Materials.

Property	Symbol	Muscovite[1]	Surlyn	IM7/977-3[2]	AF 163-2[3]
Tensile modulus of elasticity [GPa]	E_1	178[4]	0.28[5]	162	1.10
	E_2	178[4]	0.28[5]	8.34	1.10
Shear modulus of elasticity [GPa]	G_{12}	70.7[4]	0.11[6]	4.96	0.41
Poisson's ratio	v_{12}	0.26[7]	0.3[8]	0.34	0.34
Strain to tension failure [%]	ε_1^{TU}	unkn.	8.00[5]	1.46	unkn.
Mode I fracture toughness [J/m^2]	ε_2^{TU}	unkn.	8.00[5]	0.77	unkn.
	G_{IC}	1.30[9]	1200[10]	316	3682

[1]Average in-plane properties in the plane parallel to the basal cleavage, which coincides with the battery plane.
[2]Cytec IM7/977-3 data sheet.
[3]3M Scotch-Weld Structural Adhesive Film AF 163-2 data sheet.
[4]McNeil *et al.*, *J Phys.: Condens. Matter* 5, 1681 (1993).
[5]Yield strain, ref. NCAR Report FRB-4 (1965).
[6]Calculated assuming isotropy and ? = 0.3.
[7]Calculated assuming isotropy in the battery plane.
[8]Assumed.
[9]Hill *et al.*, *Int. J. Fracture* 119/120, 365 (2003).
[10]Compston *et al.*, *J Mater. Sci. lett.* 20, 509 (2001).

of 178 GPa, which is in the range of intermediate modulus CFRP materials. Surlyn is a high toughness thermoplastic polymer with a melting temperature of 98°C. A compatibility study to the composite curing process revealed that in some batteries the Surlyn layer is affected by long strands of bubbles along the edges of the active components, and that during curing of the TFB-CFRP laminate bubbles diffused within the sealant layer and coalesced into a disbonded front, Figure 6. These defects could potentially cause delamination onset within the battery packaging, Figure 7.

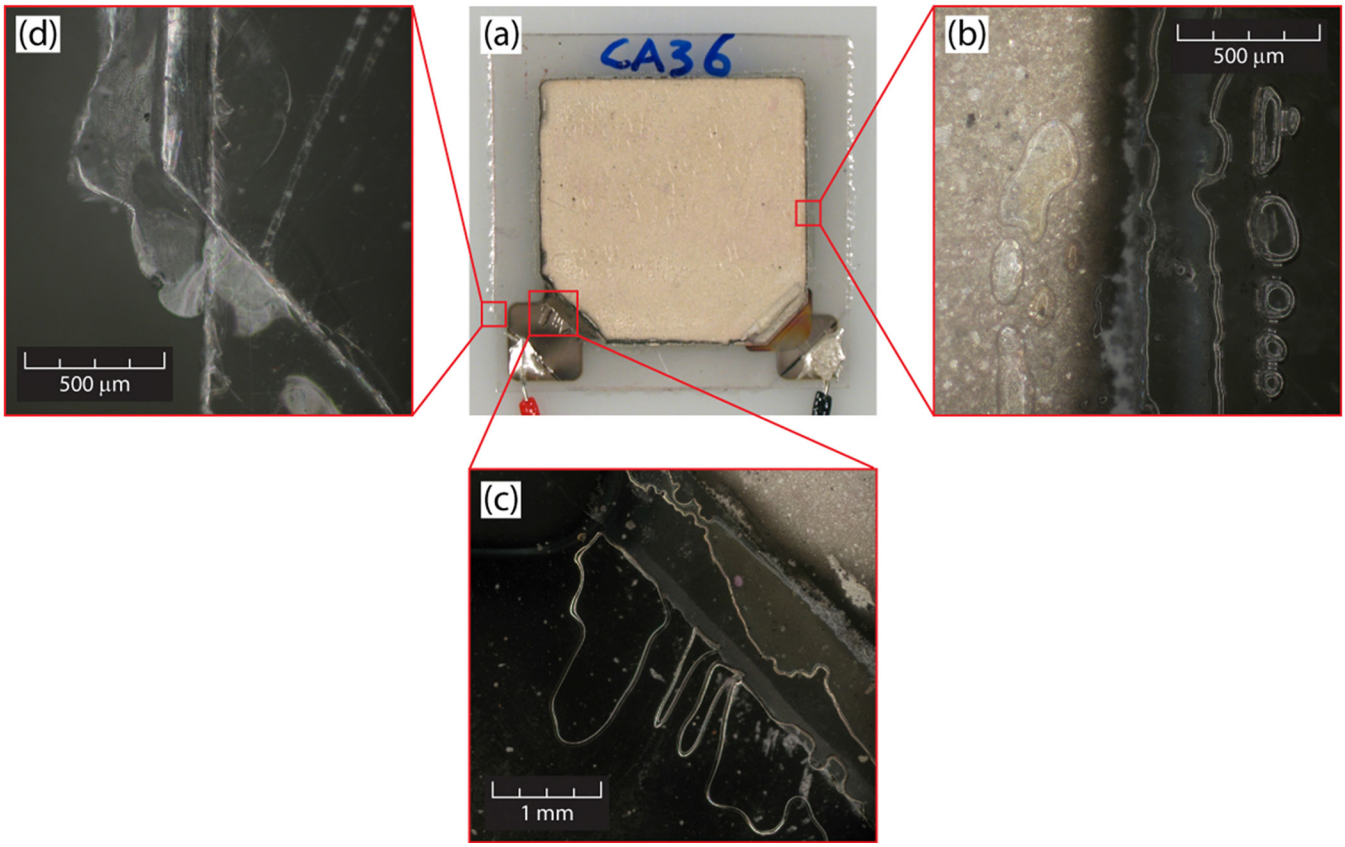

Figure 6. *Micrographs of a TFB after processing at 121°C for one hour under vacuum bag (–711 mmHg) showing sealant bubbling and a disbonded front along the edge of the active components.*

Figure 7. *Cross-sectional schematic of the TFB with locations of disbonded areas, as shown in Figure 6, highlighted with dotted lines.*

The TFB-CFRP laminates were cured by heated press molding of IM7/977-3 prepreg tape materials at 132°C and 590 kPa, with a cure time of two hours. In the case of embedded TFB, the battery was laminated within the prepreg material prior to curing and without the addition of adhesive film (AF). For the externally bonded TFB configuration, the CFRP laminate was pre-cured with the same process and the battery was subsequently bonded using one layer of epoxy adhesive film 3M AF163-2 cured for 1.5 hours at 121°C in the vacuum bag. These cure cycles were validated by the authors in order to retain the full functionality of the battery. The mechanical properties for the carbon/epoxy material and the adhesive film are listed in Table 2.

For the electromechanical characterization of the TFB-CFRP laminate, the battery was connected to the testing circuit through flat flexible cables (FFC), Nicomatic 254PW01E6095 polyester coated single copper conductor. The FFCs weree 0.25 mm thick and 5.12 mm wide. They were connected to the TFB leads using MG Chemicals silver conductive epoxy 8331-14G. For the embedded battery configuration they were laminated within the CFRP at the laminate mid-plane.

Unlike previous studies [24,25], the battery was not encased within a pre-cured polymeric case, but silicone conformal coating MG Chemicals 422-55 was applied on the exposed leads only, Figure 2, to insulate the connections and prevent electrical shorting with carbon fibers.

2.2. Experimental

The experimental campaign was comprised of five test types: double cantilever beam (DCB); uniaxial mechanical tension; battery thickness variation occurring during charge/discharge cycling; uniaxial mechanical tension with battery capacity monitoring and four point bending with battery capacity monitoring, Table 3 The battery thickness variation test setup and procedure were conceived ad hoc since a test standard is not available. The remaining tests adopted ASTM standard methods for reinforced plastics modified to cope with the multifunctional system.

The specimens for DCB test were 25.4 mm wide, which is equal to the TFB width, and 304.8 mm long. Tests were conducted according to the ASTM standard [34]. Three baseline specimens, comprised of thirty plies oriented at 0° for a laminate thickness of 3.8 mm, were tested to determine the mode I fracture toughness G_{IC} of the CFRP material. Three additional specimens with a TFB embedded at the laminate mid-plane were then tested. These specimens featured a battery embedded at specimen mid-span, leading to the staking sequence (0_{30}) away from the battery and (0_{15}/TFB/0_{15}) at battery location. The crack was started from the loaded end of the specimen, at the laminate mid-plane, and propagated towards the TFB. A precrack was induced so that a delamination was visually observed on the edge of the specimen before staring the test. The objective was to determine the G_{IC} and the crack propagation path. The G_{IC} was calculated by dividing the total strain energy released during the test by the final crack surface measured from the tip of the precrack.

Uniaxial mechanical tension tests with full-field strain monitoring were performed in order to characterize the stress-strain field for different laminate lay-ups. The procedure complies with the standard ASTM test [35], except for an increased specimen width of 76.2 mm, Figure 8. This modification was introduced to minimize the interaction between the edge effect and the stress-strain gradient caused by the TFB, which was located at the center of the speci-

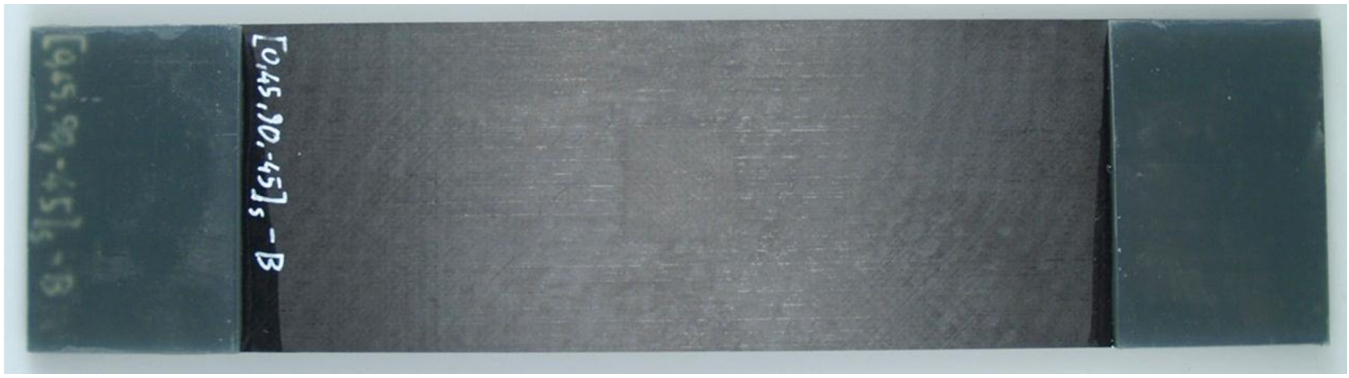

Figure 8. *Uniaxial mechanical tension test specimen with embedded TFB at laminate mid-plane. Laminate stacking sequence is (0/45/90/–45/TFB/–45/90/45/0).*

Table 3. Summary of Tests.

Test Description	Lay-ups	Repetitions
Double cantilever beam (DCB)	(0_{30})	3
	$(0_{15}/TFB/0_{15})$	3
Uniaxial mechanical tension with full-field strain monitoring	(0/90/TFB/90/0)	1
	$(0_2/TFB/0_2)$	1
	(0/45/90/–45/TFB/–45/90/45/0)	1
	$[(0/45/90/–45)_S/AF/TFB]$	1
	$(0_8/AF/TFB)$	1
TFB thickness variation during charge/discharge cycling	TFB alone	1
Uniaxial mechanical tension with TFB capacity monitoring	[0/45/90/–45/TFB/–45/90/45/0]	2
Four point bending with TFB capacity monitoring	$[(0/45/90/–45)_3/TFB/(–45/90/45/0)_3]$	2
	$[(0/45/90/–45)_{3S}/AF/TFB]$	2
	$[TFB/AF/(–45/90/45/0)_{3S}]$	2

men. A total of three lay-ups with embedded battery were investigated: a 4-ply cross-ply laminate, a 4-ply unidirectional laminate tested along the 0° direction and an 8-ply quasi-isotropic laminate. The embedding method adopted throughout this study is referred to as interlaminar embedding, since it consisted of enclosing the battery in the space between two plies, as opposed to enclosing it into a ply cut-out. This design avoided sharp stress-strain gradients to arise at the battery edges, although it led to resin pockets at the TFB ends, Figure 9. The applied strain was increased only up to a far-field strain of approximately 3000 µstrain in order to observe the elastic behavior. The failure behavior for this laminate configuration was already reported in [24,25].

Two additional 8-ply lay-ups with an externally bonded TFB were tested in uniaxial tension: a unidirectional laminate tested along the 0° direction and a quasi-isotropic laminate. Their stacking sequences at battery location were $(0_8/AF/TFB)$ and $[(0/45/90/–45)_S/AF/TFB]$ respectively. A specimen with an externally bonded battery is shown in Figure 10. The test procedure was the same as for the embedded TFB configuration, but the applied load was increased up to failure in order to investigate the elastic stress-strain field as well as the failure mode.

For all the uniaxial mechanical tension tests a digital image correlation (DIC) technique was adopted to monitor the surface strain of the specimen. To avoid using FFCs that would alter the strain field or interfere with the optical measurement technique, the electrical response of the TFB-CFRP laminate under loading was investigated separately.

Contrary to the common perception that their thickness remains constant, the lithium ion batteries expand during charge and contract during discharge. This thickness, thus

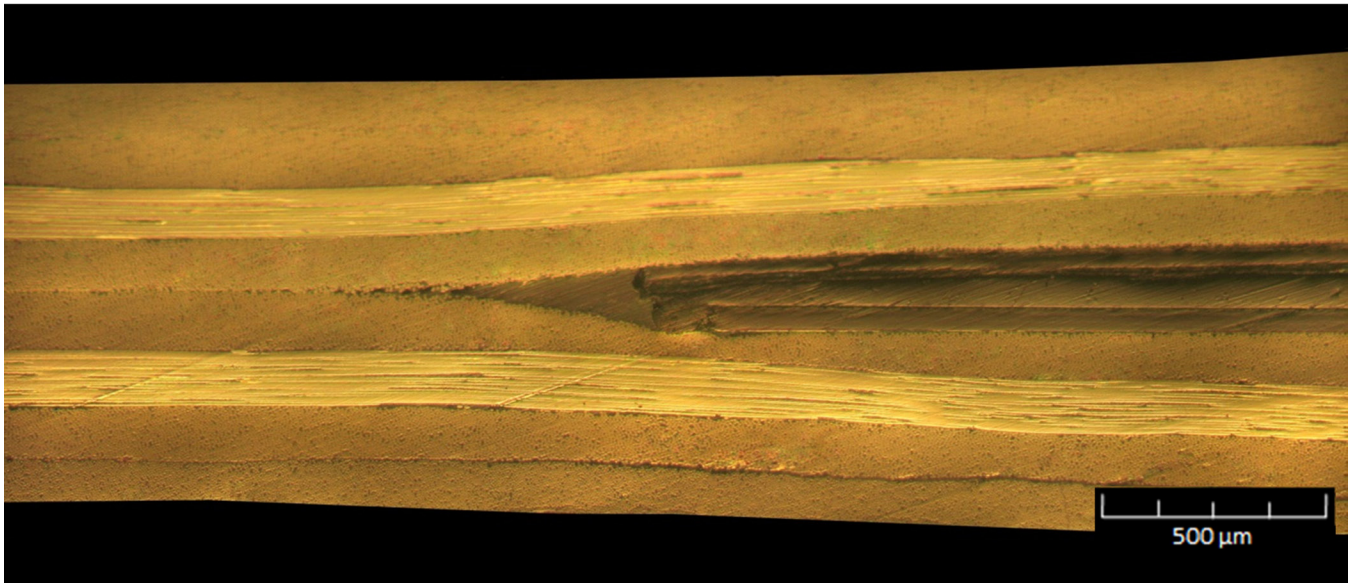

Figure 9. *Micrograph of quasi-isotropic laminate with TFB embedded at laminate mid-plane. Laminate stacking sequence is (0/45/90/–45/TFB/–45/90/45/0).*

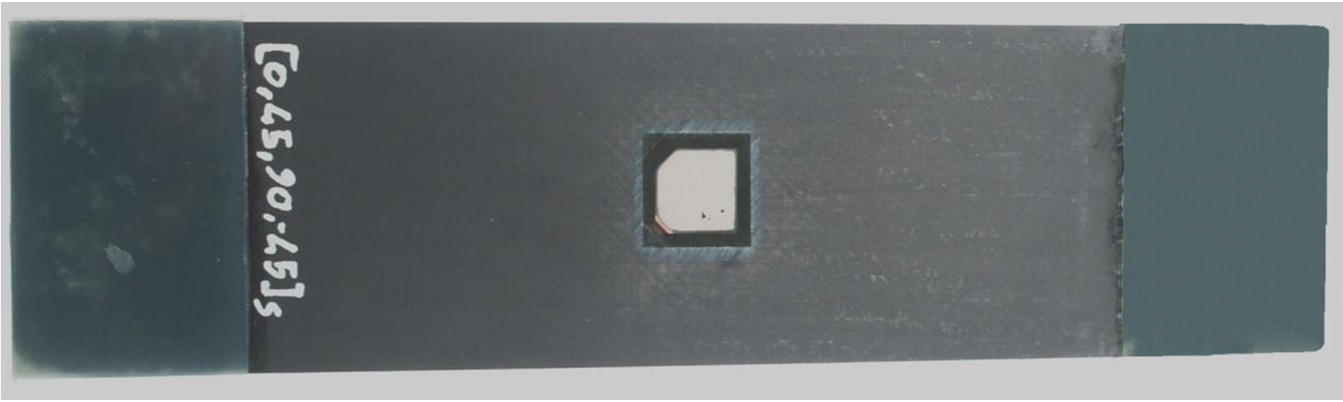

Figure 10. *Uniaxial mechanical tension specimen with externally bonded TFB. Laminate stacking sequence at battery is* $[(0/45/90/-45)_S/AF/TFB]$.

volume, change is caused by lithium ion intercalation into host electrode materials. Since the TFB has a metallic lithium anode instead of an intercalation compound, the thickness increase is attributed to the plating of lithium at the anode during the charging process. The DIC was employed for monitoring the thickness increase of one TFB alone during a full electric charge process. A full charge/discharge cycle was performed before the test in order to condition the battery. Discharge was operated under a constant resistive load of 3.8 kΩ, which led to an average discharge rate of 1C (i.e. 1 ma discharge current). Charge took place at a constant voltage of 4.2 V. The battery was considered fully discharged when the voltage reached 3 V, the lower limit to avoid overdischarge, while full charge was reached when the current dropped below 50 μA. The DIC measured the out-of-plane displacement of the TFB outer surface at anode side with time intervals of 2 minutes, starting from the fully discharged state, which was taken as the reference state. Therefore the displacement field corresponding to the fully charged state was equal to the maximum thickness increase. The TFB temperature was monitored for the entire duration of the test with an infrared (IR) camera with ±1°C accuracy.

Lastly, an electrochemical characterization of the TFB-CFRP laminate subjected to uniaxial tension and flexure was conducted. The purpose was to assess the operational envelope and to determine the interaction between electrical and mechanical failure modes, where electrical failure was the partial or total capacity loss. Two specimens with a stacking sequence (0/45/90/–45/TFB/–45/90/45/0) were tested up to failure through uniaxial mechanical tension. The selected laminate lay-up showed the best correlation between experimentally measured and calculated strain field in the mechanical tests, thereby increasing the degree of confidence for the calculation of the strain at failure. The dimensions of the specimens matched those of the previously described mechanical tension tests, but in this case FFCs were connected to the battery and laminated within the CFRP plies. Figure 11 shows the cables exiting from the laminate and connecting to the charge/discharge circuit (not shown) to allow for capacity monitoring. The discharge or charge capacity was calculated by numerically integrating the discharge or charge current over time. The procedure and characteristics of the charge and discharge circuit were as previously described.

For the mechanical tension tests with capacity monitoring, constant strain intervals of increasing magnitude were applied until failure, where the duration of an interval corresponded to the time required to perform a full discharge followed by a full charge for capacity measurement under

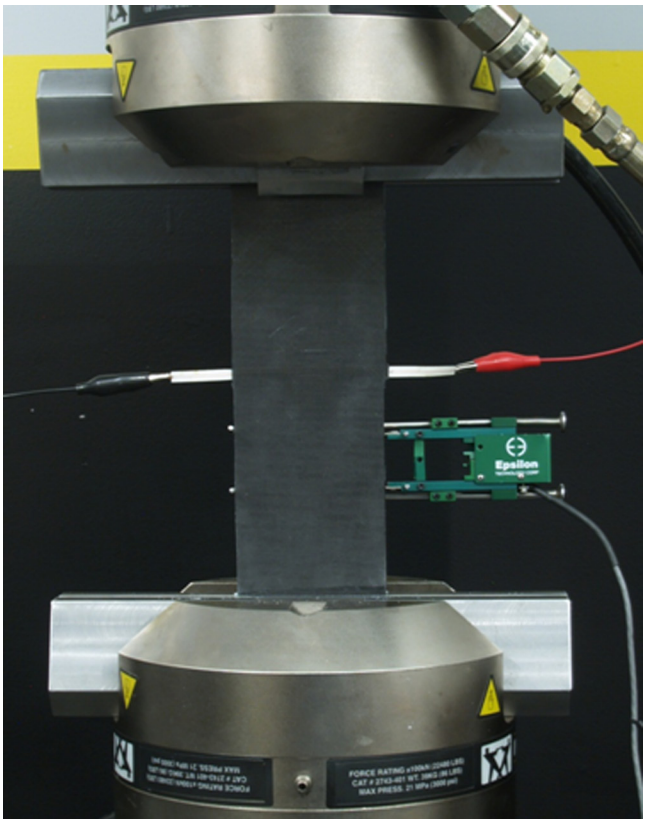

Figure 11. *Electromechanical uniaxial tension test setup showing the hybrid TFB/graphite laminate specimen clamped by the grips of test frame. Laminate stacking sequence is (0/45/90/–45/TFB/–45/90/45/0).*

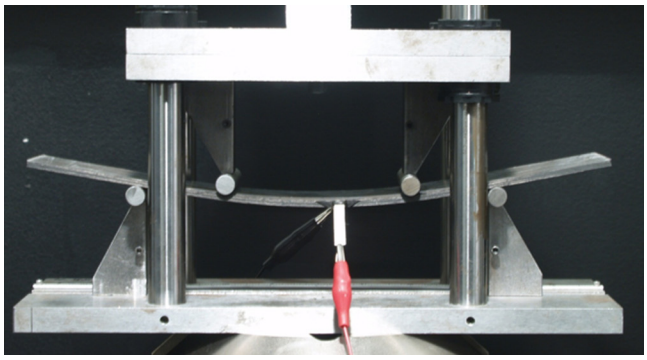

Figure 12. *Electromechanical flexure test setup with standard 60:1 span to thickness ratio, showing the hybrid TFB/graphite laminate specimen loaded by the four point bending fixture. Laminate stacking sequence is* $[(0/45/90/–45)_3/TFB/(–45/90/45/0)_3]$.

constant strain. Load was released after each strain interval and capacity was measured again at zero strain. The far-field strain was measured by an extensometer, Figure 11, for control and data acquisition, while the strain at failure location was calculated using the analysis methods described in the following section.

Similarly, four point bending tests were conducted on laminates with embedded or externally bonded battery configurations, Figure 12. While in the first configuration the TFB was subjected to pure curvature, the second led to curvature and compressive or tensile in-plane strain depending on which side of the specimen the TFB was bonded on. The width of the specimen was always 76.2 mm, while the support span to thickness ratio was initially set to 60:1 with a support span of 180 mm and a loading span of 90 mm. The laminate stacking sequences were $[(0/45/90/–45)_3/TFB/(–45/90/45/0)_3]$, $[(0/45/90/–45)_{3S}/AF/TFB]$ and $[TFB/AF/(–45/90/45/0)_{3S}]$. For the embedded battery configuration, a stacking sequence (0/90/TFB/90/0) was also tested with an increased span-to-thickness ratio of 145:1. Support and loading span were 72.5 mm and 36.5 mm respectively. This modified setup, which does not comply with the ASTM standard [36], was designed for applying higher curvatures to the battery without experiencing mechanical failure of the laminate. The same load-hold load-unload procedure with increasing curvature intervals was adopted, but in this case the test was conducted under displacement control. The curvature applied by a given displacement of the test frame was calculated through integration of the elastic line equation. Small deformations, normality condition of the sections and uniform bending stiffness were assumed. The uniformity of the bending stiffness is applicable only if the presence of the battery does not significantly change the section inertia of the CFRP laminate. The far-field strain applied to the battery was then calculated by multiplying the curvature by half the CFRP laminate thickness. The curvature is reported in the results section as the radius of curvature, which was assumed equal to the inverse of the curvature.

2.3. Analysis

Classical laminate theory (CLT), finite element analysis (FEA) and a closed form elasticity solution of the TFB-CFRP laminate were utilized to interpret the experimental results and calculate the strain at failure. These methods were validated by comparing their results with the experimentally measured elastic strain field from the uniaxial mechanical tension tests. Given the applied far-field strain ε_0, the strain field at the center of the specimen, which was affected by the presence of the TFB, was calculated and compared to the surface strain field measured by the DIC.

The first analysis method used CLT to calculate the apparent modulus of elasticity in the x-direction at a point away from the battery, where the laminate was comprised of the CFRP layers only, and at the battery location. The model accounted for the stiffness of the battery substrate, sealant and the adhesive film. The x-direction was defined as the loading direction. The laminate strain at the battery was then calculated by multiplying the far-field strain by the ratio of the two moduli multiplied by their respective thicknesses. The results obtained with this method are identified in the results section with the acronym CLT.

At specimen mid-span, the section was not constant across the width due to the presence of the battery. In order to account for the resulting stress redistribution, which was ignored by the first analysis method, a second analysis method that employs a linear finite element solution with NX Nastran SOL101 was developed. FEA also accounted for the extension-bending coupling caused by the laminate asymmetry. The entire specimen was modeled with linear shell elements (CQUAD4) and a mesh size of 1.524 mm that matched the DIC resolution. The element formulation used the CLT for computing element stiffness and outputs, therefore plane stress and uniform strain through-the-thickness were assumed. The desired far-field strain was applied by an enforced nodal displacement at the loaded end. The transverse strain was unconstrained.

The third analysis method was a linear elastic shear lag model that was developed in order to capture the extensive three-dimensional stress-strain field of the externally bonded battery configuration. The sealant, identified by the letter *s*, and the adhesive film, identified by *af*, were assumed to carry only shear, while the bending and shearing deformation of the upper and lower substrates, *su* and *sl* respectively, were neglected. The carbon/epoxy composite material was modeled as an equivalent isotropic material with the apparent laminate Young's modulus in the x-direction calculated according to the CLT. Bending and shearing deformation of the CFRP were also neglected. Perfect bonding was assumed at all interfaces and the presence of the active components was neglected due to their relatively small thickness. Based on these assumptions, when a far-field stress σ_0 is applied to the CFRP laminate, a normal stress σ_x is generated in the

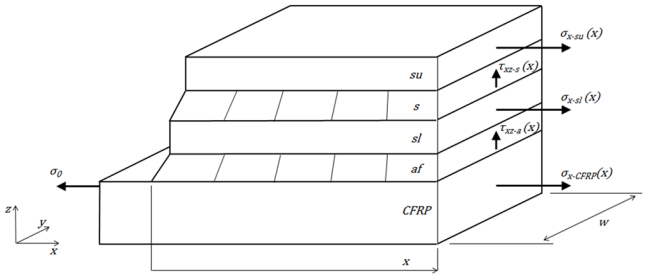

Figure 13. *Shear lag elasticity model of the externally bonded TFB, stress representation. Laminate layers are: carbon/epoxy sub-laminate (CFRP); adhesive film (a); lower substrate (sl); sealant (s); upper substrate (su).*

CFRP, *su* and *sl* layers, and a shear stress τ_{xz} is carried by the *a* and *s* layers, Figure 13. No other stress components arise, therefore the equilibrium equations are reduced to three, one for each of the layers that carries axial loading. The addition of the strain-displacement and stress-strain equations leads to a system of thirteen equations with thirteen unknowns.

The resulting governing equations are

$$\begin{cases} \dfrac{d^2\sigma_{x-su}}{dx^2} - \lambda_1^2\sigma_{x-su} - \beta_1\sigma_{x-CFRP} + C_1 = 0 \\ \dfrac{d^2\sigma_{x-CFRP}}{dx^2} - \lambda_2^2\sigma_{x-CFRP} - \beta_2\sigma_{x-su} + C_2 = 0 \end{cases} \tag{5}$$

where the known parameters are conveniently grouped as follows

$$\begin{aligned} \lambda_1^2 &= \frac{G_s}{t_s}\left(\frac{1}{t_{su}E_{su}} + \frac{1}{t_{sl}E_{sl}}\right) \\ \beta_1 &= \frac{t_{CFRP}G_s}{t_{su}t_{sl}t_sE_{sl}} \\ C_1 &= \sigma_0\frac{t_{CFRP}G_s}{t_{su}t_{sl}t_sE_{sl}} \\ \lambda_2^2 &= \frac{G_{af}}{t_{af}}\left(\frac{1}{t_{sl}E_{sl}} + \frac{1}{t_{CFRP}E_{CFRP}}\right) \\ \beta_2 &= \frac{t_{su}G_{af}}{t_{sl}t_{CFRP}t_{af}E_{sl}} \\ C_2 &= \sigma_0\frac{G_{af}}{t_{sl}t_{af}E_{sl}} \end{aligned} \tag{6}$$

In the above definitions *t*, *E* and *G* identify thickness, Young's modulus and shear modulus of elasticity.

Equation (3) is a system of coupled second-order linear ordinary differential equations, whose general solutions are

$$\sigma_{x-su}(x) = B_1\cosh(A_1x) + B_2\sinh(A_1x) + B_3\cosh(A_2x) + B_4\sinh(A_2x) \tag{7}$$

$$\begin{aligned} \sigma_{x-CFRP}(x) = \frac{1}{B_1}[&(A_1^2-\lambda_1^2)B_1\cosh(A_1x) \\ &+(A_1^2-\lambda_1^2)B_2\sinh(A_1x) + (A_2^2-\lambda_1^2)B_3\cosh(A_2x) \\ &+(A_2^2-\lambda_1^2)B_4\sinh(A_2x) - \lambda_1^2C + C_1] \end{aligned} \tag{8}$$

The known parameters A_1 and A_2 are defined as

$$\begin{aligned} A_1 &= \sqrt{\frac{1}{2}\left[\lambda_1^2 + \lambda_2^2 + \sqrt{(\lambda_1^2-\lambda_2^2)^2 + 4\beta_1\beta_2}\right]} \\ A_2 &= \sqrt{\frac{1}{2}\left[\lambda_1^2 + \lambda_2^2 - \sqrt{(\lambda_1^2-\lambda_2^2)^2 + 4\beta_1\beta_2}\right]} \\ C &= \frac{\lambda_2^2C_1 - \beta_1C_2}{\lambda_2^2\lambda_1^2 - \beta_1\beta_2} \end{aligned} \tag{9}$$

The terms B_1 to B_4 were calculated for the following boundary conditions

$$\begin{aligned} x = 0 \rightarrow \sigma_{x-su} = 0;\ \ \sigma_{x-CFRP} = \sigma_0 \\ x = l \rightarrow \sigma_{x-su} = 0;\ \ \sigma_{x-CFRP} = \sigma_0 \end{aligned} \tag{10}$$

leading to

$$\begin{aligned} B_1 &= \frac{-A_2^2C + C_1 - \sigma_0\beta_1}{A_2^2 - A_1^2} \\ B_2 &= \left(\frac{A_2^2C - C_1 + \sigma_0\beta_1}{A_2^2 - A_1^2}\right)\frac{\cosh(A_1l) - 1}{\sinh(A_1l)} \\ B_3 &= \frac{A_1^2C - C_1 - \sigma_0\beta_1}{A_2^2 - A_1^2} \\ B_4 &= \left(\frac{A_1^2C - C_1 + \sigma_0\beta_1}{A_2^2 - A_1^2}\right)\frac{1 - \cosh(A_2l)}{\sinh(A_2l)} \end{aligned} \tag{11}$$

All the other unknowns of the system, such as the remaining stresses, strains and displacements, were then solved by algebraic substitution.

The results provided in the next section are based on the actual thicknesses taken from microscopies of polished specimen sections, similar to the micrograph shown in Figure 9. The following thicknesses were used: 0.125 mm for the CFRP plies; 0.06 mm for the TFB substrates; 0.08 mm for the TFB sealant and 0.09 mm for the adhesive film.

3. RESULTS

Typical load displacement plots for the DCB tests are shown in Figure 14. The crack propagated through the carbon/epoxy laminate in a 'stick-slip' manner, the crack advancing at finite increments, and crossed the battery with an unstable propagation along the whole battery length. The initial slope of the curves obtained from the laminates with

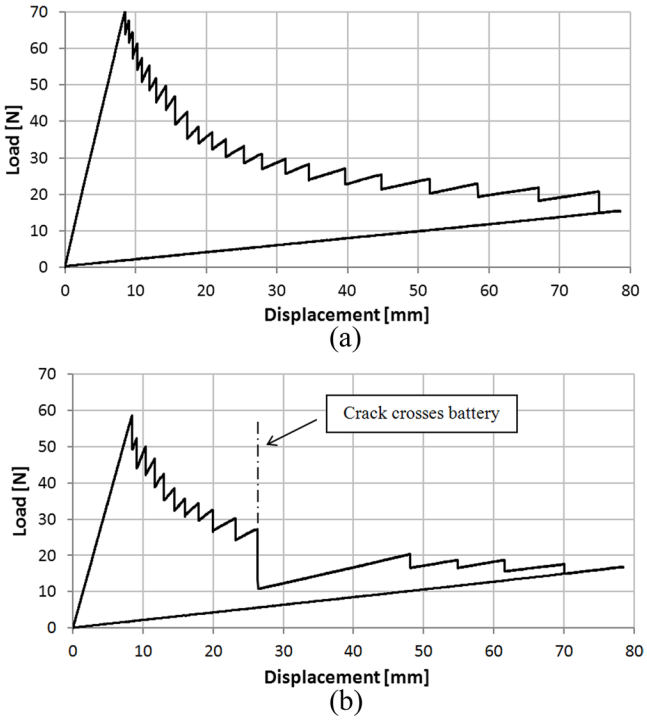

Figure 14. *Typical load-displacement profiles for double cantilever beam test (a) without embedded TFB and (b) with embedded TFB.*

embedded TFB was slightly lower than for those without, because the specimens with the embedded battery were 1.9 mm narrower than the nominal width. As expected from its low fracture toughness (Table 2), the crack propagated through the muscovite substrate for all the three test repetitions, splitting one of the two substrates along a cleavage plane, whereas the bond between the substrate and the carbon/epoxy composite remained intact, Figure 15. The average G_{IC} was reduced 15% by the presence of the battery, which was equal to the amount of crack surface occupied by the TFB, Table 4. This proved that the crack propagated through the battery without releasing a significant amount of strain energy.

The uniaxial mechanical tests gave evidence that the strain measured at the surface of a TFB-CFRP laminate with an embedded battery decreased sharply at the center of the specimen, where the TFB was located. An example of a full-field strain plot measured experimentally using DIC on the

Table 4. Average Mode I Fracture Toughness (G_{IC}) and Standard Deviation (σ) Resulting from Double Cantilever Beam (DCB) Testing.

	Average G_{IC} [J/m^2]	σ [%]
Specimens without TFB	315.5	2.27
Specimens with TFB	267.0	1.55
Specimens with TFB—net crack surface[1]	315.7	1.77

[1]Crack surface of thin film battery (TFB) is excluded from G_{IC} calculation

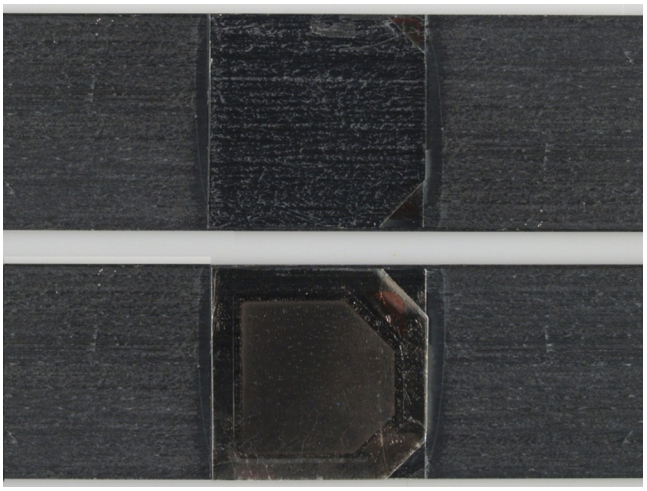

Figure 15. *Close-up image of crack surfaces after double cantilever beam.*

cross-ply laminate is shown in Figure 16. The corresponding strain field calculated by FEA is plotted in Figure 17 using consistent contour levels for comparison. The correlation between experiments and analysis was assessed based on the strain distribution along the longitudinal center-line of the specimen, identified by line a-a in Figure 16. The experimental and calculated strain values along line a-a are plotted in Figure 18. The FEA values are averaged corner outputs. Furthermore, the strain level predicted by the simplified CLT method is plotted as a constant strain throughout the nominal battery length and as a constant far-field strain elsewhere. A strain concentration factor, defined as the ratio between the average strain over the TFB ($\bar{\varepsilon}_{TFB}$) and the far-field strain (ε_0), was calculated for each of these data sets. The summary of the strain concentration factors for the tested lay-ups is reported in Table 5, showing a good agreement between the experimental and calculated strain field for all the stacking sequences. The results seem to confirm that the TFB shared load with the laminate as desired and that its adhesion to the CFRP material remained intact within the 3000 μstrain range. Moreover, the assumptions of plane stress and uniform strain through-the-thickness appear valid to predict the

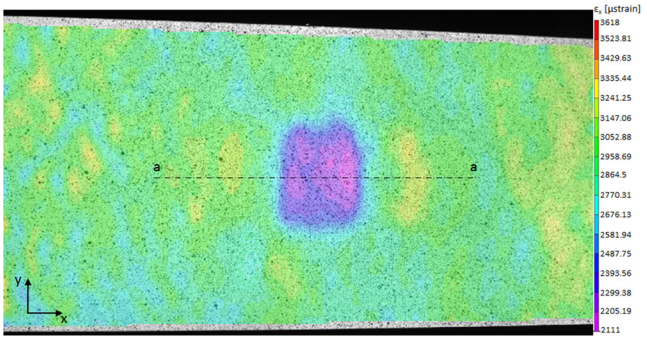

Figure 16. *Uniaxial mechanical tension test. Normal strain distribution in the loading direction (ε_x). Laminate stacking sequence at battery is (0/90/TFB/90/0). Applied far-field strain of 3107 μstrain.*

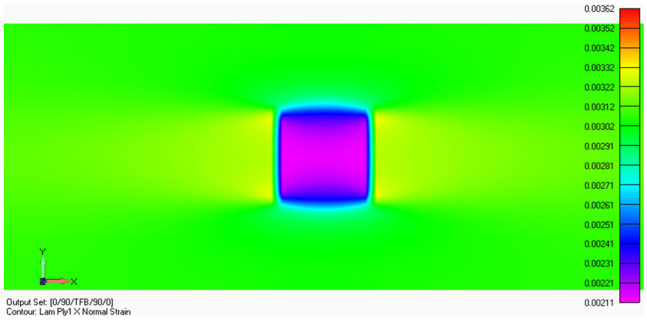

Figure 17. *Uniaxial mechanical tension test simulation. Strain distribution in the loading direction (x) calculated with finite element analysis (FEA). Laminate stacking sequence at battery is (0/90/TFB/90/0). Applied far-field strain of 3107 μstrain.*

Table 5. Uniaxial Mechanical Tension of Interlaminar TFB Embedding with Full-field Strain Monitoring. Measured and Calculated Normal x-Strain Concentration Factor Along Line a-a Shown in Figure 16. Factor is Defined as the Ratio Between Average TFB Strain $\bar{\varepsilon}_{TFB}$ and far-field strain ε_0.

	$\bar{\varepsilon}_{TFB}/\varepsilon_0$		
Lay-up	Experimental (DIC)	CLT	FEA (CLT)
(0/90/TFB/90/0)	0.75	0.66	0.71
(0_2/TFB/0_2)	0.84	0.79	0.81
(0/45/90/–45/TFB/–45/90/45/0)	0.80	0.74	0.80

overall elastic behavior of the laminate with an embedded battery. Within the limits of applicability of these assumptions, that is neglecting the three-dimensional stresses arising at lay-up transition, the interlaminar embedding did not lead to significant stress concentrations. In fact, the maximum stress concentration factor calculated with FEA was 1.07 and it occured in the $(0/90)_S$ laminate in proximity of the battery corners. This factor was calculated by dividing the maximum nodal strain in the *x*-direction by the far-field strain.

The same test procedure was adopted for the configuration with externally bonded TFB. The measured strain fields for the two tested lay-ups were characterized by higher strain gradients at the battery, in Figure 19. The highest gradient were located at the battery edges oriented transverse to the loading direction. These strain peaks were caused by a relative displacement between the upper substrate and the CFRP surface, which was detected as an apparent strain by the optical measurement instrumentation. Therefore, although this relative displacement was associated with a shear strain concentration in the sealant and in the adhesive, the normal strain peak had to be disregarded. The strain distribution over the battery, which coincides with the strain in the upper substrate, was in good agreement with the output of the shear lag model, Figure 20. As predicted by the analysis, the normal strain of the upper TFB substrate, which was zero at the battery edges, increased progressively up to a maximum at the center of the battery, without reaching the strain level predicted by the CLT. The high modulus mismatch between the adherents (substrates and CFRP sub-laminate) and the adhesives (sealant and adhesive film), as well as the relatively high thickness of the adhesives, were the causes of this extensive shear lag behavior. The calculated normal strain distributions in the adherents clearly show that the TFB length was not enough to allow for a uniform strain through-the-thickness, Figure 21. As a result, the upper substrate was affected by shear lag for the entire battery length, while the lower substrate and the CFRP sub-laminate reached a uniform strain at about one-third of the battery length. According to the shear lag model, the uniform strain region, defined as the area where the strain in the upper substrate reached at least 95% of the strain in the CFRP sub-laminate, began at a distance of 13.3 mm and 12.8 mm from the TFB edges for the $[(0/45/90/–45)_S$/AF/TFB] and (0_8/AF/TFB) laminates. Thus, in the shear lag region, which was as wide as 85 times the thickness of the battery and located next to the battery edge, the assumption of plane stress does not apply. For a sufficiently long TFB this edge effect would neg-

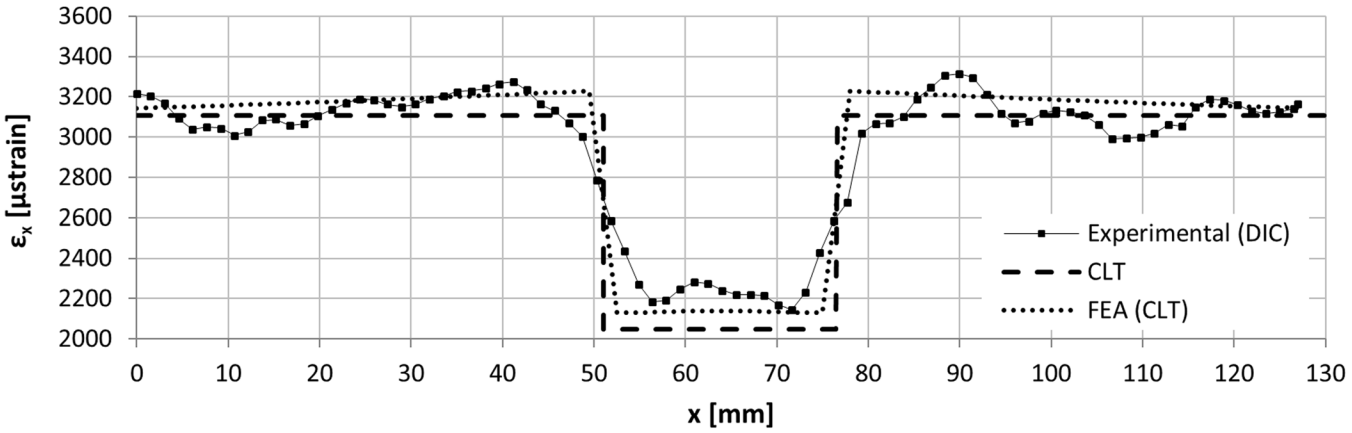

Figure 18. *Measured and calculated ε_x strain distribution along line a-a shown in Figure 16. Laminate stacking sequence at battery is (0/90/TFB/90/0).*

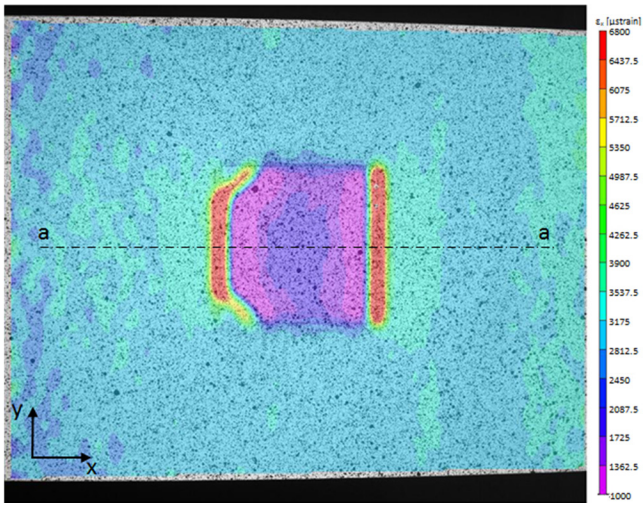

Figure 19. *Uniaxial mechanical tension test. Normal strain distribution in the loading direction (ε_x). Laminate stacking sequence at battery is [(0/45/90/–45)$_S$/AF/TFB]. Applied far-field strain of 3123 µstrain.*

ligibly reduce the load sharing efficiency of the externally bonded battery, however the three-dimensional stress-strain field poses challenges for the mechanical integrity and it is a fundamental knowledge required for the design of the TFB-CFRP laminate. The shear stress peak in the sealant occured at the battery edges, but the shear lag region extended well over the active components, Figure 22, and could trigger a mode II delamination onset at the edge of the active components, which is a known weak spot (Figure 6 and Figure 7).

Although the low sealant modulus was responsible for the extensive shear lag region, it had the advantage of leading to a low shear stress concentration factor, defined as the ratio between the peak stress and the average absolute value of the shear stress in the sealant layer. Shear stress concentration factors of 2.9 and 2.7 were calculated in the quasi-isotropic and in the unidirectional laminates, the latter being lower because the higher stiffness of the CFRP sub-laminate allowed a more gradual load transfer to the TFB. The shear stress concentration factors in the adhesive film, which had a higher modulus than the sealant, were 5.7 and 5.2 respectively.

The failure of the externally bonded battery configuration under uniaxial mechanical tension occured at an average applied far-field strain of 4898 µstrain, Table 6. This value was less than 50% of the CFRP sub-laminate critical strain. The same failure mode occurred in both the lay-ups and is attributable to the failure of the battery lower substrate. Micrographs of the failed specimens demonstrated that the interface between the adhesive film and the substrate remained intact, while the failed substrate showed multiple delaminations along the cleavage planes in proximity of the interface with the adhesive film. The unstable growth of one of these delaminations caused the battery to suddenly detach from the CFRP sub-laminate, leading to a brittle type of failure, Figure 23. The onset location of the failure can only be speculated. From the analysis of the calculated stress-strain fields it was noted that both specimens failed when the maximum shear stress occurring in the lower substrate reached 42.5 MPa, Table 6. Moreover, the TFB demonstrated during the electromechanical tension tests the capability to withstand higher normal strains than the ones calculated at failure for the externally bonded battery configuration and reported in Table 6. For these reasons a shear dominated failure starting from the substrate ends is deemed more likely than a failure caused by the peak normal stress occurring at substrate mid-span.

The results for the battery thickness increase during charging are reported in Figure 24. The small displacements involved were comparable to the sensitivity of the measuring instrumentation, therefore the surface data was affected by a fairly high amount of noise, Figure 24(a). The imprint of the anode shape in the contoured data shows that the thickness

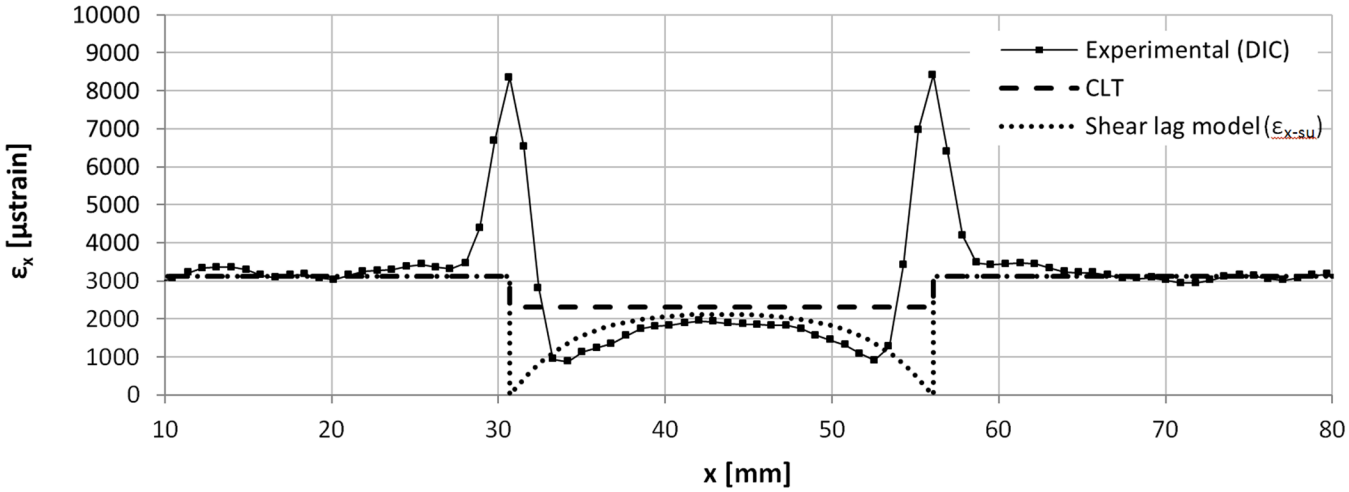

Figure 20. *Measured and calculated ε_x strain distribution along line a-a shown in Figure 19. Laminate stacking sequence at battery is [(0/45/90/–45)$_S$/AF/TFB]. The x-coordinate defined in Figure 13 is offset in order to match the DIC coordinate system.*

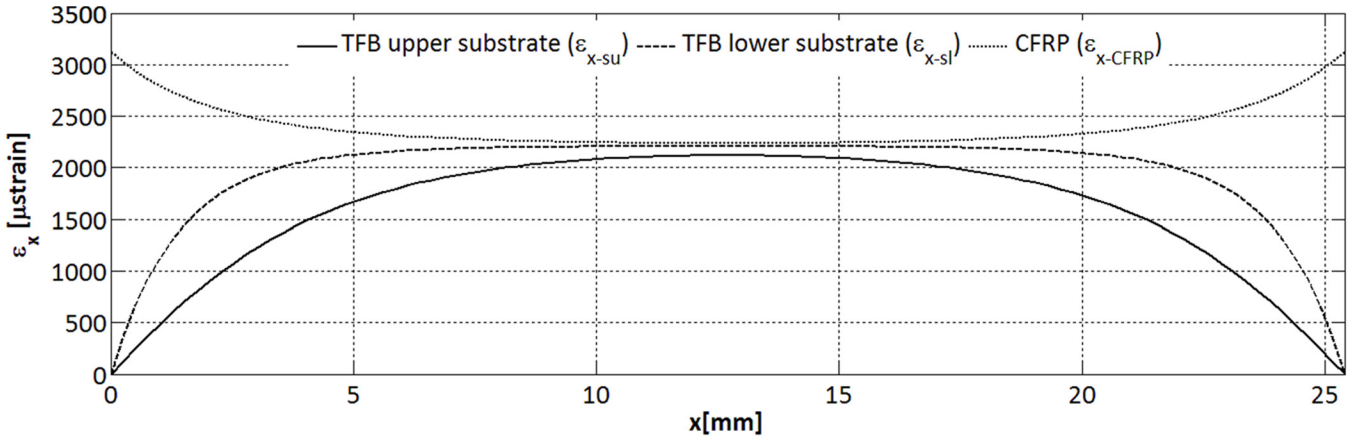

Figure 21. *Normal strain distribution in CFRP laminate and TFB substrates calculated with the shear lag model. Laminate stacking sequence at battery is [(0/45/90/–45)$_S$/AF/TFB]. Applied far-field strain of 3123 μstrain.*

increase was higher over the active components. In order to reduce the scatter, the average displacement of the area over the anode was calculated for every sampled displacement fields and plotted in Figure 24(b) as a function of the charge level. The charge level was defined as a linear function of the battery voltage during charging: 0% corresponded to the initial charging voltage and 100% to the voltage at the end of the charging process (i.e. when the charge current dropped below 50 μA). The thickness increase at full charge resulting from regression analysis of the averaged displacement data was about 4 μm. An influence from temperature variability is excluded since no significant environmental changes or battery self-heating was detected by the IR camera during the test. The perturbation introduced by a 4 μm battery cyclic expansion in terms of normal interlaminar stress and its long term effects on the integrity of the TFB-CFRP laminate are unknown at this stage of the research. However, the high coefficient of expansion demonstrated by a single TFB cell suggests that the design of future stacked multicell laminates should account for the thickness variability.

The uniaxial tension tests with capacity monitoring confirmed that the battery electrochemical performance is unaffected by the applied strain, as reported by [21,24,25]. The sequence of capacity measurements under increasing strain for one of the two specimens tested is shown in Figure 25 and demonstrates that the ability of the battery to store energy remained constant up to the electrical failure. Also the current and voltage profiles were unchanged until electrical failure occured. Failures consisted of an immediate and total loss of capacity that occured as soon as a certain strain level was exceeded. The discharge voltage measured at the beginning of the strain interval was lower than 3 V, therefore the charge/discharge circuit recorded a zero discharge capacity and switched to the charging mode. Once in charging mode, the current saturated the power supply output and remained constant at 5 mA, similar to a short circuit. The charge capacity relevant to this type of failure is reported as infinite in Figure 25. Bringing the strain back to zero did not restore the battery functioning and failure was confirmed.

The electrical failure occured when the strain at the bat-

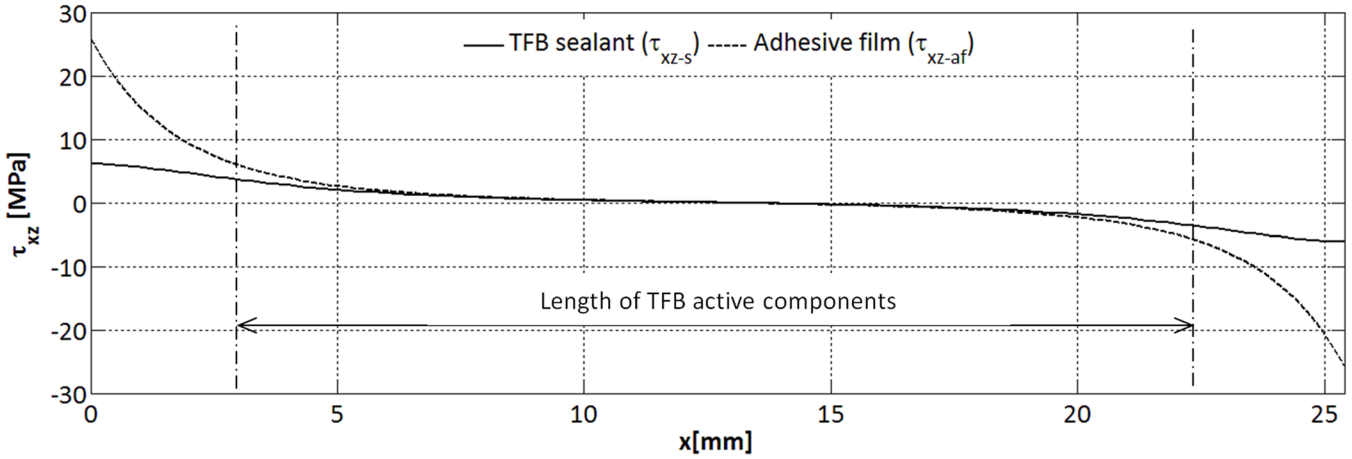

Figure 22. *Shear stress distribution in adhesive film and sealant calculated with the shear lag model. Laminate stacking sequence at battery is [(0/45/90/–45)$_S$/AF/TFB]. Applied far-field strain of 3123 μstrain. The length occupied by the active components is indicated in the plot area.*

Table 6. Uniaxial Mechanical Tension of Externally Bonded TFB. Summary of Critical Stress-strain Values at TFB Mechanical Failure. The Far-field Strain is Experimentally Measured, the Other Values are Calculated.

	Strain at Failure		Stress at Failure	
Lay-up	**Far-field ε_0 [μstrain]**	**Max. TFB $\varepsilon_{x-sl\,max}$ μstrain]**	**Max. TFB normal $\sigma_{x-sl\,max}$ [MPa]**	**Max. TFB shear $\tau_{xz-af\,max}$ [MPa]**
[(0/45/90/–45)S/AF/TFB]	5072	3588	639	42
(0_8/AF/TFB)	4724	4050	721	43
Average	4898	3819	680	42.5

tery exceeded 5100 μstrain. The critical strains reported in Table 7 are relevant to the last strain cycle preceding failure, thus they are maximum operating strain values. The strain at the battery was calculated by multiplying the far-field strain by the 0.8 strain concentration factor determined though the mechanical tests and FEA described in the preceding section, Table 5. The causes of the failure are unknown since the battery was not accessible for inspection and ultrasonic

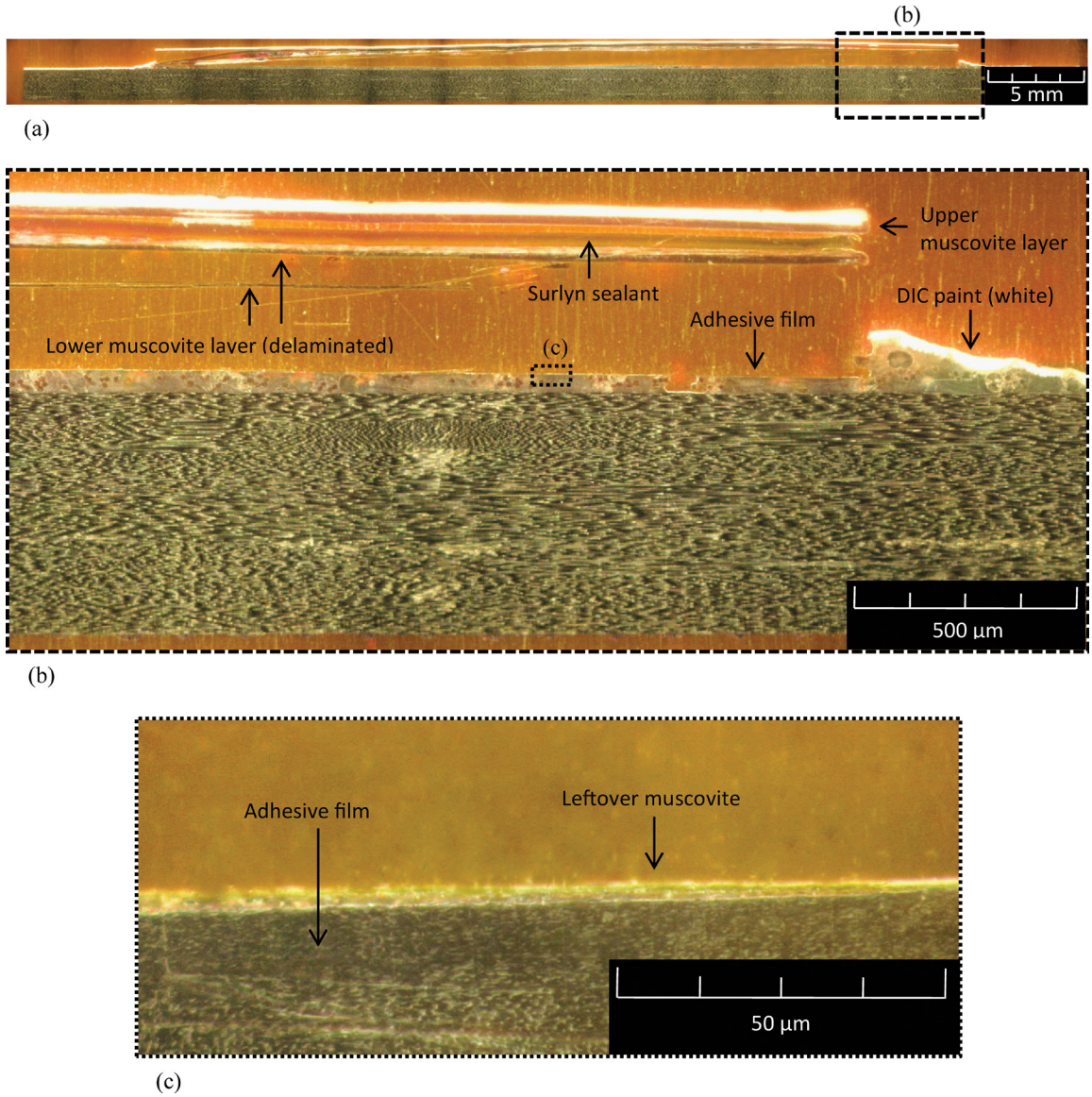

Figure 23. *Micrographs of the uniaxial tension test specimen with externally bonded TFB after failure. Laminate stacking sequence is (0_8/AF/TFB). (a) Full TFB section showing the battery lifted apart from the graphite laminate throughout the entire battery length. (b) Multiple delaminations propagate through the TFB substrate. (c) Adherent failure of the TFB substrate.*

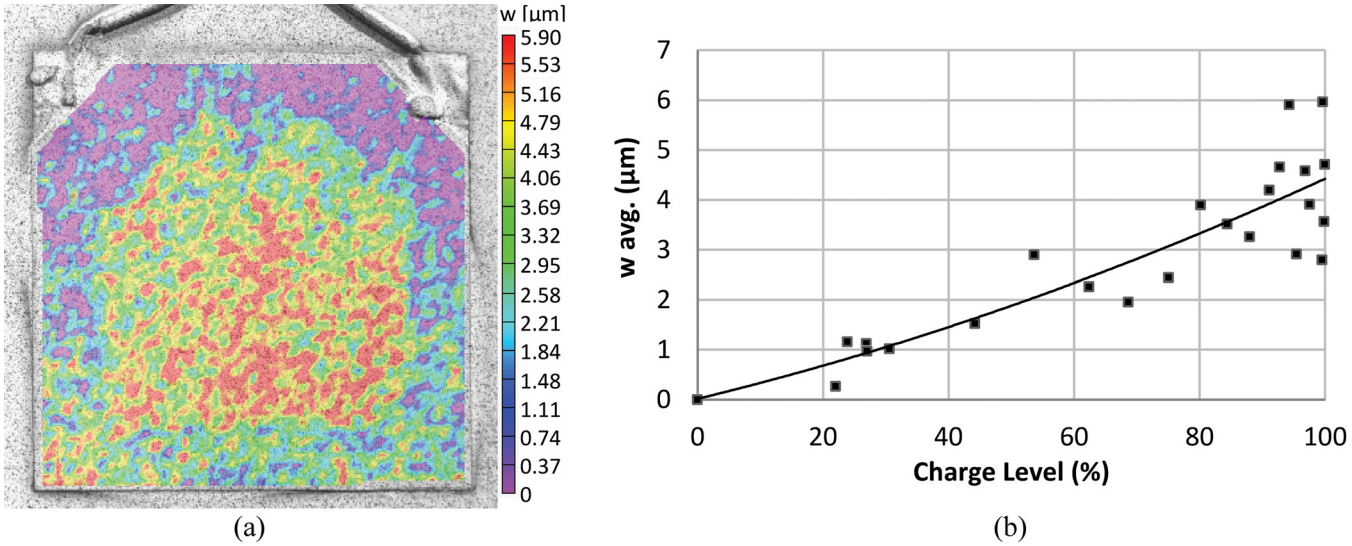

Figure 24. *(a) Anode side surface distribution of out-of-plane displacement w measured with digital image correlation (DIC) at 80% charge level. (b) Displacement w averaged over the anode area and second order polynomial regression of the data points.*

inspections had not proven to be effective for this particular structure. The in-plane stiffness of the specimens along the testing direction did not change significantly after the electrical failure occurred.

The results of the flexure tests showed that the applied curvature, similarly to the in-plane strain, does not affect the electrochemical performances up to failure. Results also gave evidence that the different combinations of strain and curvature lead to different failure modes. The specimens with an embedded battery at the laminate mid-plane and with a span-to-thickness ratio of 60:1 mechanically failed at a radius of curvature of 159 mm. The electrochemical performance remained constant up to the structural collapse of the laminate, which occured by compressive failure of the upper plies and was not affected by the presence of the battery. This was the only loading condition for which the laminate structural strength was more critical than the battery integrity, thereby showing that pure curvature of the TFB is not critical for most structural applications. In order to measure the critical radius of curvature of the battery, the span-to-thickness ratio was increased to a non-standard ratio of 145:1. This test set-up allowed achievement of the electrical failures, which occurred at an average radius of curvature of 112 mm, without being anticipated by performance fading and with the same sudden loss of discharge capacity experienced during the uniaxial tension test, Figure 26.

For the combined curvature and in-plane strain loading conditions, electrical failures were obtained at the 60:1 span-

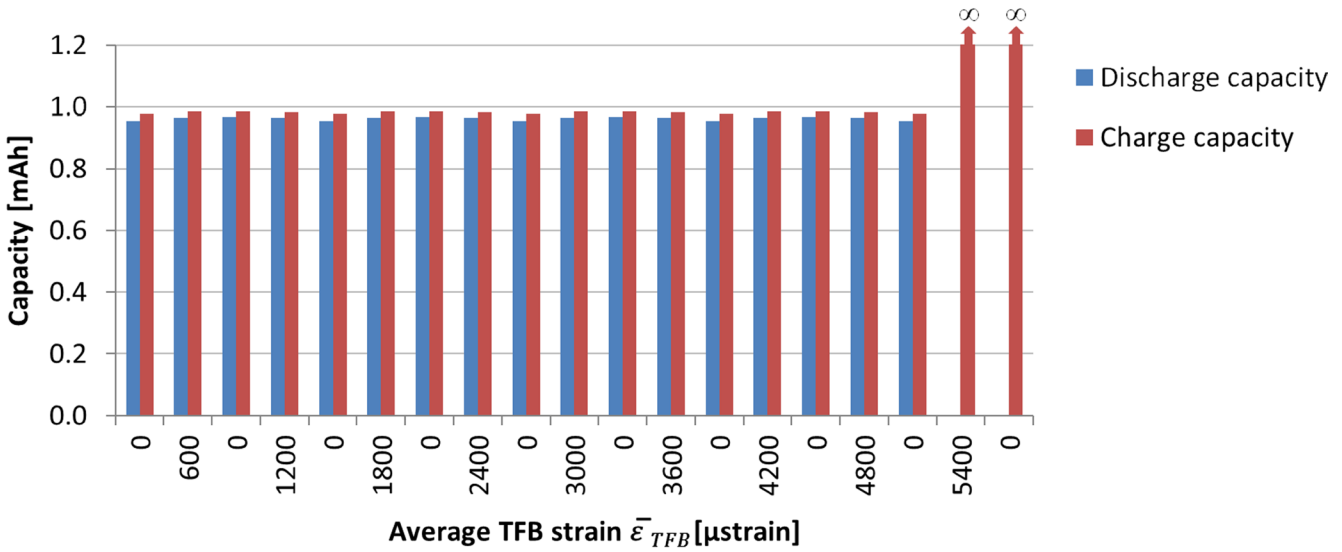

Figure 25. *Electrochemical characterization of the TFB-CFRP laminate under uniaxial mechanical tension. Capacity measured at increasing strain cycles up to failure. Laminate stacking sequence is (0/45/90/–45/TFB/–45/90/45/0).*

Table 7. Critical Strain Values for Uniaxial Mechanical Tension with TFB Electrical Capacity Monitoring of Laminate [0/45/90/–45/TFB/–45/90/45/0]. Measured Far-field Strain ε_0 and Corresponding Calculated Average TFB Strain $\bar{\varepsilon}_{TFB}$ at Electromechanical Failure.

	Strain at Electrical Failure	
Lay-up	ε_0 [μstrain]	$\bar{\varepsilon}_{TFB}$ [μstrain]
Repetition 1	6000	4800
Repetition 2	6750	5400
Average	6375	5100

to-thickness ratios. The critical radii of curvature and strains are summarized in Table 8. The compressive loading condition, with a low far-field strain at failure of 2832 μstrain, was particularly critical. Failure occurred by delamination buckling of the TFB packaging, Figure 27, and subsequent battery contamination. The failure initiation is uncertain. It can be attributed to an adhesive failure at the sealant-substrate interface, or, given its low fracture toughness, to a delamination of the substrate. A cohesive failure of the sealant is deemed unlikely because of the relatively high fracture toughness of Surlyn. The buckling of the upper substrate, shown in a close-up view in Figure 28, opened a path for air and moisture ingression through the battery packaging and it was followed by a neutral grey discoloration of the anode occurring below the wrinkle of the substrate. This chromatic change was attributed to the reaction of lithium with contaminants. Like for the failure of the embedded battery, the discharge capacity measured after failure was considered zero because the discharge voltage was lower than 3 V. On the other hand, the charge current did not saturate the power supply as mentioned for the embedded battery, but it remained constant at about 0.45 mA and it showed a fairly high amount of random high frequency oscillations with approximately 50 μA of amplitude. The charging process was declared failed after one hour.

The specimens tested in curvature and positive strain

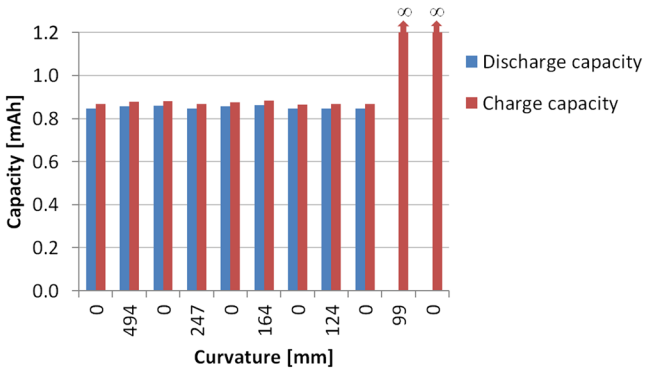

Figure 26. *Electrochemical characterization of the TFB-CFRP laminate under single curvature. Capacity measured at increasing curvature cycles up to failure. Laminate stacking sequence is [0/90/TFB/90/0].*

Table 8. Four Point Bending with TFB Electrical Capacity Monitoring. Summary of Critical Radius of Curvature and Strain at Electromechanical Failure.

		Radius of Curvature [mm]	Far-field Strain [μstrain]
Curvature	Repetition 1	124	0
	Repetition 2	99	0
	Average	112	0
Simultaneous curvature and negative in-plane strain	Repetition 1	504	–2971
	Repetition 2	557	–2692
	Average	531	–2832
Simultaneous curvature and positive in-plane strain	Repetition 1	204	7354
	Repetition 2	224	6683
	Average	214	7019

failed at an average radius of curvature of 214 mm and an average far-field strain of 7019 μstrain. The failure mode consisted of brittle fracturing of the lower substrate and battery detachment form the CFRP sub-laminate, as described for the externally bonded battery configuration subjected to uniaxial tension. Although the failure modes for these two loading conditions appeared to be the same, the critical far-field surface strain of the laminates tested in flexure was 40% higher. The cause for the mismatch is partially attributed to an error associated with the calculation of the strain at failure for the curvature and positive in-plane strain loading condition. In fact, the deflections of the specimens at failure were in excess of 10% of the support span, leading to geometrical nonlinearities. Therefore the small deformations assumption utilized for computing the strain provided overestimated values for this particular case.

4. CONCLUSIONS

The assumptions of plane stress and uniform normal strain through-the-thickness allowed the prediction of the overall elastic behavior of the hybrid thin film lithium ion—graphite battery laminates subjected to in-plane strain, for

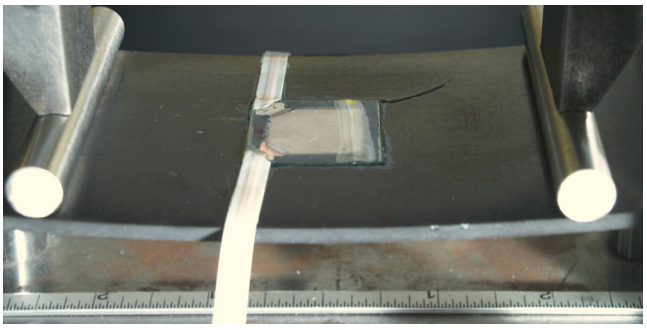

Figure 27. *Failure of TFB undertaking electromechanical flexure testing. Delamination buckling of the battery at a radius of curvature of 504 mm and compressive strain of 2971 μstrain.*

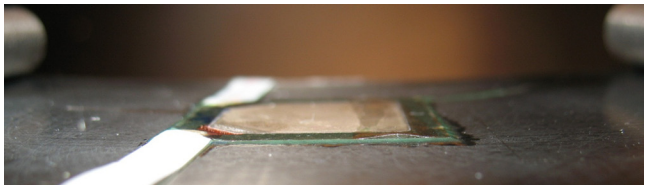

Figure 28. *Failed battery shown in Figure 27 reveals air and moisture path through the buckled substrate.*

either the embedded battery or the externally bonded battery configuration. However, besides not being applicable at lay-up transition, these assumptions did not capture the extensive shear-lag that develops in proximity of the battery edges of the externally bonded battery configuration. Therefore three-dimensional FEA or higher order laminate, zig-zag, or layerwise theories are required for an optimized design.

The operational envelope for the hybrid laminate featuring the current thin film battery technology is reduced with respect to a conventional CFRP structural laminate. The failure of the TFB-CFRP laminate, defined as the mechanical failure of any laminate component or the electrical failure of the battery, occured at an applied far-field strain of 4898 μstrain for uniaxial tension and 2832 μstrain for uniaxial compression in the worst case scenarios. The ability to tolerate curvature was equivalent to that of a conventional laminate as long as the battery was located at the laminate mid-plane and provided that the critical radius of curvature of 112 mm was not exceeded. Within these operational limits the electrochemical performance was not affected by the mechanical boundary conditions. Differences between the embedded battery and the externally bonded battery configuration were discussed in detail.

The critical failure modes of the externally bonded battery configuration included mode II dominated delamination or disbonding of the battery packaging when the laminate was subjected to mechanical tension, with failure onset at the battery edges or possibly at the edge of the active components. Delamination buckling of the battery upper substrate was critical under compressive loading. The packaging buckling failure triggered the electrical failure by cell contamination with air and moisture. The delamination or cracking of the active components were not critical failure modes with the current packaging materials. Hence the battery packaging was the weakest link for the structural and electrical integrity.

The critical failure modes for the embedded battery configuration were not identified. The test campaign gave evidence that electrical failure is more critical than mechanical failure of the laminate for the in-plane strain loading condition. Battery substrate splitting with subsequent tearing of the active components, delamination of the packaging with cell contamination, or mechanical failure of the active components are all possible failure modes. The failure of the electrical connections is excluded because the battery discharge voltage remained detectable after failure. The same uncertainties apply to the electrical failure under curvature, which is, however, less critical than the mechanical failure of the laminate.

The low fracture toughness of the muscovite substrate is the most important limiting factor for the mechanical integrity of the current battery packaging. The high modulus mismatch between the Surlyn sealant and the substrate is the second most important limiting factor. The delamination of the substrate was responsible for the failure of the externally bonded battery under in-plane tension and is suspected to be the main cause for the delamination buckling that occured under compression. The low fracture toughness of the substrate might have concealed other shortcomings such as poor mechanical strength of the electrodes and electrolyte and their bonding interfaces with the packaging, which were expected to be the critical for electromechanical survivability. A higher modulus sealant would increase the load sharing efficiency of the externally bonded battery and prevent compression buckling of the packaging. On the other hand, it would also increase the shear stress concentration factor at the battery edges, which promotes disbonding onset.

The interlaminar embedding of the battery did not have direct detrimental effects on the CFRP laminate elastic properties and mechanical strength. Perfect bonding and predictable load sharing with the composite structure up to failure were observed. Nevertheless the possible delamination onset and propagation at lay-up transition requires further investigation. Moreover, accounting for the effects of the cyclic battery thickness variation upon the interlaminar normal stress and strain energy release rate is recommended for stacked multicell architectures. The stress induced by the battery thickness increase could be reduced by curing the laminates with fully charged batteries; however the study on manufacturability conducted by the authors revealed that thermal processing at full state of charge reduces the maximum curing temperature that the batteries can tolerate without permanent capacity loss. The design of TFB-CFRP laminates would benefit from the development of appropriate electrode materials that minimize volume variation during lithiation-delithiation.

The results demonstrate the importance of the packaging for the mechanical integration of batteries and structure. The laminate stress-strain field is highly influenced by the design of the substrate and sealant layer, as shown by the analysis of the uniaxial mechanical tension tests of the embedded and externally bonded battery configurations. Moreover, all the critical electromechanical failure modes that have been identified are initiated by the failure of a packaging component. For these reasons conventional packaging materials currently adopted by standard flexible electronics are inadequate for the multifunctional application. Lightweight aeronautical materials and high temperature structural composites developed for space application should be considered for

their high elastic modulus and the ability to withstand severe stress and the high temperature associate with the manufacturing of the battery.

Based on the current performance, this multifunctional technology could be applied to a limited range of micro- and mini-UAV platforms, where the mechanical demands are minimal and the ratio of batteries to structural composites can be large enough to provide the required electrical energy and maximize the multifunctional efficiency, More demanding applications require a technological transition to improve the mechanical properties of the electrochemically active components and the packaging. In order to support the design of the next generation of airborne structural thin film batteries, modeling of the three-dimensional stress-strain field, delamination initiation and propagation are required to increase the mechanical strength and the electric survivability of the multifunctional system. The design should also account for the constraints given by the physiochemical requirements of the TFB manufacturing process and by the composite laminate curing process. Finally, the density of the packaging materials should be minimized for lightweight design, whereas the current substrate material has a too high density of 2.6 g/cm^3.

ACKNOWLEDGMENTS

This research was sponsored by the U.S. Air Force Office of Scientific Research (AFOSR) within the 5-year MURI '06 Program "Energy Harvesting and Storage Systems and Their Integration to Aero Vehicles" AF-MURI (FA9550-06-1-0326) led by the University of Washington. The authors would like to acknowledge Dr. Byung-Lip "Les" Lee, AFOSR Program manager, and Prof. Minoru Taya, MURI PI.

References

[1] Thomas J.P., Qidwai M.A., Matic P., Everett R.K. (2002). Multifunctional structure-plus-power concepts, 43rd AIAA/ASME/ASCE/AHS/ASC Structures, Structural Dynamics, and Materials Conference, Denver, CO.

[2] Thomas J.P., Qidwai M.A. (2004). Mechanical design and performance of composite multifunctional materials, *Acta Materialia,* 52: 2155–2164. http://dx.doi.org/10.1016/j.actamat.2004.01.007.

[3] Thomas J.P., Qidwai M.A. (2005). The design and application of multifunctional structure–battery material systems, *Journal of the Minerals, Metals and Materials Society,* 57(3):18–24. http://dx.doi.org/10.1007/s11837-005-0228-5.

[4] Qidway M.A., Baucom J.N., Thomas J.P., Horner D.M. (2005). Multifunctional Applications of thin film Li polimer battery cells, *Material Science Forum,* 492–493: 157–162. http://dx.doi.org/10.4028/www.scientific.net/MSF.492-493.157

[5] Owens B.B. (2000). Solid state electrolytes: overview of materials and applications during the last third of the Twentieth Century, *Journal of Power Sources,* 90: 2–8. http://dx.doi.org/10.1016/S0378-7753(00)00436-5.

[6] Liu E., Sherman E., Jacobsen A. (2008). Design and fabrication of multifunctional structural batteries, *Journal of Power Sources,* 189(1): 646–650. http://dx.doi.org/10.1016/j.jpowsour.2008.09.082.

[7] Snyder J.F., Wong E.L., Hubbard C.W. (2009). Evaluation of commercially available carbon fibers, fabrics and papers for potential use in multifunctional energy storage applications, *Journal of the Electrochemical Society,* 156(3): 215–224. http://dx.doi.org/10.1149/1.3065070.

[8] Xu C., Ma C., Taya M. (2008). Electrolyte for Laminated Polymer Lithium Rechargeable Battery. *Electroactive Polymer Actuators and Devices (EAPAD),* Proc. Of SPIE Vol. 6927, 692714. http://dx.doi.org/10.1117/12.778705.

[9] Snyder J.F., Carter R.H., Wetzel E.D. (2007). Electrochemical and mechanical behavior in mechanically robust solid polymer electrolytes for use in multifunctional structural batteries, *Chemistry of Materials,* 19(3): 3793–3801. http://dx.doi.org/10.1021/cm070213o.

[10] Snyder J.F., Wetzel E.D., Watson C.M. (2009). Improving multifunctional behavior in structural electrolytes through copolymerization of structure- and conductivity-promoting monomers, *Polymer,* 50: 4906–4916. http://dx.doi.org/10.1016/j.polymer.2009.07.050.

[11] Wetzel E.D. (2011). Structural composite capacitors, supercapacitors and batteries. Presented at the Air Force Office of Scientific Research (AFOSR) Annual Grantees/Contractors Meetting, Mechanics of Multifunctional Materials & Microsystems, Arlington, VA, August 1–5.

[12] Whittingham M.S. (2004). Lithium batteries and cathode materials, *Chemical Reviews,* 104(10): 4271–4301. http://dx.doi.org/10.1021/cr020731c. PMid:15669156.

[13] Whittingham M.S., Song Y., Lutta S., Zavalij P.Y., Chernova N.A. (2005). Some transition metal (oxy)phosphates and vanadium oxides for lithium batteries, *Journal of Material Chemistry,* 15: 3362–3379. http://dx.doi.org/10.1039/b501961c.

[14] Wang Y., Cao G. (2008). Developments in nanostructured cathode materials for high-performance lithium-ion batteries, *Advanced Materials,* 20: 2251–2269. http://dx.doi.org/10.1002/adma.200702242.

[15] Chan C.K., Peng H., Liu G., McIlwrath K., Zhang X.F., Huggins R.A., Cui Yi (2008). High performance lithium battery anodes using silicon nanowires, *Nature Nanotechnology* 3: 31–35. http://dx.doi.org/10.1038/nnano.2007.411. PMid:18654447.

[16] Trevey J.E., Wang J., DeLuca C.M., Maute K.K., Dunn M.L., Lee S.H., Bright V.M. (2011). Nanostructured silicon electrodes for solid-state 3-d rechargeable lithium batteries, *Sensors and Actuators A: Physical,* 167: 139–145. http://dx.doi.org/10.1016/j.sna.2011.02.015.

[17] Scott I.D., Jung Y.S., Cavanagh A.S., Yan Y., Dillon C.A., George S.M., Lee S.H. (2011). Ultrathin coatings on nano-$LiCoO_2$ for FaLi-ion vehicular applications, *Nano Letters,* 11: 414–418. http://dx.doi.org/10.1021/nl1030198. PMid:21166425.

[18] Liu Y., Taya M. (2009). Electrospinning fabrication and electrochemical properties of lithium cobalt nanofibers for lithium battery cathode, *Active and Passive Smart Structures and Integrated Systems*. Proc. Of SPIE Vol. 7288 728806-1. http://dx.doi.org/10.1117/12.816173.

[19] Son S.B., Trevey J.E., Roh H., Kim S.H., Kim K.B., Cho J.S., Moon J.T., DeLuca C.M., Maute K.K., Dunn M.L., Han H.N., Oh K.H., Lee S.H. (2011). Microstructure study of electrochemically driven LixSI, *Advanced Energy Materials,* 1: 1199–1204. http://dx.doi.org/10.1002/aenm.201100360.

[20] DeLuca C.M., Maute K., Dunn M.L. (2011). Effects of electrode particle morphology on stress generation in silicon during lithium insertion, *Journal of Power Sources,* 196: 9672–9681. http://dx.doi.org/10.1016/j.jpowsour.2011.07.035.

[21] Golmon S., Maute K., Dunn M.L. (2009). Numerical modeling of electrochemical–mechanical interactions in lithium polymer batteries, *Computers and Structures* 87: 1567–1579. http://dx.doi.org/10.1016/j.compstruc.2009.08.005.

[22] Pereira T., Scaffaro R., Nieh S., Arias J., Guo Z., Hahn H.T. (2006). The performance of thin-film Li-ion batteries under flexural deflection, *Journal of Micromechanics and Microengineering,* 16: 2714–2721. http://dx.doi.org/10.1088/0960-1317/16/12/026.

[23] Pereira T., Scaffaro R., Nieh S., Arias J., Hahn H.T. (2008). Performance of thin-film Lithium Energy cells under uniaxial pressure, *Advaced Engineerig Materials,* 10(4): 393–399. http://dx.doi.org/10.1002/adem.200700214.

[24] Pereira T., Scaffaro R., Nieh S., Arias J., Hahn H.T. (2008). Embedding thin-film lithium energy cells in structural composites, *Composites Science Technology,* 68/7-8: 1935–1941. http://dx.doi.org/10.1016/j.compscitech.2008.02.019.

[25] Pereira T., Scaffaro R., Nieh S., Arias J., Hahn H.T. (2009). Energy storage structural composites: a review, *Journal of Composite Materials,* 43/5: 549–560. http://dx.doi.org/10.1177/0021998308097682.

[26] Luongo C.A., Masson P.J., Nam T., Mavris D., Kim H.D., Brown D.V., Waters M., Hall D. (2009). Next generation more-electric aircraft: a potential application for HTS superconductors, *IEEE Transactions on Applied Superconductivity,* 19 (3): 1055–1068. http://dx.doi.org/10.1109/TASC.2009.2019021

[27] Bates J.B., Dudney N.J., Gruzalsky G.R., Zuhr R.A., Choudhury A., Luck C.F., Robertson J.D. (1992). Electrical properties of amorphous lithium electrolyte thin films, *Solid State Ionics,* 53-56: 647–654. http://dx.doi.org/10.1016/0167-2738(92)90442-R.

[28] Bates J.B., Dudney N.J., Neudecker B., Ueda A., Evans C.D. (2000). Thin film lithium and lithium-ion batteries, *Solid State Ionics,* 135: 33–45. http://dx.doi.org/10.1016/S0167-2738(00)00327-1

[29] Bates, J.B., Dudney, N.J., Neudecker, B.J., Hart, F.X., Jun, H.P. and Hackhey, S.A. (2000). Preferred orientation of Polycrystalline $LiCoO_2$ films, *Journal of the Electrochemical Society,* 147(1): 59–70. http://dx.doi.org/10.1149/1.1393157.

[30] Krasnov, V., Nieh, K. and Li, J. (2011). Thin film battery and manufacturing method, US Patent No. 7862927. http://dx.doi.org/10.1088/0960-1317/12/1/309.

[31] Krasnov, V., Nieh, K., Ting, S., Tang, P., Chang, F. and Lin C. (2005). Sputter deposition of lithium phosphorous oxynitride material, US Patent No. 6863699.

[32] West W.C., Whitacre J.F., White V., Ratnakumar B.V. (2002). Fabrication and testing of all solid-state microscale lithium batteries for microspacecraft applications, *Journal of Micromechanics and Microengineering,* 12: 58–62.

[33] McNeil L.E., Grimsditch M. (1993). Elastic moduli of muscovite mica, *Journal of Physics: Condensed Matter,* 5: 1681–1690. http://dx.doi.org/10.1088/0953-8984/5/11/008.

[34] ASTM D5528 – 01. Standard test method for mode I interlaminar fracture toughness of unidirectional fiber-reinforced polymer matrix composites.

[35] ASTM D3039/D3039M – 08. Standard test method for tensile properties of polymer matrix composite materials.

[36] ASTM 6272 - 10. Standard test method for flexural properties of unreinforced and reinforced plastics and electrical insulating materials by four-point bending.

Journal of Multifunctional Composites

journal homepage: http://jmc.destechpub.com

Micromechanics of Unidirectional Viscoelastic Fibrous Composites-Homogenized vs Local Characterization

SAMAD JAVID, GHODRAT KARAMI*, ASGHAR REZAEI and FARDAD AZARMI

Mechanical Engineering Department, North Dakota State University, Fargo, ND 58108-6050, USA

KEYWORDS

Microstructures
Mechanical properties
Micromechanics
Computational modeling

ABSTRACT

In this paper homogenized elastic and viscoelastic material properties are evaluated and compared for symmetric and randomly distributed fibers within the matrix of a unidirectional composite laminate. In general, homogenized properties are different from their localized values. In homogenized characterization one assumption rests on a systematic distribution of fibers which at many circumstances might not be true. We select representative volume elements (RVE) in terms of repeating unit cells (RUC) of four types of fiber distributions; two systematic types (square—SQR and hexagonal—HEX packing), and two randomly distributed (one with identical fibers—RND, and one with random geometry—RNDG packing). Employing the principles of micromechanical characterization, RUCs of the composites were exposed to six distinctive types of loadings (three axial loadings and three shear loadings) under periodic boundary conditions. Inverse analysis is conducted to characterize and determine the comprehensive volume-averaged homogenized elastic and viscoelastic material properties of the composite. To investigate the impact of constituents' material anisotropy on the behavior of the compound material, both isotropic and orthotropic fibers are employed. To examine the effect of the fiber/matrix volume ratios, the results are presented for three different fiber volume ratios. The local stress/strain distributions within each RUC are monitored in comparison with the corresponding volume-averaged stresses and strains. The local stresses and strains are compared with the volume-averaged ones by which the material is characterized and the differences are highlighted. One conclusion is that the impact of random distribution and geometry of fibers on homogenized stiffness properties might be minor, but it has considerable effect on local stress/strain distribution and hence on the strength of the composite. Among the different types of RUCs the HEX packing provides more uniform distributions of stresses and strains.

1. INTRODUCTION

Micromechanical algorithms are efficient tools which have been widely used to study the local stress/strain distribution, damage analysis, and failure prediction [1–7] and thermoelastic characterization of composite materials [8–10]. Micromechanics concepts provide a tool to measure the mechanical properties of a composite from the characteristics of its constituents. Such a tool has been enhanced with finite element analysis in recent years. In this respect, Garnich and Karami [11] developed a linear elastic finite element micromechanics model to study the stiffness and strength of wavy fiber composites. The results revealed that local stresses caused by undulation of fibers, which are not predictable by traditional continuum analyses, play an important role in the characteristic and failure of such composites. Naik *et al.* [12] proposed a micromechanical procedure to predict the mechanical properties of viscoelastic fibrous composites. They studied the effect of fiber volume fraction on the material behavior of compound material by using RUC of square and hexagonal, and bidirectional crossed fi-

*Corresponding author. Tel.: +1 701231 5859; fax: +1 701 231 8913;
Email: g.karami@ndsu.edu

doi:10.12783/issn.2168-4286/1.1/Karami

bers packing. Abolfathi *et al.* [13] presented a micromechanical procedure to predict the homogenized elastic properties of angular bidirectional fiber-reinforced composites. The comparison between the compliance/stiffness solutions of this study and those obtained from the laminated theory were in good agreement. They suggested an algorithm to determine the optimum fiber angle within matrix to attain the most efficient mechanical properties in all directions. Drago and Pindera [14] employed three types of boundary conditions on a RUC compound of multiple square packing to determine the engineering moduli of unidirectional (UD) composites. Zhang *et al.* [15] investigated the effects of nonlinearity in materials and off-axial loading on the mechanical response of viscoelastic fibrous polymeric laminates.

Fiber arrangement in matrix has definite impacts on mechanical behavior of composites. In the above mentioned studies, the fibers have been assumed to be distributed periodically in regular and symmetric arrangements within the matrix, while in reality, fibers are usually randomly distributed. Although considering regular fiber arrangements simplifies the complexity of modeling and analysis, but the impact of random arrangements must be studied to acquire realistic solutions. In this respect, Jin *et al.* [16] studied the impact of fiber configurations on residual thermal stresses in UD composites with different fiber volume ratios. They considered commonly used SQR and HEX packing, and a random distributed array as the fiber arrangement. They conducted statistical analysis on the dispensation of residual thermal stresses in the random model and compared the results to those of regular packing. The differences were considerable and proved that the distribution of fibers has a considerable impact on residual thermal stresses, particularly at greater fiber volume ratios. Everett and Chu [17] modeled the microstructure of non-uniform UD composites and showed that the fibers configuration affects the degree of non-uniformity of the compound material. Oh *et al.* [18] conducted a research work to study the fiber/matrix interfacial strain distribution in unit cells with random array of fibers.

Wongsto and Li [19] carried out a numerical analysis on UD composites to study the impacts of implementation of incorrect physical constraints on the anticipated mechanical response of unit cells with randomly distribution of fibers. They found that the imperfect boundary conditions may only change the results in the areas close to boundaries and would decay gradually away from the edges. They used the data of sub-domains far from the boundaries to characterize the mechanical properties of the compound material. Huang *et al.* [20] carried out a frequency analysis on the distribution of stress invariants within the matrix as well as traction distribution at the interfacial area between matrix and fibers to evaluate performance of random and regular fiber packing.

A micromechanical analysis of symmetrical (SQR and HEX) distribution as well as random distribution will be considered in this paper. Although the distribution may be taken of any random type, here only two examples of random fiber distributions, one with identical fiber geometry (RND) and one with random geometry (RNDG), will be examined to observe the homogenized mechanical properties as well as local stress distribution in composite constituents. Finite element micromechanical analyses are performed on the selected models representing RUCs of UD composites. The results will be compared to examine the effects of randomness of fiber distribution and geometry.

2. MICROMECHANICAL MODELING

2.1. Repeating Unit Cell Modeling of SQR, HEX, RND, and RNDG

Figure 1 shows four different types of fiber arrays assumed to be representing the microstructure of UD composites. In all cases, fibers are assumed to have uniform cylindrical shapes distributed parallel to each other within the matrix domain. In two configurations, fibers are embedded regularly and symmetrically in the matrix, with the symmetry lines define the three-dimensional repetitive square (SQR) and hexagonal (HEX) representative volume elements of the composite material [Figures 1(a) and 1(b)]. In the third configuration (RND) identical fibers are distributed randomly in matrix with a RVE involving fourteen cylindrical fibers to symbolize the microstructure of the material [Figure 1(c)]. In the fourth configuration (RNDG), cylindrical fibers with different diameters are scattered in a random pattern in matrix domain. In this packing, 27 cylindrical fibers are assumed to have four different circular cross-section areas [Figure 1(d)]. To study the impact of fiber volume ratio on the mechanical response of UD composites, each RUC is modeled with three fiber volume fractions of 0.3, 0.4 and 0.5.

2.2. Micromechanics Elastic and Linear Viscoelastic Analysis of RUCs

The relation between stresses and strains of an elastic anisotropic material can be expressed by $\varepsilon_{ij} = S_{ijkl}\sigma_{kl}$ for i, j, k, $l = 1, 2, 3$, where S_{ijkl} are components of the 6×6 matrix of compliance coefficients. The number of independent compliance coefficients depends on the degree of heterogeneity of the material under investigation. This matrix is symmetric, and thus, for a completely anisotropic material there are 21 independent compliance coefficients. For orthotropic, transversely isotropic and completely isotropic materials this number reduces to 9, 5 and 2, respectively. In the computational analysis and for characterization purposes, we assume that the composite constituted from isotropic or anisotropic components is completely anisotropic. The degree of isotropy of composites depends on the constituents, and can be revealed once the inverse analysis has been carried out. This

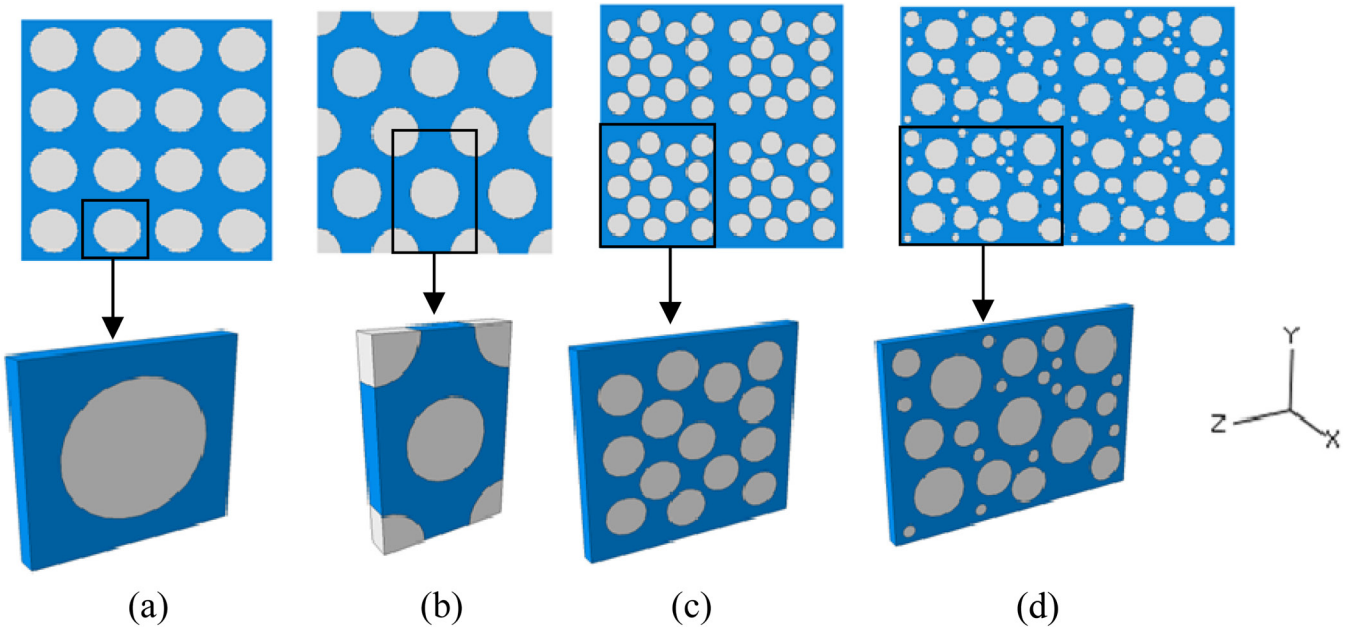

Figure 1. *RUCs representing UD composites, (a) SQR, (b) HEX, (c) RND, (d) RNDG packing. The white circular areas are fibers and the rest is matrix. The fibers are embedded parallel to each other in the X-direction.*

means by counting the number of non-zero and independent terms of S_{ijkl} the anisotropy can be found. For the inverse analysis, each RUC is exposed to six independent load cases (3 axial and 3 shear loads). For each load scenario there are six independent stress and strain components. Therefore, plugging theses values in the above equations, a set of thirty six linear equations will be resulted by which all the thirty six unknown compliance coefficients can be derived. The mechanical stiffness parameters in terms of Young's and shear moduli and Poison's ratios, in the principal directions where the material is orthotropic are related to compliance/stiffness coefficients [21].

For linear viscoelastic materials, a linear relationship between the strain history and the current value of stress which can be expressed by the following hereditary integral equation is assumed, i.e.,

$$\varepsilon_{ij}(t) = \int_0^t S_{ijkl}(t-\tau)\frac{d\sigma_{kl}}{d\tau}d\tau, \quad i,j,k,l = 1,2,3$$

The compliance coefficients are functions of time, i.e., $S_{ijkl} = S_{ijkl}(t)$ at any particular time t, and the strains can be related to stresses by equation $\varepsilon_{kl}(t) = S_{ijkl}(t)\sigma_{ij}(t)$. Therefore, the compliance coefficients and the related engineering constants should be characterized at each individual time step.

In the micromechanics finite element procedures of each RUC, stress and strain distributions will be evaluated. These localized stress and strains can then be volume-averaged over the RUC volume for the homogenization characterization procedure. The reason behind these volume-averaging is the assumption that the RUC is presenting a point within the continuum domain, and therefore has a homogenized material property.

2.3. Loading and Periodic Boundary Conditions

As shown in Figure 2, each RUC is exposed to six comprehensive independent load scenarios; three axial loads, two direct shear load cases, and one torsional shear loading. The axial loads are normal to the faces of the RUC and the shear loads are tangent to the faces. Under periodic boundary conditions axial load pairs produce pure uniaxial normal stresses, and shear load cases produce pure shear stresses for a uniform material.

Stress relaxation tests are usually used to study the time-dependent behavior of viscoelastic materials. In a stress relaxation test a constant strain (displacement) is applied on the material sample for a certain period of time. The stress (force) variation is recorded during the loading process. If the constant load is applied instantly, there is a primary fluctuation in results before they become stable. To avoid this fluctuation the load increases by a sharp ramp and reach its desired value as shown in Figure 3. In the current study, the six load cases are in the form of ramped constant strain (displacement). For elastic composites, the constant loads are applied suddenly on the unit cells and finite element static analysis is carried out to predict the mechanical behavior of them.

To generalize the characterized mechanical behavior obtained from the inverse analysis of the RUC to the whole material it is deemed that the composite material is composed of repetitive unit cells. Each RUC, which in fact simulates a continuum point of the composite material under

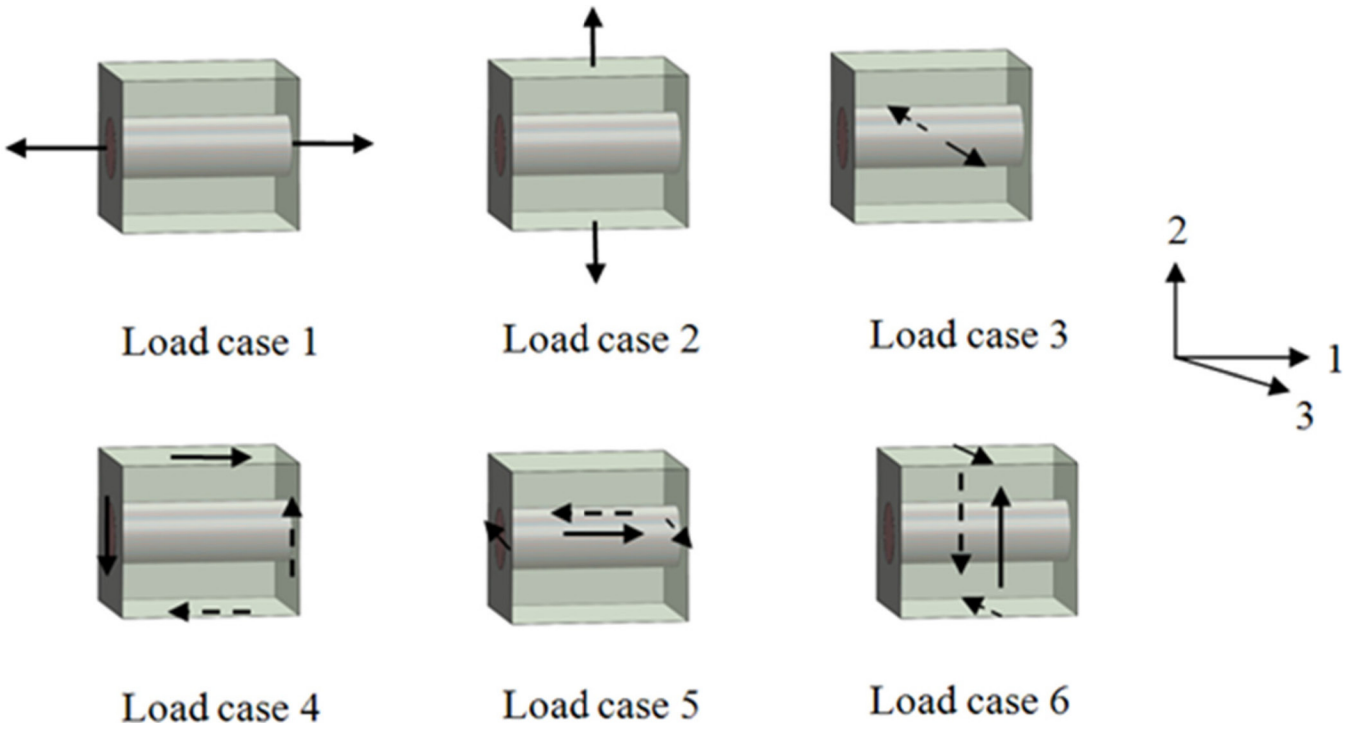

Figure 2. *Load cases defined to characterize the mechanical behavior of the UD composites.*

investigation, is exposed to a set of boundary conditions to simulate the periodicity. These boundary conditions, which are called periodicity boundary conditions, require opposite faces of the unit call undergo identical deformation. Thus constraint relations between the nodes on the parallel faces are used to enforce periodicity constraints on the RUC. To fulfill this, the number and distribution of nodes on opposite faces should be the same, and each face should have a node at its geometric center. There should be also a node at the geometrical center of the RUC. As a part of physical boundary conditions, this node would be fixed in all three directions to prevent rigid body motion in the analyses. For detailed implementation of periodicity constraints as well as the rigid body conditions on a RUC one can refer to Garnich and Karami [11] and Naik *et al.* [12].

3. NUMERICAL RESULTS AND DISCUSSION

3.1. The Material Input

Two different composite materials are employed in this study. SiC/F-Glass composite is made of F-Glass matrix (E = 59 GPa, v = 0.2) reinforced by Textron SCS-6 SiC fibers (E = 423 GPa, v = 0.15) [13], and AS4/Epoxy composite is made of AS4 carbon fibers within a viscoelastic epoxy matrix. Carbon fibers in AS4/Epoxy (with AS4 as elastic fibers and Epoxy as viscoelastic material) composite are transversely isotropic. The elastic properties of the AS4 fibers are; E_1 = 201 GPa, $E_2 = E_3$ = 13.5 GPa, $G_{12} = G_{13}$ = 95 GPa, G_{23} = 4.9 GPa, and $v_{12} = v_{13}$ = 0.22, v_{23} = 0.25 [13] and the linear viscoelastic behavior of the matrix with the time-dependent shear and bulk moduli, i.e. $G(t)$ and $K(t)$, are expressed by the following Prony series as,

$$G(t) = G_0\left(1-\sum_{k=1}^{n} g_k(1-e^{-t/\tau_k})\right)$$

and

$$K(t) = K_0\left(1-\sum_{k=1}^{n} k_k(1-e^{-t/\tau_k})\right)$$

where G_0 and K_0 are instantaneous shear and bulk moduli and g_i, k_i and τ_i are material-dependent parameters. The viscoelastic parameters of epoxy matrix of AS4/Epoxy composite are represented in Table 1 [13].

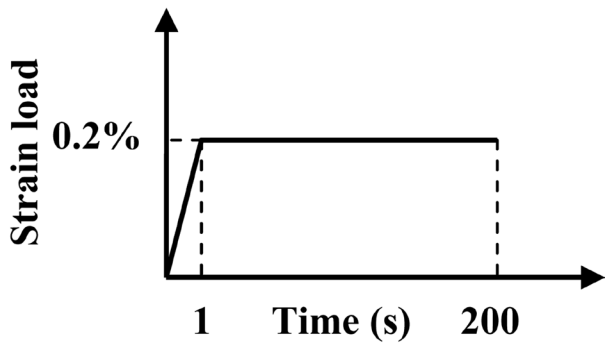

Figure 3. *Stress relaxation loading diagram.*

Table 1. Viscoelastic properties of epoxy matrix in AS4/Epoxy composite (density: 1.44428 g/cm^3, E_∞ = 8.3 GPa, v = 0.4) [13].

g_k	k_k	τ_k (sec)
0.0126233	0	1.0145e-9
0.0255204	0	1.0145e-8
0.0625175	0	1.0145e-7
0.0768628	0	1.0145e-6
0.128583	0	1.0145e-5
0.147175	0	1.0145e-4
0.181631	0	1.0145e-3
0.171479	0	1.0145e-2
0.0833645	0	1.0145e-1
0.0348822	0	1.0145
0.0120372	0	1.0145e1
0.00964421	0	1.0145e2

3.2. Elastic Analysis-Local Stress Distributions in RUCs

For SiC/F-Glass composite, RUCs with four various fiber arrays (as indicated in Figure 1) with volume fiber ratios of 0.3, 0.4, and 0.5 were analyzed under six types of loadings employing ABAQUS finite element package [22]. Figure 4 shows the stress distributions in the direction of 1 (S_{11}, Pa) within the deformed microstructural shape of the various RUCs related to SiC/F-Glass composite with fiber volume ratios of 0.5 under load case 1 (under a 0.2% stretch in the direction of fibers). As the contours of stress distributions indicate, the elements located in the fibers have the same stress but higher than those elements of the matrix domain. The stresses are distinctly uniform in each domain of the fibers and matrix. It is due to the uniform stretch of all elements in the longitudinal direction. At this load case for UD elastic composites the distribution and the geometry of fibers have almost no effect on the stress/strain distribution in the composite constituents. The reason should be sought on the fact that perfect bonding between the fibers and matrix has been assumed.

In Figure 5 the contours of shear stress (S_{12}) distributions in RUCs of SiC/F-Glass composite with fiber volume ratio of 0.5 under load case 4 (shear load tangent to face 3 in the direction of 1) are plotted. Under this load case the maximum shear stress has been experienced by RNDG packing and the least difference between the highest and lowest stresses can be seen in HEX model. For this load case the resulted shear stresses/strains are affected significantly by both distribution and geometry of the fibers in the RUCs. To study the effect of fiber configuration and geometry on the local microstructural stress distribution within a RUC of the composite in detail, an analysis has been conducted to see what will be the uniformity of the stress within each RUC under the loading.

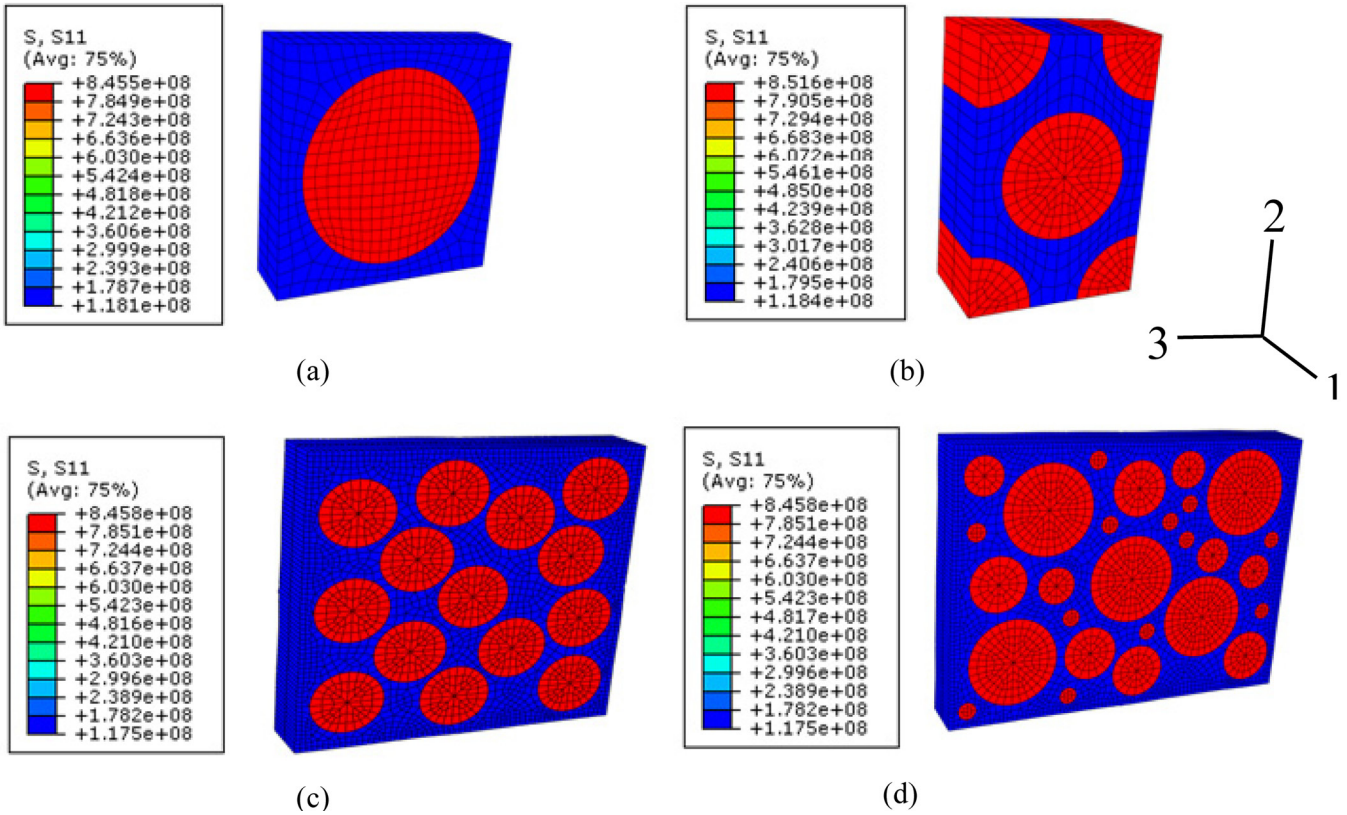

Figure 4. *Stress in direction of 1 (S_{11}, Pa) within the deformed shape of RUCs of SiC/F-Glass composite with fiber volume ratio of 0.5 under 0.2% strain in the direction of 1. The red circles are fibers and the remaining blue area is matrix. (a) SQR, (b) HEX, (c) RND, (d) RNDG model.*

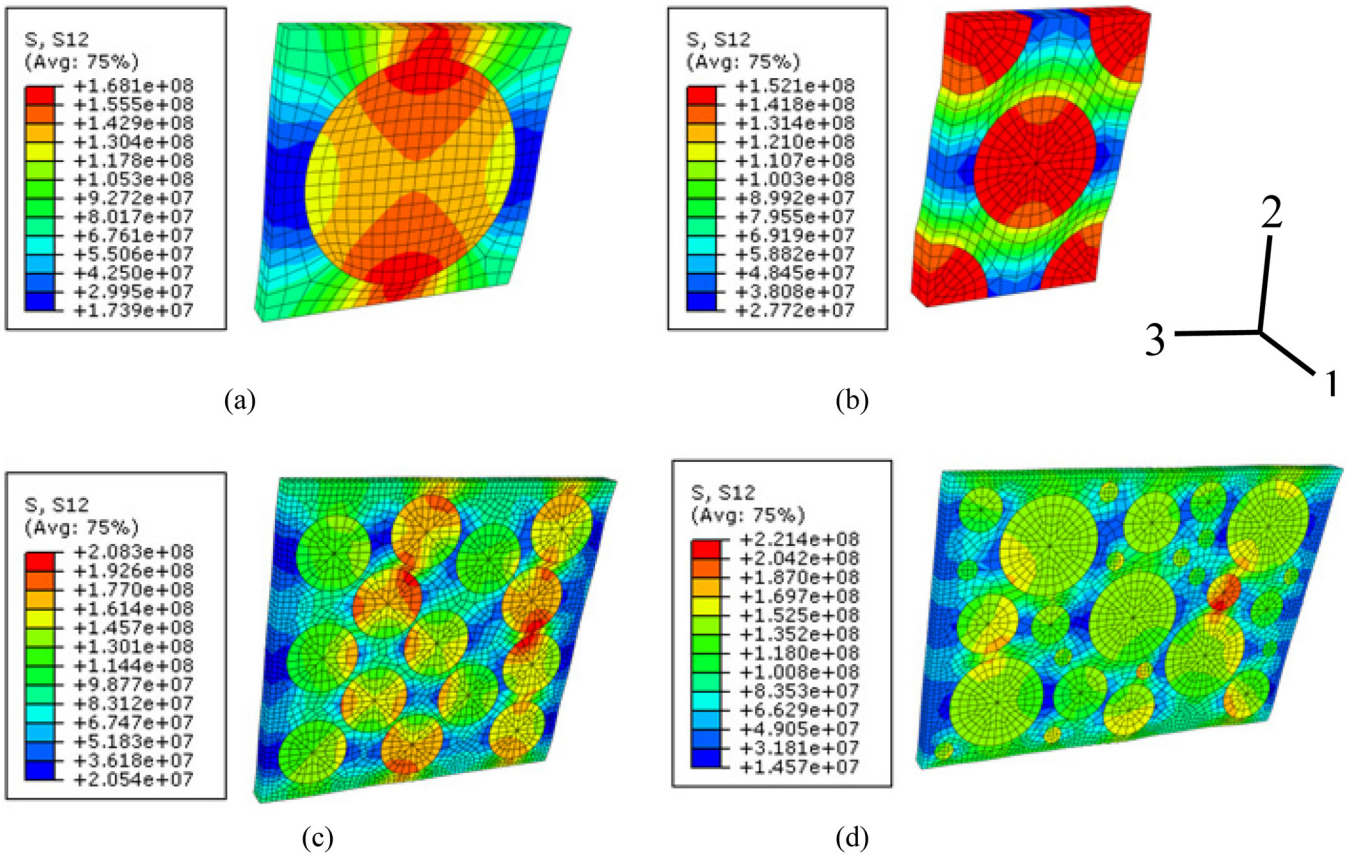

Figure 5. *Shear stress S_{12} (Pa) within the deformed shape of RUCs of Sic/F-Glass composite with fiber volume ratio of 0.5 under 0.2% shear strain of face 3 in the direction of 1. (a) SQR, (b) HEX, (c) RND, (d) RNDG model.*

For this purpose the stress values are plotted with respect to their volume percentages within the volume of each RUC. Figures 6 and 7 represent the distribution of normal stress of S_{33} and shear stress of S_{12} versus the volume percentage of the RUC of SiC/F-Glass composite with fiber volume ratio of 0.5 under load cases of 3 and 4, respectively. As these figures show under load cases of 3 and 4 the stress distribution in RUCs are completely different and one can conclude that configuration of fibers have impact on the way local stresses transfer between the constituents. Comparing Figures 6(c) and 6(d) as well as Figures 7(c) and 7(d), one can conclude that besides the configuration of fibers, their geometry have considerable effect on the stress distribution in UD composites. This analysis indicates clearly that to study the micromechanical strength of composite materials both the real distribution and geometry of fibers should be taken into account. The maximum, stress, the volume-averaged stress, and percentage of loads carried in fibers and matrix of different RUCs of SiC/F-Glass composite with a fiber volume ratio of 0.5 under different kinematical load cases (% 0.2 normal or shear strain) are tabulated in Table 2. As shown in this table, due to unidirectional assumption of fibers, various unit cells have almost identical stresses under Load case 1 (LC1) which is an extension load along the fibers. For other load cases this is not the case. Note that for each load case the dominant component of stress, i.e., for LC1, S_{11}, for LC2, S_{22}, for LC3, S_{33}, for LC4, S_{12}, for LC5, S13, for LC6, S_{23} is considered in this table. From this table one can see that the maximum stress is always several times larger than the averaged stress within the body of the unit cell. The averaged-value stresses and strains are being used for material characterization of the unit cell representing a point within the continuum of the composite under consideration. In all load cases with the exception of load case 6 (torsional shear loading) HEX packing experience the lowest maximum values of stress. For load case 6, SQR unit cell has the lowest maximum stress values in the fibers and matrix. Based on these results, the conclusion is that HEX packing produce lower maximum stresses and therefore is a better type of packing as far as the strength of the composite might be concerned.

It should not be forgotten that the distribution of stresses in the random unit cells depend on the randomness of distribution and geometry of fibers and the results presented here are just for two typical random models. However, these analyses reveal clearly that using the symmetric SQR and HEX unit cells to study the stress and strain distribution of composite won't obviously lead to accurate results in practical applications.

Table 2. The Maximum Local Stress (MLS, Mpa) Against the Homogenized Volume-averaged Stress (HVS, Mpa), and Percentages of Load Being Transferred in Fiber (F) and Matrix (M) of Different RUCs of the SiC/F-Glass Composite with a Fiber Volume Ratio of 0.5 and Under Different Kinematical Load Cases of %0.2 (normal or shear strain). For Each Load Case (LC), the Stress Under Consideration is the Dominant Component of the Stress, for LC1, S_{11}, for LC2, S_{22}, for LC3, S_{33}, for LC4, S_{12}, for LC5, S_{13}, for LC6, S_{23}.

		LC1		LC2		LC3		LC4		LC5		LC6	
		F	M	F	M	F	M	F	M	F	M	F	M
SQR	Max. local stress	845.5	119.6	388.4	403.2	388.4	403.2	168.1	166.9	168.1	166.9	111.4	10.51
	Hom. VA stress	845.5	118.8	328.7	197.9	328.7	197.9	142.5	79.2	142.5	79.2	95.8	85.4
	% load in F or M	87.7	12.3	62.4	37.6	62.4	37.6	64.3	35.7	64.3	35.7	52.9	47.1
HEX	Max. local stress	845.6	119.6	313.8	268.9	289.3	301.5	152.7	118.0	147.2	123.8	143.0	110.1
	Hom. VA stress	845.4	118.7	284.0	198.8	267.2	201.8	144.9	78.6	135.6	79.8	127.5	80.9
	% load in F or M	87.7	12.3	58.8	41.2	57.0	43.0	64.8	35.2	63.0	37.0	61.2	38.8
RND	Max. local stress	845.8	119.4	501.4	509.8	491.0	526.0	210.3	208.7	218.4	220.7	172.4	134.8
	Hom. VA stress	845.4	118.8	304.2	196.9	305.1	196.8	146.9	78.0	149.2	77.7	119.4	81.6
	% load in F or M	87.7	12.3	60.7	39.3	60.8	39.2	65.3	34.7	65.7	34.3	59.4	40.6
RNDG	Max. local stress	845.8	119.3	520.2	533.9	451.3	458.6	227.6	225.0	197.5	192.8	162.8	147.2
	Hom. VA stress	845.4	1188	297.9	197.1	302.5	196.3	142.3	78.2	144.3	77.9	113.0	82.0
	% load in F or M	87.7	12.3	60.2	39.8	60.6	39.4	64.5	35.5	64.9	35.1	58.0	42.0

3.3. Evaluation of Effective Elastic Stiffness Properties

Table 3 demonstrates the independent compliance coefficients of SiC/F-Glass composite for random and regular packing with fiber volume ratios of 0.3, 0.4, and 0.5, respectively. The SQR and HEX models determines 5 and 9 independent compliance coefficients for all fiber volume ratios, respectively. Thus, SQR unit cell predicts a transversely isotropic behavior for this composite, while HEX model anticipates an orthotropic material behavior for this composite. These conclusions are in agreement with the number of isotropic and symmetry planes in these regular models. For random unit cells, i.e. RND and RNDG packing, 13 compliance coefficients were evaluated. Therefore, from the point of views of these models the composite is a monoclinic isotropic material. For this composite with a unique fiber vol-

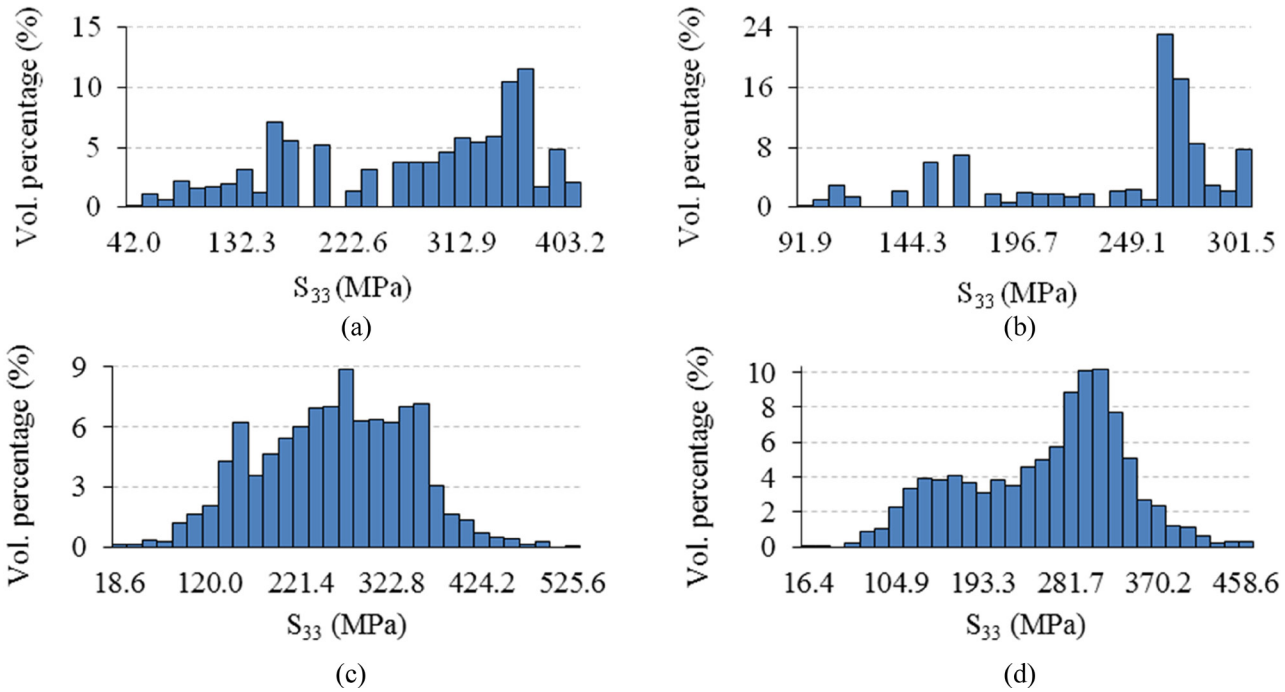

Figure 6. *Distribution of normal stress S_{33} (MPa) versus volume percentage of RUCs for SiC/FGlass composite with fiber volume ratio of 0.5 under load case 3 (0.2% stretch in the direction of 3). (a) SQR, (b) HEX, (c) RND, (d) RNDG model.*

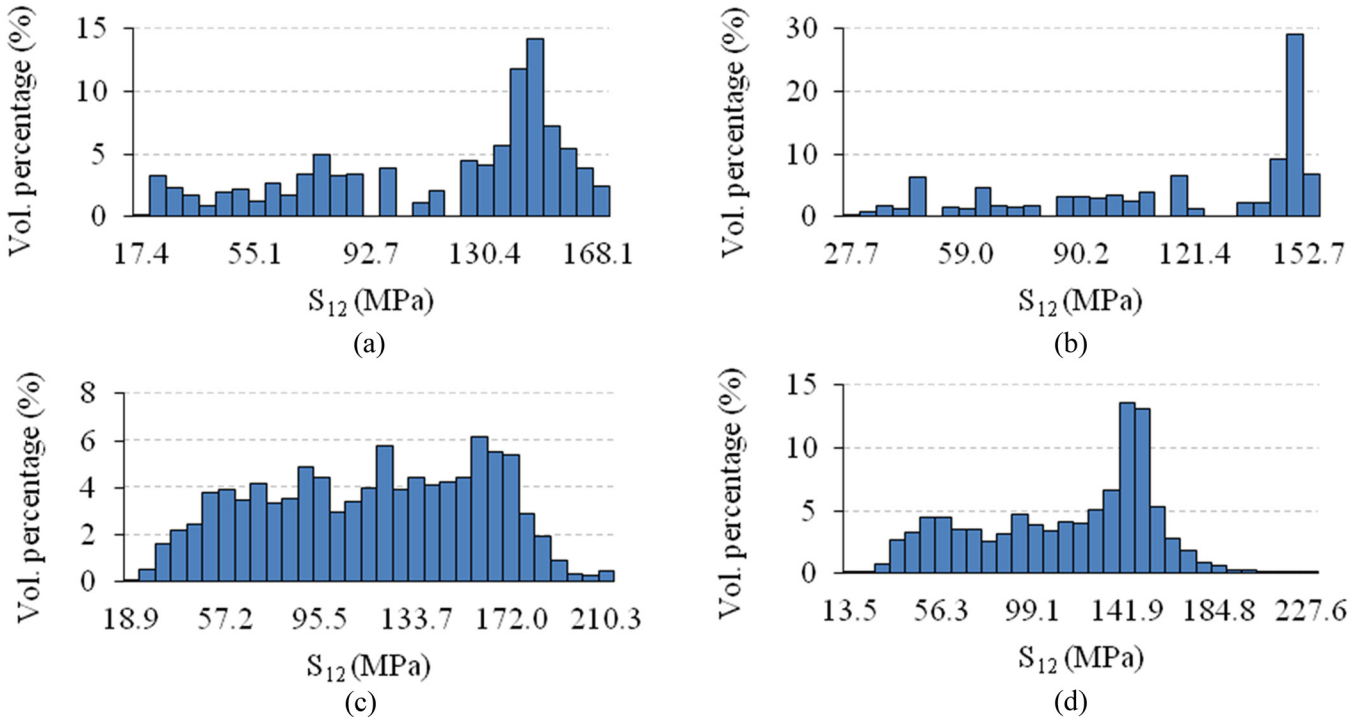

Figure 7. *Distribution of shear stress S_{12} (MPa) versus volume percentage of RUCs for SiC/FGlass composite with fiber volume ratio of 0.5 under 0.2% shear strain of plane 3 in the direction of 1. (a) SQR, (b) HEX, (c) RND, (d) RNDG model.*

ume ratio, the predicted compliance coefficients from various volume elements are slightly different. At different fiber volume ratios, the values of S_{1123}, S_{2223}, S_{3323}, and S_{1213} are very small compare to other compliance coefficients and one can approximate them as zero. Also the values of S_{1122} and S_{1133} as well as S_{1212}, and S_{1313} are very close to each other. Therefore, this composite may approximate as a transversely isotropic material.

The mechanical properties of SiC/F-Glass composite for SQR and HEX unit cells with fiber volume fractions of 0.3, 0.4, and 0.5, which are determined from the compliance coefficients, are tabulated in Table 4. At each fiber volume ratio both RUCs predict close values for E_{11}, G_{12}, G_{13}, v_{12}, and v_{13}, but they determine different values for E^{22}, E_{33}, G_{23}, and v_{23}. Due to identical stretches in fibers and matrix and perfect bonding between them, the configuration of fibers does no effect on the results related to load cases applied in the direction of fibers. At a specific fiber volume ratio the SQR model predicts higher values of Young's moduli compared to HEX model, and at higher values of fiber volume fraction the differences between the Young's moduli resulted from SQR and HEX unit cells increase.

Table 3. The Compliance Coefficients (×10^{-2}, 1/GPa) of SiC/F-Glass Composite for Various RUC Models with Fiber Volume Ratios of 0.3, 0.4 and 0.5.

V_f	RUC	S_{1111}	S_{1122}	S_{1133}	S_{1123}	S_{2222}	S_{2233}	S_{2223}	S_{3333}	S_{3323}	S_{1212}	S_{1213}	S_{1313}	S_{2323}
0.3	SQR	0.596	–0.108	–0.108	0.000	1.086	–0.223	0.000	1.086	0.000	2.555	0.000	2.555	2.888
	HEX	0.597	–0.108	–0.109	0.000	1.132	–0.271	0.000	1.140	0.000	2.544	0.000	2.573	2.714
	RND	0.604	–0.109	–0.110	–0.001	1.109	–0.250	0.007	1.125	–0.001	2.538	0.010	2.581	2.784
	RNDG	0.608	–0.111	–0.110	0.001	0.128	–0.254	0.001	1.124	–0.015	2.582	–0.022	2.572	2.797
0.4	SQR	0.490	–0.086	–0.086	0.000	0.915	–0.174	0.000	0.915	0.000	2.162	0.000	2.162	2.548
	HEX	0.491	–0.086	–0.087	0.000	0.978	–0.241	0.000	0.993	0.000	2.148	0.000	2.196	2.301
	RND	0.498	–0.087	–0.088	0.001	0.952	–0.211	–0.005	0.961	0.001	2.158	–0.004	2.173	2.398
	RNDG	0.497	–0.088	–0.087	0.001	0.964	–0.213	0.011	0.960	–0.016	2.188	–0.007	2.179	2.423
0.5	SQR	0.416	–0.071	–0.071	0.000	0.760	–0.130	0.000	0.760	0.000	1.805	0.000	1.805	2.208
	HEX	0.417	–0.071	–0.072	0.000	0.830	–0.206	0.000	0.854	0.000	1.793	0.000	1.860	1.922
	RND	0.418	–0.072	–0.071	0.001	0.801	–0.176	–0.003	0.800	–0.006	1.784	–0.014	1.769	1.994
	RNDG	0.441	–0.071	–0.071	–0.072	0.811	–0.173	0.013	0.805	–0.019	1.824	–0.008	1.810	2.058

Table 4. The Mechanical Properties of SiC/F-Glass Composite for SQR and HEX Models with Fiber Volume Ratios of 0.3, 0.4, and 0.5.

V_f	RUC Model	E_{11}	E_{22}	E_{33}	G_{12}	G_{13}	G_{23}	ν_{12}	ν_{13}	ν_{23}
		(GPa)								
0.3	SQR	167.79	92.08	92.08	39.14	39.14	34.63	0.181	0.181	0.205
	HEX	167.50	88.34	87.72	39.31	38.87	36.85	0.181	0.183	0.239
0.4	SQR	204.08	109.29	109.29	46.25	46.25	39.247	0.176	0.176	0.190
	HEX	203.67	102.25	100.70	46.55	45.54	43.46	0.175	0.177	0.246
0.5	SQR	240.38	131.58	131.58	55.40	55.40	45.290	0.170	0.170	0.171
	HEX	239.81	120.48	117.10	55.78	53.76	52.03	0.170	0.173	0.248

3.4. Viscoelastic Analysis-Local Stress Distributions within RUCs

The stress relaxation simulations were carried out on various RUCs to study the time-dependent viscoelastic behavior of AS4/Epoxy composite. Constant strain (displacement) loads were applied on the unit cells for a period of 200 seconds and stress/strain variations were recorded during the loading process. Under each load case and at each step time the averaged-volume stresses and strains were computed over each RUC which were subsequently used to calculate the time-dependent compliance coefficients of the composite.

The distributions of stresses S_{11} and S_{12} within the deformed microstructural shape of the various AS4/Epoxy RUCs with fiber volume ratios of 0.5 under load cases 1 and 4 are plotted in Figures 8 and 9 at times of 1and 200 sec. As the figures show, under load case 1, where the load is along the direction of the fibers, in all RUCs, the stress of S_{11} in the fibers remains uniform but it decays with time in viscoelastic matrix. It is due to elastic behavior of the fibers and viscoelastic nature of the matrix. Under this load case the stress relaxation in matrix does not impact the stress in the fibers. Under the other load cases, the stress distributions change by time in both the fibers and matrix. As shown for load case 4 the stress relaxation in matrix causes stress decay in the fibers.

Similar to the elastic composite, in the viscoelastic composite, under longitudinal stretch (load case 1) the stress distribution in different RUC models are almost identical and the distribution and geometry of circular fibers do not affect the distribution of stress S_{11}. However, under the other five load cases, the changes in distribution and geometry of the fibers result in non-uniform stress distributions in fiber and matrix of the RUCs.

3.5. Evaluation of Effective Viscoelastic Stiffness Properties

The independent compliance coefficients of AS4/Epoxy composite for various RUCs with fiber volume ratios of 0.3, 0.4, and 0.5 at times of 10 and 200 sec are tabulated in Table 5. Based on these data, all models of SQR and HEX RUCs predict 5 and 9 independent compliance coefficients for the viscoelastic compound material, respectively, but there are 13 independent compliance coefficients predicted by RND and RNDG unit cells. Thus, SQR and HEX models predict transversely isotropic and orthotropic behavior for this composite, respectively, while random unit cells anticipate monoclinic isotropic type material for this composite. At a unique fiber volume ratio, the predicted compliance coefficients from various unit cells are slightly different as expected.

The engineering constants in terms of Young's modulus, shear modulus, and Poisson's ratio determined from the predicted compliance coefficients for this composite with fiber volume fractions 0.3, 0.4, and 0.5 at times of 10 and 200 sec are presented in Table 6. Both Young's and shear moduli decrease with time at any specific fiber volume ratio but the Poisson's ratios increase. The increase in fiber volume ratios causes the stiffness to increase due to higher stiffness of the fibers.

The variation of compliance coefficients of this composite for different volume ratios were plotted versus time in Figures 10(a)–10(f). At any specific fiber volume ratio, all unit cells predict slightly different values for compliance coefficients. By increasing fiber volume ratio, the values of S_{1111}, S_{2222}, and S_{1212}, and S_{2323} decrease, while compliance coefficients of S_{1122} and S_{2233} increase. Among all unit cells SQR model predicts the lowest values for compliances of S_{1111}, S_{2222}, and S_{3333}, and highest values for compliances of S_{1122}, S_{1133}, S_{2233}, and S_{2323}. RNDG unit cell predicts the minimum compliance coefficient values for S_{1122} and S_{1133} and highest values for S_{1111}, S_{1212}, and S_{1313}.

4. CONCLUSIONS

A micromechanics elastic/viscoelastic analysis of UD composites with symmetric and random distributed fibers within matrix was presented. By an inverse analysis, the compliance of the composite material for SQR, HEX, RND and RNDG models considered were evaluated. At identical fiber volume ratios, while the microstructural stress/strain distributions are very much impacted by fiber distribution

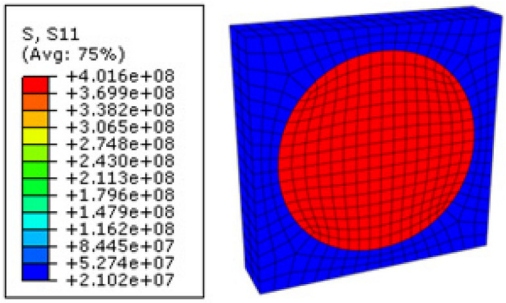

(a) SQR (time = 1 s)

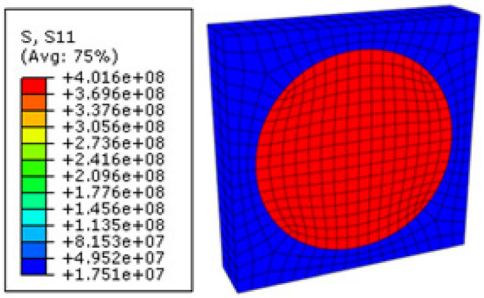

(b) SQR (time = 200 s)

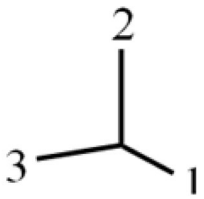

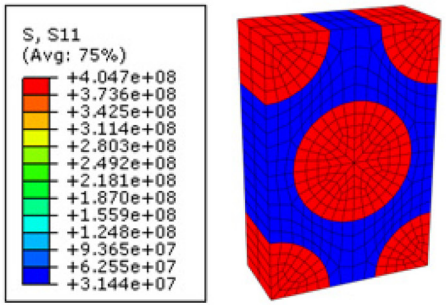

(c) HEX (time = 1 s)

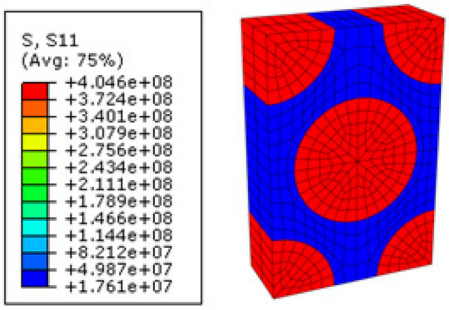

(d) HEX (time = 200 s)

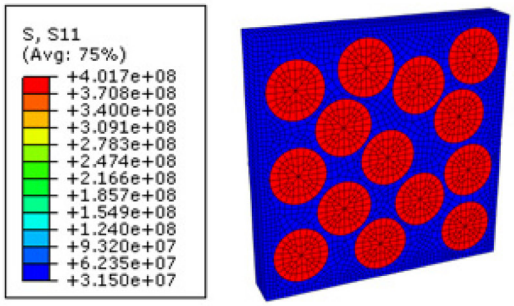

(e) RND (time = 1 s)

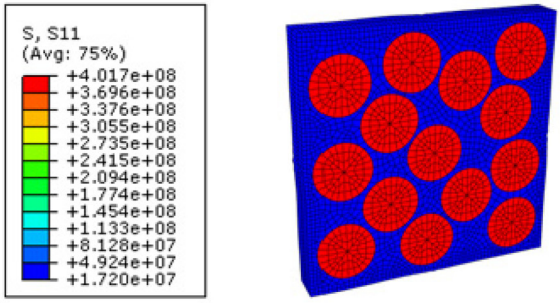

(f) RND (time = 200 s)

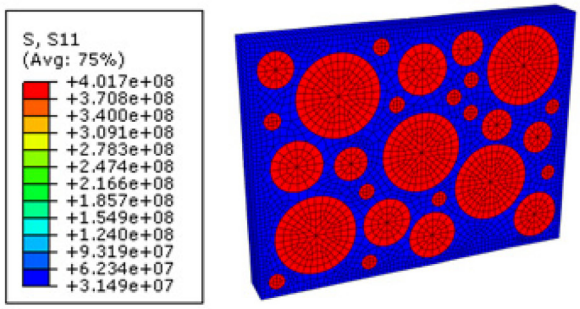

(g) RNDG (time = 1 s)

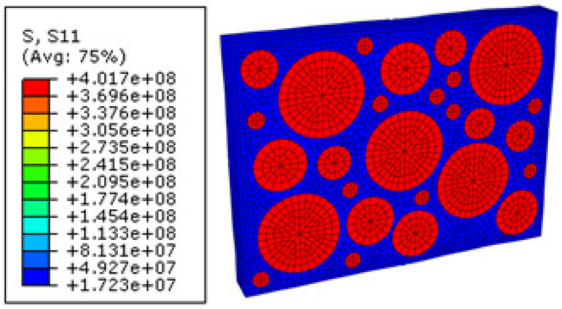

(h) RNDG (time = 200 s)

Figure 8. *Time-dependent stress S_{11} (Pa) within the deformed shape of various RUCs of AS4/Epoxy composite with fiber volume ratio of 0.5 under 0.2% strain in the direction of 1 at times of 1 and 200 sec.*

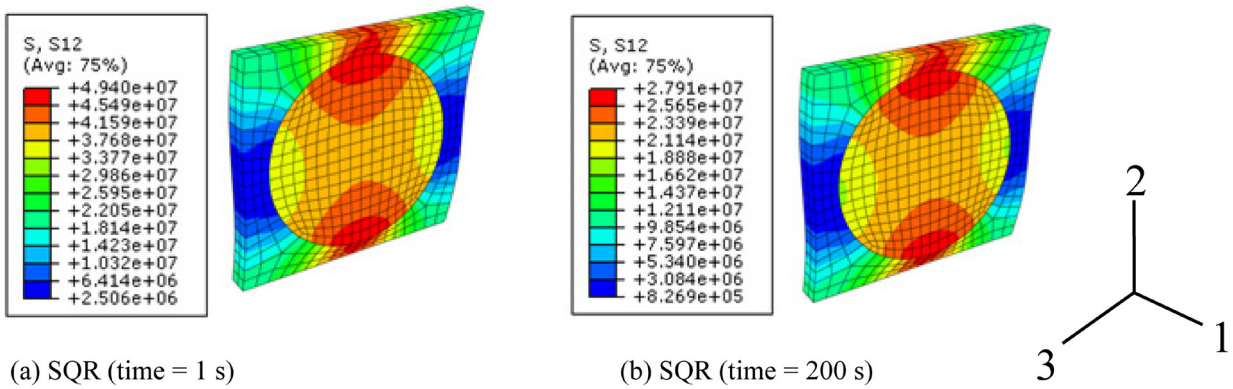

(a) SQR (time = 1 s) (b) SQR (time = 200 s)

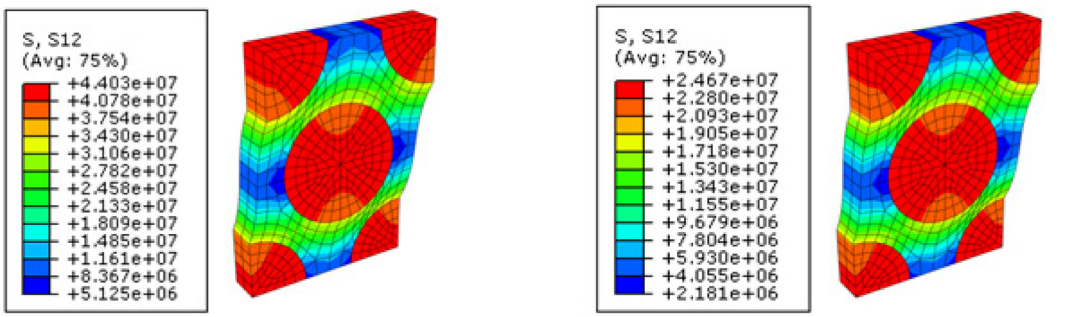

(c) HEX (time = 1 s) (d) HEX (time = 200 s)

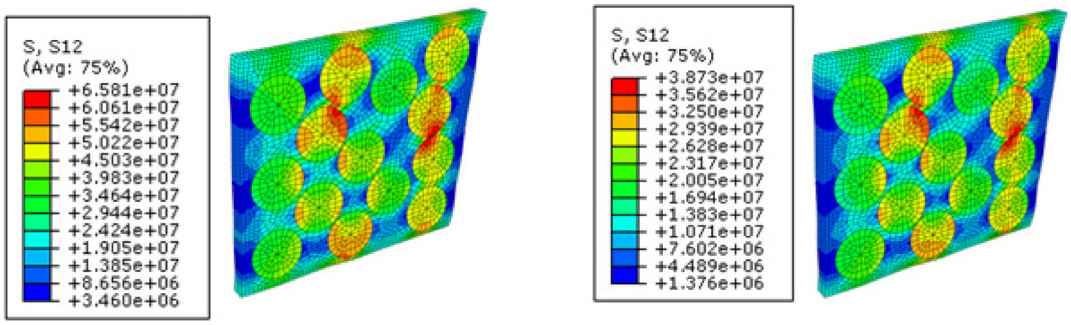

(e) RND (time = 1 s) (f) RND (time = 200 s)

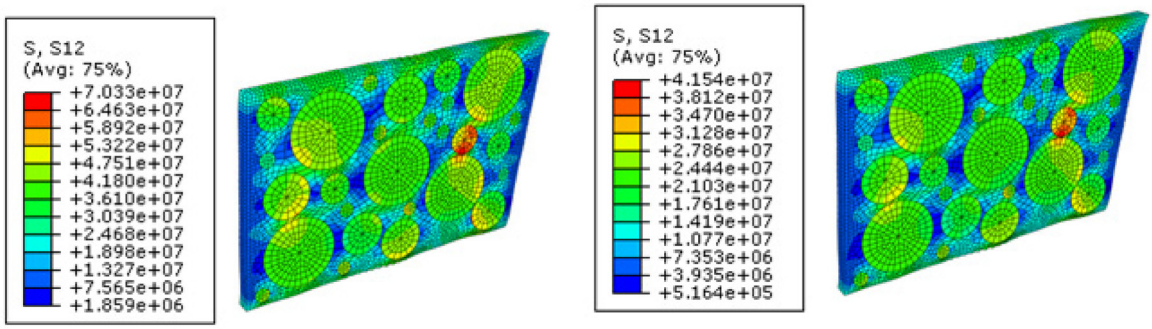

(g) RNDG (time = 1 s) (h) RNDG (time = 200 s)

Figure 9. *Time-dependent shear stress S_{12} (Pa) within the deformed shape of RUCs of AS4/Epoxy composite with fiber volume ratio of 0.5 under 0.2% strain of plane 3 in the direction of 1 at times of 1 and 200 sec.*

Table 5. The Compliance Coefficients (×10^{-2}) ,1/GPa) of AS4/Epoxy Composite by Different RUCs with Fiber Volume Ratios of 0.3, 0.4, and 0.5 at Times 10 and 200 sec.

t (s)	V_f	RUC Model	S_{1111}	S_{1122}	S_{1133}	S_{1123}	S_{2222}	S_{2233}	S_{2223}	S_{3333}	S_{3323}	S_{1212}	S_{1213}	S_{1313}	S_{2323}
10	0.3	SQR	1.494	–0.507	–0.507	0.000	8.384	–4.108	0.000	8.384	0.000	16.127	0.000	16.127	25.951
		HEX	1.497	–0.507	–0.508	0.000	8.441	–4.162	0.000	8.435	0.000	16.023	0.000	16.302	25.833
		RND	1.523	–0.517	–0.518	–0.001	8.433	–4.159	0.001	8.425	–0.004	15.869	0.103	16.293	25.930
		RNDG	1.533	–0.522	–0.521	0.001	8.435	–4.167	0.009	8.437	–0.003	16.203	–0.223	16.168	25.948
	0.4	SQR	1.162	–0.375	–0.375	0.000	8.161	–3.777	0.000	8.161	0.000	13.042	0.000	13.042	25.136
		HEX	1.166	–0.377	–0.377	0.000	8.244	–3.856	0.000	8.233	0.000	12.290	0.000	13.364	24.199
		RND	1.186	–0.384	–0.385	0.001	8.224	–3.851	–0.002	8.220	0.004	12.866	–0.036	13.025	25.102
		RNDG	1.185	–0.385	–0.384	0.001	8.219	–3.848	0.012	8.221	–0.010	13.221	–0.074	13.124	25.103
	0.5	SQR	0.950	–0.292	–0.292	0.000	7.975	–3.441	0.000	7.975	0.000	10.270	0.000	10.270	24.333
		HEX	0.954	–0.293	–0.294	0.000	8.073	–3.533	0.000	8.056	0.000	10.172	0.000	10.789	23.213
		RND	0.959	–0.295	–0.294	0.001	8.036	–3.513	0.004	8.039	0.002	9.925	–0.127	9.778	24.235
		RNDG	0.965	–0.298	–0.297	0.001	0.035	–3.517	0.013	8.039	–0.010	10.348	–0.081	10.220	24.281
20	0.3	SQR	1.513	–0.528	–0.528	0.000	9.068	–4.738	0.000	9.068	0.000	18.478	0.000	18.478	28.898
		HEX	1.517	–0.528	–0.529	0.000	9.183	–4.850	0.000	9.176	0.000	18.356	0.000	18.682	28.605
		RND	1.542	–0.539	–0.540	–0.001	9.159	–4.828	0.003	9.148	–0.007	18.169	0.121	18.666	28.794
		RNDG	1.553	–0.544	–0.543	0.001	9.165	–4.841	0.018	9.167	–0.009	18.676	–0.262	18.554	28.821
	0.4	SQR	1.172	–0.388	–0.388	0.000	8.704	–4.278	0.000	8.704	0.000	14.905	0.000	14.905	27.670
		HEX	1.175	–0.389	–0.390	0.000	8.870	–4.438	0.000	8.857	0.000	14.763	0.000	15.281	26.615
		RND	1.196	–0.398	–0.399	0.001	8.824	–4.407	–0.004	8.819	0.007	14.690	–0.041	14.877	27.515
		RNDG	1.195	–0.398	–0.397	0.001	8.817	–4.402	0.026	8.820	–0.023	15.110	–0.087	14.996	27.523
	0.5	SQR	0.956	–0.300	–0.300	0.000	8.393	–3.825	0.000	8.393	0.000	11.697	0.000	11.697	26.456
		HEX	0.960	–0.300	–0.302	0.000	8.586	–4.010	0.000	8.564	0.000	11.583	0.000	12.304	25.192
		RND	0.964	–0.304	–0.303	0.001	8.517	–3.959	0.006	8.520	0.001	11.284	–0.147	11.112	26.180
		RNDG	0.971	–0.306	–0.305	0.001	8.513	–3.960	0.027	8.518	–0.024	11.781	–0.095	11.633	26.267

Table 6. The Mechanical Properties of the AS4/Epoxy Composite for SQR and HEX Unit Cells with Fiber Volume Ratios of 0.3, 0.4, and 0.5 at Times 10 and 200 sec.

			E_{11}	E_{22}	E_{33}	G_{12}	G_{13}	G_{23}			
t (s)	V_f	RUC	(GPa)						v_{12}	v_{13}	v_{23}
10	0.3	SQR	66.934	11.928	11.928	6.201	6.201	3.853	0.339	0.339	0.490
		HEX	66.800	11.847	11.855	6.241	6.134	3.871	0.338	0.339	0.493
	0.4	SQR	86.059	12.253	12.253	7.668	7.668	3.978	0.323	0.323	0.463
		HEX	85.763	12.130	12.146	7.740	7.483	4.132	0.323	0.322	0.468
	0.5	SQR	105.263	12.539	12.539	9.737	9.737	4.110	0.307	0.307	0.432
		HEX	104.822	12.387	12.413	9.831	9.269	4.380	0.307	0.308	0.438
20	0.3	SQR	66.094	11.028	11.028	5.412	5.412	3.460	0.349	0.349	0.523
		HEX	65.920	10.890	10.898	5.448	5.353	3.496	0.348	0.349	0.528
	0.4	SQR	85.324	11.489	11.489	6.109	6.709	3.614	0.331	0.331	0.492
		HEX	85.106	11.274	11.291	6.774	6.544	3.757	0.331	0.332	0.500
	0.5	SQR	104.603	11.915	11.915	8.549	8.549	3.780	0.314	0.314	0.456
		HEX	104.167	11.647	11.677	8.633	8.127	3.970	0.313	0.315	0.467

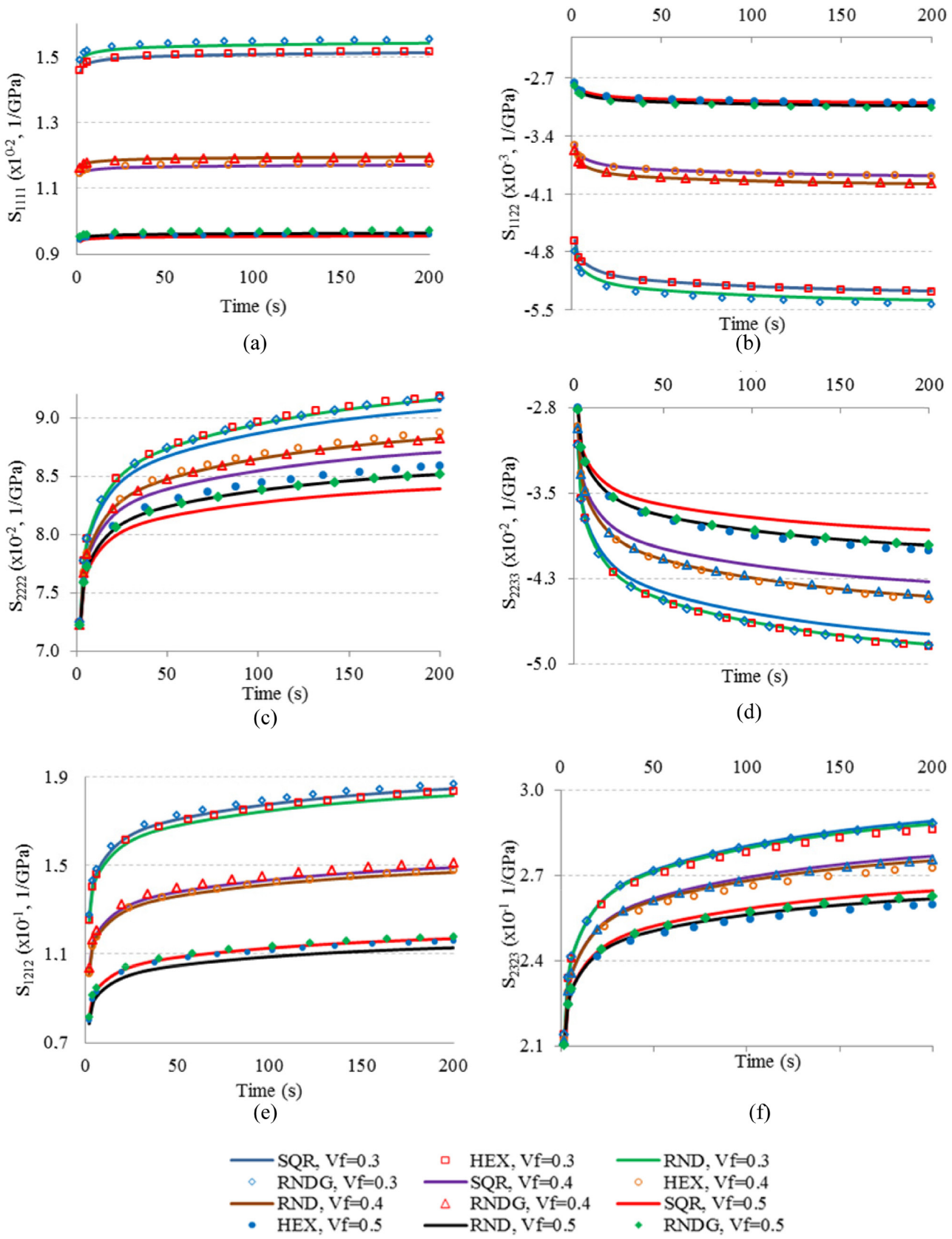

Figure 10. *Variations of compliance coefficients versus time by various RUCs of AS4/Epoxy composite with fiber volume ratios of 0.3, 0.4, and 0.5. (a) S_{1111}, (b) S_{1122}, (c) S_{2222}, (d) S_{2233}, (e) S_{1212}, (f) S_{2323}.*

model type, the evaluated homogenized stiffness of the composite will not be considerably influenced. Although the predicted homogenized stiffness values from various models are in fact very close to each other, but the localized maximum or minimum stresses are not. The microstructural stress distributions call the microstructural strength of the fiber and matrix, as well as, their interface mechanical properties, and from this point of view the type of fiber distributions have a formidable impact as was shown quantitatively in this paper.

ACKNOWLEDGEMENTS

The authors would like to acknowledge the Army Research Office (ARO) for the financial support of this research.

REFERENCES

[1] Kwon YW, Berner JM, Micromechanics model for damage and failure analyses of laminated fibrous composites, *Engineering Fracture Mechanics,* 52(2):231–242, 1995. http://dx.doi.org/10.1016/0013-7944(95)00017-P.

[2] Kok de JMM, Meijer HEH, Deformation, yield and fracture of unidirectional composites in transverse loading—I: influence of fiber volume fraction and test-temperature, *Composites Part A-Applied Science and Manufacturing,* 30(7):905–916, 1999. http://dx.doi.org/10.1016/S1359-835X(98)00170-5.

[3] Bednarcyk BA, Arnold SM. Micromechanics-based deformation and failure prediction for longitudinally reinforced titanium composites, *Composites Science and Technology,* 61(5):705–729, 2001. http://dx.doi.org/10.1016/S0266-3538(01)00004-5.

[4] Mayes JS, Hansen AC, Multicontinuum failure analysis of composite structural laminates, *Mechanics of Composite Materials and Structures,* 8(4):249–62, 2001. http://dx.doi.org/10.1080/107594101753172502.

[5] Xia Z, Chen Y, Ellyin F, A meso/micro-mechanical model for damage progression in glass-fiber/epoxy cross-ply laminates by finite-element analysis, *Composites Science and Technology,* 60(8):1171–1921, 2000. http://dx.doi.org/10.1016/S0266-3538(00)00022-1.

[6] Garnich M, Karami G, Localized fiber waviness and implications for failure in unidirectional composites, *Journal of Composite Materials,* 39(14):1225–1245, 2005. http://dx.doi.org/10.1177/0021998305048748.

[7] Zhang Y, Xia Z, Ellyin F, Evolution and influence of residual stresses/strains of fiber reinforced laminates, *Composites Science and Technology,* 64(10-11):1613–1621, 2004. http://dx.doi.org/10.1016/j.compscitech.2003.11.012.

[8] Ahci E, Talreja R, Characterization of viscoelastic and damage in high temperature polymer matrix composites, *Composites Science and Technology,* 66(14):2506–2519, 2006. http://dx.doi.org/10.1016/j.compscitech.2006.02.012.

[9] Karami G, Garnich M, Micromechanical study of thermoelastic behavior of composites with periodic fiber waviness, *Composites Part B-Engineering,* 36(3):241–248, 2005. http://dx.doi.org/10.1016/j.compositesb.2004.09.005.

[10] Karami G, Grundman N, Abolfathi N, Naik A, Thermoelastic characterization and evaluation of residual stresses in bi-directional fibrous composites, *Applied Composite Materials,* 15(4–6):259–272, 2008. http://dx.doi.org/10.1007/s10443-008-9071-5.

[11] Garnich M, Karami G, Finite element micromechanics for stiffness and strength of wavy fiber composites, *Journal of Composite Materials,* 38(4):273–292, 2004. http://dx.doi.org/10.1177/0021998304039270.

[12] Naik A, Abolfathi N, Karami G, Ziejewski M, Micromechanical viscoelastic characterization of fibrous composites, *Journal of Composite Materials,* 42(12):1–26, 2008. http://dx.doi.org/10.1177/0021998308091221.

[13] Abolfathi N, Naik A, Karami G, Ulven, C, A micromechanical characterization of angular bidirectional fibrous composites, *Computational Materials Science,* 43(4):1193–1206, 2008. http://dx.doi.org/10.1016/j.commatsci.2008.03.017.

[14] Drago A, Pindera M, Micro-macromechanical analysis of heterogeneous materials: macroscopically homogeneous vs. periodic microstructures, *Composites Science and Technology,* 67(6):1243–1263, 2007. http://dx.doi.org/10.1016/j.compscitech.2006.02.031.

[15] Zhang Y, Xia Z, Ellyin F, Nonlinear viscoelastic micromechanical analysis of fiber-reinforced polymer laminates with damage evolution, *International Journal of Solids and Structures,* 42(2):591–604, 2005. http://dx.doi.org/10.1016/j.ijsolstr.2004.06.021.

[16] Jin KK, Oh JH, Ha SK, Effect of fiber arrangement on residual thermal stress distributions in a unidirectional composite, *Journal of Composite Materials,* 41(5):591–611, 2007. http://dx.doi.org/10.1177/0021998306065290.

[17] Everett RK, Chu JH, Modeling of non-uniform composite microstructures, *Journal of Composite Materials,* 27(11):1128–1144, 1993. http://dx.doi.org/10.1177/002199839302701105.

[18] Oh JH, Jin KK, Ha SK, Interfacial strain distribution of a unidirectional composite with randomly distributed fibers under transverse loading, *Journal of Composite Materials,* 40(9):759–778, 2006. http://dx.doi.org/10.1177/0021998305055546.

[19] Wongsto A, Li S, Micromechanical FE analysis of UD fiber-reinforced composites with fibers distributed at random over the transverse cross-section, *Composites Part a-Applied Science and Manufacturing* 36(9):1246–1266, 2005.

[20] Huang Y, Jin KK, Ha SK, Effects of fiber arrangement on mechanical behavior of unidirectional composites, *Journal of Composite Materials,* 42(18):1851–1871, 2008. http://dx.doi.org/10.1177/0021998308093910

[21] Daniel IM, Ishai O. *Engineering Mechanics of Composite Materials,* second ed., Oxford University Press, New York, 2005.

[22] ABAQUS, Standard Finite Element Software, Dassault Systemes Simulia Corp. 2011.

Journal of Multifunctional Composites

journal homepage: http://jmc.destechpub.com

The Role of Substrate Elastic Modulus in the Strain-Dependent Behavior of Electromagnetic Metamaterials: Analytic Description, Multiphysics Modeling, and Test Results

BRANDON J. ARRITT[1,2,*], DAVID R. SMITH[3] and TARIQ A. KHRAISHI[2]

[1]*Air Force Research Laboratory/Space Vehicles Directorate, Albuquerque, NM, USA*
[2]*University of New Mexico, Mechanical Engineering Department, Albuquerque, NM, USA*
[3]*Center for Metamaterials and Integrated Plasmonics, Department of Electrical and Computer Engineering, Duke University, Durham, NC, USA*

KEYWORDS

Metamaterial
Mechanical strain
Elastic modulus
Shear-lag
Resonance

ABSTRACT

Metamaterial strain-dependent electromagnetic (EM) behavior is strongly influenced by its constituent materials. Metamaterials, like all composites, may exhibit complicated strain profiles when subjected to mechanical loading. At the unit cell level, the degree of non-uniformity in the strain profile is a function of loading, unit cell geometry, and the relative stiffness contributions of the composite's constituent materials (in this case, copper conductive traces and a polymer dielectric substrate). Analytic expressions and multi-physics modeling are utilized to describe the relationship between substrate modulus, strain, and EM behavior. Testing was conducted to corroborate and validate the multi-physics models. An interesting result of this research is that depending upon the Elastic Modulus of the substrate, a consistent strain profile applied at the unit cell level can result in either a positive or negative shift in the metamaterial's resonant frequency.

1. INTRODUCTION

Metamaterials derive their unique electromagnetic (EM) properties from sub-wavelength structure and geometry, as opposed to relying explicitly on chemical composition. The attributes of metamaterials enable the attainment of unnatural phenomena at frequencies where conventional materials do not provide such a response; some of the more notable examples being negative permittivity [1], negative permeability [2], and negative index of refraction [3,4]. Additionally, metamaterials enable precise, point-wise control of the EM constitutive properties throughout a structure's volume [4,5,6]. As a result, metamaterials have the potential to significantly expand the tradespace in which engineers work to control our interactions with EM radiation.

Because metamaterial EM response is so strongly tied to geometry and locally enhanced fields [2], a direct causal relationship between mechanical strain (by definition, a change in geometry) and EM properties is implied. A number of efforts have demonstrated this relationship, and many leveraged equivalent circuit models to provide insight into metamaterial strain-dependence [5,6,7,8,9,10,11].

Previous efforts by the authors [9,10] analytically described the strain-dependent resonant frequency, and permittivity and permeability of an electric-LC resonator (Figure 1), a design commonly used in metamaterials for a tailored electric response [12]. These previous studies imparted the simplifying assumption that the stiffness (Elastic/Young's modulus) of the substrate was on the order of the stiffness of the conductive traces (in this case, copper). This assumption is valid for a wide range of envisioned metamaterial implementations, particularly those where the metamaterial will be integrated directly into a load-bearing structure [13,14,15].

*Corresponding author. Tel.: 505-853-2611; Fax: 505-846-7877;
Email: afrl.rvsv@kirtland.af.mil, brandon.arritt@kirtland.af.mil

doi:10.12783/issn.2168-4286/1.1/Arritt

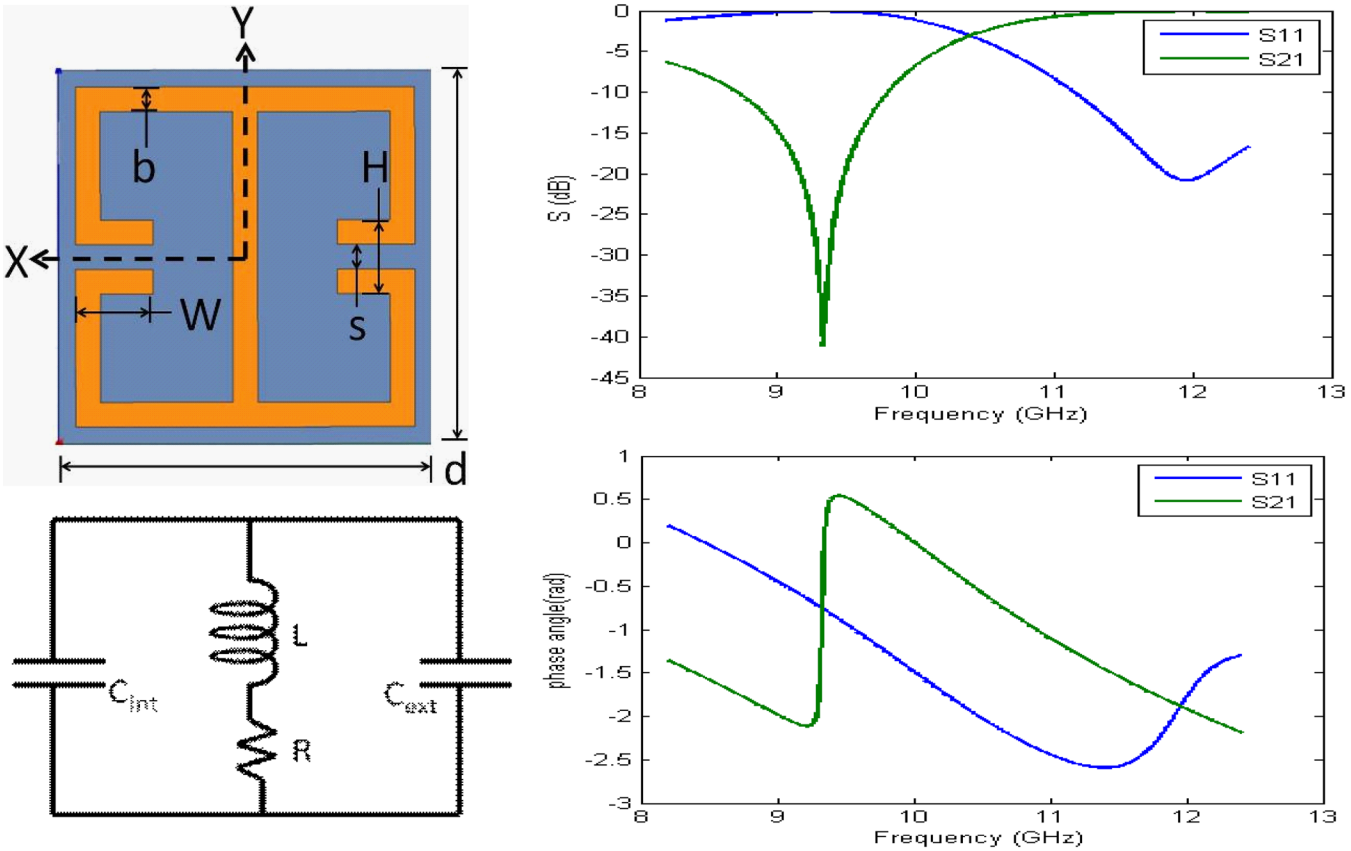

Figure 1. *ELC unit cell design, courtesy of SensorMetrix [16], showing the copper conductive traces on a dielectric substrate. C_{ext} is the cell-to-cell capacitance and C_1 is the capacitance between parallel copper traces within the unit cell. Upper Left: W = 1 mm, s = 0.254 mm, H = 0.762 mm, d = 3.85 mm. Bottom Left: equivalent circuit model, where $C_{int} = 2C_1$. Upper and Bottom Right: numerically retrieved scattering (S) parameters and phase diagram, respectively, showing a resonance at 9.33 GHz.*

This simplification imparts a near uniform in-plane strain-profile throughout the metamaterial unit cell ($E_{ij} \approx \in_{ij}$); i.e. the differential term for the in-plane mechanical strain is constant throughout the unit cell, and identical to the global value. This enables straightforward analytic description of the metamaterial's strain-dependent constitutive properties through relatively simple geometric expressions [10].

However, a number of metamaterial structures utilize lower modulus dielectrics as the substrate material. When a softer substrate is utilized, mechanical loading imparts a significantly more complicated strain profile within the unit cell, as demonstrated later, in Figure 9 and Figure 10. As a result, interpretation of the deformed geometry, and the resultant change in the geometric parameters of the equivalent circuit elements, becomes increasingly complicated.

This paper details efforts to understand the role that Elastic Modulus plays in the strain-dependent EM properties of metamaterial structures. The first section details use of shear-lag models to describe strain transfer into the conductive traces of a metamaterial, and how those strain values are integrated into equivalent circuit models, allowing approximate predictions of a metamaterial's strain-dependent EM performance. These analytic descriptions provide intuition and insight into the physical mechanisms of metamaterial strain-dependence. The next section details multi-physics numerical modeling performed to assess the validity and limitations of those analytic models. And the final section documents the development and utilization of a multi-physics test facility, and the empirical results used to verify and corroborate those models.

2. ANALYTIC MODELING

2.1. Shear-Lag Models

Shear lag models, developed and utilized for the composites-repair and structural health monitoring communities [17,18,19,20,21], describe the strain transfer into layered structural systems. These provide useful insight and intuition into the increasing level of non-homogeneity in the unit cell's strain profile as the substrate's modulus is decreased. Figure 2 depicts the geometric parameters used in the following shear-lag analysis.

The expressions from the 2-D analysis performed in [17] are normalized for a given boundary displacement (as opposed to a load at the boundary) to determine the level of

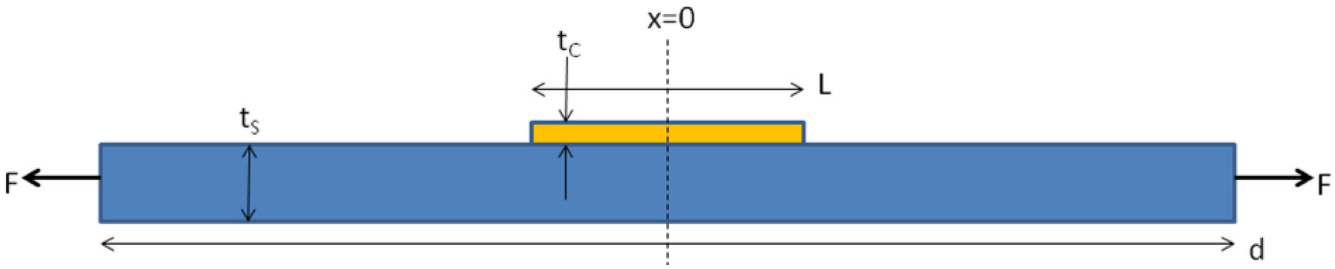

Figure 2. *Depiction of a conductive trace placed on a dielectric substrate. For the shear lag analysis, d >> L and L >> t_c, t_C = 0.034 mm and t_S = 1.5875 mm.*

stress in the conductive layer. Additionally, due to the construction of many metamaterial unit cells, it is reasonable to assume perfect bonding between the substrate and copper [22] (i.e. the substrate will fail before the bond), leading to the following expression for the stress in the copper.

$$\sigma_{XXC} = \frac{FS}{t_C(1+S)} = E_{XX}\left[\frac{St_SY_S}{t_C(1+S)}\right] \quad (1)$$

where $S = (Y_C t_C / Y_S t_S) = (1/(Y^* t^*))$, Y is the material's Young's Modulus, E_{XX} is $\Delta d/d$, t are the thicknesses (Figure 2), $t^* = t_S/t_C$, and $Y^* = Y_S/Y_C$; the subscript s refers to the substrate, and the subscript c refers to the copper. Assuming linear elastic behavior, the strain in the conductive layer is then found via Hook's Law,

$$\in_{XXC} = \frac{\sigma_{XXC}}{Y_C} = \frac{E_{XX}}{Y_C}\left[\frac{St_SY_S}{t_C(1+S)}\right] = E_{XX}\left[\frac{Y^*t^*}{Y^*t^*+1}\right] \quad (2)$$

Figure 3 shows the strain level in the copper ($\Delta L/L = \in_{ii}$), as a function of modulus ratio (Y^*) and strain at the boundaries .

As Figure (3) demonstrates, due to the thicknesses of the substrate and conductive layers, $\Delta L/L$ experiences a relatively minor change, even when there is a significant disparity in the moduli (10:1) of the materials. As a result, there is little difference in the strain-dependent EM-performance of the Y^* = 10% and Y^* = 100% metamaterial structures. However, as the modulus ratio is further reduced, the extension of the copper decreases appreciably; implying a significantly different geometry and resultant strain-dependent EM response. These implications are validated later in this paper, via multi-physics FEM analyses.

While the preceding shear-lag analysis was conducted on an idealized geometry (i.e. 2-D and $d >> L$, which are not representative of the geometry of a metamaterial unit cell), and does not account for shear-lag effects near the edges of the copper layer, the insight shall prove beneficial for understanding the interplay between substrate elastic modulus and the metamaterial's strain-dependent EM response.

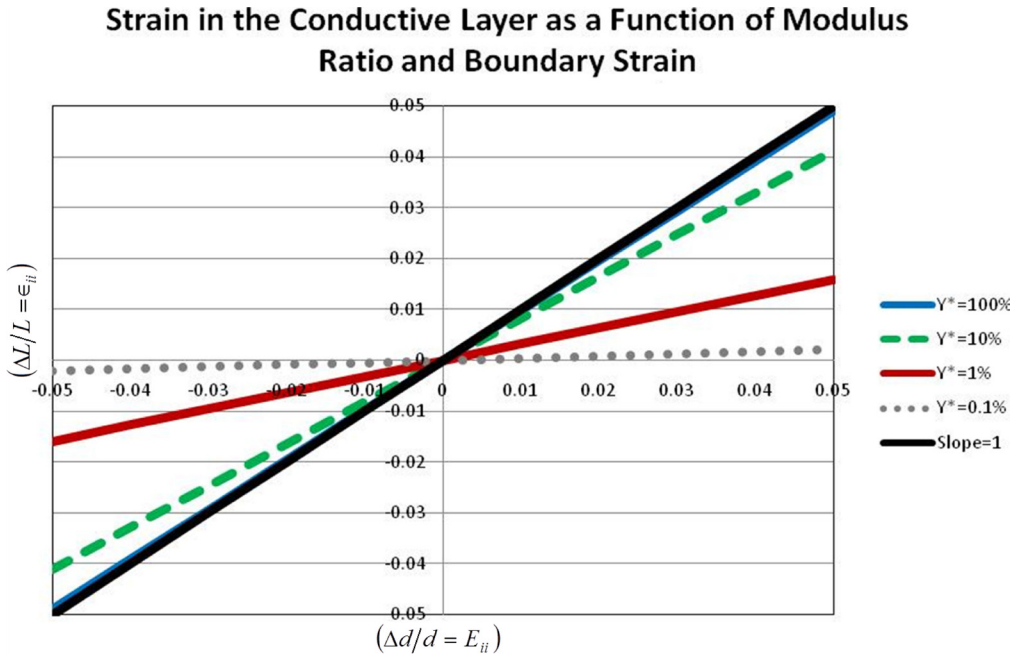

Figure 3. *Strain in the copper layer ($\Delta L/L = \in_{ii}$), as a function of modulus ratio (Y*) and edge displacement ($\Delta d/d = E_{ii}$). A slope of 1 ($\Delta L/L = \Delta d/d$) is provided for reference. As shown in the graph, softer substrates are able to convey lesser amounts of strain into the overlaying copper layer.*

2.2. Description via Equivalent Circuit Elements

As demonstrated in [7,8,9,10,11], the use of equivalent circuit elements can be extremely powerful tools for gaining insight into the strain-dependent behavior of metamaterial structures. In [9], the strain-dependent resonant frequency for an ELC was predicted through the use of analytic expressions. The angular resonant frequency ($\omega_0 = 2\pi f_0$) for the deformed unit cell is given by

$$\omega_0' = \sqrt{\frac{1}{L'C'}} = \omega_0 \sqrt{\frac{LC}{L'C'}} = \omega_0 \frac{1}{\sqrt{L^* C^*}} \tag{3}$$

Where the primes denote the deformed geometry and the unprimed values are the baseline/unstrained parameters, and $L^* = L'/L$ and $C^* = C'/C$. The self-inductance (L) of a thin, conducting strip can be approximated as [23]

$$L = \frac{\mu_0 l}{2\pi}\left[\ln\left(\frac{2l}{b}\right) + \frac{1}{2} + \frac{b}{3l} - \frac{b^2}{24l^2}\right] \tag{4}$$

where l is length and b (Figure 1) is the width of the conducting strip. Loop inductance can be neglected, due to the symmetry of this unit cell [9,10,24]. The capacitance (C) for a co-planar capacitor can be approximated as [25]

$$\begin{aligned} C &= C_a + C_s \\ C_a &= \varepsilon_0 \frac{2}{\pi} \ln\left(2\alpha \frac{2b+s}{s}\right) W \\ C_s &= \varepsilon_0 \frac{\varepsilon_s - 1}{\frac{s}{t_s} + \frac{4}{\pi}\ln\alpha} W \end{aligned} \tag{5}$$

where the geometric parameters are detailed in Figure 1 and Figure 2, the subscript a and s refer to air and substrate, respectively, and $\alpha = 5/2$.

As mentioned previously, [9,10] analyzed a metamaterial that was constructed on a thick, high modulus substrate. These simplifying assumptions enabled direct integration of the strained geometry into the above analytic expressions, and ensured the capacitors remained approximately parallel in the strained condition. However, as the substrate modulus is decreased, the strain-profile for a mechanically-loaded unit cell becomes increasing complex (as depicted in Figure 9 and Figure 10) and defies such straightforward description via analytic expressions.

However, utilizing the values for the strain in the copper that were determined in Section 2.1, as well as the geometry of the unit cell (Figure 2), it is possible to generate first-order approximations of the changes in dimensions for both the copper layer, and the substrate regions between conductive traces. The strain level in the conductive traces is found via Equation (2)

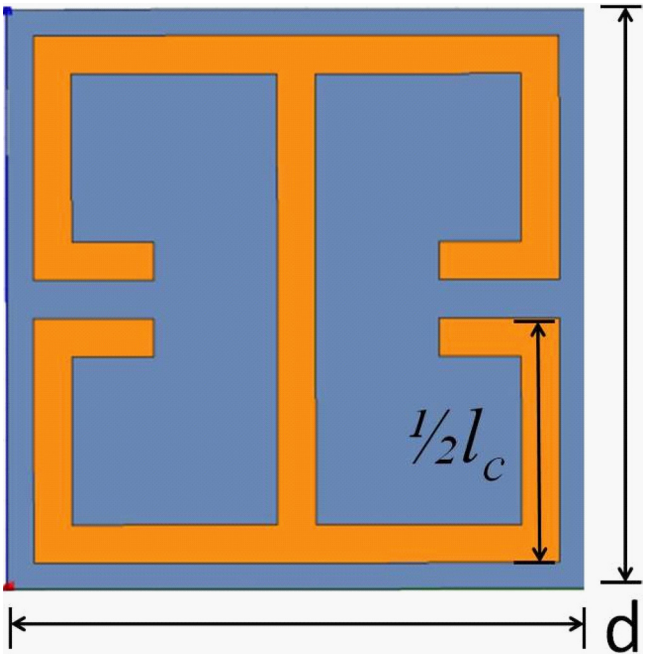

Figure 4. *Length of copper used to calculate C_1 when subjected to E_{YY}. l_c is dependent upon the geometry of the unit cell, as well as the direction of the loading.*

$$\in_{iiC} = \beta E_{ii} = \left[\frac{Y^* t^*}{Y^* t^* + 1}\right] E_{ii} \tag{6}$$

where β is the ratio of the strain in the copper to the strain in the unit cell. To determine the strain level in the substrate layer, between conductive traces, we can leverage a natural consequence of strain compatibility in solid mechanics; because the analysis is limited to linear-elastic behavior, strain is a continuous function and does not allow regions of material gapping or overlap [26]. The following equation details that the total extension of the unit cell is equal to the sum of the extensions in the unit cell's components (conductive traces plus regions of substrate between conductive traces)

$$\begin{aligned} d(1+E_{ii}) &= l_c(1+\beta E_{ii}) + l_s(1+\chi E_{ii}) \\ &= l_c(1+\beta E_{ii}) + (d-l_c)(1+\chi E_{ii}) \end{aligned} \tag{7}$$

where l_c is the length of the conductive trace along the path of interest (Figure 4), l_s is the total length of substrate along the same path ($l_s = d - l_c$), and χ is the ratio of the strain in the substrate (between conductive traces) to the strain at the unit cell level.

Solving Equation (7) for χ leads to

$$\chi = \frac{1}{E_{ii}}\left(\frac{d(1+E_{ii}) - l_c(1+\beta E_{ii})}{d-l_c} - 1\right) = \frac{d - l_c\beta}{d-l_c} \tag{8}$$

The strain level in the substrate it then determined via the following equation,

$$\in_{iiS} = \chi E_{ii} = \frac{d - l_c\beta}{d - l_c} E_{ii}$$
$$= \frac{d - l_c\left(\frac{Y^* t^*}{Y^* t^* + 1}\right)}{d - l_c} E_{ii} = \frac{1 - \frac{l_c}{d}\left(\frac{Y^* t^*}{Y^* t^* + 1}\right)}{1 - \frac{l_c}{d}} E_{ii} \quad (9)$$

Table 1 shows β and χ for a variety of Y^* values, for a unit cell subjected to an edge displacement in the Y-direction (displacement in the X-direction is held constant) and the dimensions shown in Figure (1) and Figure (2). As the table shows, a reduction in Y^* implies a reduction in the strain level in the conductive traces (β details the reduction in strain transfer into the copper, as the substrate modulus is decreased) and a corresponding increase in the strain values in the substrate region between conductive traces (χ details how low degrees of strain transfer into the copper layer imply large amounts of strain in the interlaying substrate regions).

These values for $\in_{iiC}$ and $\in_{iiS}$ can then be incorporated into Equations (4) and (5) to determine the deformed geometry which are used describe the metamaterial's strain-dependent inductance and capacitance. The values for L and C are then used to determine the resonant frequency as a function of modulus ratio and strain/boundary displacement,

Table 1. Strain Multipliers for the Conducting and Substrate Regions of the Metamaterial Sample. Analysis Utilized Dimensions Detailed in Figure 1 and Figure 2; t* = 46.7 and l_c = 3.264 mm.

Y^*	β	χ
∞	1	1
100%	0.98	1.11
10%	0.82	1.95
1%	0.32	4.67
0.1%	0.04	6.13
0	0	6.39

via Equation (3). It is important to note that this analysis is approximate because the analysis of Section 2.1 does not properly account for (a) the finite dimensions of the unit cell, (b) the unit cell's resistance to rotations in the conductive traces, and (c) Equation (5) assume parallel capacitor pads when the unit cell is deformed under load; an assumption that is violated for certain loading scenarios, as the modulus ratio decreases (Figure 9 and Figure 10). As a result, this analysis tends to underpredict the extension in the copper, and overpredict the extension in the unreinforced substrate layers.

Figure 5 and Figure 6 show the analytically-derived shifts in resonant frequency as a function of modulus ratio and E_{XX} and E_{YY}, respectively. As Figure 5 demonstrates, the metamaterial's sensitivity to E_{XX} decreases monotonically with reduced modulus ratios. However, Figure 6 (E_{YY}) shows significantly different behavior. As the modulus ratio is reduced

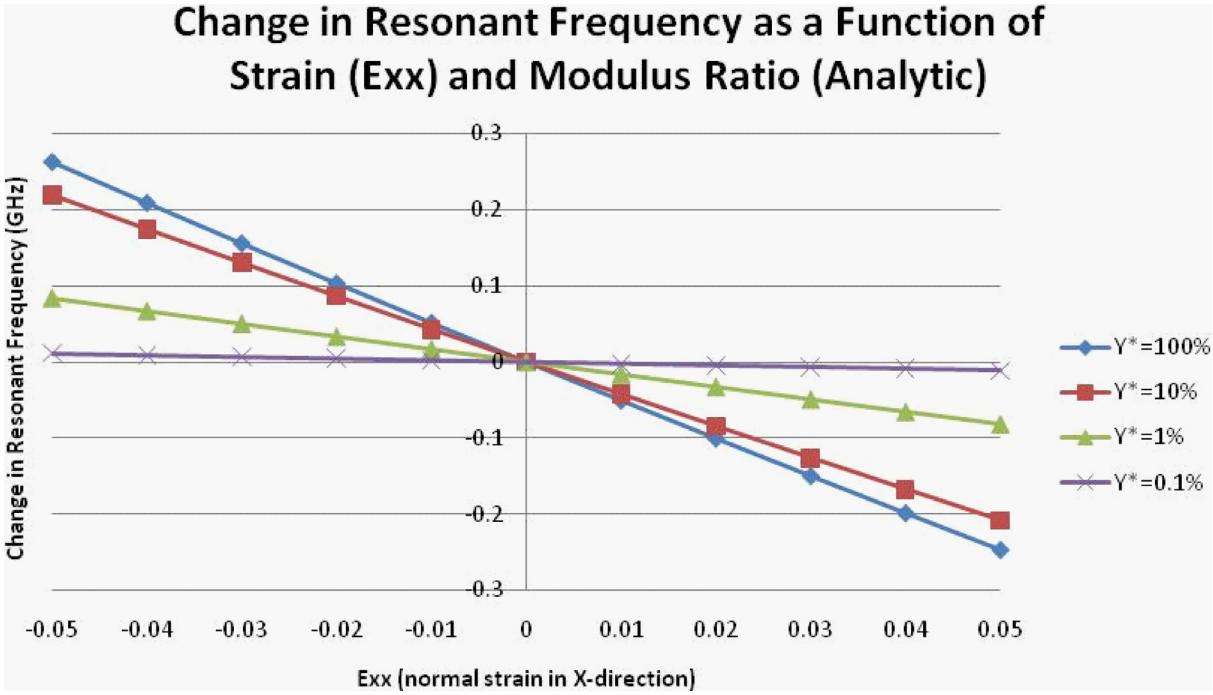

Figure 5. *Analytically derived shift in resonant frequency as a function of strain (E_{xx}) and modulus ratio. Change in resonant frequency:* $\Delta f_0 = f_0' - f_0 = (\omega_0' - \omega_0)/2\pi$.

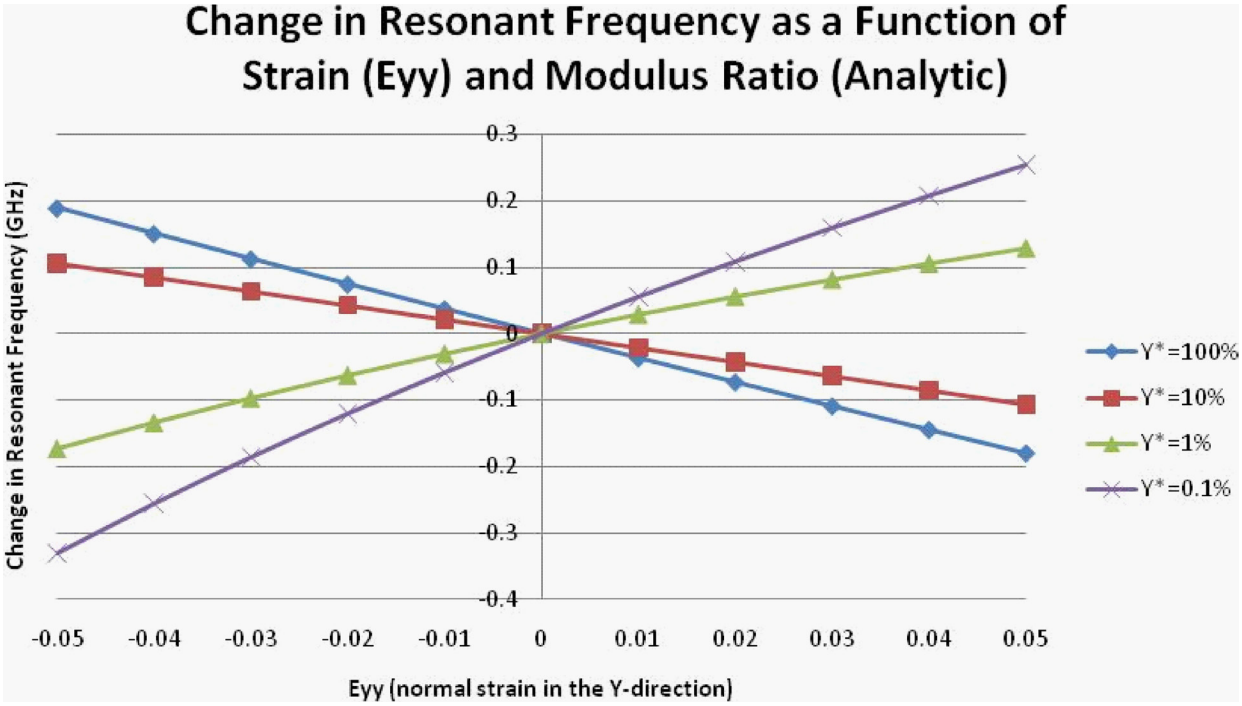

Figure 6. *Analytically derived shift in resonant frequency as a function of strain (E_{yy}) and modulus ratio. Change in resonant frequency:* $\Delta f_0 = f_0' - f_0 = (\omega_0' - \omega_0)/2\pi$.

from 100% to 10%, the unit cell exhibits decreased sensitivity to loading in the Y-direction; similar to the results in Figure 5. However, as the modulus ratio is decreased further, the trend reverses direction (i.e. a tensile load now induces an increase, as opposed to a decrease, in the resonant frequency) and departs from linearity.

3. NUMERICAL MODELING

To effectively model the complex interplay between mechanical loading, constituent mechanical properties, and EM performance, COMSOL Multiphysics 3.5a [27] was utilized to directly measure the EM performance of the mechanically-strained unit cell. The unit cell does not incorporate electro- or magneto-strictive materials so it is assumed that the relationship between mechanical strain and EM performance is causal (as opposed to coupled), implying that mechanical strain influences the EM performance, but the EM environment does not directly impart mechanical loading/strain on the unit cell. Consistent with the previous analysis, mechanical loads/strains are conveyed into the unit cell via displacements at the periodic boundary surfaces to enable direct comparison of the strain-dependent response of metamaterials with differing substrate moduli. Additionally, this loading method enabled direct comparison with the ANSYS-HFSS [28] results from [9,10,29], which ensured consistency between the disparate models and software packages (i.e. model verification) and allowed model validation with the test results, presented later.

The Structural Mechanics module in COMSOL was utilized to determine the complex, 3-D deformed geometry of the loaded metamaterial unit cell (some examples shown in Figure 9 and Figure 10). As in [9,10,29], the mechanical model assumes linear elastic behavior in the constituent materials. The deformed geometry was then tracked by the Arbitrary Lagrangian-Eulerian (ALE) moving mesh mode in order to serve as the configuration for the EM analysis in the RF Module.

The model was constructed to take advantage of nested parameter sweeps. Boundary displacements were stepped from –5 to +5% ($\Delta d/d$), in one direction, while the orthogonal boundaries were constrained. Within each loading step, the deformed geometry was incorporated into the RF Module in order to perform a frequency sweep and extract S-parameter data. Figure 7 and Figure 8 show the COMSOL results detailing the change in resonant frequency as a function of strain and modulus ratio. The dimensions and parameters are the same as those described in Figure 1 and Figure 2. As in [9], the shift in the metamaterial's resonant frequency is the superposition of the influence of the individual strain components. Note the similarity between the numerical results (Figure 7 and Figure 8) and the first-order analytic approximations (Figure 5 and Figure 6).

As in Figure 5, Figure 7 shows a reduction in modulus ratio leads to a decrease in the metamaterial's sensitivity to X-directed normal strains. As described earlier, a softer substrate conveys less strain into the conductive traces, resulting in less change in the unit cell's inductance and capaci-

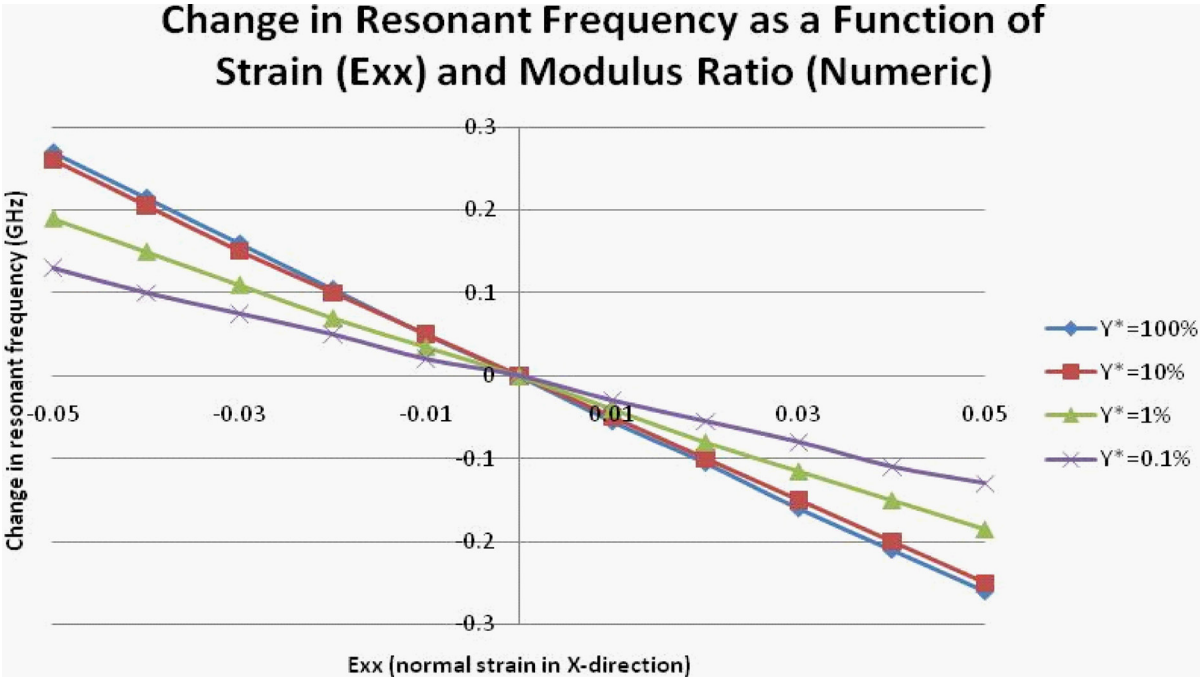

Figure 7. *Numerically derived (from COMSOL) shift in resonant frequency as a function of strain (E_{xx}) and modulus ratio. Change in resonant frequency:* $\Delta f_0 = f_0' - f_0 = (\omega_0' - \omega_0)/2\pi$.

tances. Additionally, the trend remains approximately linear over the range of material properties investigated.

Figure 8 shows the metamaterial's shift in resonant frequency as a function of modulus ratio and strain in the Y-direction. Similar to the trends depicted in Figure 6, as the substrate's modulus is continuously decreased, the numerical results predict a decrease in the metamaterial's sensitivity to strain, eventually resulting in a departure from linearity, and an eventual reversal of the trend. As detailed in Section 2.2, when the modulus of the substrate drops below a criti-

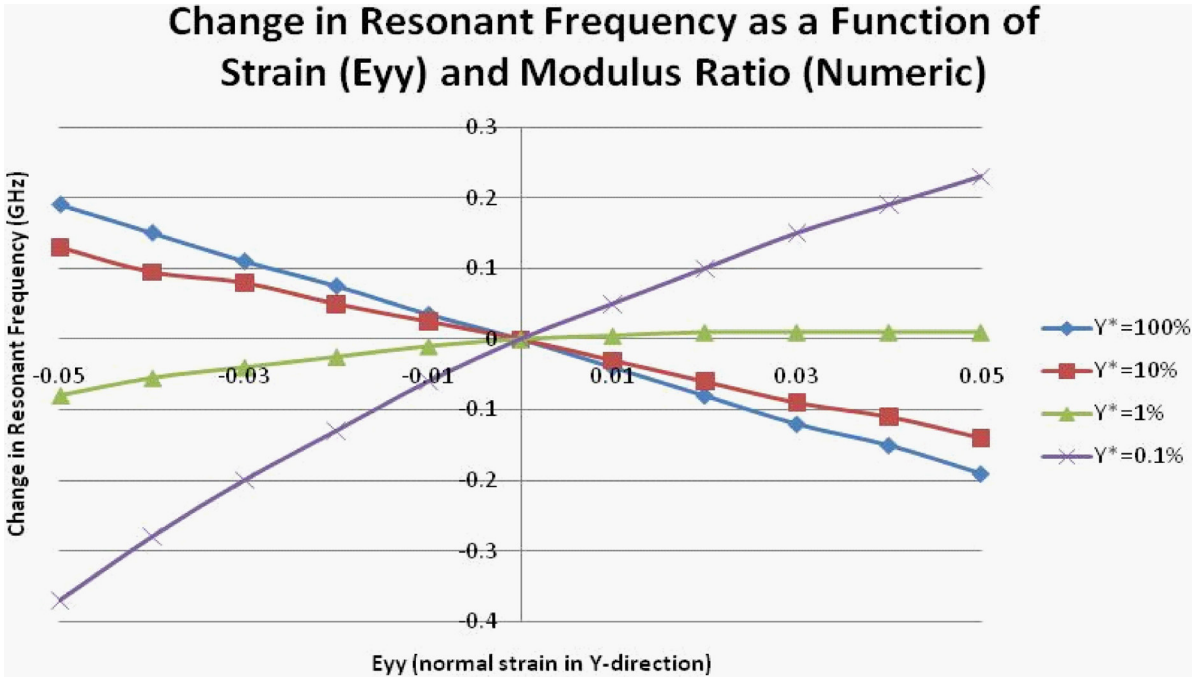

Figure 8. *Numerically derived (from COMSOL) shift in resonant frequency as a function of strain (E_{yy}) and modulus ratio. Change in resonant frequency:* $\Delta f_0 = f_0' - f_0 = (\omega_0' - \omega_0)/2\pi$.

cal value, a tensile strain in the Y-direction now results in an increase in the metamaterial's resonant frequency.

Figure 9 and Figure 10 show some of the simulation results depicting the electric fields superimposed over the deformed geometry of the unit cell. Figure 9 (E_{XX}) shows that the capacitors remain approximately parallel, even when utilizing a low modulus substrate and applying relatively large levels of strain. Additionally, the softer substrate conveys a diminished level of strain into the conductive traces, resulting in decreased sensitivity to the applied boundary displacements.

Figure 10 (E_{YY}) demonstrates a similar reduction of the extension in the conductive layer, when using a softer substrate. However, of particular interest are the exaggeration of the capacitive gap and the non-parallel orientation between the capacitor faces, for low values Y^*. Both of these factors help to explain the departure from linearity as the modulus of the substrate is reduced.

4. TESTING/EMPIRICAL RESULTS

4.1. Metamaterial Samples

The metamaterial samples tested in this effort featured a 6″ × 6″ metamaterial section (array of copper traces), centered on a 6″ × 12″ piece of dielectric substrate material. This provided a large metamaterial region for free-space characterization, and provided a near-uniform strain-field within the central portion of the sample; where the majority of the energy from the Gaussian beam was focused. The substrate materials chosen for this effort were Rogers RT/Duroid 5880 [30] and Pyralux [31].

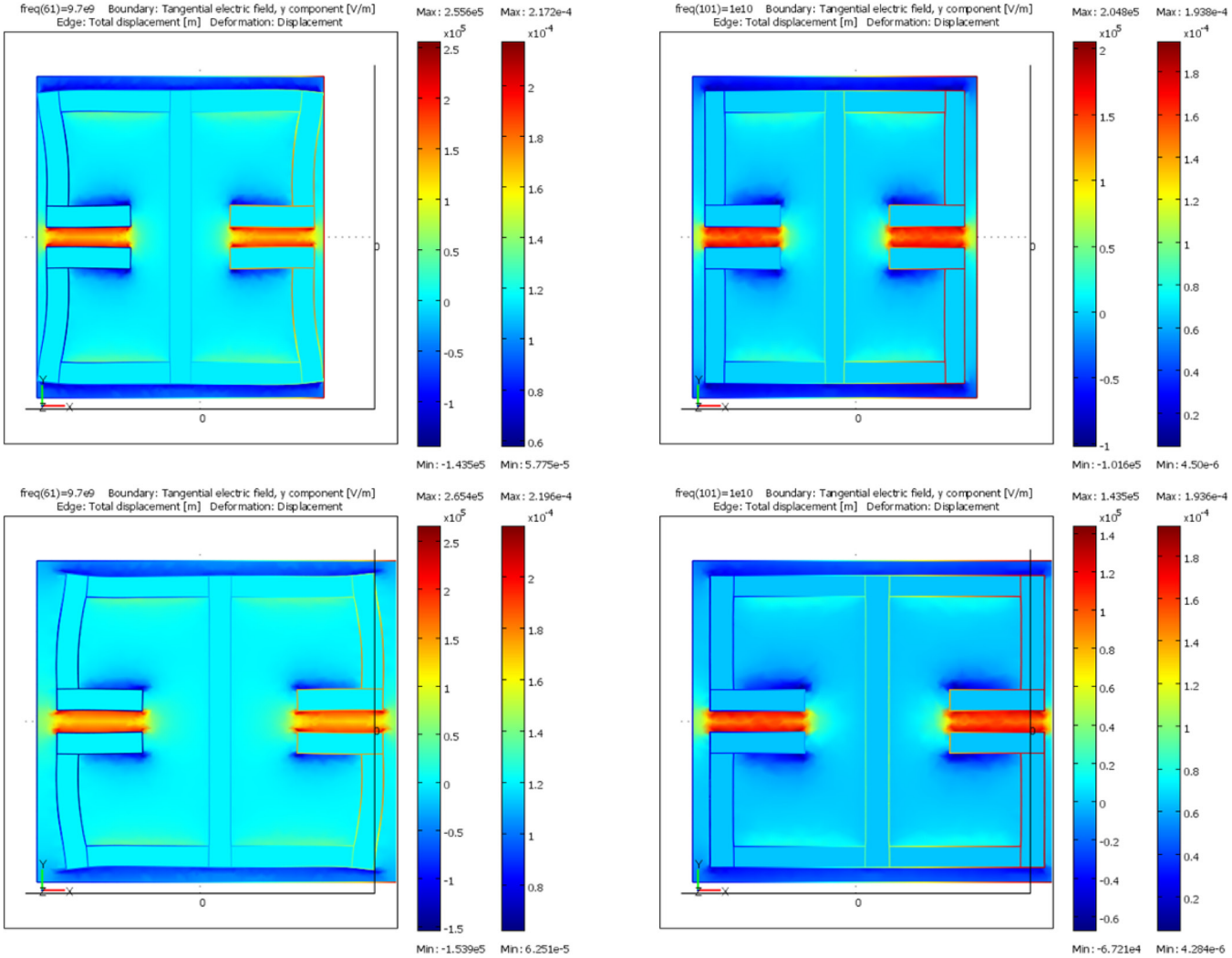

Figure 9. *Electric field, superimposed on the (software exaggerated) deformed geometry. On the left are samples with low modulus substrates (Y* = 1%), on the right are samples with high modulus substrates (Y* = 100%). Top two pictures depict E_{xx} = –5%, bottom two pictures depict E_{xx} = +5%. The two scales to the right of each picture detail the strength of the electric field (left bar) and total displacement (right bar). Simulations were run in COMSOL.*

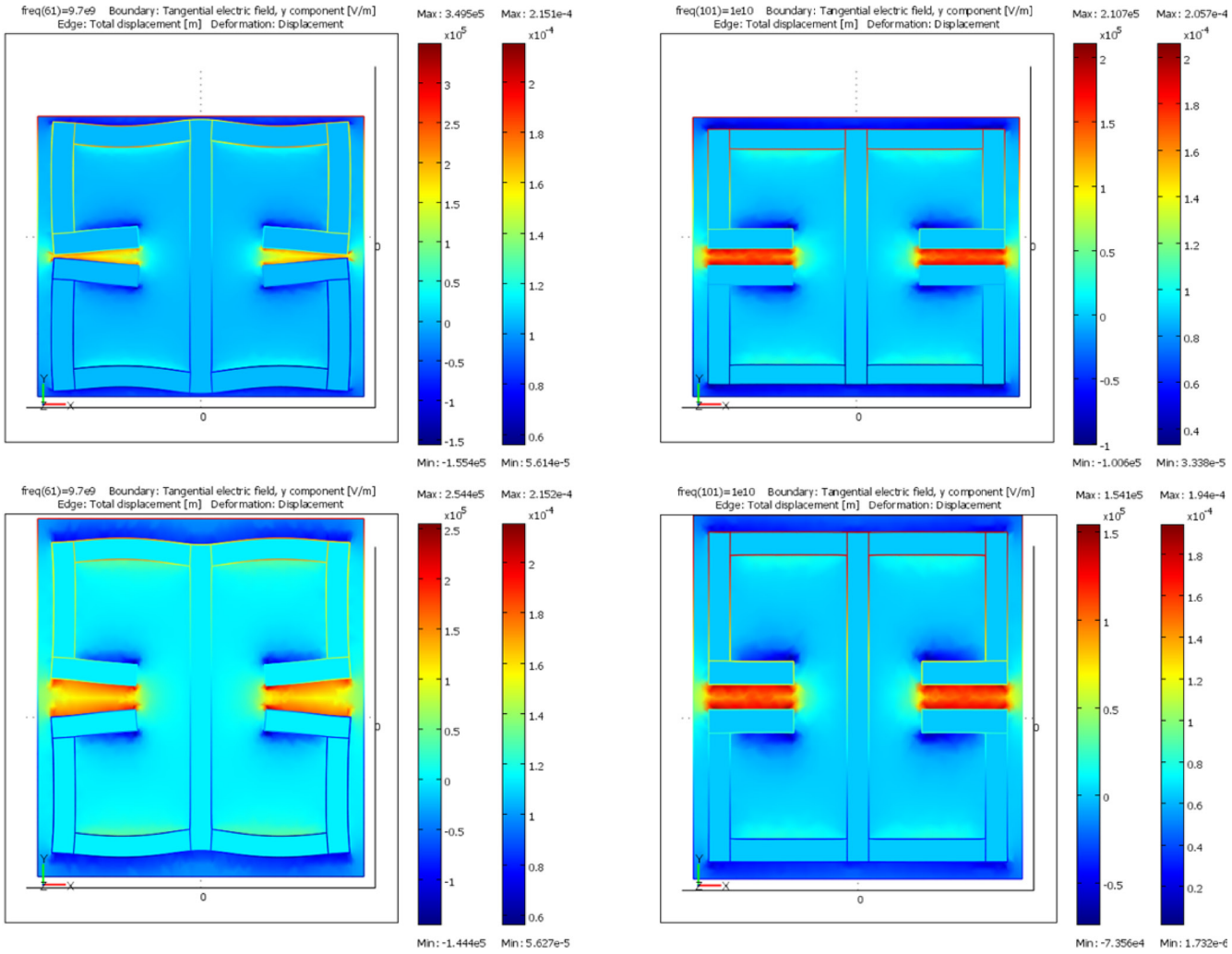

Figure 10. *Electric field, superimposed on the (software exaggerated) deformed geometry. On the left are samples with low modulus substrates (Y* = 1%), on the right are samples with high modulus substrates (Y* = 100%). Top two pictures depict E_{yy} = –5%, bottom two pictures depict E_{yy} = +5%. The two scales to the right of each picture detail the strength of the electric field (left bar) and total displacement (right bar). Simulations were run in COMSOL.*

Three different configurations, with two samples per configuration, were produced to test different strain profiles and material properties. The sample configurations are shown in Table 2.

4.1.1. Mechanical Characterization

To verify the mechanical properties required for analytic and numerical analyses, as well as the development of the loadframe control schemes (detailed later), substrate materials were tested in accordance with ASTM D 3039 [32] or ASTM D 882 [33], depending upon the thickness of the materials. Figure 11 and Figure 12 show the stress strain curves for the 5880 and Pyralux, respectively.

As seen in the curves, the 5880 is an inherently non-linear material; removing the load also demonstrated the material to be inelastic over the tested range. The Pyralux, on the other hand, demonstrated a higher degree of linearity and

Table 2. Metamaterial Sample Configurations. The Table Includes Modulus Ratio (Y*), Thickness Ratio (t*), Copper Strain Transfer Ratio (β), Substrate Strain Transfer Ratio (χ), Permittivity of the Substrate (ε_s).

Substrate Material	Copper Thickness	Y*	t*	Y*t*	β	χ	ε_s
Pyralux	0.5 oz/17 μm	7.3%	12.3	0.9	0.33	4.6	3.5
Pyralux	1 oz/34 μm	7.3%	6.2	0.5	0.44	4.0	3.5
5880	1 oz/34 μm	1.6%	46.7	0.8	0.47	3.8	2.2

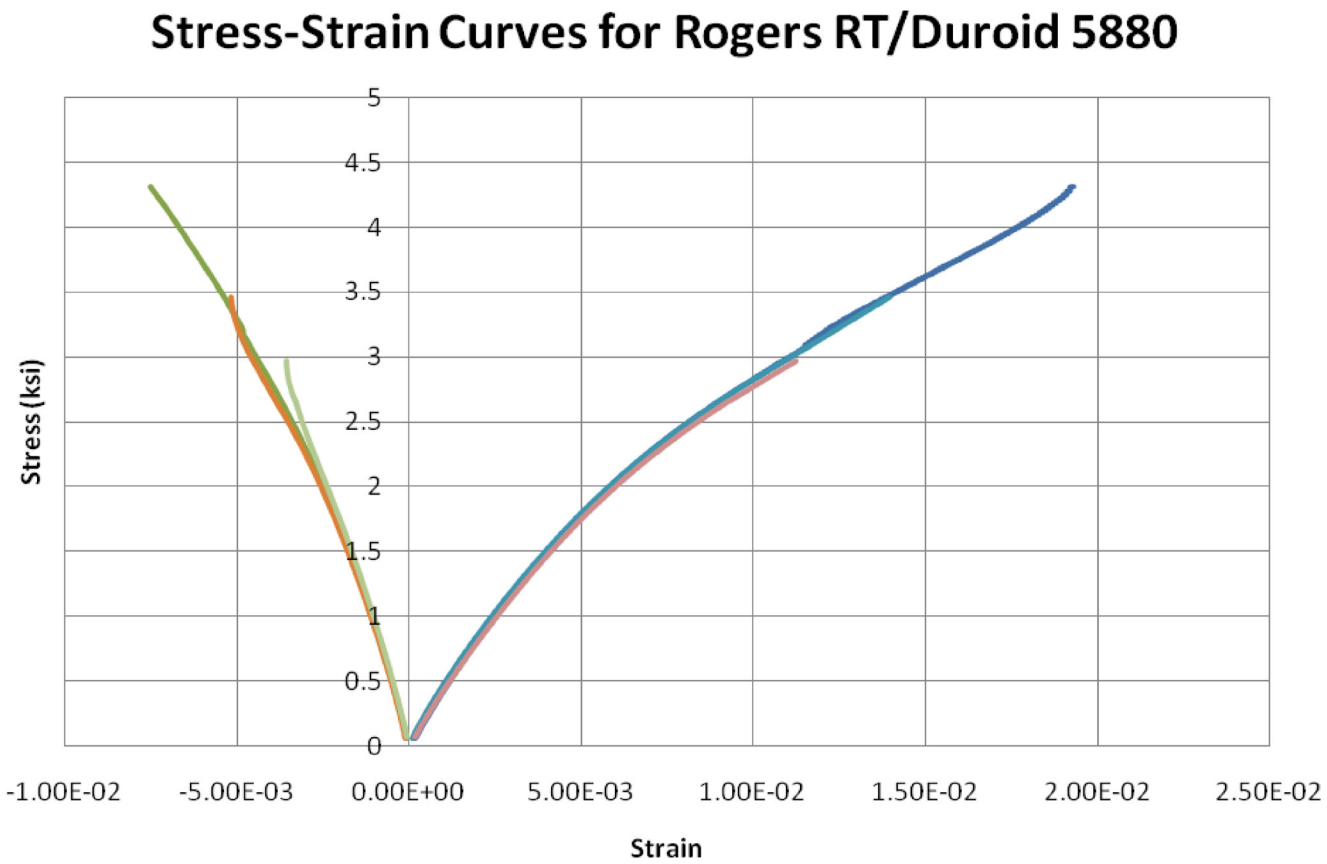

Figure 11. *Tensile stress-strain curves for RT/Duroid 5880 material samples. Curves to the right show strain in the direction of loading, curves to the left show strain in the orthogonal direction.*

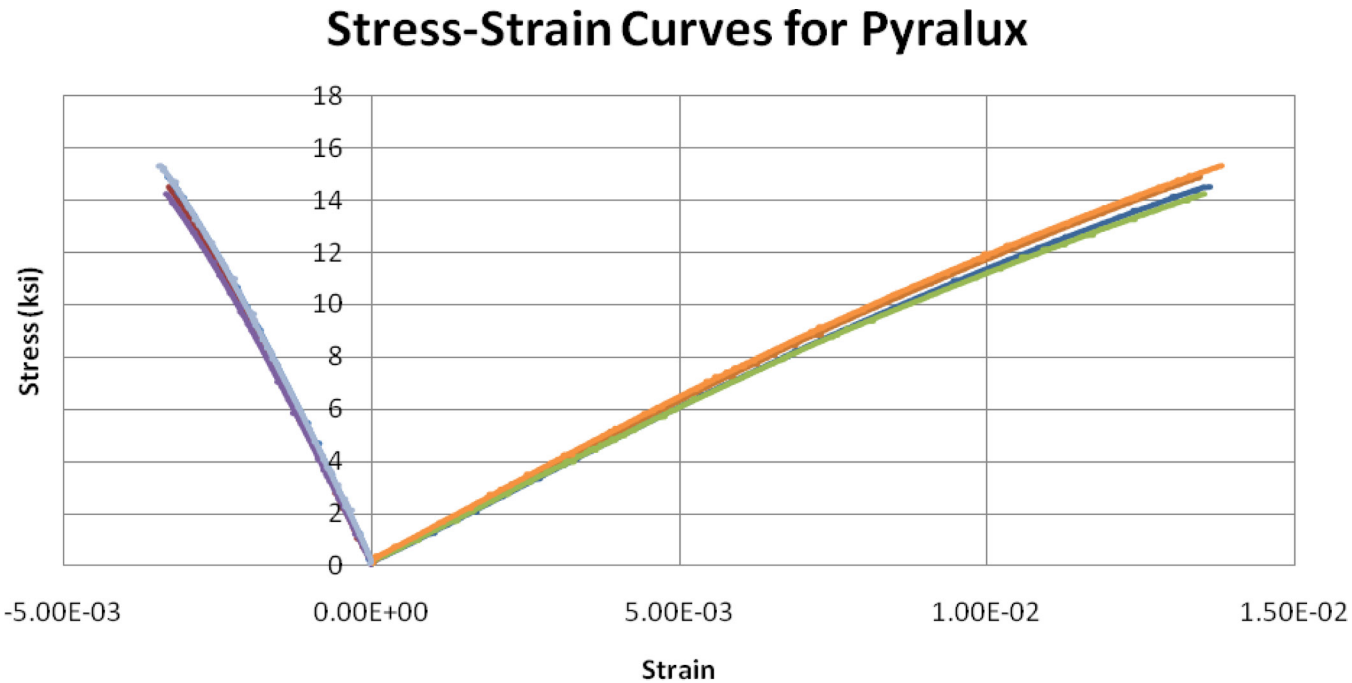

Figure 12. *Tensile stress-strain curves for the Pyralux material samples. Curves to the right show strain in the direction of loading, curves to the left show strain in the orthogonal direction.*

elasticity. For both materials, it was assumed they could be approximated as linear, for the range of anticipated strains, with minimal loss of accuracy. For the 5880, a Young's Modulus of 1.75 GPa/254 ksi was utilized, while a value of 8 GPa/1160 ksi was used for the Pyralux. Both values were significantly higher than the published values provided by the vendors.

Table 2 shows the different configurations, and the as-tested values of Y^*, t^*, β, χ, and ε_s for the samples.

4.1.2. Numerically-Predicted Strain-Dependence

COMSOL was used to predict the metamaterial samples' sensitivity to boundary displacements. Figure 13 shows the results from the multi-physics modeling. Of note is the similarity in the trends. While the modulus of the 5880 is much lower than that of the Pyralux, the 5880 samples were significantly thicker. Additionally, the copper traces were much thinner (i.e. "b" in Equations (4) and (5) was ~0.1 mm, as opposed to the 0.254 mm specified to the vendor), resulting in less structural rigidity and a greater amount of strain being conveyed into the copper. According to the COMSOL simulation results (Figure 13), the shift in resonant frequency can be described via the following set of equations, which allow predictions of the resonant frequency for arbitrary strain profiles (values of E_{XX} and E_{YY}) in the metamaterial:

$$\Delta f_0^{Pyralux} = -4.37E_{XX} - 1.87E_{YY}$$
$$\Delta f_0^{5880} = -4.78E_{XX} - 1.97E_{YY} \quad (10)$$

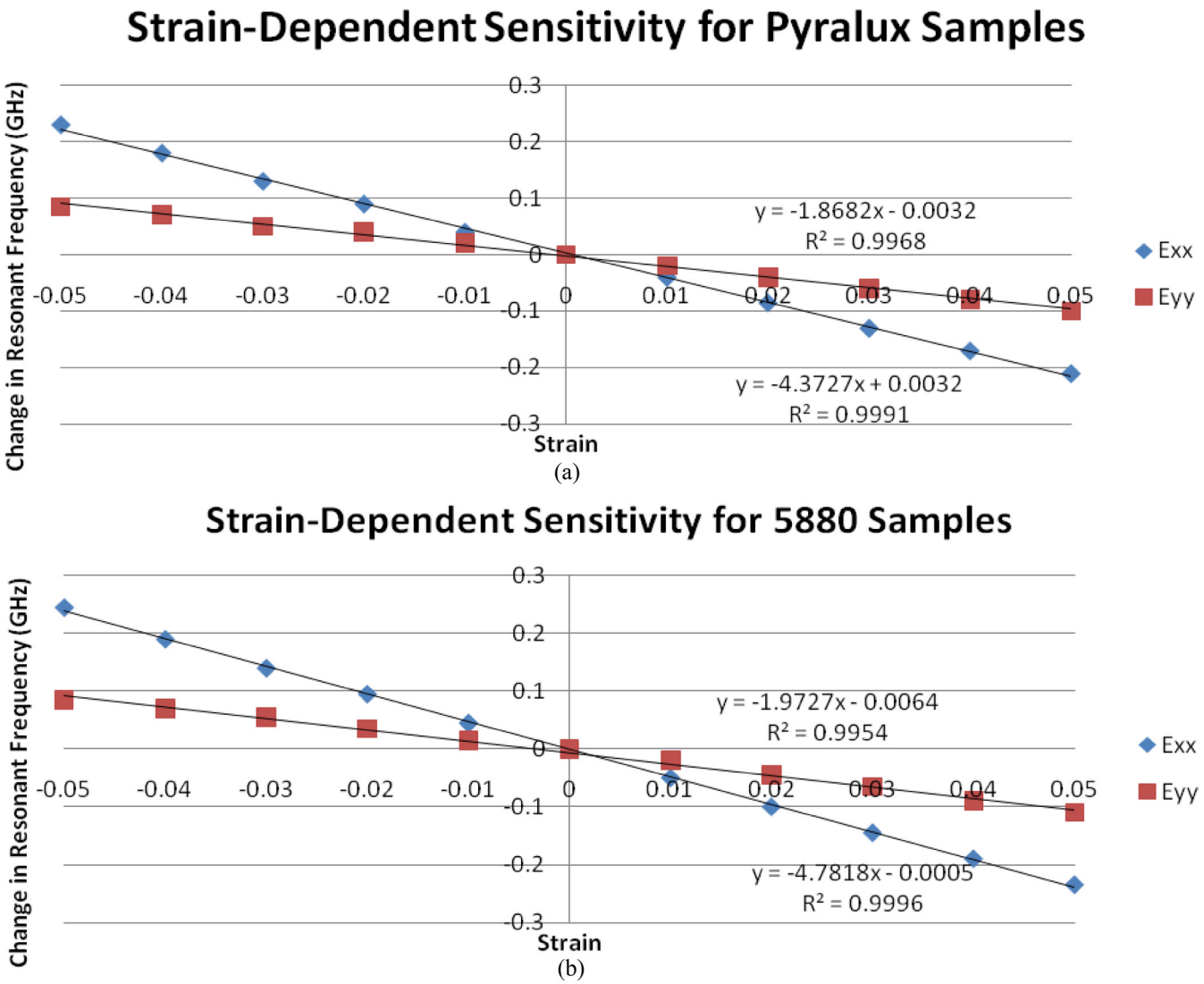

Figure 13. *Numerically derived (COMSOL) resonant frequency shift, as a function of applied strain for both the Pyralux and 5880 samples. Included are linear curves, fit to the data. These trends are required to correlate the strain profile seen during testing, with the predicted change in resonant frequency. The Pyralux samples with 1/2 and 1 oz copper traces exhibited a 2% difference in the trends predicted in the modeling, so a single trend was utilized for both configurations.*

4.2. EM Characterization of Mechanically-Loaded Metamaterials

4.2.1. Set-Up

A unique test facility was established at the Center for Metamaterials and Integrated Plasmonics at Duke University in order to generate empirical data on the strain-dependent EM performance of metamaterial samples. An Instron [34] 5567, 30 kip electromechanical loadframe served as the centerpiece for the facility and was used to impart mechanical loads into the metamaterial sample, via a set of 6-inch wide wedge grips, developed by Wyoming Test Fixtures [35]. The wedged design grips the sample with a compressive force proportional to the tensile load applied via the loadframe (i.e. the clamping force increases as the loading on the sample is increased). This prevents the sample from prematurely tearing due to excessive compressive loading at the grip faces. Due to the smooth surface finish of the metamaterial samples, tungsten-carbide grit was chosen for the grip-face surfaces in order to prevent slippage during tensile testing. Additionally, the design of the wedges ensure the central plane of the sample is coincident with the load axis of the test frame. S-parameter characterization of the metamaterial sample was accomplished with an Agilent Technologies N5245A PNA-X Network Analyzer [36]. Rozendal Associates [37] RF Horns (frequencies of operation: 8.2–12.4 GHz) with 2 foot focal length lenses, provided a focused Gaussian beam at the center of the metamaterial sample. Figure 14 shows the test facility at Duke University.

This research also required a method for assessing the strain-field on the metamaterial surface. Photogrammetry was chosen because it (a) provides a continuous description of the strain-field over a large area and (b) does not interfere with the RF characterization of the metamaterial. A 16 megapixel Nikon/Kodak Professional SLR camera [38], with a non-zooming, wide angle lens, and high performance flash were used to generate the high-resolution imagery necessary to determine the strain profile on the loaded metamaterial samples.

4.2.2. Test Conduct

To prepare the facility for the metamaterial characterization, a thick metal plate was placed in the wedge grips and tension was applied from the loadframe. This was performed to ensure the wedge grips were coplanar (not rotated with respect to one another) and maintained that relationship as load was applied to the sample. Twin laser levels were then aligned with witness marks on the sides of the wedge grips. The mechanical linkage between the loadframe and wedge grips provided some laxity about the Y-axis. The laser levels

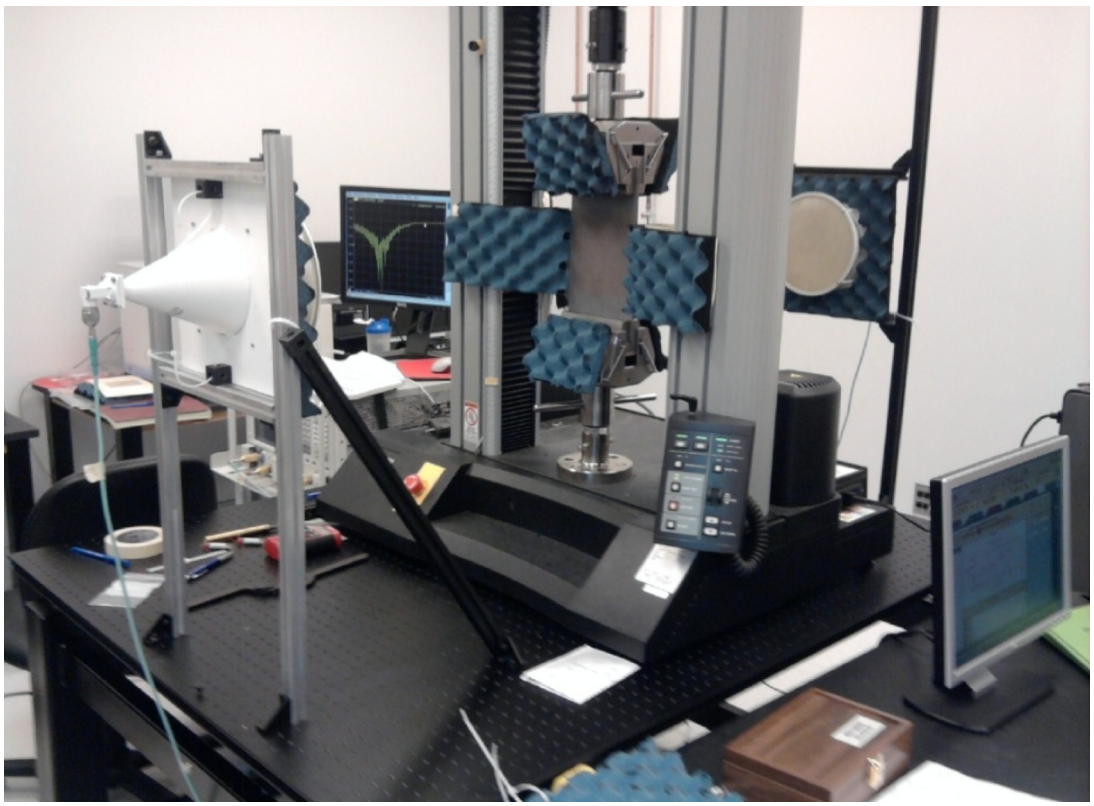

Figure 14. *Multiphysics metamaterial test facility. Shown in the picture are the metamaterial sample, the loadframe, loadframe control computer, wedge grips, RF horns and focusing lenses, and vector network analyzer.*

provided assurance that the front plane did not translate or rotate between the calibration steps and testing of the metamaterial samples (critical for future retrieval of the sample's permittivity and permeability). In tests conducted at the Air Force Research Laboratory/Space Vehicles Directorate, a VICON IR motion capture system [39] validated this process, determining out-of-plane displacements (between samples) were on the order of λ/50. The laser levels and witness marks were utilized every time a sample was replaced, ensuring the grips did not rotate between RF characterization steps. Additionally, the "return to zero" function on the loadframe was utilized to ensure a consistent Y-location of the grips, for all calibration and metamaterial tests.

This testing required a high level of resolution in the S-parameter data generated from the testing. As a result, a Gated Reflect Line (GRL) calibration, utilizing the Agilent's Freespace Calibration software [36], was performed to mitigate the effects of standing waves in the facility. To ensure the accuracy of the GRL calibration, samples (acrylic, styrene) with known material properties (permittivity and permeability) were tested to validate the quality of the calibration.

After calibration, the metamaterial sample was clamped, via the wedge grips, within the loadframe. Baseline/no load RF characterization was performed on the sample. A number of time-gates were utilized to ensure the test data captured the resonant behavior of the metamaterial while minimizing the effects of standing waves. Figure 15 shows the S-parameters retrieved from two samples, using a variety of time-gates. The time gates used are shown in Table 3; a time of zero equates to the time at which the electromagnetic wave hits the front surface of the sample. All test results given in the remainder of this paper utilize time gate #2.

After RF characterization, a precision scale (ruler) was attached to the front of the sample (provided a length reference for the photogrammetry) and a number of pictures were taken, from a variety of angles, in order to determine the baseline geometry of the sample. Figure 16 contains two pictures taken during this effort.

After collecting data on the baseline RF performance and geometry, tensile loading was applied to the metamaterial sample. The loadframe was controlled via Bluehill2 version 2.9 [34] software, and utilized several programmed hold points during the loading profile. Once the loadframe hit a pre-determined load level, a "hold" was initiated to maintain a constant cross-head displacement/strain level. The sample was allowed to stress-relieve for 2–3 minutes (depending upon material) to ensure the unit cell geometry was stable at the new displacement level. Figure 17 shows the load history from one of the tests. The curve shows evidence of significant stress-relieving in the metamaterial sample.

Once the load level had attained a near steady state, RF characterization was performed at the deformed geometry, the scale/ruler re-applied, and pictures taken for assessing the sample's strain profile at the loaded/deformed geometry. The "hold" on the loadframe control was ended, and the process (load the specimen to the next programmed hold, allow material stress-relieving to settle, perform RF characterization, take photographs) was repeated for each "hold" position delineated in the control scheme.

Table 3. Entrance and Exit Times for the Timegates Used for the RF Characterization of the Metamaterial Samples. For the Times Shown, a Value of Zero Indicates the Time at Which the Electromagnetic Wave Hits the Front Surface of the Sample.

	Gate Entrance	Gate Exit
Gate 1	–500 ps	1 ns
Gate 2	–500 ps	2 ns
Gate 3	–500 ps	3 ns
Gate 4	–500 ps	4 ns

4.2.3. Results

To correlate the COMSOL model predictions with the results, it was necessary to determine the strain profile (E_{XX} and E_{YY} values) of the metamaterial sample. Photomodeler version 6 [40] software was utilized to integrate the 10–12 photographs at each load increment and determine the spacing between the points denoted in Figure 16. That number of photographs over-defined the geometry, but improved the precision of the generated geometric solution. Assessing the strain in the loaded sample was then distilled to determining the change in length between points. Multiple examination distances were recorded to (a) ensure a consistent strain field over the center of the metamaterial sample, and (b) provide better statistics for the strain values and the resultant shift in resonant frequency.

Table 4 details the strains that were ascertained via photogrammetry (given as a range of values). The values were input into Equation (10) to determine the software predicted shift (Δf_{ave}) in the metamaterial's resonant frequency. This is also given in Table 4, along with the standard deviation in the predictions, and the results from the free-space EM characterization. As the table shows, the predictions are in strong agreement with the tests. This agreement is noteworthy, due to the numerous sources of errors in the process: mechanical properties and the approximation as a linear trend, dimensional tolerances of the sample, numerical analysis, the onset of plasticity in the samples, the photogrammetric determination of the strain values, and the accumulation of multiple round-off errors.

Table 4 also demonstrates how the different materials exhibit disparate EM responses when subjected to similar loading scenarios. Applying a Y-directed load to the Pyralux samples generated a decrease in the resonant frequency, while the same load input generated an increase in

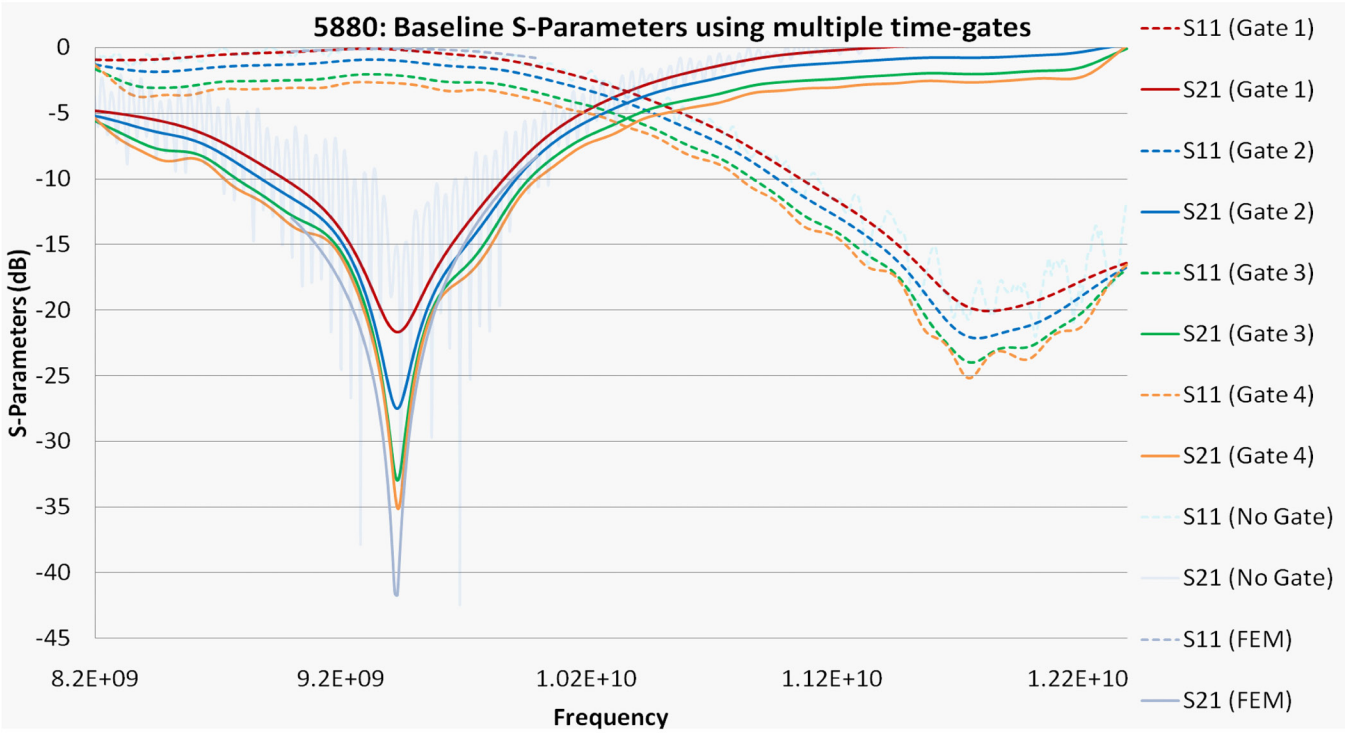

(a)

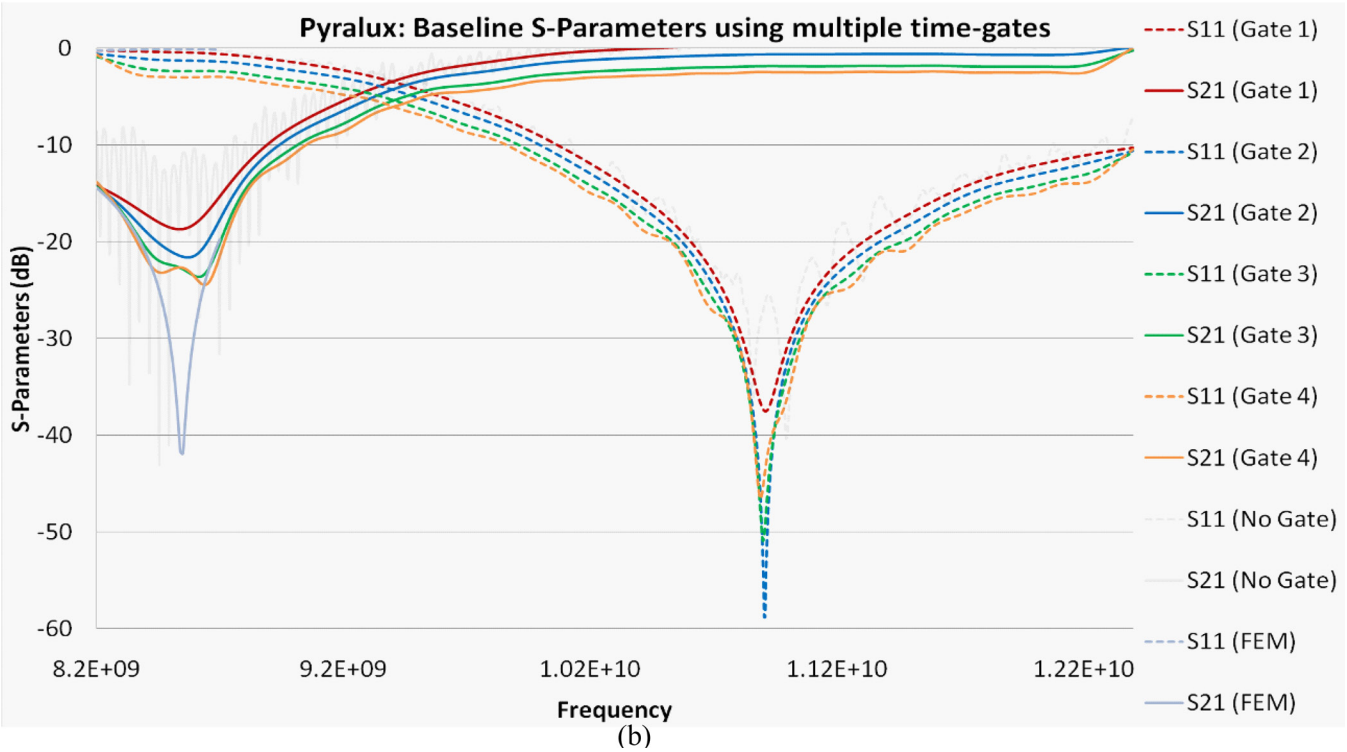

(b)

Figure 15. *Experimental baseline readings on a 5880 and Pyralux sample, showing a number of timegates. As the graphs demonstrate, an increase in the window for data collection allows improved capture of the resonant response, but at the expense of also capturing additional spurious reflections from the test facility. The response with no time gating is shown for reference. Also shown are numerical simulation results (COMSOL). The simulated frequency range was truncated to focus on the resonance, in an effort to reduce computation time.*

Table 4. Comparison of the Predicted Shifts in Resonant Frequency and Empirical Results. Also Shown are the Strain Values Determined via Photogrammetry, Which are Required to Determine the Predicted Shift.

	Pyralux, 1/2 oz Cu, Sample 1, 2400 lbs	Pyralux, 1/2 oz Cu, Sample 2, 2400 lbs	Pyralux, 1oz Cu, Sample 1, 2400 lbs	Pyralux, 1oz Cu, Sample 2, 2400 lbs	5880, Sample 1, 1200 lbs	5880, Sample 1, 1600 lbs	5880, Sample 2, 1250 lbs
EXX (%)	–1.12 to –1.06	–1.12 to –0.99	–1.25 to –1.19	–1.12 to –1.06	–0.73 to –0.59	–1.26 to –0.99	–0.79 to –0.66
EYY (%)	4.16 to 4.3	4.03 to 4.1	3.76 to 3.96	4.03 to 4.1	1.10 to 1.14	1.83 to 1.87	1.10 to 1.14
Predicted Δf_0 (GHz)	–0.032	–0.030	–0.020	–0.029	+0.009	+0.018	+0.012
Stand Dev Δf_0 (GHz)	0.002	0.003	0.002	0.001	0.006	0.003	0.003
Test Results Δf_0 (GHz)	–0.039	–0.032	–0.026	–0.029	+0.011	+0.018	+0.013

the resonant frequency of the 5880 samples. As Figure 13 shows, both materials exhibit similar sensitivities to each of the strain components (E_{XX} and E_{YY}). However, Figure 11 and Figure 12 show that the substrate materials exhibit significantly different Poisson's ratios ($-E_{XX}/E_{YY}$: 0.4 for the 5880 and 0.25 for the Pyralux), so the same externally applied load/strain results in different strain values in the orthogonal direction. When these strain profiles are input into Equation (10), they lead to predicted shifts in opposing directions.

Figure 18 shows the S21 values retrieved during a test on one of the samples. Of note is the decrease in the strength of the resonant response when the sample is loaded. Unlike standard "dog-bone" tensile specimens [32], which provide consistent levels of stress and strain throughout the test section, the edges of the metamaterial sample (with its thin and wide configuration) display significant deviations from the strain profile at the center of the sample. While the majority of the EM energy does interact with the center of the metamaterial sample, the non-uniformity in the strain profile effectively spreads the spectrum of the response (because unit cells with different strain profiles resonate at different frequencies) and decreases the metamaterial's overall resonant response. Other efforts experimentally demonstrated this phenomenon [7,8], but did not detail the underlying physical mechanisms.

5. CONCLUSIONS

This paper demonstrates that the substrate's modulus plays a significant role in the strain-dependent electromagnetic performance of metamaterial structures. Depending upon the relative thickness and modulus of the constituent materials, the metamaterial can exhibit dramatically different strain-dependent responses when subjected to mechanical loading. Shear-lag models were utilized to describe load transfer from the dielectric substrate into the conductive traces on the surface of the substrate, and how load transfer changes as a function of substrate modulus. Equivalent circuit parameters are leveraged to explain how the different strain values in the substrate and conductive traces translate into changes in the metamaterial's resonant frequency. Mul-

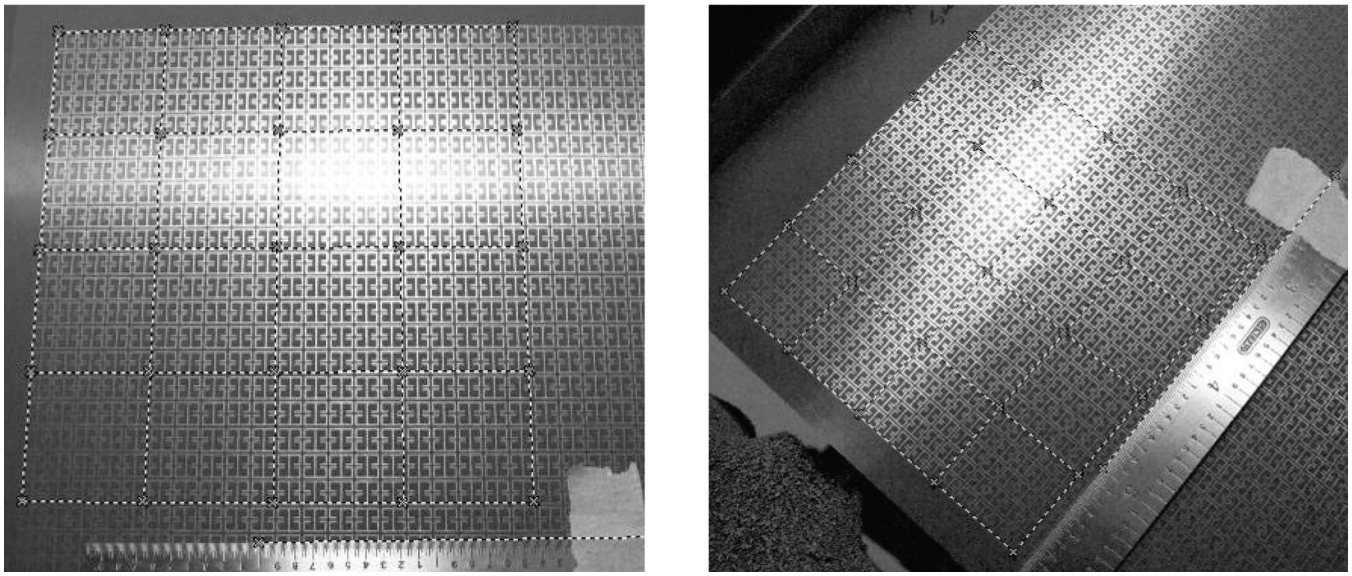

Figure 16. *Pictures of the metamaterial surface for strain-mapping via photogrammetry. Photographs were taken from a variety of angles in accordance with best practices [40]. Included in both pictures is the ruler used to provide a length reference.*

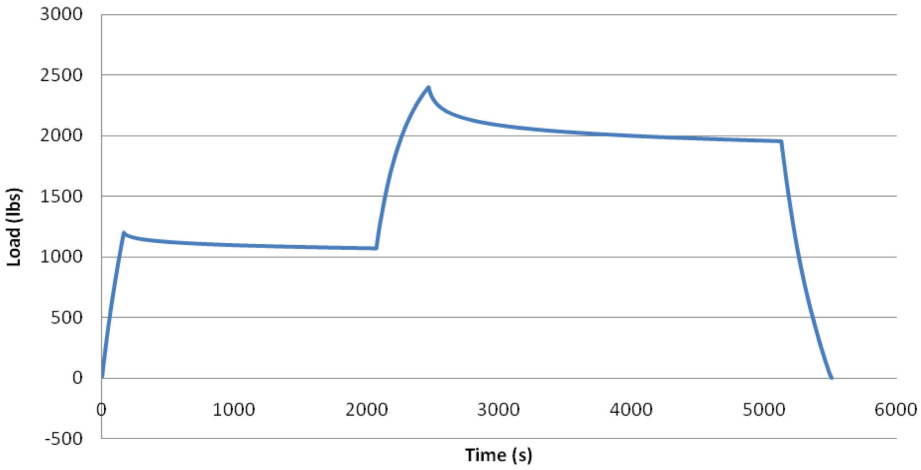

Figure 17. *Typical load/time curve from one of the Pyralux sample tests. The graph demonstrates significant stress relieving in the samples during each of the programmed holds (i.e. mechanical loadframe crosshead maintains constant position). RF characterization and photography from strain mapping were performed after the load had stabilized during one of the hold periods.*

tiphysics modeling is then utilized to predict the relationship between mechanical strain, material moduli, and electromagnetic performance. To validate these models, a unique test facility at Duke University was established to generate empirical data on the EM performance of mechanically-loaded metamaterial samples.

In order to successfully transition metamaterials onto operational systems, these relationships must be understood to enable predictions of EM performance in a relevant environment. Additionally, developing a better understanding of the intimate linkage between mechanical properties and EM performance will allow engineers to more intelligently design and perform multi-dimensional optimization of these unique multifunctional structures.

NOMENCLATURE

β = Ratio of the strain in the conducting layer, to the strain at the unit cell level, $(\Delta l/l)/(\Delta d/d)$

E_{ii} = Strain of the unit cell in the i-direction, $\Delta d_i/d_i$

ϵ_{ii} = Differential strain at a point. Analysis is restricted to normal strains, $\partial u_i/\partial x_i$

f_0 = Resonant Frequency. $f_0 = \omega_0/2\pi$

χ = Ratio of the strain in the substrate, between conductive traces, to the strain at the unit cell level, $(\Delta s/s)/(\Delta d/d)$

ω_0 = Angular resonant frequency. $\omega_0 = 2\pi f_0$

Y = Young's, or Elastic, Modulus. The use of a subscript denotes a particular material.

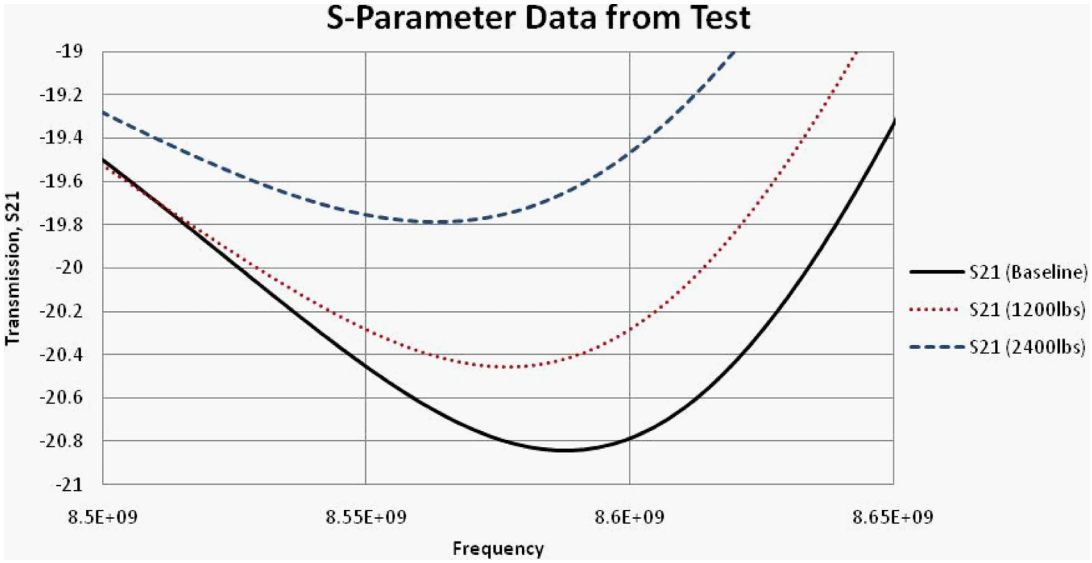

Figure 18. *Data set from one metamaterial sample (Pyralux, 1oz, #1). The loads shown refer to the loadframe hold points at which the data was taken. Typical of the results from the testing conducted during this effort, the figure demonstrates: (a) the strain-dependent shift in the resonant frequency, and (b) spreading of the spectral response and (c) a decrease in the resonant strength, at load.*

ACKNOWLEDGEMENT

BJA would like to acknowledge the technical and programmatic support of Dr. Joycelyn Harrison and the US Air Force Office of Scientific Research.

REFERENCES

[1] J. B. Pendry, A. J. Holden, W. J. Stewart, I. Youngs, "Extremely Low Frequency Plasmons in Metallic Mesostructures," *Phys. Rev. Lett.,* **76**, 4773 (1996). http://dx.doi.org/10.1103/PhysRevLett.76.4773. PMid:10061377.

[2] J.B. Pendry, A.J. Holden, D.J. Robbins, W.J. Stewart, "Magnetism from Conductors and Enhanced Nonlinear Effects," *IEEE Trans. Micro. Theory and Tech.*, **47**, 0018-9480 (1999).

[3] D.R. Smith, W.J. Padilla, D.C. Vier, S.C. Nemat-Nasser and S. Schultz, "A Composite Medium with Simultaneously Negative Permeability and Permittivity," *Phys. Rev. Lett.,* **84**, 4184 (2000). http://dx.doi.org/10.1103/PhysRevLett.84.4184. PMid:10990641.

[4] D.R. Smith, J.J. Mock, A. Starr, D. Schurig, "Gradient Index Metamaterials," *Phys. Rev. E,* **71**, 036609 (2005). http://dx.doi.org/10.1103/PhysRevE.71.036609. PMid:15903607.

[5] R. Liu, C. Ji, J.J. Mock, J.Y. Chin, T.J. Cui, D.R. Smith, "Broadband Ground-Plane Cloak", *Science,* **323**, 5912, pp 366–369, (2009). http://dx.doi.org/10.1126/science.1166949. PMid:19150842.

[6] D. Schurig, J. Mock, B. Justice, S. Cummer, J.B. Pendry, A. Starr, D. R. Smith, "Metamaterial Electromagnetic Cloak at Microwave Frequencies," *Science*, **314**, 977 (2006). http://dx.doi.org/10.1126/science.1133628. PMid:17053110.

[7] R. Melik, E. Unal, N.K. Perkgoz, C. Puttlitz, H.V. Demir, "Metamaterial-based Wireless Strain Sensors," *Appl. Phys. Letts.,* **95**, 011106 (2009). http://dx.doi.org/10.1063/1.3162336.

[8] R. Melik, E. Unal, N.K. Perkgoz, C. Puttlitz, H.V. Demir, "Flexible Metamaterials for Wireless Strain Sensing," *Appl. Phys. Lett.,* **95**, 181105 (2009). http://dx.doi.org/10.1063/1.3250175.

[9] B.J. Arritt, B. Adomanis, T. Khraishi, D.R. Smith, "Parametric Analysis of the Strain-Dependent Behavior of a Metamaterial Electric Resonator," *Appl. Phys. Lett.,* **98**, 191907 (2010). http://dx.doi.org/10.1063/1.3507892.

[10] B.J. Arritt, D.R. Smith, T. Khraishi, "Equivalent Circuit Analysis of Metamaterial Strain-Dependent Effective Medium Parameters," *Journ. Appl. Phys.*, **109**, 073512 (2011). http://dx.doi.org/10.1063/1.3569742.

[11] I. Pryce, K. Aydin, Y.A. Kelaita, R.M. Briggs, H.A. Atwater, "Highly Strained Compliant Optical Metamaterials with Large Frequency Tunability," *Nano Lett.*, **10**, 4222 (2010). http://dx.doi.org/10.1021/nl102684x. PMid:20857941.

[12] D. Schurig, J.J. Mock, D.R. Smith, "Electric-Field-Coupled Resonators for Negative Permittivity Metamaterials," *Appl. Phys. Lett.*, **88**, 041109 (2005). http://dx.doi.org/10.1063/1.2166681.

[13] S. Sajuyigbe, B. Justice, A. Starr, D.R. Smith, "Design and analysis of three-dimensionalized ELC Metamaterial Unit Cell," *IEEE Antennas and Wireless Propagation Letters*, **8**, 1268–1271 (2009). http://dx.doi.org/10.1109/LAWP.2009.2036572.

[14] S. Sajuyigbe, M. Ross, P. Geren, S.A. Cummer, M.H. Tenalian, D.R. Smith, "Wide angle impedance matching metamaterials for waveguide-fed phased-array antennas," *IET Microwaves, Antennas, and Propagation*, **4**, 8, pp 1063-1072 (2010). http://dx.doi.org/10.1049/iet-map.2009.0543.

[15] K. Siwiak, T. Dowling, L. Lewis, "Boresight errors induced by missile radomes," *IEEE Transactions on Antennas and Propagation,* **27**, 6, pp 832-841 (1979). http://dx.doi.org/10.1109/TAP.1979.1142193.

[16] SensorMetrix, 10211 Pacific Mesa Blvd, Ste 408, San Diego, CA 82121, USA.

[17] S.A. Martin, J.L. Blackshire, "Effect of Adhesive Material Properties on Induced Stresses in Bonded Sensors," *Defense Technical Information Center report number AFRL-ML-WP-TP-2006-476,* approved for public release (2006).

[18] J.L. Blackshire, S.A. Martin, A. Cooney, "Characterization and Modeling of Bonded Piezoelectric Sensor Performance and Durability in Simulated Aircraft Environments," *Proceedings of the Third European Workshop on Structural Health Monitoring,* pp 283–289, Granada, Spain (2006).

[19] U.A. Handge, "Analysis of a shear-lag model with nonlinear elastic stress transfer for sequential cracking of polymer coatings," *Journal of Materials Science,* **37**, 4775–4782 (2002). http://dx.doi.org/10.1023/A:1020814314019.

[20] J. Sirohi, I. Chopra, "Fundamental Understanding of Piezoelectric Strain Sensors," *Journal of Intelligent Material Systems and Structures,* **11**, 246 (2000).

[21] W.B. Fraser, "Bending of a stretched plate containing an eccentrically plate reinforced hole of arbitrary shape," *International Journal of Solids and Structures,* **11**, pp 1245–1256 (1975). http://dx.doi.org/10.1016/0020-7683(75)90113-4.

[22] C. Haag, H. Suhr, "Improved Adhesion of Pre-Etched Polytetrafluoroethylene by PECVD Deposited Thin Metallic Layers," *Applied Physics A,* **47**, 199–203 (1988). http://dx.doi.org/10.1007/BF00618885.

[23] E.B. Rosa, *Bulletin of the Bureau of Standard* (Washington Government Printing Office, Washington, D.C., 1908), **4**, pp 301–344.

[24] W. Withayachumnankul, C. Fumeaux. D. Abbott, "Compact Electric-LC Resonators for Metamaterials," *arXiv:1009.0139v1[Physics.Optics]* (2010).

[25] O.G. Vendik, S.P. Zubko. M.A. Nikol'skii, "Modeling and Calculations of the Capacitance of a Planar Capacitor Containing a Ferroelectric Thin Film," *Tech. Phys.,* **44**, 4, pp 349–355 (1999). http://dx.doi.org/10.1134/1.1259300.

[26] G.T. Mase, G.E. Mase, *Continuum Mechanics for Engineers,* (CRC Press, New York, NY, 1999). http://dx.doi.org/10.1201/9781439832578.

[27] COMSOL, Inc., 10850 Wilshire Blvd, Suite 800, Los Angeles, CA 90024, USA.

[28] ANSYS, Inc., Southpointe, 275 Technology Dr., Canonsburg, PA 15317, USA.

[29] B.J. Arritt, D. R. Smith, T.A. Khraishi, "Analytically Describing the Temperature-Dependent Constitutive Parameters of a Metamaterial," *Journal of Intelligent Material Systems and Structures,* **23**, 4, p.463–471, (2012). http://dx.doi.org/10.1177/1045389X11433496.

[30] Roger Corp., 100 S. Roosevelt Ave., Chandler, AZ 85226, USA.

[31] DuPont, 1007 Market St., Wilmington, DE 19898, USA.

[32] ASTM D3039-08 "Standard Method for Tensile Properties of Polymer Matrix Composite Materials".

[33] ASTM D882-10 "Standard Test Method for Tensile Properties of Thin Plastic Sheeting".

[34] Instron, 825 University Ave, Norwood, MA 02062, USA.

[35] Wyoming Test Fixtures, Inc., 2960 E. Millcreek Canyon Rd., Salt Lake City, UT 84109, USA.

[36] Agilent Technologies, Inc., 5301 Stevens Creek Blvd., Santa Clara, CA 95051, USA.

[37] Rosendal Associates, Inc., 9530 Pathway St., Suite 101, Santee, CA 92071, USA.

[38] Nikon, Fuji Bldg., 2-3 Marunouchi 3-chome, Chiyoda-ku, Tokyo 100-8331, Japan.

[39] Vicon, 5419 McConnell Ave., Los Angeles, CA 90066, USA.

[40] EOS Systems, Inc., 210-1847 W. Broadway, Vancouver, British Columbia, Canada V6J 1Y6.

Journal of Multifunctional Composites

journal homepage: http://jmc.destechpub.com

High-Fidelity Analyses of Composites at Various Length Scales with Discrete Damage Representations

Q. D. YANG[1,*], X. J. FANG[1,3], W. LIU[1] and B. N. COX[2]

[1]*Department of Mechanical & Aerospace Engineering, University of Miami, Coral Gables, Florida*
[2]*Teledyne Scientific Co LLC, Thousand Oaks, California*
[3]*Now with Global Engineering Materials, Inc. Princeton, New Jersey*

KEYWORDS

Finite element analysis
Composites
Cohesive models
Composite fracture

ABSTRACT

High-fidelity strength prediction of composites requires advanced numerical methods that can explicitly resolve the multiple damage processes and their nonlinear coupling at various scales. Nonlinear fracture models such as cohesive zone models are critical for damage descriptions and need to be properly embedded in a numerical framework so that correct coupling between different damage process zones can be guaranteed. This paper reviews the recent developments in advanced numerical methods that have the potential to address the important issue of progressive damage evolution in composites. Candidate FE-based numerical methods, including X-FEM, A-FEM, and phantom node methods, are reviewed and their capabilities in handling the multiple damage coupling in composites are assessed. Successful simulations of composites at various scales using the framework of A-FEM are presented and the numerical and material issues associated with these high-fidelity analyses are highlighted. Finally, we address the question of how to integrate all these different scale analyses into a single multiscale numerical framework by using the Arlequin coupling method.

1. INTRODUCTION

The use of advanced composites in lieu of traditional metals has been considerably expanded over the last couple of decades. Recent examples include the new commercial airplanes such as the Boeing 787 Dreamliner and the Airbus 380 and several other high profile military applications (Joint Strike Fighters of US Air Force and the DD-X multimission destroyer of US Navy, for example), all featuring high use of composite materials. Compared to structural metals, composites offer several key advantages such as significant weight savings, better reliability and durability, and lower manufacturing and maintenance costs.

However, owing to the highly heterogeneous nature of composites, predicting composite strength and durability directly from constituent material properties (i.e., matrix, fiber, and matrix-fiber interface properties) remains an unresolved challenge despite decades of intensive research. Many of the challenging issues are related to the difficulty of developing practicable formulations for dealing with materials containing complex material heterogeneity in the composites. Heterogeneity poses special problems with accurate prediction of local stress and strain fields, which can vary strongly with local material features; and with predicting cracks and localized damage bands, which can appear during damage evolution not only on the material boundaries, but also on other surfaces that cannot be specified *a priori*. Such highly heterogeneous materials present unique challenges that cannot be resolved by mainstream formulations of conventional materials/structures modeling.

One challenge is that the scale of material heterogeneity is on the same scale as that of the features of the structures, which negates the common strategy of homogenizing the material properties in simulations. In the past, many strength criteria based on various homogenization theories have been

*Corresponding author. Tel: 305-284-3221; Email: qdyang@miami.edu

doi:10.12783/issn.2168-4286/1.1/Yang

proposed. To name a few, Hashin's mechanism based criterion, Tsai-Wu criterion, and many continuum damage mechanics (CDM) based criteria such as in [1–4]. The success of these phenomenological criteria in assessing composite strength has been limited. A recent report on blind failure prediction of unidirectional polymer matrix composites (PMCs) revealed rather disturbing predictive capabilities of composite theories based on such strength criteria: virtually none of these homogenized composite theories can predict laminate strength satisfactorily under general loading conditions. Discrepancies among different theoretical predictions are more than 100% and up to 1500% in extreme cases [5].

The continuum damage mechanics (CDM) has also been used to better account for the progressive damage in composites. This approach considers the gradual reduction of load-bearing capability due to damage by introducing a damage parameter (or a tensor) into the material constitutive relation, which leads to irreversible damage evolution [2–4, 6,7]. The CDM based theories can be conveniently formulated into traditional finite element programs. But there are two inherent difficulties associated with this approach: (1) it cannot deal with highly concentrated crack-like damage, which is universal in composites; and (2) damage parameters calibrated from individual modes do not account for multiple damage mode coupling [8,9]. Linear elastic fracture mechanics (LEFM) and its computational form virtual crack closure technique (VCCT) have been used to study delamination cracks in laminated composites. But this method requires pre-existing cracks of finite size; therefore cannot deal with damage initiation from pristine materials or from traction-free composite edges [10].

Multiscale hierarchical modeling approach based on unit cell (UC) or representative volume element (RVE) analyses and followed by homogenization from one scale to next higher level scale (hierarchical model) has also been pursued to account for the progressive damage evolution on macroscopic composite properties [11–17]. But without explicit inclusion of the multiple damage coupling, the homogenization process will have to rely on either theoretical hypothesis or costly experimental program to calibrate key parameters (and in composites there are many of them!).

Another unresolved challenge, which is even more critical to composite structural safety and durability, is how to accurately account for the damage initiation and propagation and liken their detrimental effects on structural integrity in a quantifiable way. For example, a distinctive feature of composite failure is that it is a progressive process involving many types of damage initiating and propagating in a strongly coupled fashion until final, catastrophic failure occurs. In composite laminates, the damage manifests as ply cracking, delamination, fiber rupture (in tension), and kink band formation (in compression), etc. Strength criteria calibrated from individual damage modes cannot account for the nonlinear coupling of the many complex damage systems.

These challenges call for advanced numerical analysis platforms that can (1) efficiently deal with arbitrary material heterogeneity and possible progressive damage/debonding along material interfaces; (2) explicitly representing multiple damage modes and their nonlinear coupling during damage evolution. To achieve such high-fidelity analysis capability, several important numerical and material barriers need to be overcome: (1) full understanding of the mechanisms that control the initiation and propagation of these different types of damage and the length scales they operate on; (2) accurate accounting for the interaction among the co-evolving damage modes; (3) faithfully generating the multiple transverse cracks without knowing their locations *a priori.*

In this paper, we shall review and discuss the recent development of advanced numerical methods that can potentially meet the challenge of faithfully simulating the coupled multiple damages at various scales in composite materials.

2. NONLINEAR FRACTURE MODELS FOR COMPOSITE MATERIALS

Most damage modes in composites are in the form of crack-like entities and they interact with each other at various scales. When dealing with multiple crack interactions the nonlinear cohesive zone models (CZMs) are essential because they unify the processes of crack initiation and growth within a single physically-consistent model [18–27]. Most fracture process zones in PMCs are of size 0.1–1.0 mm. As will be seen shortly, the cohesive zone models allow for correct accounting of the nonlinear interaction of different fracture processes, while the linear elastic fracture mechanics (LEFM), due to its non-physical nature at the limit of small crack length, cannot guarantee such correct coupling [26,28–41].

Figure 1 gives an example that strongly supports this view point. In Figure 1(a) the load-displacement of a bonded polycarbonate (PC) specimen with a pre-existing notch with root angle 120° under three-point bending test is shown. The bond-line is at an angle of 30° to the specimen longitudinal direction and the fracture toughness along the bond-line is at least three times smaller than that of the PC. The LEFM, which simply compares the energy release rates (ERRs) ratio of the interface crack to its toughness (G_i/Γ_{ic}), against the ERR ratio of a local mode-I kink crack (G_k/Γ_{kc}) [42], predicts a complete interfacial crack propagation. However, repeated tests showed that kinking crack would form as shown in Figure 1(b). Only with cohesive zone modeling and with proper consideration of crack branching [43,44], were the fracture behavior and load-displacement curves correctly predicted [Figure 1(a) and 1(c)].

This example on bonded bulk PC specimens has a significant implication on composite fracture analyses because such crack kinking and coalescence processes are quite

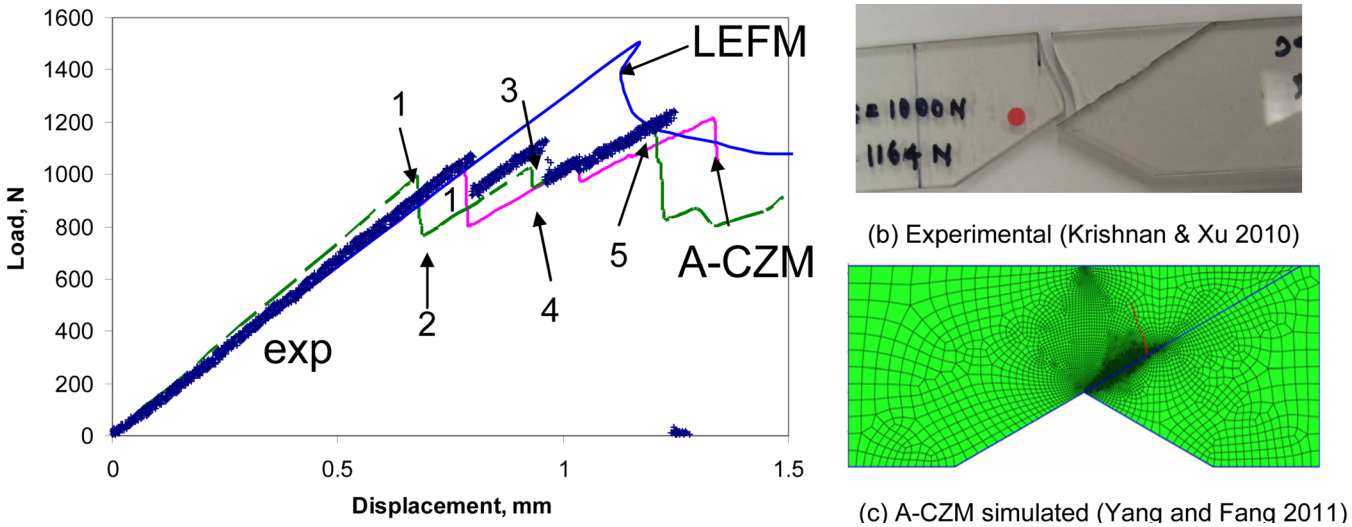

Figure 1. *(a) comparison of experimentally measured, CZM simulated, and LEFM predicted load-displacement curve of an adhesively-bonded, pre-notched PC specimen under three-point bending. (b) experimental observation of kinked crack; and (c) simulated kinking using nonlinear cohesive zone model.*

universal in laminated or textile composites. For example, crack jumping from one interface to another [44] involves both transverse crack kinking (from one interface into a transply) and crack merging (from transply into another interface). One of the important messages from this study is that, crack branching is a competition between two fracture process zones and careful numerical treatment is needed to ensure proper stress and deformation coupling between the two fracture process zones. The LEFM view that a kinking process is purely determined by the two competing ERR-toughness ratios is non-physical. Both the ERRs and cohesive strengths play an important role in determining whether an interface crack should kink into the neighbouring ply (a similar observation has also been made by Thouless and colleagues in [37,45]). The above successful simulation was done using an augmented cohesive element (ACZ) recently developed by Fang, Yang *et al.* [43], which will be introduced in more detail shortly. We note that the common practice of coupling X-FEs or A-FEs with *standard* CZ elements, as in many previous analyses cannot yield the correct response in this case [46,47].

While the cohesive zone models are excellent in describing the fracture processes in composites, they need to be incorporated into numerical platforms such as FE programs as special elements. This implementation has a major shortcoming because it needs a crack path to be known *a priori* so that the CZ elements can be properly defined in a numerical model. However, in composites such information is not available. Recent developments in advanced numerical methods for introducing arbitrary discontinuity in a continuum have made it possible to include most cohesive descriptions of major crack systems in structural models to account for the progressive damage. This will be reviewed in more detail in next section.

3. ADVANCED NUMERICAL METHODS FOR ARBITRARY CRACKING

3.1. PoU Finite Element Based X-FEM and PNM

Standard FEM cannot adequately describe a discontinuous displacement field within an element because the shape function for intra-element displacement interpolation is continuous. This can be seen from the standard elemental interpolation below,

$$\mathbf{u}^h(\mathbf{x}) = \sum_{i=1}^{n_e}\left(\sum_{j=1}^{m_e^i} N_j^i(\mathbf{x})\mathbf{u}_j^i\right) \tag{1}$$

where $\mathbf{u}^h(\mathbf{x})$ is the approximate displacement field. m_e^i is the number of nodes in element i and n_e is the total number of elements. Since the shape functions, $N_j^i(\mathbf{x})$, are continuous, such a formulation cannot describe intra-element discontinuities. Any discontinuities have to be arranged along inter-element boundaries. Recently, this difficulty has been successfully overcome by the partition-of-unit based finite element methods (PUFEM) [48,49], including the extended finite element method (X-FEM) [33,50–57] and the phantom node method (PNM) [46,58–61]. The seminal theory of PoU enables these methods to deal with discrete discontinuities (cracks and shear bands, etc) by adding extra nodal DoFs (as in X-FEM) or phantom nodes (as in PNM) within the finite element framework.

The X-FEM method treats a crack explicitly by introducing local enrichment to cracked elements. The local enrichment procedure employs the known asymptotic displacement field for crack tip regions and the generalized Heaviside function for the crack wake region. In such cases,

the displacement field can be expressed in a general form as follows

$$\mathbf{u}^h(\mathbf{x}) = \sum_j^n N_j(\mathbf{x})\mathbf{u}_j + \sum_{j=J_k} N_j(\mathbf{x})(d_{jk}H(\mathbf{x})) + \sum_{j=J_l} N_j(\mathbf{x})(\phi_{jl}p_l(\mathbf{x})) \tag{2}$$

where n is the total number of nodes; J_k is the node set that contains the nodes that are cut by traction free cracks; and J_l is the node set that influenced by a crack-tip singular displacement function (enrichment function) $p_l(\mathbf{x})$. $H(\mathbf{x})$ is the generalized Heaviside function. d_{jk} and ϕ_{jl} are the associated DoFs to $H(\mathbf{x})$ and $p_l(\mathbf{x})$, respectively. Note that in Equation (2) the $\mathbf{u}_j$ is *not* the complete nodal displacements, but the continuous part of it. The discontinuous part is accounted for by $d_{jk}H(\mathbf{x})$ and $\phi_{jl}p_l(\mathbf{x})$. For a moving cohesive crack, by introducing $H(\mathbf{x})$ and $p_l(\mathbf{x})$ as enrichment functions, Equation (2) can fully account for the discontinuous displacement field. Moreover, the discontinuity treatment is local in the sense that only those nodes whose support domains are cut by a crack need to be enriched.

An inconvenience associated with the X-FEM is that this enrichment process requires the addition of extra DoFs dynamically to these nodes, i.e., it requires nodal DoFs be adjustable depending on whether a node is being completely cut or not [50,53,60,62–65]. This makes it difficult to integrate such methods into standard finite element programs.

Although it has been demonstrated that the X-FEM is very efficient in dealing with arbitrary cracks in homogeneous materials, successful reports of X-FEM in analyzing arbitrarily cracking heterogeneous materials such as laminated or textile composites remain relatively few [53,54]. The major difficulty comes from the inconvenient handling of both the material heterogeneity and the crack coalescence/bifurcation within the X-FEM framework. First of all, analytical forms of enrichment functions for bi-material interfaces may not be readily available; secondly for multiple crack interaction the enrichment level will be unduly high and it quickly becomes intractable when crack number increases. Furthermore, tracing the evolution of complex fracture surfaces of multiple cracks in X-FEM or PNM quickly becomes extremely tedious and numerically burdensome because in such cases, there are no universal tracking algorithms that can judiciously assign different copies of DoFs or nodes to different cracks for complex crack configurations [66].

Another approach that requires less or no additional DoFs when treating intra-element discontinuities is the embedded discontinuity approach. This method follows the earlier research in smeared localization models or enhanced finite element methods [67–71] and it has been extended to account for discrete discontinuities by several research groups [72–80]. This approach seeks to enrich the elemental strain field by introducing displacement jumps with certain deformation modes (constant, linear, etc) in addition to the normal continuous displacement field. The coefficients of the deformation modes are considered as additional DoFs, which are either assigned to additional nodes as a global DoFs such as in [77], or fully condensed at elemental level as in [75,76]. As discussed above, adding extra nodes for each discontinuity may cause extra numerical burden for tracing multiple interactive cracks. The internal DoF condensation approach is therefore more appealing when dealing multiple crack interactions. However, this method suffers from possible stress locking because in many cases the assumed deformation modes are not permissible with the sub-domain elemental deformation modes. Furthermore, construction of an enhanced or augmented element with embedded multiple cracks to permit arbitrary crack merging and bifurcation becomes extremely tedious and difficult.

3.2. Augmented Finite Element Method (A-FEM)

An alternative numerical method that can also treat the arbitrary cracking problem but is not based on PoU method is the augmented finite element method (A-FEM) based on the seminal work of Hansbo and Hansbo [81,82]. The essence of this method is to use overlapping paired elements to describe a strong (e.g. a distinct crack) or weak (e.g. a bi-material interface) discontinuity in a physical element that is bisected by a discontinuity. One of the advantages of this method is that it uses only standard finite element (FE) shape functions (i.e., more compatible with existing FE programs) and it can conveniently consider both weak and strong discontinuities [83,84]. Based on this concept, Ling, Yang *et al.* [85] recently proposed an element with one or multiple copies of element nodes, to account for an arbitrary intra-element crack but otherwise remain a standard finite element. This so-called augmented finite element (A-FE) is fully compatible with existing FE programs and has been implemented into a commercial FE program as a user-defined element [44,86,87]. Below we briefly introduce the A-FEM formulation with embedded cohesive damage descriptions.

Referring to Figure 2(a), two bonded solid elements are assigned two sets of corner nodes (4-3-8-7-4′-3′-8′-7′ for the top element and 5-6-2-1-5′-6′-2′-1′ for the bottom element). For each A-FE, the first four nodes are physical nodes and the next four nodes with superscript " ′ " are virtual nodes. If the prescribed crack initiation criterion is met, one or both of the solid A-FEs will be augmented to allow for displacement discontinuity across the intra-element crack(s) [Figure 2(b)]. For example, the top A-FE will be augmented into two Mathematical Elements (MEs), i.e., ME1 with 4-3′-8′-7 and ME2 with 4′-3-8-7′. The two MEs may be connected by nonlinear spring elements or cohesive tractions for a cohesive crack. Both MEs employ standard FE shape functions for elemental displacement interpolation, i.e.,

$$\mathbf{u}_\alpha(\mathbf{x}) = \mathbf{N}_\alpha(\mathbf{x})\mathbf{d}_\alpha \tag{3}$$

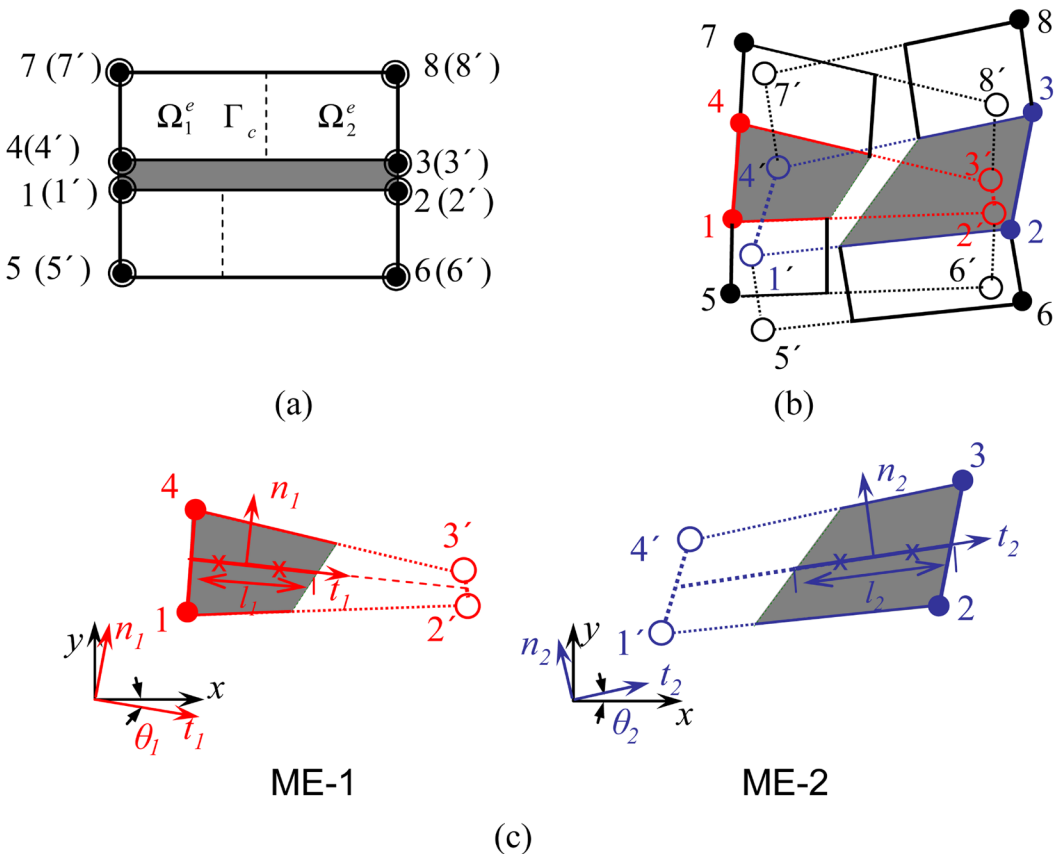

Figure 2. *(a) Two A-FEs bonded by a ACZ element before deformation, all with doubly assigned nodes for possible intra-element cracking. (b) after deformation (assuming both solid A-FEs are cracked, the ACZ will be augmented into two mathematical elements with their own local coordinates as shown in (c). For each ME, the two Gaussian points are indicated by the two symbols "×", which are located in the ME's active cohesive integration domain (shaded area). The interface is exaggerated for illustration purposes.*

where $\mathbf{N}(\mathbf{x})$ are the standard FE shape functions and $\mathbf{d}_\alpha$(α = 1 and 2) are the nodal displacements of ME-α. Equation (3) now allows for different displacement fields in physical domains Ω_1^e and Ω_2^e, which makes it possible to account for the discontinuous displacements (or displacement jumps) across the cohesive crack Γ_c. The displacement jumps across the crack in the A-FE can be simply obtained as:

$$\mathbf{w}(\mathbf{x}) = \mathbf{u}_2(\Gamma_c) - \mathbf{u}_1(\Gamma_c) = \mathbf{N}(\Gamma_c)(\mathbf{d}_2 - \mathbf{d}_1) \tag{4}$$

Here $\mathbf{w}(\mathbf{x})$ is the crack displacement in global coordinates. If the two MEs are connected by a cohesive crack, the displacement jumps are the cohesive opening displacement expressed in global coordinates. Denote by $\mathbf{R}$ the rotational matrix that links the global coordinates to the local coordinates defined by the solid crack direction and the direction normal to it, i.e.,

$$\mathbf{R} = \begin{bmatrix} \cos\theta & -\sin\theta \\ \sin\theta & \cos\theta \end{bmatrix}$$

with θ being the angle between crack line and global x-direction. The local displacement jumps can be written as

$$\boldsymbol{\delta} = \{\delta_t \quad \delta_n\}^T = \mathbf{R}\mathbf{w} \tag{5}$$

The superscript "T" denotes matrix transpose. δ_t and δ_n are the shear and normal crack displacements measured in local coordinates. It follows that the cohesive traction associated with the crack is

$$t' = \{\tau \quad \sigma\}^T = \{f_t(\boldsymbol{\delta}) \quad f_n(\boldsymbol{\delta})\}^T \tag{6}$$

where τ and σ are shear and tensile cohesive stresses in the local coordinates, respectively, and $f_t(\boldsymbol{\delta})$ and $f_n(\boldsymbol{\delta})$ are traction-separation relations for shear and opening mode, respectively.

Substituting the above displacement and cohesive tractions into the virtual work principle and following the standard procedure, the weak form of the equilibrium equations for static analysis can be derived [85],

$$\int_{\Omega_1^e} \mathbf{B}^T\boldsymbol{\sigma}\, d\Omega + \int_{\Gamma_c} \mathbf{N}^T\mathbf{t}\, d\Gamma = \int_{\Gamma_{F_1}} \mathbf{N}^T\mathbf{F}_1\, d\Gamma \tag{7a}$$

$$\int_{\Omega_2^e} \mathbf{B}^T\boldsymbol{\sigma}\, d\Omega + \int_{\Gamma_c} \mathbf{N}^T\mathbf{t}\, d\Gamma = \int_{\Gamma_{F_2}} \mathbf{N}^T\mathbf{F}_2\, d\Gamma \tag{7b}$$

where $\mathbf{B}$ is the strain matrix, $\boldsymbol{\sigma}$ is the stress matrix, $\mathbf{F}_\alpha$ (α =1 and 2) are the external forces applied on ME-α, and $\mathbf{t}(\boldsymbol{\delta}) = \mathbf{R}^T\mathbf{t}'(\boldsymbol{\delta})$ is the cohesive traction array. Since $\mathbf{t}(\boldsymbol{\delta})$ is typically nonlinear, Equation (7) typically needs to be linearized. But it is straightforward to linearize the equation using an incremental scheme. The incremental form of the equilibrium equations is:

$$\begin{bmatrix} \mathbf{K}_{11} & \mathbf{K}_{12} \\ \mathbf{K}_{21} & \mathbf{K}_{22} \end{bmatrix} \begin{Bmatrix} \Delta\mathbf{d}_1 \\ \Delta\mathbf{d}_2 \end{Bmatrix} = \begin{Bmatrix} \int_{\Gamma_{F_1}} \mathbf{N}^T\mathbf{F}_1 d\Gamma \\ \int_{\Gamma_{F_2}} \mathbf{N}^T\mathbf{F}_2 d\Gamma \end{Bmatrix} \tag{8a}$$

where $\Delta\mathbf{d}_\alpha$ and $\Delta\mathbf{F}_\alpha$ ($\alpha = 1, 2$) are incremental nodal displacements and external loads, respectively. The matrices $\mathbf{K}_{ij}$ are

$$\begin{aligned} \mathbf{K}_{11} &= \int_{\Omega_1^e} \mathbf{B}^T\mathbf{D}_1\mathbf{B} d\Omega + \int_{\Gamma_c} \mathbf{N}^T\mathbf{R}^T\mathbf{D}_{coh}\mathbf{R}\mathbf{N}\, d\Gamma \\ \mathbf{K}_{22} &= \int_{\Omega_2^e} \mathbf{B}^T\mathbf{D}_2\mathbf{B} d\Omega + \int_{\Gamma_c} \mathbf{N}^T\mathbf{R}^T\mathbf{D}_{coh}\mathbf{R}\mathbf{N}\, d\Gamma \\ \mathbf{K}_{12} &= \mathbf{K}_{21} = -\int_{\Gamma_c} \mathbf{N}^T\mathbf{R}^T\mathbf{D}_{coh}\mathbf{R}\mathbf{N}\, d\Gamma \end{aligned} \tag{8b}$$

where $\mathbf{D}_\alpha$ (α =1 and 2) are the stiffness matrices of the bonded solid elements and $\mathbf{D}_{\text{coh}}$ is the tangential stiffness matrix of the cohesive law (in local coordinates), i.e.,

$$\mathbf{D}_{coh} = \begin{bmatrix} \partial f_t / \partial \delta_t & \partial f_t / \partial \delta_n \\ \partial f_n / \partial \delta_t & \partial f_n / \partial \delta_n \end{bmatrix} \tag{9}$$

The above stiffness integration within a mathematical element is performed on the active material domain (i.e., Ω_1^e for ME1 or Ω_2^e for ME2), rather than on the entire elemental domain $\Omega^e (= \Omega_1^e \cup \Omega_2^e)$. This is important because it offers extra flexibility in handling material heterogeneity across the discontinuity: simply using different $\mathbf{D}_\alpha$ during the integration will achieve this purpose. Subdomain integration is needed for the stiffness integration of Equation (8) and we employed the triangularization scheme used in [50].

3.3. Augmented Cohesive Zone (ACZ) Element for Crack Bifurcation and Coalescence

The above A-FEM with embedded cohesive fracture description can effectively deal with multiple arbitrary cracks within any lamina (i.e., transply cracks). However, in laminated PMCs the interface delamination is often strongly coupled with the transply cracks. Such strongly coupled process zones need special numerical treatment to guarantee correct stress coupling during crack bifurcation and coalescence. If traditional cohesive element were used together with the A-FEM or X-FEM, the local stress transfer during the nonlinear interaction will be in significant error. The reason is that, although a traditional cohesive element can effectively account for the displacement discontinuity across the interface, it cannot resolve the displacement discontinuity within the element along the interface introduced by the cracking of its abutting solid elements [43]. Fortunately, with the idea of augmented FEM, it is possible to develop augment cohesive elements (ACZs) that can allow for arbitrary separation according to the cracking configuration in the abutting solid elements to achieve accurate load transfer.

The ACZ element can be defined with two sets of corner nodes shared with the abutting solid A-FEs [e.g. 1-2-3-4-1′-2′-3′-4′ as shown in Figure 2(a)]. If neither of the solid A-FEs is cracked, all the virtual nodes are tied with the corresponding real nodes and both the solid A-FEs and ACZ element behave like standard FE and traditional CZ element. However, if either or both of the abutting solid elements are cracked and the crack tip(s) reaches the interface, the cohesive element will be augmented accordingly. Figure 2(b) shows the augmented configuration when both solid A-FEs have cracked. In this case, the ACZ can be augmented into two MEs for cohesive stress integration with 1-2′-3′-4 for ME-1 and 1′-2-3-4′ for ME-2 as shown in Figure 2(b) and 2(c). The respective cohesive stress integration domains for the MEs are shown in the figure by shaded areas.

For each ME-α (α = 1 or 2), a local coordinate system can be established by defining the tangential direction ($\mathbf{t}_\alpha$) along the line that connects the mid-points of edge 14 and 2′3′ for ME-1, or, that connects the mid-points of 1′4′ and 23 for ME-2, as shown in Figure 2(c). The respective normal directions ($\mathbf{n}_\alpha$) are perpendicular to $\mathbf{t}_\alpha$. Thus the rotational matrix for each ME, can be obtained as $\mathbf{Q}_{i\alpha} = Diag\{\mathbf{R}_{i\alpha}, \mathbf{R}_{i\alpha}, \mathbf{R}_{i\alpha}, \mathbf{R}_{i\alpha}\}$. Here $\mathbf{R}_{i\alpha}$ is computed using the rotation angle θ_α of cohesive ME-α as shown in Figure 2(c). Note that from here on we shall denote all quantities associated with the ACZ interface element with subscript "*i*".

The nodal displacements of ME-α in local coordinates can be obtained as:

$$\mathbf{d}'_{i\alpha} = \mathbf{Q}_{i\alpha}\mathbf{d}_{i\alpha} \tag{10}$$

The local displacement jumps (crack displacements) across the ME-α can be obtained as:

$$\boldsymbol{\delta}_{i\alpha} = \{\delta_t \quad \delta_n\}^T_{i\alpha} = \mathbf{N}\mathbf{d}'_{i\alpha} = \mathbf{N}\mathbf{Q}_{i\alpha}\mathbf{d}_{i\alpha} \tag{11}$$

where

$$\mathbf{N} = \begin{bmatrix} -N_1 & 0 & -N_2 & 0 & N_2 & 0 & N_1 & 0 \\ 0 & -N_1 & 0 & -N_2 & 0 & N_2 & 0 & N_1 \end{bmatrix}_\alpha$$

is the interpolation matrix consisting of 1D standard nodal shape functions, i.e., $N_1 = (1 - \xi)/2$ and $N_2 = (1 + \xi)/2$ with $\xi \in [-1,1]$.

The incremental form of the interface cohesive stresses

can be obtained from interfacial cohesive laws, $g_{ti}(\boldsymbol{\delta}_i)$ and $g_{ni}(\boldsymbol{\delta}_i)$, as follows

$$\Delta \mathbf{t}'_{i\alpha} = \mathbf{D}_{i\ \mathrm{coh}} \Delta \boldsymbol{\delta}'_{i\alpha} = \mathbf{D}_{i\ \mathrm{coh}} \mathbf{N} \mathbf{Q}_{i\alpha} \Delta \mathbf{d}_{\ \alpha i} \tag{12}$$

where $\mathbf{D}_{i\ \mathrm{coh}}$ is the tangential stiffness matrix of the interface cohesive law (in local coordinates), which can be obtained from Equation (9) by replacing $f_t(\boldsymbol{\delta})$ and $f_n(\boldsymbol{\delta})$ with interface cohesive laws, $g_{ti}(\boldsymbol{\delta}_i)$ and $g_{ni}(\boldsymbol{\delta}_i)$, respectively.

From the principle of virtual work the equilibrium equation of the ME-α in incremental form can be derived straightforwardly as below:

$$\left(\int_{l_\alpha} \mathbf{Q}_{i\alpha}^T \mathbf{N}^T \mathbf{D}_{i\ \mathrm{coh}} \mathbf{N} \mathbf{Q}_{i\alpha} dl \right) \Delta \mathbf{d}_{i\alpha} = \Delta \mathbf{F}_{i\alpha} \tag{13}$$

The integral in the parenthesis "()" is the tangential stiffness of the ME-α. In this study, Gaussian integration is used. For each ME-α, the two Gaussian points are located in the active cohesive integration segment only and they are indicated in Figure 2(c) by symbol "×".

The 3D version of the A-CZ has also been developed and implemented into the ABAQUS (6.9) as a user-defined element, which works together with the A-FEM for solving the arbitrary cracking problems in composites.

4. A-FEM SIMULATION OF COMPOSITES AT VARIOUS LENGTH SCALES

The A-FEM and ACZ element described above enables detailed composite analyses at various scales. In this section, we shall introduce several recent successful examples. Discussions will be focused on numerical and material issues that need to be addressed regarding the nonlinear fracture processes and their coupling behavior at different length scales.

4.1. Structural Scale Damage Coupling

We first analyze the progressive damage evolution in the double notch tension specimen reported in [88]. The experimentally observed damages at three different load levels are shown in Figure 3. When this double-notched $(0/90)_s$ laminate was loaded at about 25% of the final load, a splitting crack in 0°-ply and a transverse crack in 90°-ply were already formed at the notch-root [Figure 3(a)]. As the load increased, the splitting crack propagated gradually towards the loading boundary and was accompanied by the generation of many transverse cracks [vertical lines in Figure 3(b)]. Meanwhile, delamination cracks were also formed around the splitting cracks in a self-similar fashion (dark triangular regions in Figures 3(b) and 3(c). The delaminating shape and transverse crack density are results of complex interplay of the different types of cohesive damage while they evolve [87]. It is possible to model the splits and transverse cracks using CDM based material degradation model. However, in doing so, the evolving nonlinear interaction between the ply cracks and delamination cannot be followed. As a result, the delamination shape and area, as well as the splitting crack growth rate as a function of applied stress would be inaccurate [28,89].

The simulation was done at coupon level with each ply modeled by plane-stress A-FEM elements to allow for multiple ply cracks and 3D ACZ elements for delamination and correct coupling. All possible damage modes of importance to structural integrity, i.e., splitting, transply cracking, interply delamination, and fiber rupture, were included in a single structural model as shown in Figure 4(b). In addition, continuous plasticity that represents irreversible damage occurring in small volumes of the polymer matrix (at micron scales) was included.

A detailed account of how the elastic/plastic properties and cohesive fracture properties were calibrated from literature data has been given in [87], where the excellent mesh independent results were also demonstrated for specimen compliance, splitting crack growth rate, transverse crack spacing, and delamination shape and area.

A direct comparison of the simulated and experimental results is summarized in Figure 4. The A-FEM simulation successfully reproduces all the important features observed ex-

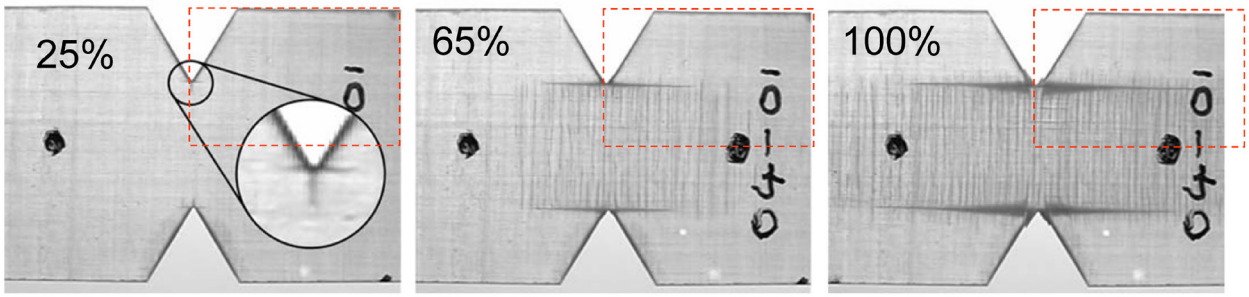

Figure 3. *X-ray radiography reveals damage mechanisms viewed through the ply stack in a double-notch tension specimen with symmetric orthogonal ply stack ($(0/90)_s$) [88].*

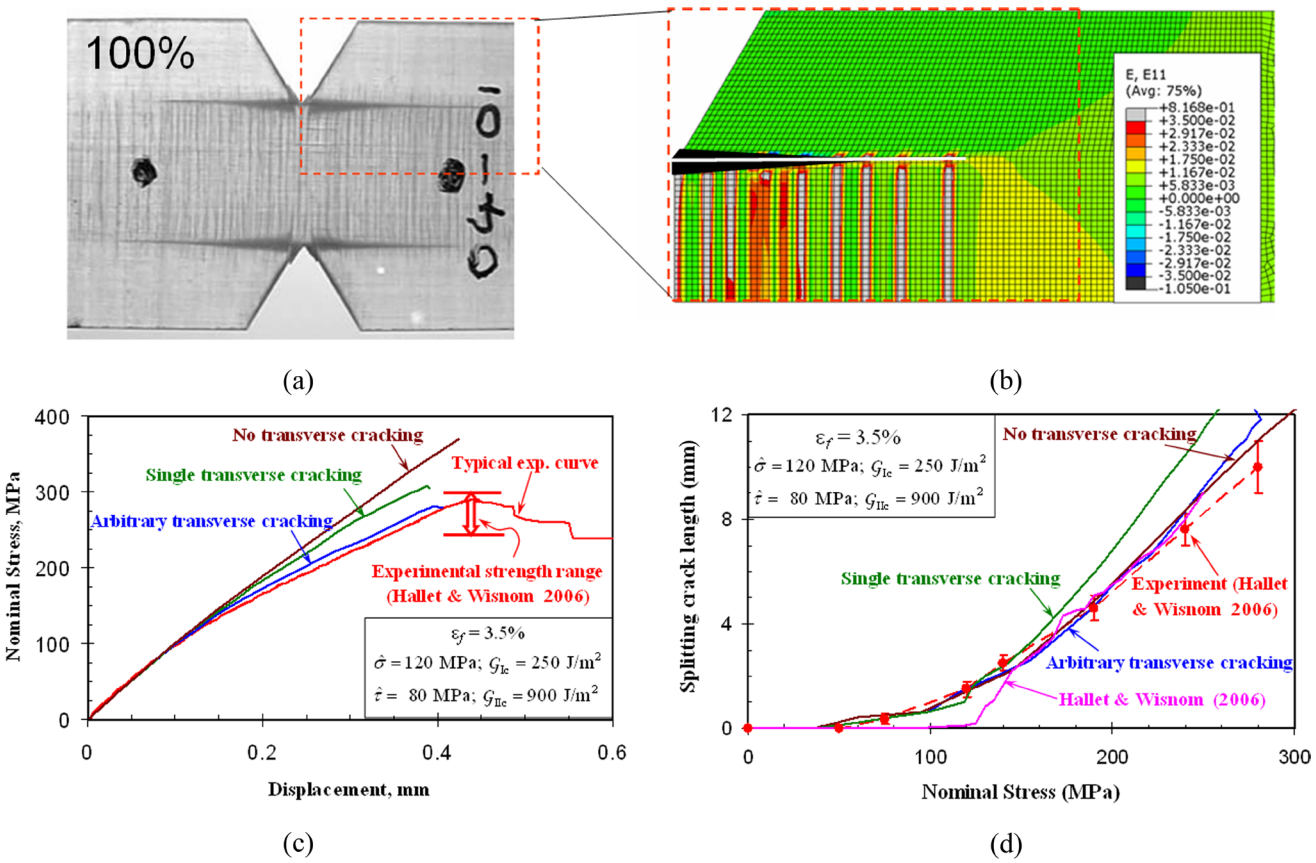

Figure 4. *(a) Image taken immediately before specimen failure with clearly coupled splitting cracks, transply cracks, and wedge-shaped delamination zones. (b) predicted damages closely follow the experimentally observed damage pattern. (c) comparison of measured and predicted load-displacement data; and (d) comparison of splitting crack length as a function of applied stress [87].*

perimentally on the three cracking systems. The self-similar delamination zone angle is predicted to be 8°, in agreement with the experimental value of 7°–10°. The splitting crack growth rate (as a function of applied stress), and multiple transverse cracks and their spacing are also well captured. In particular, the gradual decrease of specimen stiffness due to multiple transverse cracking in the load-displacement curve is accurately captured.

We emphasize that, to achieve this unprecedented level of fidelity it is critical to include the multiple transverse cracking in the simulation. Had this not been included, the predicted delamination area and shape would be significantly different from the experiment [c.f. the curve in Figure 4(c) labeled as "no transverse cracking"]. Another important finding is that the continuous shear plasticity must be included. Otherwise the delamination crack propagation rate and shape would be in significant error. Evidence of crack-tip shear nonlinearity has recently been confirmed by μCT data of similar specimens [90].

In the above structural level simulations, it is implicitly assumed that, once a transverse crack or splitting crack is initiated, it immediately propagates as a steady-state crack, because the in-situ strength is derived from steady-state crack analysis based on LEFM and the assumption that the interface remains fully bonded (tunneling or channeling crack mode) [91,92]. Judging from the simulated results, this assumption appears valid at least for the current analysis. However, whether this should be true for other composites remains a question. This question can be answered from a more detailed analysis at a smaller scale, which will be described as follows.

4.2. Damage Coupling at Sublaminar Scale

To focus on coupling between delamination and an individual transply crack, the sublaminar level model shown in Figure 5 was studied. The transverse crack is bounded in one direction by the ply thickness, but extends along the fiber direction.

Simulations revealed that tunneling crack initiation can occur either from an arbitrarily located small flaw as a penny-shaped crack or from a free edge. However, even if initiation occurs first from the flaw, the cohesive crack at the free edge initiates before the penny-shaped crack reaches the ply interfaces; then the two quickly link up and propagate in unison towards the interfaces and thus form a mature tunneling crack [93]. Depending on the mode-II to mode-I toughness ratio and cohesive strength, there may be two tunneling

modes. For PMCs, which typically have mode II toughness several times larger than mode I toughness, transply cracks will not trigger significant local delamination during their initiation and propagation (as channeling or tunneling cracks). Rather, delamination occurs after transply cracking processes are completed and upon further loading, which is indicative from the experimental images of Figure 1. In such condition, the transply crack initiation stress is only 5% less than the steady-state propagation stress [93].

LEFM is inaccurate in predicting the stress for initiating the delamination crack that is subsequently triggered by the transverse crack, which depends on both the toughness ratio and cohesive strength ratio and is heavily influenced by the presence of a free edge [93]. This again highlights the need of using of nonlinear cohesive models for delamination of composites, especially in cases that there are no large-sized preexisting delamination cracks.

The other mode, i.e., the unstable tunneling with delamination mode, is not commonly seen in typical PMCs, but observations have been reported of analogous cracks in other material systems such as in thin films bonded to thick substrates [94–96]. Direct observation of the tunneling mode of propagation has not been made for transverse microcracks in laminates, which calls for new experimental observation techniques.

The question that naturally follows from this sublaminar model analysis is whether one can predict fracture toughness and cohesive strength based on the properties of the matrix, fibers, and fiber-matrix interface? To answer this, one increases modeling resolution to the microscopic scale, with explicit representation of matrix, fibers and the interfaces that bond them. Such an analysis is given below.

4.3. Microscopic Fiber/Matrix Interaction

At the microscopic level (single fiber scale), stochastic matrix and fiber properties need to be considered. A-FEM is well positioned to address this issue. Figure 6 gives an example of a failure analysis of a representative volume containing 28 randomly distributed fibers embedded in a matrix (fiber volume 50%) under uniaxial tension. A-FEM elements were used for the matrix and ACZ elements were used to join the matrix domain and elastic fibers.

The simulation reveals multiple cracking in the matrix domain before a final cracking path is chosen by connecting microcracks in the matrix with fiber-matrix interface debonds (inset of Figure 6). It is also found that fiber position, which is a random variable due to the manufacturing process, significantly influences the final cracking path and is responsible for the observed sample-to-sample variation of measured toughness, which is typically 10–15%.

The nominal stress-separation curves of several such simulations are given in Figure 6. In this case, the assigned toughness and strength are: for the matrix, 200 J/m^2 and 100 MPa; for interfaces, 100 J/m^2 and 60 MPa. The predicted peak strength (cohesive strength) of 80 MPa is bounded by the matrix and interface strength and is relatively insensitive to fiber randomness. However, the derived fracture toughness, i.e., the energy dissipation divided by the nominal crack area, predicted to be 180 ± 20 J/m^2, is significantly influenced by fiber positioning because different fiber organization leads to significantly different final cracking paths. Thus the microscopic analysis at least offers the possibility of predicting nonlinear cohesive laws that can be used at the sublaminar or structural level.

However, note that the fidelity of such microscopic analyses depends strongly on accurate input for the material properties of the matrix, fibers, and interfaces at the microscopic scale, which is not easily obtained. In the future, this problem may benefit from nano or molecular dynamics analyses to determine nanoscopic or sub-microscopic material behavior.

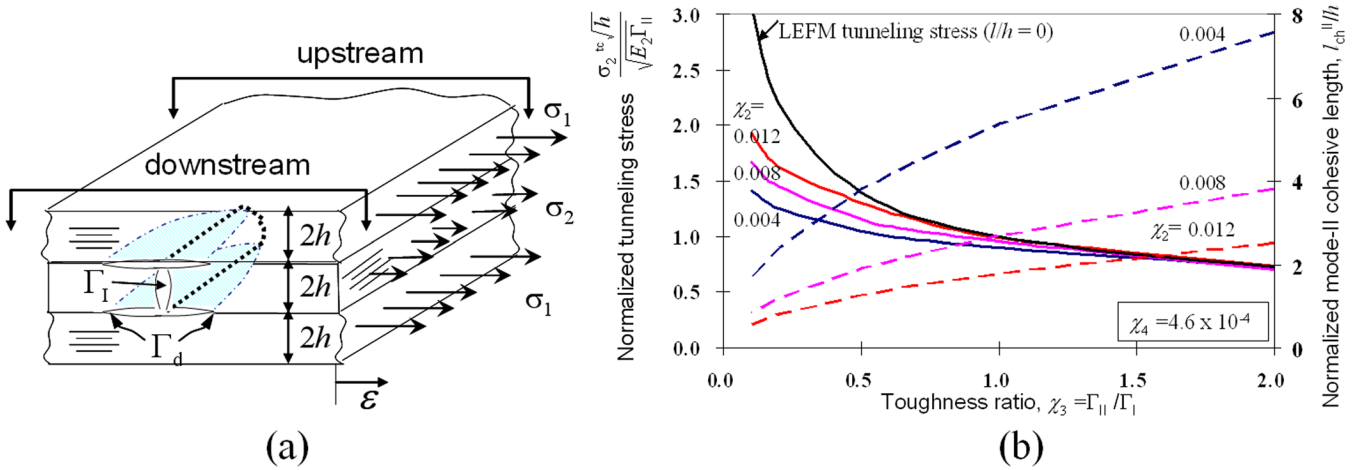

Figure 5. *(a) A (0/90/0) laminate with a tunneling crack that is accompanied by four delamination cracks. (b) Numerically determined tunneling initiation stress (left Y-axis) and delamination process zone size (right Y-axis) as functions of toughness ratio Γ_{II}/Γ_I [93].*

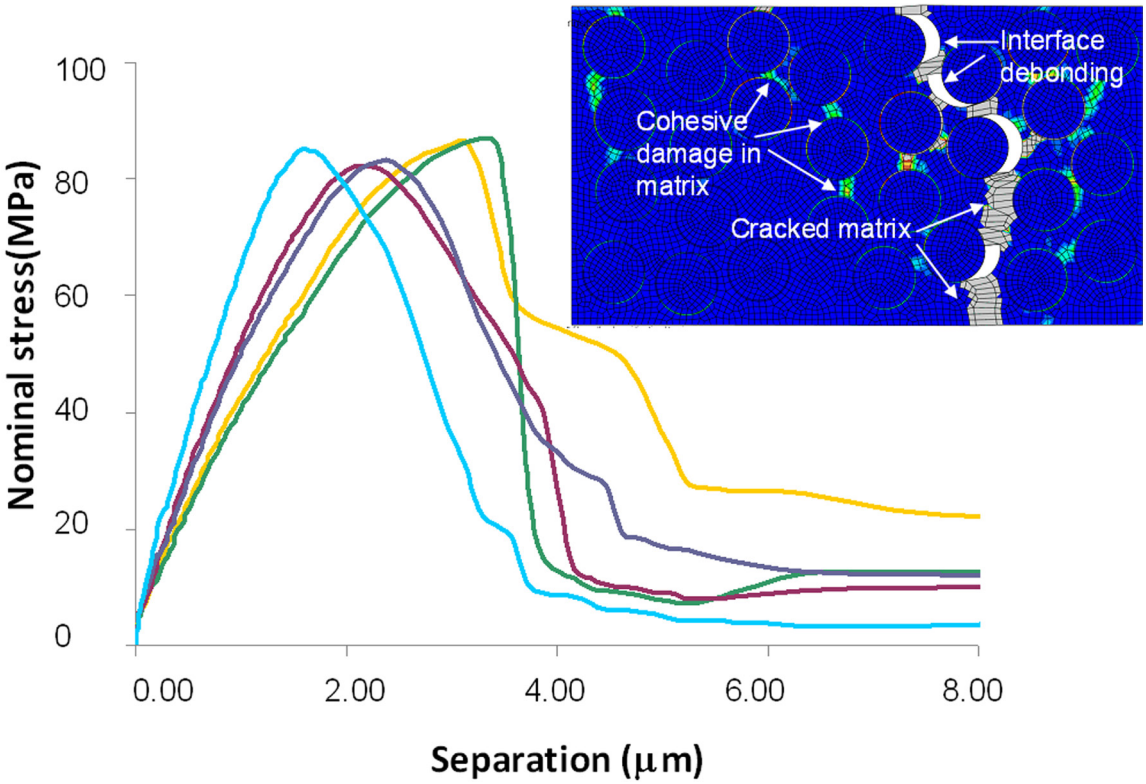

Figure 6. *A-FEM simulated progressive failure of a microscopic representative volume element with explicit consideration of matrix cracking, fiber/matrix debonding, and randomly located fibers. The five nominal stress vs. separation curves are different runs with randomly assigned fiber organizations. The inset shows the multiple cohesive damage in matrix and the final cracking path of connected microcracks in matrix and fiber/matrix interfaces [97].*

5. FURTHER DISCUSSIONS—SEAMLESS COUPLING AMONG VARIOUS SCALES

It is desired to unify the different scale analyses into a single multiscale framework so that the structural level (global) deformation and those local damage processes are seamlessly coupled. Given sufficient computational resources, the A-FEM with cohesive damage descriptions, facilitated with ACZ for handling material boundaries, is inherently multiscale and can achieve faithful global-local coupling. Nevertheless current computational power limits our analysis at coupon level structural scales.

To improve numerical efficiency, one possibility is to develop multiscale hierarchical modeling approaches based on unit cell (UC) or representative volume element (RVE) analyses and followed by homogenization from one scale to next higher level scale (hierarchical model), such as those in [11–17]. However, as emphasized previously any attempt to homogenize discrete damage processes leads to loss of direct damage coupling, which has been shown critical for composite strength analyses (section 4.1).

A recent report on two scale modeling using X-FEM and level set functions shed a promising light [53]. It has been demonstrated in that paper that it is possible to use two sets of meshes, a coarse mesh for structural responses and a fine mesh allowing for microscopic details of material heterogeneity and localized damage, to achieve global-local coupling with much reduced computational cost while maintaining reasonable simulation fidelity. The two sets of meshes were coupled through a variational multiscale method (VMM) which guarantees energy balance across the coarse-fine mesh boundaries, but the displacements were enforced in a weak sense. While this method guarantees global energy consistency through the variational analysis, local energy expenditure among different types of damage at different scales, especially when they coalesce into each other, is not guaranteed.

On the A-FEM front, recent breakthroughs in the author's group [98] have been made it possible for the new A-FEM to account for multiple, arbitrary intra-elemental discontinuities without the need for additional virtual nodes or nodal DoFs. This new A-FEM is especially convenient when dealing with the material heterogeneities (and the cracking issues associated with it) in complex materials such as textile composites.

Figure 7 shows an example that demonstrates the new A-FEM's excellent capability in dealing with highly heterogeneous textile composites. A cross-section of a real 3D interlock textile composite wherein the geometries and allocations of weft tows, warp tows and matrix pockets were

replicated using real specimen data obtained from μCT characterization. Thus statistics of material heterogeneities are naturally built in. The 2D A-FEM simulated results as compared to the experimental observations and measurements are shown in Figure 7. Despite the simulation is 2D while the actual specimen is 3D, the new A-FEM is able to capture all the major damage modes [see legend in Figure 7(c)]. The crack locations are also well predicted. The nominal stress-strain curve follows the experimental data closely up to the point when first major transverse cracking event occur [crack 2 and 4 in Figure 7(a) and 7(b)]. After that the curves are different because the 2D model cannot realistically account for the 3D interlock effects in 3D textiles. The example clearly demonstrates the great potential of the new A-FEM. It also highlights the urgent need of 3D A-FEM development which is an on-going research task.

Since the A-FEM is fully compatible with existing FE programs, it is very convenient to connect A-FEs with other multiscale methods such as the Arlequin method [99] to directly couple critical areas (with high-resolution A-FEM & ACZ elements) to non-critical areas (with low resolution regular elements). The most attractive feature of the Arlequin method is that it can couple two different mechanical states accurately and the numerical coupling cost is minimal. We have recently developed a suite of Arlequin coupling elements, including 2D-2D, 1D-2D, 1D-3D, 2D-3D, and shell-3D. These elements are compatible with commercial package ABAQUS [100].

An example of simulated four-point shear/bend test with A-FEM and Arlequin coupling is given in Figure 8. In Figure 8(a) the finer mesh region was A-FEs while the coarse mesh region is standard FEs. The two regions were coupled with two layers of Arlequin coupling elements. With such set up, the simulated load vs. crack mouth sliding displacement were correctly captured with a saving of computational time of 60% as compared to the case of using fine mesh only. Further study on adapting the method into a two-scale or even multiscale modeling approach is currently on-going.

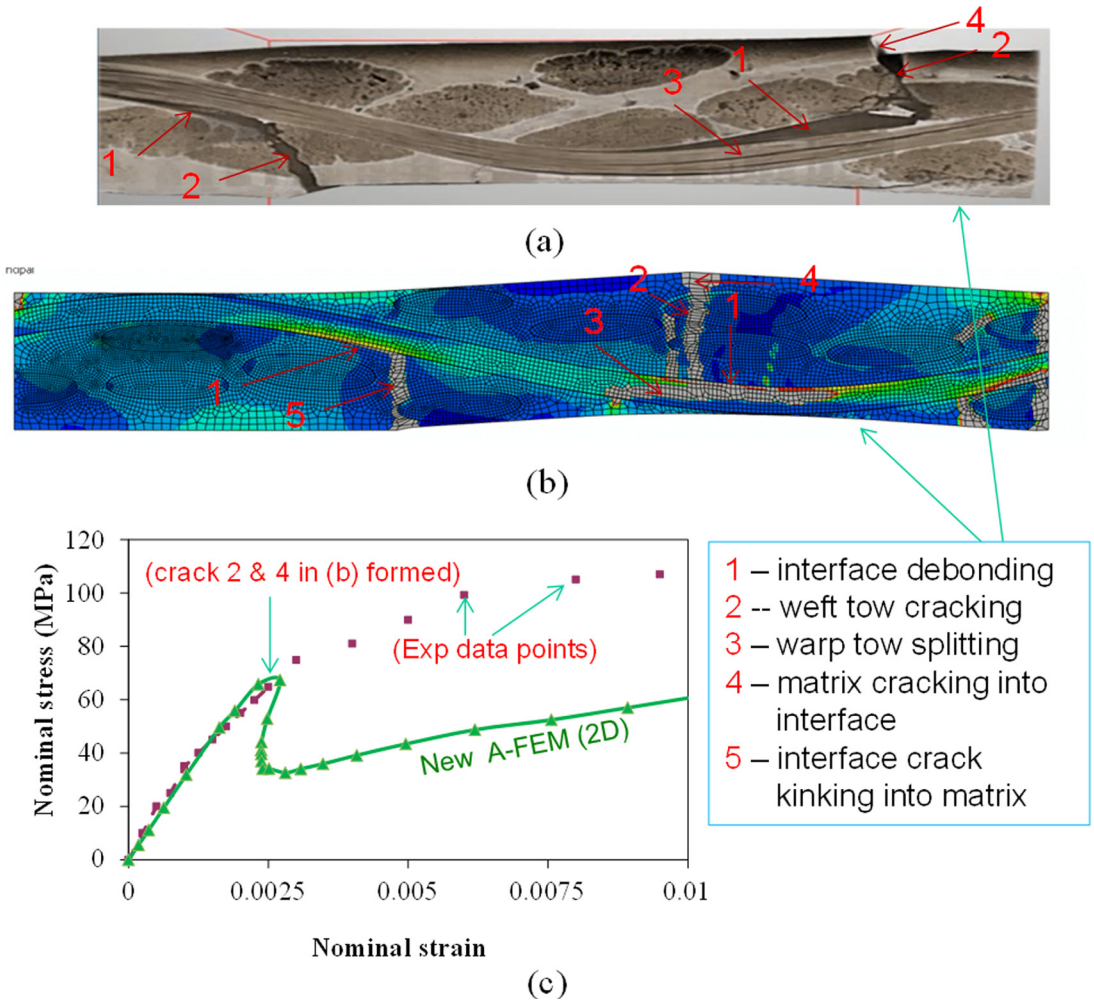

Figure 7. *(a) Experimentally observed damages (2D cross-sectional view), (b) the 2D A-FEM predicted damages capturing all the damage modes observed in the experiments, and (c) predicted nominal stress-strain curve showing the 2D A-FEM in excellent agreement with measured curve up to first major cracking events.*

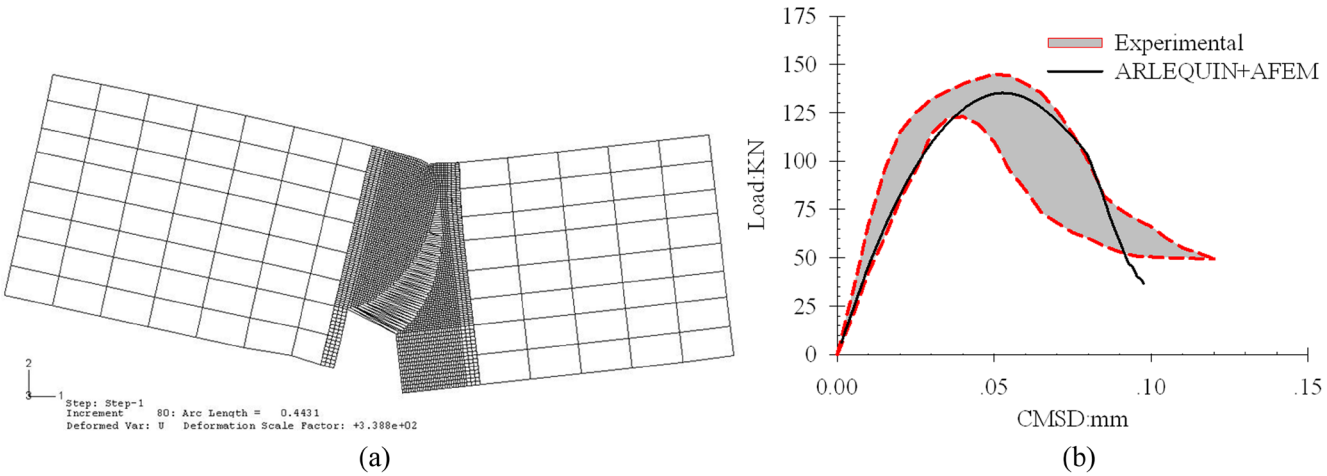

Figure 8. *(a) A-FEM simulated fracture of a 4-point shear test of a notched specimen. (b) comparison A-FEM predicted and experimentally measured load vs. crack-mouth shear displacement (CMSD) curve.*

6. CONCLUDING REMARKS

In this paper, the necessity of explicitly addressing multiple damage processes and their nonlinearly coupled evolution at various length scales to achieve high-fidelity strength prediction of composite materials has been highlighted. This requires advanced numerical simulation frameworks that can (1) explicitly account for major damage modes and their nonlinear coupling; (2) seamlessly integrate nonlinear material failure modes such as CZMs at different length scales; and (3) adequately account for global-local coupling so that direct influence functions between local damage events and global structural integrity can be established.

Recent developments in advanced numerical methods that can meet these challenges, including the X-FEM framework, phantom node method, and the A-FEM framework, have been reviewed. All these methods can adequately handle the arbitrary crack generation and propagation which is critical to describe discrete damage in composites. However, A-FEM has the advantage of easy handling of material heterogeneity and the nonlinear coupling of multiple cracking systems. In particular, the augmentation method can apply to cohesive interface elements so that they can correctly resolve the stress coupling when cracks merge or bifurcate. Detailed formulations of an 8-node A-FE and the associated A-CZ element have been given. Successful application of this framework to composite failure analyses on three distinct length scales, i.e., structural level, sublaminar level, and microscopic level, has been demonstrated. The associated numerical and length scale issues have been discussed. Finally, the Arlequin method that has the potential to establish a tightly coupled multiscale approach to adequately account for global-local coupling has been reviewed. This method can potentially lead to the establishment of direct influence functions between local damage events and global structural integrity.

ACKNOWLEDGEMENTS

This work was supported by the Air Force Office of Scientific Research (Dr. Ali Sayir) and NASA (Dr. Anthony Calomino) under the National Hypersonics Science Center for Materials and Structures (AFOSR Contract No. FA9550-09-1-0477). QDY also wishes to acknowledge the support by the National Science Foundation under Grant No. CMMI-0922825.

REFERENCES

[1] McCartney, L.N., Physically based damage models for laminated composites. *Journal of Materials: Design and Applications,* 2003. 217(3): p. 163–199.

[2] Chang, K.Y., S. Liu, and F.K. Chang, Damage Tolerance of Laminated Composites Containing an Open Hole and Subjected to Tensile Loadings. *Journal of Composite Materials,* 1991. 25: p. 274–301.

[3] Shokrieh, M.M. and L.B. Lessard, Progressive Fatigue Damage Modeling of Composite Materials, Part I: Modeling. *Journal of Composite Materials,* 2000. 34(13): p. 1056–1080.

[4] Chaboche, J.L., P.M. Lesne, and J.F. Maire, Continumm Damage Mechanics, Anisotropy and Damage Deactivation for Brittle Materials Like Concrete and Ceramic Composites. *International Journal of Damage Mechanics,* 1995. 4(1): p. 5–22. http://dx.doi.org/10.1177/105678959500400102.

[5] Kaddorur, A.S., M.J. Hinton, and P.D. Soden, A comparison of the predictive capabilities of current failure theories for composite laminates: Additional contributions. *Composites Science and Technology,* 2004. 64: p. 449–476. http://dx.doi.org/10.1016/S0266-3538(03)00226-4.

[6] de Borst, R., *et al.*, On gradient-enhanced damage and plasticity models for failure in quasi-brittle and frictional materials. *Computational Mechanics,* 1995. 17(1–2): p. 130–141. http://dx.doi.org/10.1007/BF00356485.

[7] Chaboche, J.L., R. Girard, and P. Levasseur, On the interface debonding models. *Int. J. Damage MEch.,* 1997. 6: p. 220–256. http://dx.doi.org/10.1177/105678959700600302.

[8] Talreja, R., Mulitscale modeling in damage mechanics of composite materials. *Journal of Material Science,* 2006. 41: p. 6800–6812. http://dx.doi.org/10.1007/s10853-006-0210-9.

[9] Van de Meer, F.P. and L.J. Sluys, Continuum Models for the

Analysis of Progressive Failure in Composite Laminates. *Journal of Composite Materials,* 2009. 43: p. 2131–2156. http://dx.doi.org/10.1177/0021998309343054.

[10] Tay, T.-E., Characterization and Analysis of Delamination Fracture in Composites: An Overview of Developments from 1990 to 2001. *Applied Mechanics Review,* 2003. 56(1): p. 1–32. http://dx.doi.org/10.1115/1.1504848.

[11] Oden, J.T., K. Vemaganti, and N. Moes, Hierarchical modeling of hetrogeneous solids. *Computer Methods in Applied Mechanics and Engineering,* 1999. 172: p. 3–25. http://dx.doi.org/10.1016/S0045-7825(98)00224-2.

[12] Tang, X.D., *et al.*, Progressive failure analysis of 2 × 2 briaded composites exhibiting multiscale heterogeneity. *Composite Science and Technology,* 2006. 66: p. 2580–2590. http://dx.doi.org/10.1016/j.compscitech.2006.01.026.

[13] Inglis, H.M., *et al.*, Cohesive modeling of dewetting in particulate composites: micromechanics vs. multiscale finite element analysis. *Mechanics of Materials,* 2007. 39: p. 580–595. http://dx.doi.org/10.1016/j.mechmat.2006.08.008.

[14] Fish, J. and A. Ghouali, Multiscale analysis sensitivity analysis for composite materials. *International Journal for Numerical Methods in Engineering,* 2001. 50: p. 1501–1520. http://dx.doi.org/10.1002/1097-0207(20010228)50:6<1501::AID-NME84>3.0.CO;2-0.

[15] Reddy, J.N., *Multiscale Computational Model for Predicting Damage Evolution in Visoelastic Composites Subjected to Impact Loading,* 2005. p. 31.

[16] Gonzalez, C. and J. LLorca, Multiscale Modeling of fracture in fiber-reinforced composites. *Acta Materialia,* 2006. 54: p. 4171–4181. http://dx.doi.org/10.1016/j.actamat.2006.05.007.

[17] Ladeveze, P., Multiscale Modelling and computational strategies. *International Journal for Numerical Methods in Engineering,* 2004. 60: p. 233–253. http://dx.doi.org/10.1002/nme.960.

[18] Barenblatt, G.I., *The mathematical theory of equilibrium cracks in brittle fracture, in Advances in Applied Mechanics,* H.L. Dryden and T. Von Karman, Editors. 1962, Academic Press. p. 55–129.

[19] Dugdale, D.S., Yielding in steel sheets containing slits. *Journal of the Mechanics and Physics of Solids,* 1960. 8: p. 100–104. http://dx.doi.org/10.1016/0022-5096(60)90013-2.

[20] Hillerborg, A., M. Modéer, and P.E. Peterson, Analysis of crack propagation and crack growth in concrete by means of fracture mechanics and finite elements. *Cement and Concrete Research,* 1976. 6: p. 773–782. http://dx.doi.org/10.1016/0008-8846(76)90007-7.

[21] Thouless, M.D. and Q.D. Yang, A parametric study of the peel test. *International Journal of Adhesion & Adhesives,* 2008. 28: p. 176–184. http://dx.doi.org/10.1016/j.ijadhadh.2007.06.006.

[22] Yang, Q.D. and M.D. Thouless, Mixed Mode Fracture of Plastically-Deforming Adhesive Joints. *International Journal of Fracture,* 2001. 110: p. 175–187. http://dx.doi.org/10.1023/A:1010869706996.

[23] Xu, X.P. and A. Needleman, Numerical simulations of fast crack growth in brittle solids. *Journal of the Mechanics and Physics of Solids,* 1994. 42(9): p. 1397–1434. http://dx.doi.org/10.1016/0022-5096(94)90003-5.

[24] Hutchinson, J.W. and A.G. Evans, Mechanics of Materials: Top-Down Approaches to Fracture. *Acta Materialia,* 2000. 48: p. 125–135. http://dx.doi.org/10.1016/S1359-6454(99)00291-8.

[25] Yang, Q.D., A.J. Rosakis, and B.N. Cox, Dynamic Fiber Sliding Along Debonded Frictional Interface. *Proc. Roy. Soc. A,* 2006. 462(1081–1106). http://dx.doi.org/10.1098/rspa.2005.1602.

[26] Song, S.J. and A.M. Waas, Energy-based mechanical model for mixed mode failure of laminated composites. *AIAA Journal,* 1995. 33: p. 739–745. http://dx.doi.org/10.2514/3.12639.

[27] Turon, A., *et al.*, A damage model for the simulation of delamination in advanced composites under variable-mode loading. *Mechanics of Materials,* 2006. 38: p. 1072–1089. http://dx.doi.org/10.1016/j.mechmat.2005.10.003.

[28] Cox, B.N. and Q.D. Yang, In quest of virtual tests for structural composites. *Science,* 2006. 314: p. 1102–1107. http://dx.doi.org/10.1126/science.1131624. PMid:17110566.

[29] Yang, Q.D. and B.N. Cox, Cohesive models for damage evolution in laminated composites. *International Journal of Fracture,* 2005. 133(2): p. 107–137. http://dx.doi.org/10.1007/s10704-005-4729-6.

[30] Corigliano, A., Formulation, identification and use of interface models in the numerical analysis of composite delamination. *International Journal of Solids and Structures,* 1993. 30: p. 2779–2811. http://dx.doi.org/10.1016/0020-7683(93)90154-Y.

[31] de Borst, R., Numerical aspects of cohesive-zone models. *Engineering Fracture Mechanics,* 2003. 70: p. 1743–1757. http://dx.doi.org/10.1016/S0013-7944(03)00122-X.

[32] Elices, M., *et al.*, The cohesive zone model: Advantages, limitations and challenges. *Engineering Fracture Mechanics,* 2002. 69: p. 137–163. http://dx.doi.org/10.1016/S0013-7944(01)00083-2.

[33] Moës, N. and T. Belytschko, Extended finite element method for cohesive crack growth. *Engineering Fracture Mechanics,* 2002. 69: p. 813–833. http://dx.doi.org/10.1016/S0013-7944(01)00128-X.

[34] Needleman, A., An Analysis of Decohesion along an Imperfect Interface. International Journal of Fracture, 1990. 42: p. 21–40. http://dx.doi.org/10.1007/BF00018611.

[35] Remmers, J.J.C., R. de Borst, and A. Needleman, A cohesive segments method for the simulation of crack growth. *Computational Mechanics,* 2003. 31(1-2): p. 69–77. http://dx.doi.org/10.1007/s00466-002-0394-z.

[36] Wisnom, M.R. and F.-K. Chang, Modelling of Splitting and Delamination in Notched Cross-Ply Laminates. *Composites Science and Technology,* 2000. 60: p. 2849–2856. http://dx.doi.org/10.1016/S0266-3538(00)00170-6.

[37] Parmigiani, J. and M.D. Thouless, The Roles of Toughness And Cohesive Strength on Crack Deflection at Interfaces. *J. Mech. Phys. Solids,* 2006. 54: p. 266–287. http://dx.doi.org/10.1016/j.jmps.2005.09.002.

[38] Xie, D., *et al.*, Discrete cohesive zone model to simulate static fracture in 2D tri-axially braided carbon fiber composites. *Journal of Composite Materials,* 2006. 40: p. 2025–2046. http://dx.doi.org/10.1177/0021998306061320.

[39] Yang, Q. and M.D. Thouless, Mixed mode fracture of plastically-deforming adhesive joints. *International Journal of Fracture,* 2001. 110: p. 175–187. http://dx.doi.org/10.1023/A:1010869706996.

[40] Yang, Q.D., M.D. Thouless, and S.M. Ward, Numerical Simulations of Adhesively-Bonded Beams Failing with Extensive Plastic Deformation. *Journal of the Mechanics and Physics of Solids,* 1999. 47: p. 1337–1353. http://dx.doi.org/10.1016/S0022-5096(98)00101-X.

[41] Yang, Q.D., M.D. Thouless, and S.M. Ward, Elastic-Plastic Mode-II Fracture of Adhesive Joints. *International Journal of Solids and Structures,* 2001. 38: p. 3251–3262. http://dx.doi.org/10.1016/S0020-7683(00)00221-3.

[42] He, M.-Y. and J.W. Hutchinson, Crack Deflection at an Interface Between Dissimilar Materials. *Int. J. Solids Struct.,* 1989. 25: p. 1053–1067. http://dx.doi.org/10.1016/0020-7683(89)90021-8.

[43] Fang, X.J., *et al.*, An Augmented Cohesive Zone Element for Arbitrary Crack Coalescence and Bifurcation in Heterogeneous Materials. *International Journal for Numerical Methods in Engineering,* 2011. 88: p. 841–861. http://dx.doi.org/10.1002/nme.3200.

[44] Ling, D.S., *et al.*, Nonlinear fracture analysis of delamination crack jumps in laminated composites. Journal of Aerospace Engineering, 2011. 24: p. 181–188. http://dx.doi.org/10.1061/(ASCE)AS.1943-5525.0000008.

[45] Parmigiani, J. and M.D. Thouless, The Effects of cohesive strength and toughness on mixed-mode delamination of beam-like geometries. *Engin. Fract. Mech.,* 2007. 74: p. 2675–2699. http://dx.doi.org/10.1016/j.engfracmech.2007.02.005.

[46] Van de Meer, F.P. and L.J. Sluys, A phantom node formulation with mixed mode cohesive law for splitting in laminates. *Int J Fracture,* 2009. 158: p. 107–124. http://dx.doi.org/10.1007/s10704-009-9344-5.

[47] Van de Meer, F.P., C. Oliver, and L.J. Sluys, Computational analysis of progressive failure in a notched laminate including shear nonlinearity and fiber failure. *Composite Science and Technology,* 2010. 70: p. 692–700. http://dx.doi.org/10.1016/j.compscitech.2010.01.003.

[48] Babuška, I. and J.M. Melenk, The partition of unity method. *International Journal for Numerical Methods in Engineering,*

1997. 40: p. 727–758. http://dx.doi.org/10.1002/(SICI)1097-0207(19970228)40:4<727::AID-NME86>3.0.CO;2-N.

[49] Melenk, J.M. and I. Babuška, The partition of unity finite element method: Basic theory and applications. *Computer Methods in Applied Mechanics and Engineering,* 1996. 139(1-4): p. 289–314. http://dx.doi.org/10.1016/S0045-7825(96)01087-0.

[50] Moës, N., J. Dolbow, and T. Belytschko, A finite element method for crack growth without remeshing. *International Journal for Numerical Methods in Engineering,* 1999. 46: p. 131–150. http://dx.doi.org/10.1002/(SICI)1097-0207(19990910)46:1<131::AID-NME726>3.0.CO;2-J.

[51] Strouboulis, T., K. Copps, and I. Babuška, The generalized finite element method. *Computational Mechanics Advances,* 2001. 190: p. 4801–4193.

[52] Daux, C., *et al.*, Arbitrary branched and intersecting cracks with the extended finite element method. *International Journal for Numerical Methods in Engineering,* 2000. 48: p. 1741–1760. http://dx.doi.org/10.1002/1097-0207(20000830)48:12<1741::AID-NME956>3.0.CO;2-L.

[53] Hettich, T., A. Hund, and E. Ramm, Modeling of failure in composites by X-FEM and level sets within a multiscale framework. *Computer Methods in Applied Mechanics and Engineering,* 2008. 197(5): p. 414–424. http://dx.doi.org/10.1016/j.cma.2007.07.017.

[54] Huynh, D.B.P. and T. Belytschko, The extended finite element method for fracture in composite materials. *International Journal for Numerical Methods in Engineering,* 2009. 77: p. 214–239. http://dx.doi.org/10.1002/nme.2411.

[55] Wells, G.N. and L.J. Sluys, A new method for modeling cohesive cracks using finite elements. *International Journal for Numerical Methods in Engineering,* 2001. 50: p. 2667–2682. http://dx.doi.org/10.1002/nme.143.

[56] Wells, G.N. and L.J. Sluys, Three-dimensional embedded discontinuity model for brittle fracture. *International Journal of Solid and Structures,* 2001. 38(5): p. 897–913. http://dx.doi.org/10.1016/S0020-7683(00)00029-9.

[57] Wells, G.N., L.J. Sluys, and R. de Borst, Simulating the propagation of displacement discontinuities in a regularized strain-softening medium. *International Journal for Numerical Methods in Engineering,* 2002. 53(5): p. 1235–1256. http://dx.doi.org/10.1002/nme.375.

[58] Song, J.H., P.M.A. Areias, and T. belytschko, A method for dynamic crack and shear band propagation with phantom nodes. *Inter. J. Numer. Meth. Engng,* 2006. 67: p. 868–893. http://dx.doi.org/10.1002/nme.1652.

[59] Remmers, J.C., *Discontinuities in Materials and Structures—A Unifying Computational Approach,* 2006, Delft University.

[60] Remmers, J.J.C., R. de Borst, and A. Needleman, A cohesive segments method for the simulation of crack growth. *Computational Mechanics,* 2003. 31(1-2 spec.): p. 69–77.

[61] Hansbo, A. and P. Hansbo, A finite element method for the simulation of strong and weak discontinuities in solid mechanics. *Computer Methods in Applied Mechanics and Engineering,* 2004. 193: p. 3523–3540. http://dx.doi.org/10.1016/j.cma.2003.12.041.

[62] Dolbow, J., N. Moës, and T. Belytschko, Discontinuous enrichment in finite elements with a partition of unity method. *Finite Elements in Analysis and Design,* 2000. 36: p. 235–260. http://dx.doi.org/10.1016/S0168-874X(00)00035-4.

[63] Budyn, E.R.L., *Multiple Crack Growth by the Extended Finite Element Method[D]*. 2004, Northwestern University: Evanston, Illinois.

[64] Fries, T.P. and T. Belytschko, The intrinsic XFEM: a method for arbitryr discontinuities without additional unknowns. *International Hournal for Numerical Methods in Engineering,* 2006. 68: p. 1358–1385. http://dx.doi.org/10.1002/nme.1761.

[65] de Borst, R., J.J.C. Remmers, and A. Needleman, Mesh-independent discrete numerical representations of cohesive-zone models. *Engineering Fracture Mechanics,* 2006. 73(2): p. 160–177. http://dx.doi.org/10.1016/j.engfracmech.2005.05.007.

[66] Borden, M.J., *et al.*, *A Phase-field Description of Dynamic Brittle Fracture,* 2011, The Institute for Computational Engineering and Sciences, The University of Texas at Austin.

[67] Belytschko, T., J. Fish, and B.E. Engelmann, A finite element with embedded localization zones. *Computer Methods in Applied Mechanics and Engineering,* 1988. 70(1): p. 59–89. http://dx.doi.org/10.1016/0045-7825(88)90180-6.

[68] Dvorkin, E.N., A.M. Cuitiño, and G. Gioia, Finite elements with displacement interpolated embedded localization lines insensitive to mesh size and distortions. *International Journal for Numerical Methods in Engineering,* 1990. 30(3): p. 541–564. http://dx.doi.org/10.1002/nme.1620300311.

[69] Ortiz, M., A. Leroy, and A. Needleman, A finite element method for localized failure analysis. *Computational methods in Applied Mechanics and Engineering,* 1987. 61: p. 189–214. http://dx.doi.org/10.1016/0045-7825(87)90004-1.

[70] Simo, J.C., J. Oliver, and F. Armero, An analysis of strong discontinuities induced by softening solutions in rate-independent solids. *Journal of Computaional Mechanics,* 1993. 12: p. 277–296. http://dx.doi.org/10.1007/BF00372173.

[71] Armero, F. and K. Garikipati, An analysis of strong discontinuities in multiplicative finite strain plasticity and their relation with the numerical simulation of strain localization in solids. *International Journal of Solids & Structures,* 1996. 33: p. 2863–2885. http://dx.doi.org/10.1016/0020-7683(95)00257-X.

[72] Alfaiate, J., G.N. Wells, and L.J. Sluys, On the use of embedded discontinuity elements with crack path continuity for mode-I and mixed-mode fracture. *Engineering Fracture Mechanics,* 2002. 69: p. 661–686. http://dx.doi.org/10.1016/S0013-7944(01)00108-4.

[73] Ibrahimbegovic, A. and S. Melnyk, Embedded discontinuity finite element method for modeling of localized failure in heterogeneous materials with structured mesh: an alternative to extended finite element method. *Computational Mechanics,* 2007. 40(1): p. 149–155. http://dx.doi.org/10.1007/s00466-006-0091-4.

[74] Sluys, L.J. and A.H. Berends, Discontinuous failure analysis for mode-I and mode-II localization problems. *Int. J. Solids Struct.,* 1998. 35: p. 4257–4274. http://dx.doi.org/10.1016/S0020-7683(97)00313-2.

[75] Linder, C. and F. Armero, Finite elements with embedded branching. *Finite Elements in Analysis and Design,* 2009. 45: p. 280–293. http://dx.doi.org/10.1016/j.finel.2008.10.012.

[76] Linder, C. and F. Armero, Finite elements with embedded strong discontinuities for themodeling of failure in solids. *International J. Numer. Meth. Engng,* 2007. 72: p. 1391–1433. http://dx.doi.org/10.1002/nme.2042.

[77] Dias-da-Costa, D., *et al.*, Towards a generalization of a discrete strong discontinuity approach. *Computational methods in Applied Mechanics and Engineering,* 2009. 198: p. 3670–3681. http://dx.doi.org/10.1016/j.cma.2009.07.013.

[78] Pineda, E.J., , Progressive damage and failure modeling in notched laminated fiber reinforced composites. *International Journal of Fracture,* 2009. 158: p. 125–143. http://dx.doi.org/10.1007/s10704-009-9370-3.

[79] Rudraraju, S., *et al.*, In-plane fracture of laminated fiber reinforced composites with varying fracture resistance: Experimental observations and numerical crack propagation simulations. *International Journal of Solids and Structures,* 2010. 47: p. 901–911. http://dx.doi.org/10.1016/j.ijsolstr.2009.12.006.

[80] Rudraraju, S., *et al.*, Experimental observations and numerical simulations of curved crack propagation in laminated fiber composites. *Composites Science and Technology,* 2011. xx: p. xxx–xxx.

[81] Hansbo, A. and P. Hansbo, A finite element method for the simulation of strong and weak discontinuities in solid mechanics. *Computational methods in Applied Mechanics and Engineering,* 2004. 193: p. 3523–3540. http://dx.doi.org/10.1016/j.cma.2003.12.041.

[82] Hansbo, A. and P. Hansbo, An unfitted finite element method, based on Nitsche's method, for elliptic interface problems. *Computational methods in Applied Mechanics and Engineering,* 2002. 191: p. 5537–5552. http://dx.doi.org/10.1016/S0045-7825(02)00524-8.

[83] Jager, P., P. Steinmann, and E. Kuhl, On local tracking algorithms for the simulation of three-dimensional discontinuities. *Computational Mechanics,* 2008. 42: p. 395-406. http://dx.doi.org/10.1007/s00466-008-0249-3.

[84] Mergheim, J., E. Kuhl, and P. Steinmann, A finite element method for the computational modeling of cohesive cracks. *International Journal for Numerical Methods in Engineering,* 2005. 63: p. 276–289. http://dx.doi.org/10.1002/nme.1286.

[85] Ling, D.S., Q.D. Yang, and B.N. Cox, An augmented finite element method for modeling arbitrary discontinuities in composite materials. *International Journal of Fracture,* 2009. 156: p. 53–73. http://dx.doi.org/10.1007/s10704-009-9347-2.

[86] Yang, Q.D., *et al.*, A-FEM for complex multi-scale damage evolution in laminated composites , May 2010. *Proceddings of SAMPE Technical Conference,* Paper #465, 2010. 42: p. 1–8.

[87] Fang, X.J., *et al.*, High-Fidelity Simulations of Multiple Fracture Processes in a Laminated Composites in Tension. *Journal of the Mechanics and Physics of Solids,* 2011. 59: p. 1355–1373. http://dx.doi.org/10.1016/j.jmps.2011.04.007.

[88] Hallett, S.R. and M.R. Wisnom, Experimental Investigation of Progressive Damage and the Effect of Layup in Notched Tensile Tests. *Journal of Composite Materials,* 2006b. 40: p. 119–141. http://dx.doi.org/10.1177/0021998305053504.

[89] Yang, Q. and B.N. Cox, Cohesive Models for damage evolution in laminated composites. *International Journal of Fracture,* 2005. 133: p. 107–137. http://dx.doi.org/10.1007/s10704-005-4729-6.

[90] Wright, P., *et al.*, High resolution tomographic imaging and modelling of notch tip damage in a laminated composite. *Composites Science and Technology,* 2010. 70: p. 1444–1452. http://dx.doi.org/10.1016/j.compscitech.2010.04.012.

[91] Davila, C.G., P.P. Camanho, and C.A. Rose, Failure Criteria for FPR Laminates. *Journal of Composite Materials,* 2005. 39: p. 323–345. http://dx.doi.org/10.1177/0021998305046452.

[92] Camanho, P.P., *et al.*, Prediction of in situ strengths and matrix cracking in composites under transverse tension and in-plane shear. *Composite Part A: Applied Science and Manufacturing,* 2006. 37: p. 165–176. http://dx.doi.org/10.1016/j.compositesa.2005.04.023.

[93] Zhou, Z.Q., *et al.*, The evolution of a transverse intra-ply crack coupled to delamination cracks. *Inter. J. Fract,* 2010. 165: p. 77–92. http://dx.doi.org/10.1007/s10704-010-9506-5.

[94] Dvorak, G.J. and N. Laws, Analysis of progressive matrix cracking in composite laminates II. First ply failure. *Journal of Composite Materials,* 1987. 21: p. 309–329. http://dx.doi.org/10.1177/002199838702100402.

[95] Ho, S. and Z. Suo, Microcracks tunneling in brittle matrix composites driven by thermal expansion mismatch. *Acta Metallurgica et Materialia,* 1992. 40(7): p. 1685–1690. http://dx.doi.org/10.1016/0956-7151(92)90111-Q

[96] Cox, B.N. and D.B. Marshall, Crack initiation in brittle fiber reinforced laminates. *Journal of the American Ceramic Society,* 1996. 79(5): p. 1181–1188. http://dx.doi.org/10.1111/j.1151-2916.1996.tb08570.x.

[97] Yang, Q.D., *et al.*, Virtual Testing for Advanced Aerospace Composites: Advances and Future Needs. *Journal of Engineering Materials and Technology,* 2011. 133: p. 11002–11008. http://dx.doi.org/10.1115/1.4002637.

[98] Liu, W., *et al.*, An Accurate and Efficient Augmented Finite Element Method for Arbitrary Crack Interactions. *Journal of Applied Mechanics,* 2012. In press.

[99] Ben Dhia, H. and G. Rateau, The Arlequin method as a flexible engineering design tool. *International Journal for Numerical Methods in Engineering,* 2005. 62: p. 1442–1462. http://dx.doi.org/10.1002/nme.1229.

[100] Qiao, H., *et al.*, Implementation of the Arlequin method into ABAQUS: Basic formulation and applications. *Advances in Engineering Software,* 2011. 42: p. 197–207.